

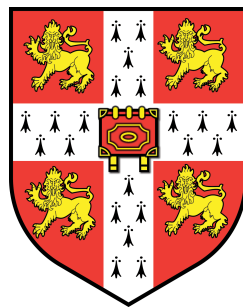
A study of charged $B \rightarrow DK$ and $B \rightarrow D\pi$ decays with the LHCb experiment

Susan Carol Haines

of

Jesus College

University of Cambridge



A dissertation submitted to the University of Cambridge

for the degree of Doctor of Philosophy

December 2011



Abstract

The LHCb experiment at the Large Hadron Collider is dedicated to making precision measurements of \mathcal{CP} -violation and rare decays, thereby searching indirectly for new phenomena beyond the Standard Model (SM) of particle physics. The Ring Imaging Cherenkov (RICH) subdetectors provide essential particle identification information for many LHCb physics analyses, including the analysis detailed in this thesis. Selection criteria have been developed which allow the monitoring of the refractive indices of the RICH radiators using isolated Cherenkov light rings, both with and without information from other subdetectors. This, in turn, ensures that the information provided by the RICH subdetectors is of the highest quality.

The decay $B^\pm \rightarrow \bar{D}^0/D^0(K_S^0\pi^+\pi^-)K^\pm$ allows a measurement of the CKM angle γ to be made using the GGSZ (Dalitz) method. This provides a SM benchmark against which new phenomena can be compared. Accurate RICH particle identification is vital in separating signal $B^\pm \rightarrow \bar{D}^0/D^0(K_S^0\pi^+\pi^-)K^\pm$ decays from those of the control channel $B^\pm \rightarrow \bar{D}^0/D^0(K_S^0\pi^+\pi^-)\pi^\pm$. The selection of signal decays has been optimised using simulated events. In the first proton-proton collision data collected at a centre-of-mass energy of 7 TeV during 2010 and corresponding to an integrated luminosity of $\sim 36.5 \text{ pb}^{-1}$, the ratio of branching fractions $\frac{\text{Br}(B^\pm \rightarrow \bar{D}^0/D^0(K_S^0\pi^+\pi^-)K^\pm)}{\text{Br}(B^\pm \rightarrow \bar{D}^0/D^0(K_S^0\pi^+\pi^-)\pi^\pm)} = 0.12_{-0.05}^{+0.06} \pm 0.03$ has been measured, where the first error is statistical and the second systematic. A further data set, recorded in 2011 and corresponding to an integrated luminosity of $\sim 342 \text{ pb}^{-1}$ at $\sqrt{s} = 7 \text{ TeV}$, has been used to measure the ratio of branching fractions to higher precision. The results were extracted using two independent samples of $B^\pm \rightarrow \bar{D}^0/D^0(K_S^0\pi^+\pi^-)K^\pm$ and $B^\pm \rightarrow \bar{D}^0/D^0(K_S^0\pi^+\pi^-)\pi^\pm$ decays where the K_S^0 decay occurs either near to the proton-proton interaction point or further into the LHCb detector. The results are $\frac{\text{Br}(B^\pm \rightarrow \bar{D}^0/D^0(K_S^0\pi^+\pi^-)K^\pm)}{\text{Br}(B^\pm \rightarrow \bar{D}^0/D^0(K_S^0\pi^+\pi^-)\pi^\pm)} = 0.089_{-0.014}^{+0.015} \pm 0.006$ and $0.07 \pm 0.02 \pm 0.01$ respectively, where the first errors are statistical and the second systematic.

Declaration

This dissertation is the result of my own work and includes nothing which is the outcome of work done in collaboration except where specifically indicated in the text. It has not been submitted for another qualification to this or any other university. This dissertation does not exceed the word limit for the respective Degree Committee.

Susan Haines

Acknowledgements

I would like to express my gratitude to all those who have provided support, guidance and advice during my studies. I would like to thank STFC for their funding of this work and the Fellows of Jesus College for providing additional support. In particular, I wish to thank Val Gibson, my supervisor, for invaluable discussions, for advice and for being infinitely patient when I have asked very basic questions! Thanks to Chris Jones for not laughing too much when faced with my best attempts at coding in my first (and last!) term and for making my foray into the murky depths of the reconstruction software fairly painless. I would also like to thank Jeremy Dickens, Ying Ying Li and Gareth Rogers for providing help when they almost certainly had better things to be doing. Without their advice the details of DaVinci, ROOT and RooFit would still be a mystery to me. Thanks to my LHCb collaborators, in particular the RICH group and my physics working group, and to Mitesh Patel for providing advice at a crucial time in my analysis work. In addition, thanks to all of the other current and former members of the Cambridge HEP group, especially to those who have made tea breaks, lunchtimes and pub trips so entertaining. A special mention must go to John Hill and Steve Wotton for resurrecting my PC on all of the occasions that I upset it by doing something unreasonable, like trying to run OpenOffice.

Finally, I would like to thank my parents and friends for their encouragement and support throughout the past four years.

Preface

The Standard Model of particle physics is the theory comprising our current understanding of fundamental particles and their interactions. It successfully describes experimental observations for three of the four forces of nature, but still leaves open many questions, for example the origin of the observed matter-antimatter asymmetry in the Universe. The phenomenon of \mathcal{CP} -violation, along with \mathcal{C} -violation, baryon number violation and departure from thermal equilibrium, is required in order to explain this dominance of matter over antimatter [1]. \mathcal{CP} -violation can be accommodated in the Standard Model but the level at which it is included is insufficient to explain the matter-antimatter asymmetry observations. The LHCb experiment at the Large Hadron Collider is dedicated to making precision measurements of \mathcal{CP} -violation and rare decays, thereby allowing indirect searches for new phenomena beyond the Standard Model to be made.

This thesis primarily describes the first studies of $B^\pm \rightarrow \bar{D}^0/D^0(K_S^0\pi^+\pi^-)K^\pm$ and $B^\pm \rightarrow \bar{D}^0/D^0(K_S^0\pi^+\pi^-)\pi^\pm$ decays and in particular measurements of the ratio of branching fractions $\frac{\text{Br}(B^\pm \rightarrow \bar{D}^0/D^0(K_S^0\pi^+\pi^-)K^\pm)}{\text{Br}(B^\pm \rightarrow \bar{D}^0/D^0(K_S^0\pi^+\pi^-)\pi^\pm)}$ with LHCb data. This is an initial step towards the use of $B^\pm \rightarrow \bar{D}^0/D^0(K_S^0\pi^+\pi^-)K^\pm$ decays to make a tree-level measurement of the CKM angle γ using the GGSZ (Dalitz) method. The tree-level measurement provides a benchmark of γ in the Standard Model against which other measurements can be compared; $B^\pm \rightarrow \bar{D}^0/D^0(K_S^0\pi^+\pi^-)\pi^\pm$ decays are an important control sample in this analysis.

Good performance of kaon and pion particle identification from the LHCb RICH sub-detectors is vital in separating $B^\pm \rightarrow \bar{D}^0/D^0(K_S^0\pi^+\pi^-)K^\pm$ from $B^\pm \rightarrow \bar{D}^0/D^0(K_S^0\pi^+\pi^-)\pi^\pm$ decays. In order to ensure the highest possible quality of the data, it is therefore important to monitor the conditions within the RICH subdetectors from data.

Chapter 1 outlines the phenomenon of \mathcal{CP} -violation, with particular reference to the Standard Model and the B-meson system. An overview of the Large Hadron Collider and the LHCb experiment, including details of the aspects of the experimental apparatus specifically optimised for the study of b-hadron decays, is given in Chapter 2. As described in Appendix B, isolated rings in the LHCb RICH subdetectors can be used to allow the monitoring of the refractive indices of the RICH radiators from data. A description of the optimisation of selection criteria for $B^\pm \rightarrow \bar{D}^0/D^0(K_S^0\pi^+\pi^-)K^\pm$ decays using simulated events is outlined in Chapter 3. The criteria are used to select $B^\pm \rightarrow \bar{D}^0/D^0(K_S^0\pi^+\pi^-)K^\pm$ and $B^\pm \rightarrow \bar{D}^0/D^0(K_S^0\pi^+\pi^-)\pi^\pm$ candidate decays from $\sim 36.5 \text{ pb}^{-1}$ of $\sqrt{s} = 7 \text{ TeV}$ proton-proton collision data recorded in 2010. These candidates are then used to evaluate the ratio of branching fractions $\frac{\text{Br}(B^\pm \rightarrow \bar{D}^0/D^0(K_S^0\pi^+\pi^-)K^\pm)}{\text{Br}(B^\pm \rightarrow \bar{D}^0/D^0(K_S^0\pi^+\pi^-)\pi^\pm)}$, as detailed in Chapter 4. Further, more precise measurements of the ratio of branching fractions, made using candidate decays from $\sim 342 \text{ pb}^{-1}$ of proton-proton collision data at $\sqrt{s} = 7 \text{ TeV}$ recorded in 2011, are described in Chapter 5. A summary of the studies of this thesis and of future prospects is given in Chapter 6.

Contents

1	Charge-parity violation in the B-meson system	1
1.1	The \mathcal{C} , \mathcal{P} and \mathcal{T} operators	2
1.2	Model independent \mathcal{CP} -violation	2
1.2.1	Neutral meson mixing	3
1.2.2	Types of \mathcal{CP} -violation	6
1.3	\mathcal{CP} -violation in the Standard Model	11
1.3.1	The CKM matrix	13
1.4	Constraining the CKM parameters	18
1.4.1	Current status of CKM matrix element magnitude measurements	18
1.4.2	Indirect CKM measurements	19
1.4.3	Direct CKM measurements	20
1.5	The time-independent measurement of γ from $B \rightarrow DK^{(*)}$ decays	24
1.5.1	The GLW method	27
1.5.2	The ADS method	30
1.5.3	The GGSZ (Dalitz) method	31
1.5.4	Combined time-independent γ measurement	34
1.6	Summary	35
2	The LHCb experiment at the LHC	37

2.1	The Large Hadron Collider	37
2.2	The LHCb experiment	40
2.2.1	LHCb luminosity	40
2.2.2	Heavy flavour production	40
2.2.3	b-hadron decays	44
2.2.4	Beam-pipe	47
2.2.5	Vertex locator	48
2.2.6	Tracking system	54
2.2.7	Dipole magnet	58
2.2.8	The RICH subdetectors and particle identification	59
2.2.9	Calorimeters	67
2.2.10	Muon system	69
2.2.11	LHCb trigger system	73
2.3	Detector control, monitoring and data flow	77
2.4	LHCb software and Monte-Carlo simulation	78
2.4.1	Monte-Carlo event simulation	78
2.4.2	HLT (software trigger)	79
2.4.3	Event reconstruction and analysis	79
2.5	2010 and 2011 data-taking	80
2.6	Summary	84
3	$B^\pm \rightarrow D(K_S^0 \pi^+ \pi^-)K^\pm$ candidate reconstruction and selection	85
3.1	$B^\pm \rightarrow D(K_S^0 \pi^+ \pi^-)K^\pm$ reconstruction	85
3.2	Monte-Carlo event samples	86
3.3	Selection variables and the signal preselection	87

3.4	Optimisation of the $B^\pm \rightarrow D(K_S^0 \pi^+ \pi^-) K^\pm$ candidate selection	91
3.5	Selection optimisation results	97
3.6	Estimated candidate yields	109
3.7	Summary	109
4	A measurement of the ratio of branching fractions $\text{Br}(B^\pm \rightarrow DK^\pm) / \text{Br}(B^\pm \rightarrow D\pi^\pm)$ using 2010 data	111
4.1	Introduction	113
4.2	Decay selection criteria	114
4.3	Mass fit	119
4.3.1	Signal and background fits to Monte-Carlo	119
4.3.2	Fit to 2010 data	125
4.3.3	Fit results and ratio of yields	130
4.4	Determination of efficiencies	133
4.5	Evaluation of the ratio of branching fractions	137
4.6	Systematic uncertainties	137
4.6.1	Systematic error from integrated luminosity measurements and statistical errors	139
4.6.2	Systematic error from global average branching fraction errors	140
4.6.3	Systematic error from estimation of the trigger efficiency	140
4.6.4	Systematic error from the determination of the PID efficiency	142
4.6.5	Systematic error from the mass fit PDF parameterisation	144
4.6.6	Total systematic uncertainty	147
4.7	Summary	148
5	A measurement of the ratio of branching fractions $\text{Br}(B^\pm \rightarrow DK^\pm) / \text{Br}(B^\pm \rightarrow D\pi^\pm)$ using 2011 data	149

5.1	Decay selection criteria	149
5.2	Mass fit	154
5.2.1	Signal and background fits to Monte-Carlo	154
5.2.2	Fit to 2011 data	173
5.2.3	Fit results and ratio of yields	178
5.3	Determination of efficiencies	183
5.4	Evaluation of the ratio of branching fractions	189
5.5	Systematic uncertainties	189
5.5.1	Systematic error from integrated luminosity measurements and statistical errors	190
5.5.2	Systematic error from global average branching fraction errors . .	192
5.5.3	Systematic error from the determination of the PID efficiency . .	192
5.5.4	Systematic error from the mass fit PDF parameterisation	193
5.5.5	Total systematic uncertainties	195
5.6	Summary	196
6	Summary and outlook	199
6.1	Summary	199
6.2	Outlook	201
A	Cherenkov radiation	207
B	Isolated Cherenkov rings in the LHCb RICH subdetectors	209
B.1	Isolated RICH rings with tracks	210
B.1.1	Cherenkov angles θ and ϕ	211
B.1.2	Selection criteria	211

B.1.3	Cherenkov angle resolution distributions from isolated rings with tracks	216
B.1.4	Background contributions	220
B.1.5	Changes in resolution with variation of radiator pressure	221
B.2	Isolated trackless rings	222
B.2.1	Selection criteria	223
B.2.2	Ring radius distribution and changes with varying radiator pressure	224
B.3	Usage in proton-proton collision data-taking	227
B.3.1	Monitoring with isolated rings with tracks	227
B.3.2	Monitoring with isolated trackless rings	227
B.4	Summary	229
C	Comparison of MC10 and 2010 data	231
	List of Figures	239
	List of Tables	249
	Bibliography	251

Chapter 1

Charge-parity violation in the B-meson system

The Standard Model (SM) [2–4] is the theory embodying our current understanding of particles and their interactions, successfully describing experimental observations for three of the four fundamental forces of nature. Symmetries play an important role in nature and are central to our description of the behaviour of matter. The SM is composed of three independent continuous symmetry groups, denoted $SU(3) \times SU(2) \times U(1)$, providing a unified framework in gauge field theory for the strong, weak and electromagnetic interactions. The SM does not, however, provide a complete description of fundamental processes, indicating that it may be a low-energy effective theory of a higher energy scale unified fundamental theory. The SM leaves open many questions about the inclusion of gravity, the origin of mass, the fermion mass hierarchy and the matter-antimatter asymmetry in the Universe; it is therefore vital to extend our understanding beyond the SM. As the quark sector uniquely spans the full SM local gauge symmetry, flavour physics is the ideal area in which to do this by testing the SM to its limits and searching for New Physics (NP) phenomena.

This chapter begins with an introduction to the underlying symmetries of the SM in Section 1.1 and continues with a description of model independent \mathcal{CP} -violation in Section 1.2. \mathcal{CP} -violation within the SM is discussed in Section 1.3, followed by an overview of experimental constraints on the Cabibbo-Kobayashi-Maskawa (CKM) parameters of the SM in Section 1.4. Finally, in Section 1.5, the experimental methods used to measure the CKM angle γ with $B \rightarrow DK^{(*)}$ decays and the current experimental results for these methods are summarised.

1.1 The \mathcal{C} , \mathcal{P} and \mathcal{T} operators

There are three discrete symmetry operators, \mathcal{C} , \mathcal{P} and \mathcal{T} , which are key to SM field interactions. The actions of these operators can be interpreted in terms of the Lorentz four-vector of a particle as follows:

- the charge conjugation operator, \mathcal{C} , acts to turn a particle into its antiparticle, leaving its spin and momentum unchanged;
- the parity operator, \mathcal{P} , acts to flip the spatial coordinate system of the particle, $(t, \vec{x}) \rightarrow (t, -\vec{x})$. This is equivalent to a mirror reflection followed by a 180° rotation and reverses the momentum of the particle but leaves its spin and angular momentum unchanged; and
- the time reversal operator, \mathcal{T} , acts to reverse the time coordinate of the particle, $(t, \vec{x}) \rightarrow (-t, \vec{x})$. It reverses both its spin and momentum.

Local field theories have an exact symmetry under the action of the combination of the three operators \mathcal{CPT} [5–7] and most SM interactions are also invariant under the action of \mathcal{C} , \mathcal{P} and \mathcal{T} separately. The weak interaction, however, violates both \mathcal{C} and \mathcal{P} symmetries [8–10]. Many gauge field theories such as Quantum Electrodynamics (QED) and Quantum Chromodynamics (QCD) are invariant under a combined \mathcal{CP} transformation and it was expected that \mathcal{CP} would be a good symmetry of nature. In 1964, however, \mathcal{CP} -violation was observed in the neutral kaon system [11]. Predictions for \mathcal{CP} -violation in the B-meson system were made in the 1980s [12, 13], but experimental observations of the effect at BaBar and Belle [14–17], the experiments at the B-factories, were not made until 2001. \mathcal{CP} -violation is physically important as its existence is required in order to explain the dominance of matter over antimatter in our Universe [1].

1.2 Model independent \mathcal{CP} -violation

This section outlines the phenomenology of \mathcal{CP} -violation with specific reference to the B-meson system, starting with neutral meson mixing.

1.2.1 Neutral meson mixing

Mesons are colour-singlet states formed from a quark and an antiquark. B-mesons are bound states of the b-quark (antiquark), the lightest member of the third generation SM quark doublet, with an u, d, c or s antiquark (quark), forming the flavour eigenstates B^- (B^+), \bar{B}_d^0 (B_d^0), B_c^- (B_c^+) and \bar{B}_s^0 (B_s^0) respectively.

Neutral mesons can, in general, oscillate between particle and antiparticle states as a result of the lack of flavour conservation in the weak interaction; the Feynman diagrams for this behaviour in the neutral B-meson system are shown in Figure 1.1.

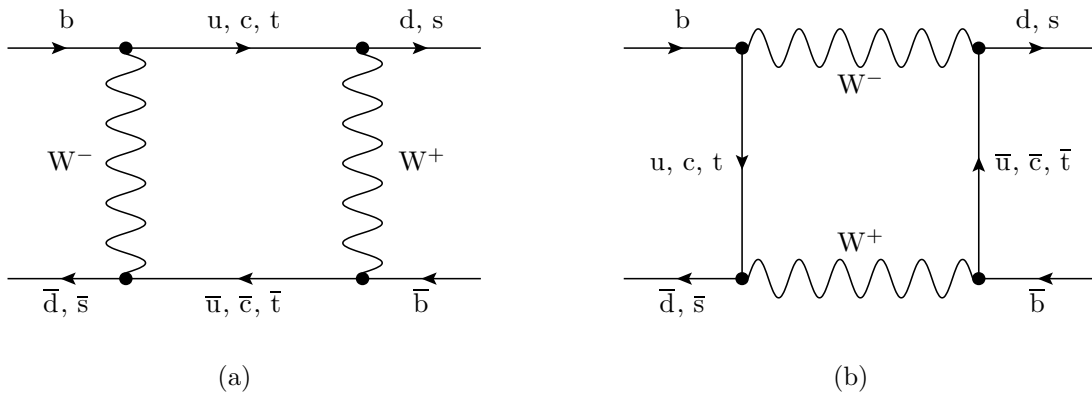


Figure 1.1: Feynman diagrams for neutral B-meson mixing.

In this chapter, X^0 denotes any neutral meson and \bar{X}^0 denotes its antiparticle. The time evolution of an arbitrary linear combination of the flavour eigenstates

$$a(t)|X^0\rangle + b(t)|\bar{X}^0\rangle \quad (1.1)$$

can be described by the time-dependent differential equation

$$i\frac{\partial}{\partial t} \begin{pmatrix} a \\ b \end{pmatrix} = \underbrace{\begin{pmatrix} M_{11} - \frac{i}{2}\Gamma_{11} & M_{12} - \frac{i}{2}\Gamma_{12} \\ M_{12}^* - \frac{i}{2}\Gamma_{12}^* & M_{22} - \frac{i}{2}\Gamma_{22} \end{pmatrix}}_H \begin{pmatrix} a \\ b \end{pmatrix}, \quad (1.2)$$

where the elements of the effective Hamiltonian matrix H_{ij} have been decomposed into M_{ij} and Γ_{ij} , elements of the mass and decay matrices respectively. These elements are associated with measurable quantities; invariance under the \mathcal{CPT} symmetry operator implies that particle and antiparticle masses and lifetimes are equal, hence $M_{11} = M_{22} \equiv$

M and $\Gamma_{11} = \Gamma_{22} \equiv \Gamma$. Diagonalising H results in two stationary eigenstates which can be expressed as linear combinations of the particle and antiparticle states,

$$|X_1\rangle = p|X^0\rangle + q|\bar{X}^0\rangle \quad (1.3)$$

$$|X_2\rangle = p|X^0\rangle - q|\bar{X}^0\rangle \quad (1.4)$$

where p and q are complex constants representing the amount of meson state mixing, normalised by the condition $|p|^2 + |q|^2 = 1$. The energy eigenvalues of $|X_{1,2}\rangle$, $E_{1,2}$, are obtained from the characteristic equation

$$|H - EI| = 0, \quad (1.5)$$

giving

$$\begin{aligned} E_{1,2} &= M_{1,2} - \frac{i}{2}\Gamma_{1,2} \\ &= M - \frac{i}{2}\Gamma \pm \sqrt{(M_{12} - \frac{i}{2}\Gamma_{12})(M_{12}^* - \frac{i}{2}\Gamma_{12}^*)} \\ &= \left(M \mp \frac{\Delta M}{2}\right) - \frac{i}{2}\left(\Gamma \mp \frac{\Delta\Gamma}{2}\right) \end{aligned} \quad (1.6)$$

where $M_{1,2}$ and $\Gamma_{1,2}$ are the masses and decay widths of the eigenstates; $\Delta M = M_1 - M_2$ and $\Delta\Gamma = \Gamma_1 - \Gamma_2$. The eigenvector equations

$$(H - EI) \begin{pmatrix} p \\ \pm q \end{pmatrix} = 0 \quad (1.7)$$

can be used to extract the relationship between the admixture constants p and q ,

$$\frac{q}{p} = \sqrt{\frac{M_{12}^* - \frac{i}{2}\Gamma_{12}^*}{M_{12} - \frac{i}{2}\Gamma_{12}}}. \quad (1.8)$$

The time evolution of the eigenstates $|X_1\rangle$ and $|X_2\rangle$ is given by

$$|X_{1,2}(t)\rangle = |X_{1,2}\rangle e^{-i(M_{1,2} - \frac{i}{2}\Gamma_{1,2})t}. \quad (1.9)$$

Substituting this into rearrangements of Equations 1.3 and 1.4 gives the time evolution

of the initial particle and antiparticle states,

$$|X^0(t)\rangle = f_+(t)|X^0\rangle + \frac{q}{p}f_-(t)|\bar{X}^0\rangle \quad (1.10)$$

$$|\bar{X}^0(t)\rangle = f_+(t)|\bar{X}^0\rangle + \frac{p}{q}f_-(t)|X^0\rangle \quad (1.11)$$

where

$$f_{\pm}(t) = \frac{1}{2} \left[e^{-i(M_1 - \frac{i}{2}\Gamma_1)t} \pm e^{-i(M_2 - \frac{i}{2}\Gamma_2)t} \right] . \quad (1.12)$$

Equation 1.10 results in probabilities of finding states $|X^0\rangle$ and $|\bar{X}^0\rangle$ at time t from an initially pure $|X^0\rangle$ state:

$$P(X^0 \rightarrow X^0 : t) = |\langle X^0 | X^0(t) \rangle|^2 = |f_+(t)|^2 \quad (1.13)$$

$$P(X^0 \rightarrow \bar{X}^0 : t) = |\langle \bar{X}^0 | X^0(t) \rangle|^2 = \left| \frac{q}{p} f_-(t) \right|^2 \quad (1.14)$$

with

$$|f_{\pm}(t)|^2 = \frac{1}{4} \left[e^{-\Gamma_1 t} + e^{-\Gamma_2 t} \pm 2e^{-\bar{\Gamma}t} \cos(\Delta M t) \right] \quad (1.15)$$

where $\bar{\Gamma} = \frac{(\Gamma_1 + \Gamma_2)}{2}$ is the average decay width. Similarly, the probabilities of finding states $|\bar{X}^0\rangle$ and $|X^0\rangle$ at time t from an initially pure $|\bar{X}^0\rangle$ state are

$$P(\bar{X}^0 \rightarrow \bar{X}^0 : t) = |\langle \bar{X}^0 | \bar{X}^0(t) \rangle|^2 = |f_+(t)|^2 \quad (1.16)$$

$$P(\bar{X}^0 \rightarrow X^0 : t) = |\langle X^0 | \bar{X}^0(t) \rangle|^2 = \left| \frac{p}{q} f_-(t) \right|^2 . \quad (1.17)$$

The last term of Equation 1.15 describes the oscillation behaviour between the $|X^0\rangle$ and $|\bar{X}^0\rangle$ states, with the size of the oscillation parameter, $x = \frac{|\Delta M|}{\bar{\Gamma}}$, being key to the character of the oscillation. In the B^0 systems, the global average of the difference between the masses in the B_s^0 case ($\Delta M_s = (117.0 \pm 0.8) \times 10^{-10} \text{ MeV}/c^2 = (17.77 \pm 0.12) \text{ ps}^{-1}$ [18]) is much larger than in the B_d^0 case ($\Delta M_d = (3.337 \pm 0.033) \times 10^{-10} \text{ MeV}/c^2 = (0.507 \pm 0.004) \text{ ps}^{-1}$ [18]). Oscillations in the B_s^0 case are therefore much more rapid ($x_s = 26.2 \pm 0.5$ [18]) than in the B_d^0 case ($x_d = 0.771 \pm 0.008$ [18]). ΔM_d and ΔM_s have

also been measured at LHCb, giving the results $\Delta M_d = (0.499 \pm 0.032 \pm 0.003) \text{ ps}^{-1}$ [19] and $\Delta M_s = (17.725 \pm 0.041 \pm 0.026) \text{ ps}^{-1}$ [20], where the first errors are statistical and the second systematic. The LHCb measurement of ΔM_s is currently the world's best measurement of B_s^0 mixing.

1.2.2 Types of \mathcal{CP} -violation

\mathcal{CP} -violation manifests itself in three forms as detailed below [21]. The three cases can be determined from the comparison of the rate for an initially pure X^0 state to decay to final state f

$$\Gamma(X^0(t) \rightarrow f) = |A_f|^2 \{ |f_+(t)|^2 + |\lambda_f|^2 |f_-(t)|^2 + 2 \Re(\lambda_f f_+^*(t) f_-(t)) \} \quad (1.18)$$

with the rate for an initially pure \bar{X}^0 state to decay to final state \bar{f} , the conjugate state of f ,

$$\Gamma(\bar{X}^0(t) \rightarrow \bar{f}) = |\bar{A}_{\bar{f}}|^2 \{ |f_+(t)|^2 + |\bar{\lambda}_{\bar{f}}|^2 |f_-(t)|^2 + 2 \Re(\bar{\lambda}_{\bar{f}} f_+^*(t) f_-(t)) \}. \quad (1.19)$$

Here, $f_{\pm}(t)$ is given in Equation 1.12, the amplitudes for the transitions of X^0 and \bar{X}^0 to f and \bar{f} are

$$\begin{aligned} A_f &\equiv \langle f|T|X^0 \rangle & A_{\bar{f}} &\equiv \langle \bar{f}|T|X^0 \rangle \\ \bar{A}_f &\equiv \langle f|T|\bar{X}^0 \rangle & \bar{A}_{\bar{f}} &\equiv \langle \bar{f}|T|\bar{X}^0 \rangle, \end{aligned} \quad (1.20)$$

and the complex quantities λ_f and $\bar{\lambda}_{\bar{f}}$ are given by

$$\lambda_f \equiv \frac{q \bar{A}_f}{p A_f} \quad \text{and} \quad \bar{\lambda}_{\bar{f}} \equiv \frac{1}{\lambda_{\bar{f}}} \equiv \frac{p A_{\bar{f}}}{q \bar{A}_{\bar{f}}}. \quad (1.21)$$

Any difference between the decay rates (Equations 1.18 and 1.19) indicates the presence of \mathcal{CP} -violation.

\mathcal{CP} -violation in the mixing

\mathcal{CP} -violation can occur in neutral meson mixing if the magnitudes of the off-diagonal elements of the mass and decay matrices are not equal,

$$\left| M_{12} - \frac{i}{2}\Gamma_{12} \right| \neq \left| M_{12}^* - \frac{i}{2}\Gamma_{12}^* \right| ; \quad (1.22)$$

from Equation 1.8 this corresponds to

$$\left| \frac{q}{p} \right| \neq 1. \quad (1.23)$$

\mathcal{CP} -violation in the mixing is also known as *indirect* \mathcal{CP} -violation. It results from the mass eigenstates being different to the \mathcal{CP} eigenstates and is independent of the final decay state. Physically, it can be seen from Equations 1.14 and 1.17 that the condition of Equation 1.23 causes a difference between the rates of $X^0 \rightarrow \bar{X}^0$ and $\bar{X}^0 \rightarrow X^0$ transitions.

\mathcal{CP} -violation in neutral B-meson mixing has been measured through the \mathcal{CP} asymmetry in semi-leptonic decays,

$$\begin{aligned} A_{sl} &= \frac{\Gamma(\bar{B}^0 \rightarrow \ell^+ \nu X) - \Gamma(B^0 \rightarrow \ell^- \nu X)}{\Gamma(\bar{B}^0 \rightarrow \ell^+ \nu X) + \Gamma(B^0 \rightarrow \ell^- \nu X)} \\ &= \frac{1 - |q/p|^4}{1 + |q/p|^4}. \end{aligned} \quad (1.24)$$

The current global averages are $A_{sl, B_d^0} = (-0.5 \pm 5.6) \times 10^{-3}$ (from B-factory results only) and $A_{sl, B_s^0} = (-3.6 \pm 9.4) \times 10^{-3}$ for the B_d^0 and B_s^0 systems respectively [18]. The mixing induced contribution to \mathcal{CP} -violation in the SM B-meson system is small, due in part to the small size of $\Delta\Gamma$.

\mathcal{CP} -violation in the decay

\mathcal{CP} -violation in the decay, or *direct* \mathcal{CP} -violation, causes a difference between the partial decay rate of the process $X \rightarrow f$ and the rate of its charge conjugate $\bar{X} \rightarrow \bar{f}$. The decay

amplitudes for these processes,

$$A_f \equiv \langle f|T|X \rangle \quad \text{and} \quad \bar{A}_{\bar{f}} \equiv \langle \bar{f}|T|\bar{X} \rangle, \quad (1.25)$$

can be written as a sum over contributing topological amplitudes,

$$A_f = \sum_m A_m e^{i\phi_m} e^{i\delta_m} \quad \text{and} \quad \bar{A}_{\bar{f}} = \sum_n A_n e^{-i\phi_n} e^{i\delta_n}, \quad (1.26)$$

where $A_{m,n}$ are real. $\phi_{m,n}$ are weak (\mathcal{CP} -odd) phases which appear with opposite signs in A_f and $\bar{A}_{\bar{f}}$ and usually originate from complex couplings in the Lagrangian. $\delta_{m,n}$ are strong (\mathcal{CP} -even) phases which come from final state interaction scatterings; they appear with the same sign in A_f and $\bar{A}_{\bar{f}}$.

If the decay can proceed via two or more decay mechanisms with different amplitudes, weak and strong phases, then interference will occur between the contributions, meaning that

$$\left| \frac{\bar{A}_{\bar{f}}}{A_f} \right| = \left| \frac{\sum_n A_n e^{-i\phi_n} e^{i\delta_n}}{\sum_m A_m e^{i\phi_m} e^{i\delta_m}} \right| \neq 1, \quad (1.27)$$

which corresponds to \mathcal{CP} -violation in the decay. An additional condition for this form of \mathcal{CP} -violation is that $\left| \frac{\bar{A}_{\bar{f}}}{A_f} \right| \neq 1$.

Charged B-meson decays are affected by this type of \mathcal{CP} -violation. The \mathcal{CP} asymmetry in charged B decays,

$$\begin{aligned} A_{\mathcal{CP}}^{\pm} &= \frac{\Gamma(\text{B}^- \rightarrow \bar{f}) - \Gamma(\text{B}^+ \rightarrow f)}{\Gamma(\text{B}^- \rightarrow \bar{f}) + \Gamma(\text{B}^+ \rightarrow f)} \\ &= \frac{|\bar{A}_{\bar{f}}/A_f|^2 - 1}{|\bar{A}_{\bar{f}}/A_f|^2 + 1}, \end{aligned} \quad (1.28)$$

can be found experimentally, but there are hadronic uncertainties in the calculations of the magnitudes and strong phases which make it difficult to extract weak phase information from the asymmetry.

\mathcal{CP} -violation in the decay was first observed in the neutral kaon system [11] and has since been observed in many B-meson decays. A recent measurement of $A_{\mathcal{CP}}^0$ for the

decay $B_d^0 \rightarrow K^+\pi^-$ at LHCb gave a value of $A_{\mathcal{CP}}^0 = -0.074 \pm 0.033 \pm 0.008$ [22], where the first error is statistical and the second systematic. This measurement is consistent with the global average value $A_{\mathcal{CP}}^0 = -0.098 \pm 0.013$ [18].

\mathcal{CP} -violation in the interference between mixing and decay

\mathcal{CP} -violation can also occur when a neutral meson X^0 or its antiparticle \bar{X}^0 decay to the same final state f or \bar{f} , either directly or after mixing. This type of \mathcal{CP} -violation is referred to as \mathcal{CP} -violation in the interference between the mixing and decay amplitudes.

As described above, the amplitudes for X^0 and \bar{X}^0 to decay to f and \bar{f} are

$$\begin{aligned} A_f &\equiv \langle f|T|X^0\rangle & A_{\bar{f}} &\equiv \langle \bar{f}|T|X^0\rangle \\ \bar{A}_f &\equiv \langle f|T|\bar{X}^0\rangle & \bar{A}_{\bar{f}} &\equiv \langle \bar{f}|T|\bar{X}^0\rangle. \end{aligned} \quad (1.29)$$

The complex quantities λ_f and $\lambda_{\bar{f}}$, which are defined in Equation 1.21 and appear in Equations 1.18 and 1.19, can be used to quantify \mathcal{CP} -violation; overall \mathcal{CP} conservation requires that

$$\lambda_f = \frac{1}{\lambda_{\bar{f}}}. \quad (1.30)$$

In the case where neither \mathcal{CP} -violation in the mixing nor \mathcal{CP} -violation in the decay is present, $|\lambda_f| = \frac{1}{|\lambda_{\bar{f}}|}$. It is possible, however, that interference between the phases of the two ratios contributing to λ will lead to

$$\arg(\lambda_f) + \arg(\lambda_{\bar{f}}) \neq 0, \quad (1.31)$$

thus causing \mathcal{CP} -violation in the interference between the mixing and decay amplitudes. If the decays are to a \mathcal{CP} eigenstate $f = \bar{f}$, then $|\lambda_f| = 1$ and the condition for \mathcal{CP} -violation only in the interference (from Equation 1.31) becomes

$$\Im\{\lambda_f\} \neq 0. \quad (1.32)$$

In the B-meson system, it is convenient to define time-dependent decay rates to the

state f in terms of the particle-antiparticle basis,

$$\Gamma_f(t) = \Gamma(B(t) \rightarrow f) = \frac{|A_f|^2}{2} e^{-\bar{\Gamma}t} [I_+(t) + I_-(t)] \quad (1.33)$$

$$\bar{\Gamma}_f(t) = \Gamma(\bar{B}(t) \rightarrow f) = \frac{|\bar{A}_f|^2}{2|\lambda_f|^2} e^{-\bar{\Gamma}t} [I_+(t) - I_-(t)] , \quad (1.34)$$

where the time-dependent functions $I_{\pm}(t)$ are given by

$$\begin{aligned} I_+(t) &= (1 + |\lambda_f|^2) \cosh\left(\frac{\Delta\Gamma t}{2}\right) - 2\Re\{\lambda_f\} \sinh\left(\frac{\Delta\Gamma t}{2}\right) \\ I_-(t) &= (1 - |\lambda_f|^2) \cos(\Delta Mt) + 2\Im\{\lambda_f\} \sin(\Delta Mt) . \end{aligned} \quad (1.35)$$

It can be assumed that $\left|\frac{q}{p}\right| \approx 1$, since for heavy neutral mesons \mathcal{CP} -violation in the mixing is negligible compared to \mathcal{CP} -violation in the interference. By substituting the expressions of Equations 1.33 and 1.34 into the expression below, it can be shown that the time-dependent \mathcal{CP} asymmetry

$$A_{\mathcal{CP}}(t) = \frac{\Gamma_f - \bar{\Gamma}_f}{\Gamma_f + \bar{\Gamma}_f} \quad (1.36)$$

becomes

$$A_{\mathcal{CP}}(t) = \frac{(1 - |\lambda_f|^2) \cos(\Delta Mt) + 2\Im\{\lambda_f\} \sin(\Delta Mt)}{(1 + |\lambda_f|^2) \cosh\left(\frac{\Delta\Gamma t}{2}\right) - 2\Re\{\lambda_f\} \sinh\left(\frac{\Delta\Gamma t}{2}\right)} . \quad (1.37)$$

In the B_d^0 system, $\Delta\Gamma = \Gamma_1 - \Gamma_2$ is small, meaning that $A_{\mathcal{CP}}(t)$ reduces to

$$A_{\mathcal{CP}}(t) = \underbrace{\left(\frac{1 - |\lambda_f|^2}{1 + |\lambda_f|^2}\right)}_C \cos(\Delta Mt) + \underbrace{\left(\frac{2\Im\{\lambda_f\}}{1 + |\lambda_f|^2}\right)}_S \sin(\Delta Mt) . \quad (1.38)$$

The first term in Equation 1.38 is the contribution from direct \mathcal{CP} -violation, while the second term comes from \mathcal{CP} -violation in the interference. In the special case where the final state f is a \mathcal{CP} eigenstate with decays dominated by a single weak phase, $|\lambda_f| = 1$ implying $C = 0$. In addition, $\Im\{\lambda_f\} \neq 0$ and therefore $S \neq 0$, so only \mathcal{CP} -violation

in the interference is observed via the asymmetry. This is advantageous as all hadronic uncertainties associated with direct \mathcal{CP} -violation are removed, leaving the asymmetry dominated by a single weak phase which can be cleanly interpreted in terms of electro-weak parameters.

Measurements of $A_{\mathcal{CP}}(t)$ in the channels $B_d^0 \rightarrow c\bar{c}K^{0(*)}$, which are decays to \mathcal{CP} eigenstates, have been made at the B-factories and at LHCb. The most recent values of C and S , consistent with $C = 0$ and $S \neq 0$, were found by BaBar [23], Belle [24] and LHCb [25] respectively.

1.3 \mathcal{CP} -violation in the Standard Model

The SM describes particle interactions in terms of gauge field theories. \mathcal{CP} -invariant Lagrangians are used to construct the electromagnetic (QED) and strong (QCD) theories as \mathcal{CP} is experimentally observed to be conserved in these interactions, but the weak interaction violates \mathcal{CP} symmetry and so must have a \mathcal{CP} -violating Lagrangian.

A chiral gauge theory, in which only left-handed (Weyl) fermions ψ_L interact with the gauge bosons, can be constructed with the Lagrangian

$$\mathcal{L} = -\frac{1}{4}F_{\mu\nu}F^{\mu\nu} + \bar{\psi}_L i\sigma D\psi_L. \quad (1.39)$$

This Lagrangian violates \mathcal{P} but is invariant under the action of \mathcal{CP} ; \mathcal{CP} is a natural symmetry of massless gauge theories [26]. \mathcal{CP} -violation can only be incorporated in theories where mass has been introduced. An explicit Lagrangian mass term for fermions such as

$$m\bar{\psi}\psi \equiv m(\bar{\psi}_L\psi_R + \bar{\psi}_R\psi_L) \quad (1.40)$$

mixes chiralities, violating the $SU(2)$ gauge symmetry and therefore implying that $m = 0$. Left-handed fermions are not massless in nature and so the mass term of Equation 1.40 cannot be used to introduce mass to the theory. The Lagrangian (Equation 1.39) must be modified in some other way, so as to preserve gauge invariance but also introduce mass for the fermions and weak interaction gauge bosons, W^\pm and Z^0 . In the SM this modification is provided by the Higgs mechanism [27, 28] which introduces a scalar field that couples to the fermion and gauge boson fields in such a way as to leave the

Lagrangian gauge invariant. The Higgs field acquires a particular vacuum expectation value (VEV) and in doing so spontaneously breaks the symmetry (gauge invariance), allowing the fermions and gauge bosons to become massive.

The full SM Lagrangian is then given by three terms,

$$\mathcal{L}_{SM} = \mathcal{L}_{Gauge}(\psi_L, \psi_R, W, \phi) + \mathcal{L}_{Higgs}(\phi) + \mathcal{L}_{Yukawa}(\psi_L, \psi_R, \phi), \quad (1.41)$$

where ϕ is the scalar Higgs field, W is the gauge boson field and ψ_L and ψ_R are the left- and right-handed fermion fields. The term \mathcal{L}_{Gauge} describes the kinematics of the fields and their gauge interactions; the \mathcal{L}_{Higgs} term describes the potential experienced by the scalar fields. In the SM, both of these terms are \mathcal{CP} -invariant, and so \mathcal{L}_{Yukawa} must be the source of \mathcal{CP} -violation. This term represents the fermion-scalar field interactions which induce mass terms after spontaneous symmetry breaking. It can be written as

$$\mathcal{L}_{Yukawa} = -\lambda_{Yukawa,ij}^d \bar{Q}_L^i \cdot \Phi d_R^j - (\lambda_{Yukawa,ij}^d)^* \bar{d}_R^j \Phi^\dagger \cdot Q_L^i + \text{up quark terms} \quad (1.42)$$

where the indices i, j run over the generations, λ_{Yukawa} are the Yukawa couplings, Q_L^i denotes the $SU(2)_L$ quark doublet (u_L^i, d_L^i) and Φ is the $SU(2)_L$ Higgs doublet (ϕ^+, ϕ^0). The second term in Equation 1.42 is the complex conjugate of the first, thus satisfying the condition that the Lagrangian should be Hermitian.

Under the combined \mathcal{CP} operation, the quark and Higgs fields transform as

$$\bar{Q}_L^i \cdot \Phi d_R^j \xrightarrow{\mathcal{CP}} \bar{d}_R^j \Phi^\dagger \cdot Q_L^i \quad (1.43)$$

meaning that \mathcal{L}_{Yukawa} is \mathcal{CP} -invariant if $\lambda_{Yukawa} \equiv \lambda_{Yukawa}^*$. If λ_{Yukawa} is complex, however, \mathcal{CP} -violation is introduced by the complex phase in the coupling; this phase is the only source of \mathcal{CP} -violation accommodated in the SM.

After spontaneous symmetry breaking, the Yukawa couplings λ_{Yukawa} form 3×3 mass matrices for the up-type and down-type quark weak interaction eigenstates, $u^{(weak)}$ and $d^{(weak)}$ respectively. In order to express the theory in terms of experimentally observable mass eigenstates, these matrices must be diagonalised. The weak eigenstates are transformed into the mass eigenstates by matrices $U^{(u,d)}$,

$$u_i^{(weak)} = U_{ij}^{(u)} u_j^{(mass)}, \quad d_i^{(weak)} = U_{ij}^{(d)} d_j^{(mass)}. \quad (1.44)$$

This has no effect on neutral interactions because the matrices $U^{(u,d)}$ only rotate the

basis and are therefore unitary, meaning that $\bar{u}_i^{(weak)} u_i^{(weak)} = \bar{u}_i^{(mass)} u_i^{(mass)}$. For weak charged interactions, however,

$$\bar{u}_i^{(weak)} d_i^{(weak)} \rightarrow \bar{u}_i^{(mass)} (U^{(u)})^\dagger U^{(d)} d_i^{(mass)}. \quad (1.45)$$

The matrix $\mathbf{V}_{CKM} \equiv (U^{(u)})^\dagger U^{(d)}$ describes the strength of the coupling for down-type quarks decaying to up-type quarks, taking the place of the λ_{Yukawa} couplings in Equation 1.42. It also contains the complex phase necessary for \mathcal{CP} -violation. This matrix is called the Cabibbo-Kobayashi-Maskawa (CKM) matrix and is discussed in the following section.

1.3.1 The CKM matrix

The CKM matrix, \mathbf{V}_{CKM} , is an extension of the 2×2 Cabibbo quark mixing matrix [29] to a unitary 3×3 matrix including the third generation of quarks [30]. The matrix is \mathcal{CP} -violating, with elements V_{ij} representing the coupling of the i -th up-type quark to the j -th down-type quark. The strengths of these couplings are not predicted in the SM and must be constrained experimentally. The matrix can be written explicitly as

$$\mathbf{V}_{CKM} = \begin{pmatrix} V_{ud} & V_{us} & V_{ub} \\ V_{cd} & V_{cs} & V_{cb} \\ V_{td} & V_{ts} & V_{tb} \end{pmatrix}. \quad (1.46)$$

The couplings between antiquarks are given by the complex conjugates of the elements, V_{ij}^* .

\mathbf{V}_{CKM} is unitary because the matrices $U^{(u,d)}$ are unitary. A 3×3 unitary matrix can, in general, be parameterised by three Euler angles and six complex phases. In the case of \mathbf{V}_{CKM} , however, five of the complex phases are unphysical and can be “rotated away”; this is because quark fields appear in the Lagrangian as $\bar{\psi}\psi$ and $\bar{\psi}\partial\psi$ terms, meaning that the Lagrangian is invariant under field transformations of the form $q \rightarrow qe^{i\omega}$. This leaves one irreducible complex phase, δ , which is responsible for \mathcal{CP} -violation in the SM.

There are many possible parameterisations of the CKM matrix. The “Chau-Keung” [31] representation emphasises the extension of the two-generation Cabibbo mixing mecha-

nism to the three-generation CKM matrix:

$$\begin{aligned}
\mathbf{V}_{CKM} &= \begin{pmatrix} 1 & 0 & 0 \\ 0 & c_{23} & s_{23} \\ 0 & -s_{23} & c_{23} \end{pmatrix} \begin{pmatrix} c_{13} & 0 & s_{13}e^{-i\delta} \\ 0 & 1 & 0 \\ -s_{13}e^{-i\delta} & 0 & c_{13} \end{pmatrix} \underbrace{\begin{pmatrix} c_{12} & s_{12} & 0 \\ -s_{12} & c_{12} & 0 \\ 0 & 0 & 1 \end{pmatrix}}_{\text{Cabibbo matrix}} \\
&= \begin{pmatrix} c_{12}c_{13} & s_{12}c_{13} & s_{13}e^{-i\delta} \\ -s_{12}c_{23} - c_{12}s_{23}s_{13}e^{i\delta} & c_{12}c_{23} - s_{12}s_{23}s_{13}e^{i\delta} & s_{23}c_{13} \\ s_{12}s_{23} - c_{12}c_{23}s_{13}e^{i\delta} & -s_{23}c_{12} - s_{12}c_{23}s_{13}e^{i\delta} & c_{23}c_{13} \end{pmatrix} \quad (1.47)
\end{aligned}$$

where $c_{ij} = \cos \theta_{ij}$ and $s_{ij} = \sin \theta_{ij}$; $\theta_{12} \equiv \theta_c$ (the Cabibbo angle [29]), θ_{23} and θ_{13} are the three Euler angles and δ is the complex phase.

The Wolfenstein perturbative parameterisation gives an indication of the relative sizes of the couplings [32]. It uses four independent parameters,

$$\lambda \equiv s_{12}, \quad A \equiv \frac{s_{23}}{s_{12}^2}, \quad \rho \equiv \frac{s_{13} \cos \delta}{s_{12}s_{23}} \quad \text{and} \quad \eta \equiv \frac{s_{13} \sin \delta}{s_{12}s_{23}},$$

which are fundamental parameters of the SM. The elements of \mathbf{V}_{CKM} can be written in terms of these parameters as a power expansion in λ to order λ^3

$$\mathbf{V}_{CKM}^{(3)} = \begin{pmatrix} 1 - \frac{1}{2}\lambda^2 & \lambda & A\lambda^3(\rho - i\eta) \\ -\lambda & 1 - \frac{1}{2}\lambda^2 & A\lambda^2 \\ A\lambda^3(1 - \rho - i\eta) & -A\lambda^2 & 1 \end{pmatrix} + \mathcal{O}(\lambda^4) \quad (1.48)$$

and to order λ^5

$$\mathbf{V}_{CKM}^{(5)} = \begin{pmatrix} 1 - \frac{1}{2}\lambda^2 - \frac{1}{8}\lambda^4 & \lambda & A\lambda^3(\rho - i\eta) \\ -\lambda + \frac{1}{2}A^2\lambda^5(1 - 2(\rho + i\eta)) & 1 - \frac{1}{2}\lambda^2 - \frac{1}{8}\lambda^4(1 + 4A^2) & A\lambda^2 \\ A\lambda^3(1 - \bar{\rho} - i\bar{\eta}) & -A\lambda^2 + A\lambda^4\left(\frac{1}{2} - \rho - i\eta\right) & 1 - \frac{1}{2}A^2\lambda^4 \end{pmatrix} + \mathcal{O}(\lambda^6) \quad (1.49)$$

where $\bar{\rho} = \rho(1 - \frac{1}{2}\lambda^2)$ and $\bar{\eta} = \eta(1 - \frac{1}{2}\lambda^2)$. η is the complex phase responsible for \mathcal{CP} -violation and it appears in the CKM matrix elements with coefficient $\mathcal{O}(\lambda^3)$ or higher, indicating that the contribution to \mathcal{CP} -violation incorporated in the SM is small. In the past, the expansion $\mathbf{V}_{CKM}^{(3)}$ has been sufficient for discussion of \mathcal{CP} -violation in the B-meson system, however as the LHC will reach sensitivities of $\mathcal{O}(10^{-2})$, the further expansion $\mathbf{V}_{CKM}^{(5)}$ is now required.

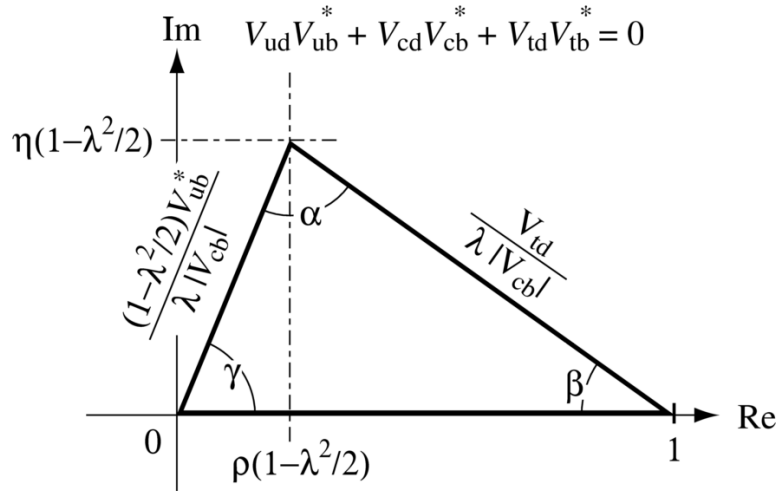
The unitarity of \mathbf{V}_{CKM} means that it satisfies the condition

$$\mathbf{V}_{CKM}(\mathbf{V}_{CKM})^\dagger = (\mathbf{V}_{CKM})^\dagger\mathbf{V}_{CKM} = 1 \quad (1.50)$$

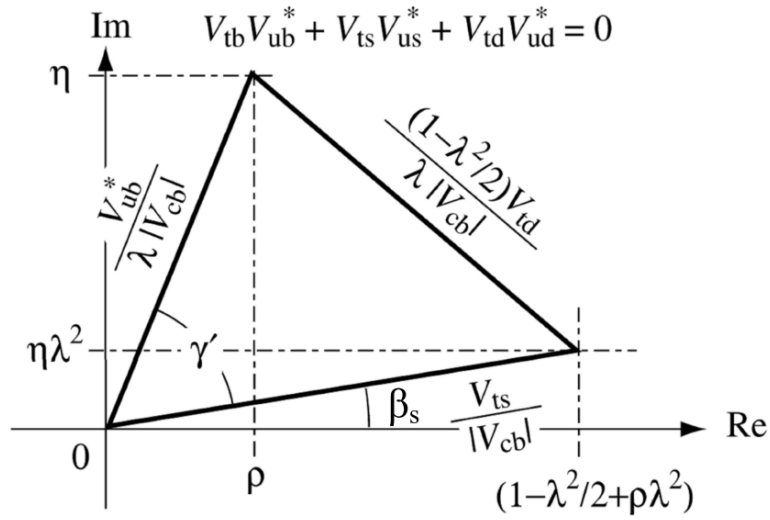
which can be expressed as a set of conditions on the matrix elements; six of these are orthogonality conditions between the matrix rows and columns:

$$\begin{aligned} V_{ud}^*V_{cd} + V_{us}^*V_{cs} + V_{ub}^*V_{cb} &= 0, \quad (cu) \\ V_{ud}^*V_{td} + V_{us}^*V_{ts} + V_{ub}^*V_{tb} &= 0, \quad (tu) \\ V_{cd}^*V_{td} + V_{cs}^*V_{ts} + V_{cb}^*V_{tb} &= 0, \quad (tc) \\ V_{ud}V_{us}^* + V_{cd}V_{cs}^* + V_{td}V_{ts}^* &= 0, \quad (sd) \\ V_{ud}V_{ub}^* + V_{cd}V_{cb}^* + V_{td}V_{tb}^* &= 0, \quad (bd) \\ V_{us}V_{ub}^* + V_{cs}V_{cb}^* + V_{ts}V_{tb}^* &= 0, \quad (bs) \quad . \end{aligned} \quad (1.51)$$

These expressions can be represented graphically as triangles in the complex plane. The single complex phase implies that the areas of these triangles are all the same and equal to $J_{CP}/2$; J_{CP} is the Jarlskog parameter, $\mathcal{O}(10^{-5})$, which is an indicator of the amount of \mathcal{CP} -violation contained in the SM [33]. Four of the triangles are difficult to constrain experimentally as two of their sides are much longer than the third, resulting in triangles which have one very small angle, but the (bd) and (tu) triangles have sides of comparable magnitude, $\mathcal{O}(\lambda^3)$. Choosing $V_{cd}V_{cb}^*$ to be real and normalising (bd) and (tu) by $|V_{cd}V_{cb}^*| = A\lambda^3$ gives two triangles, shown in Figure 1.2, which are identical to $\mathcal{O}(\lambda^3)$ and differ only by $\mathcal{O}(\lambda^5)$ corrections. λ has been measured experimentally to high accuracy, so the dimensions of the triangles depend on the position of the apex $(\bar{\rho}, \bar{\eta})$ which in turn can be determined by measurements of $|V_{cb}|$, $|V_{ub}|$ and $|V_{td}|$. The B-meson sector is ideal for performing these measurements as B-mesons have many decay channels.



(a)



(b)

Figure 1.2: The CKM unitarity triangles (*bd*) (Figure 1.2(a)) and (*tu*) (Figure 1.2(b)) in the complex plane.

The (bd) triangle, shown in Figure 1.2(a), is commonly known as *the unitarity triangle* or UT. The internal angles α , β and γ are defined as

$$\alpha \equiv \arg\left(-\frac{V_{td}V_{tb}^*}{V_{ud}V_{ub}^*}\right) = \arg\left(-\frac{1-\rho-i\eta}{\rho+i\eta}\right), \quad (1.52)$$

$$\beta \equiv \arg\left(-\frac{V_{cd}V_{cb}^*}{V_{td}V_{tb}^*}\right) = \arg\left(\frac{1}{1-\rho-i\eta}\right) \text{ and} \quad (1.53)$$

$$\gamma \equiv \arg\left(-\frac{V_{ud}V_{ub}^*}{V_{cd}V_{cb}^*}\right) = \arg(\rho+i\eta). \quad (1.54)$$

Terms $\mathcal{O}(\lambda^5)$ introduce a phase into V_{ts} , so that the angles β and γ above are shifted into the corresponding angles β' and γ' of the tu triangle in Figure 1.2(b),

$$\beta' \equiv \arg\left(-\frac{V_{ts}V_{us}^*}{V_{td}V_{ud}^*}\right) = \beta + \beta_s \quad (1.55)$$

$$\gamma' \equiv \arg\left(-\frac{V_{tb}V_{ub}^*}{V_{ts}V_{us}^*}\right) = \gamma - \beta_s, \quad (1.56)$$

where

$$\beta_s \equiv \arg\left(-\frac{V_{ts}V_{tb}^*}{V_{cs}V_{cb}^*}\right). \quad (1.57)$$

The complex argument of \mathbf{V}_{CKM} is

$$\arg(\mathbf{V}_{CKM}) = \begin{pmatrix} 0 & 0 & -\gamma \\ 0 & 0 & 0 \\ -\beta & \beta_s + \pi & 0 \end{pmatrix} \quad (1.58)$$

where the small correction to V_{cd} arising from the normalisation convention has been neglected. Comparing this to $\mathbf{V}_{CKM}^{(5)}$ allows β_s to be related to the Wolfenstein parameters:

$$\beta_s = \arctan\left(\frac{\lambda^2\eta}{1+\lambda^2(\rho-\frac{1}{2})}\right) \approx \lambda^2\eta. \quad (1.59)$$

In the SM, $\beta_s \approx 0.02$ rad [34]. \mathcal{CP} -violating $t \rightarrow s$ transitions occur at order λ^4 in

$\mathbf{V}_{CKM}^{(5)}$, but decays involving $b \rightarrow u$ and $d \rightarrow t$ transitions contribute to \mathcal{CP} -violation at order λ^3 in $\mathbf{V}_{CKM}^{(3)}$.

1.4 Constraining the CKM parameters

SM flavour physics is based around the CKM matrix, but the theory cannot predict the sizes of the elements of the matrix. The couplings must be constrained by experiment; the CKM phases can either be determined indirectly via measurements of the lengths of the sides of the UT or directly via measurements of the UT angles in \mathcal{CP} -violating processes and their asymmetries. Overconstraining the UT in this way allows for a unique test of the SM and for searches for NP to be performed. A disagreement between indirect and direct measurements of the phases would indicate the presence of NP contributions from new particles appearing as virtual particles in loop processes. NP contributions can be extracted by comparing precision measurements from tree-level processes, which depend only on the SM, with those from loop-level processes, which may be affected by NP. The current experimental constraints on the magnitudes and phases of the CKM elements are summarised in the following sections.

1.4.1 Current status of CKM matrix element magnitude measurements

The magnitudes of the CKM matrix elements have been measured in the following processes [18]:

- $|V_{ud}|$ in superallowed $0^+ \rightarrow 0^+$ nuclear β decays;
- $|V_{us}|$ in kaon decays $K_L^0 \rightarrow \pi \ell \nu$, $K_S^0 \rightarrow \pi e \nu$ and $K^\pm \rightarrow \pi^0 \ell \nu$, exclusive τ decays and the decay width of semi-inclusive $\tau \rightarrow s$ decays;
- $|V_{ub}|$ in exclusive and inclusive semileptonic $B \rightarrow X \ell \nu$ decays;
- $|V_{cd}|$ in neutrino/antineutrino interactions and semileptonic D decays;
- $|V_{cs}|$ in leptonic D_s decays and semileptonic D decays;
- $|V_{cb}|$ in exclusive and inclusive semileptonic B decays to charm;

- $|V_{td}|$ and $|V_{ts}|$ in neutral B-meson oscillations; also in rare (loop-mediated) K and B decays; and
- $|V_{tb}|$ from single top production.

These methods give the following values for the magnitudes of the matrix elements [34]

$$|V_{CKM}| = \begin{pmatrix} 0.97426^{+0.00022}_{-0.00014} & 0.22539^{+0.00062}_{-0.00095} & 0.003501^{+0.000196}_{-0.000087} \\ 0.22526^{+0.00062}_{-0.00095} & 0.97345^{+0.00022}_{-0.00018} & 0.04070^{+0.00116}_{-0.00059} \\ 0.00846^{+0.00043}_{-0.00015} & 0.03996^{+0.00114}_{-0.00062} & 0.999165^{+0.000024}_{-0.000048} \end{pmatrix}. \quad (1.60)$$

1.4.2 Indirect CKM measurements

Indirect measurements are used to place constraints on the apex of the UT in the $(\bar{\rho}, \bar{\eta})$ plane. The measured values for $|V_{ub}|$ and $|V_{cb}|$ from Section 1.4.1 form a circular constraint, centred at $(0, 0)$; measurements of ΔM_d and ΔM_s from neutral B-meson mixing provide a second circular constraint, centred at $(1, 0)$. A final indirect measurement, ϵ_K , which characterises \mathcal{CP} -violation in neutral kaon mixing, provides a hyperbolic constraint. Figure 1.3 shows the constraints on the UT at 95% confidence level from these measurements.

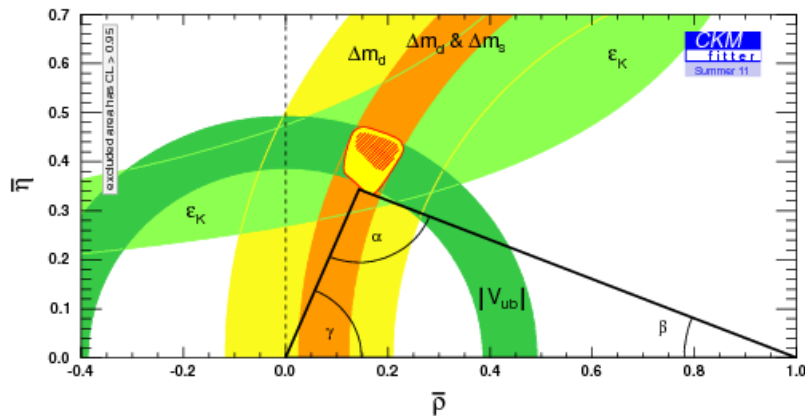


Figure 1.3: The constraints on the CKM unitarity triangle from indirect measurements [34]. The red hashed region corresponds to the 68% confidence level on the apex position from the combined fit to these measurements; the yellow region with red boundary to the 95% confidence level. The superimposed triangle shows the result of the global UT fit including both indirect and direct measurements.

1.4.3 Direct CKM measurements

As \mathcal{CP} -violation arises from the complex phase in the CKM matrix, the internal angles of the UT, which are related to this phase, can be directly constrained from asymmetry measurements of \mathcal{CP} -violating observables in B-meson decays.

Angle α

Time-dependent \mathcal{CP} asymmetries in $b \rightarrow u\bar{d}$ dominated decays allow direct measurements of the angle α to be made. Unfortunately, penguin $b \rightarrow d$ amplitudes have a different CKM phase to $b \rightarrow u\bar{d}$ tree decay amplitudes but the same order of magnitude (in terms of λ), so there is potentially a large amount of pollution from penguin loop processes [35]. Belle and BaBar measurements in the channels $B \rightarrow \pi\pi$, $B \rightarrow \rho\rho$ and $B_d^0 \rightarrow \pi^+\pi^-\pi^0$ dominate the current constraints on the angle α .

The time-dependent analysis of $B_d^0 \rightarrow \pi^+\pi^-$ measures $\sin(2\alpha + 2\Delta\alpha)$ rather than $\sin 2\alpha$ because of loop contributions [18]; $2\Delta\alpha$ is the phase difference between $e^{2i\gamma}\bar{A}_{\pi^+\pi^-}$ and $A_{\pi^+\pi^-}$, where $\bar{A}_{\pi^+\pi^-}$ and $A_{\pi^+\pi^-}$ are the amplitudes for $B_d^0 \rightarrow \pi^+\pi^-$. The isospin relation between the amplitudes $A_{\pi\pi}$ of $B_d^0 \rightarrow \pi^+\pi^-$, $B_d^0 \rightarrow \pi^0\pi^0$ and $B^+ \rightarrow \pi^+\pi^0$,

$$\frac{1}{\sqrt{2}}A_{\pi^+\pi^-} + A_{\pi^0\pi^0} - A_{\pi^+\pi^0} = 0, \quad (1.61)$$

along with a similar expression for the amplitudes $\bar{A}_{\pi\pi}$, allows α and $\Delta\alpha$ to be separated [36]. This method only provides loose constraints on α with many possible values extracted. Using this method, the Belle collaboration has excluded the angle α in the range $11^\circ - 79^\circ$ at 95% confidence level [37] and the BaBar collaboration has excluded the range $23^\circ - 67^\circ$ at 90% confidence level [38].

The decays $B \rightarrow \rho\rho$ can also be used to extract α with an isospin analysis. Values of $\alpha = (91.7 \pm 14.9)^\circ$ [39] and $\alpha = (92.4_{-6.5}^{+6.0})^\circ$ [40] have been found at Belle and BaBar, respectively.

A time-dependent Dalitz analysis of $B_d^0 \rightarrow \pi^+\pi^-\pi^0$ allows for the extraction of α with one ambiguity, $\alpha \rightarrow \alpha + \pi$, assuming knowledge of the variation of the strong phase in the interference. Results from the use of this method at Belle ($68^\circ < \alpha < 95^\circ$ [41]) and BaBar ($\alpha = (87_{-13}^{+45})^\circ$ [42]) are at 68% confidence level and ignore the mirror solutions.

The current best fit value of α is [34]

$$\alpha = (90.9^{+3.5}_{-4.1})^\circ.$$

Angle β

The angle β can be extracted directly from time-dependent \mathcal{CP} asymmetries, using B^0 and \bar{B}^0 decays to the same \mathcal{CP} eigenstate, f . In this case, as detailed in Section 1.2.2, the terms of Equation 1.38 reduce to leave only the sine term in the asymmetry.

The theoretically cleanest β measurements are in tree $b \rightarrow c\bar{c}s$ transitions, for example in the process $B_d^0 \rightarrow J/\psi K_{S,L}^0$. For these decays, it can be assumed that \mathcal{CP} -violation in the mixing and \mathcal{CP} -violation in the decay are both negligible. Under these assumptions,

$$\lambda_f = -\eta_f e^{-2i\beta}, \quad (1.62)$$

where $\eta_f = \pm 1$ is the \mathcal{CP} eigenvalue of the final state and 2β is the phase difference between the decays $B^0 \rightarrow f$ and $\bar{B}^0 \rightarrow f$. This results in the coefficient of the sine term of Equation 1.38 being proportional to $\sin 2\beta$. BaBar [23], Belle [24] and LHCb [25] have performed recent analyses; the current global best fit value is [34]

$$\begin{aligned} \sin 2\beta &= 0.691^{+0.020}_{-0.020}, \\ \beta &= (21.84^{+0.80}_{-0.76})^\circ. \end{aligned}$$

Angle γ

The angle γ can be measured directly from SM tree-level processes without pollution from loop-level processes. High statistics are required to make precision measurements of γ because the decays of interest have small branching fractions $\mathcal{O}(10^{-6})$. Belle and BaBar have made the first direct measurements but it is expected that running conditions at the LHC will allow for the direct measurement of γ to a few degrees. A summary of the main time-independent tree-level methods is given in Section 1.5. Time-dependent measurements of γ can also be made, for example using $B_s^0 \rightarrow D_s^\mp K^\pm$ decays, although a measurement of γ in this channel requires a separate measurement of the B_s^0 mixing phase to be made. The decay has been observed and an initial measurement of the branching fraction has been made at LHCb [43],

$\text{Br}(B_s^0 \rightarrow D_s^\mp K^\pm) = (1.97 \pm 0.18(\text{stat.})_{-0.20}^{+0.19}(\text{syst.})_{-0.10}^{+0.11}(f_s/f_d)) \times 10^{-4}$, where f_s/f_d is the B_s^0 and B_d^0 production fraction ratio.

Global constraints from direct measurements

Figure 1.4 shows the constraints on the UT from direct measurements of the angles α , β and γ at 95% confidence level. It can be seen from the shaded allowed regions that the current best direct constraint is from $\sin 2\beta$ and the current direct constraint on γ is poor (approximately $\pm 10^\circ$).

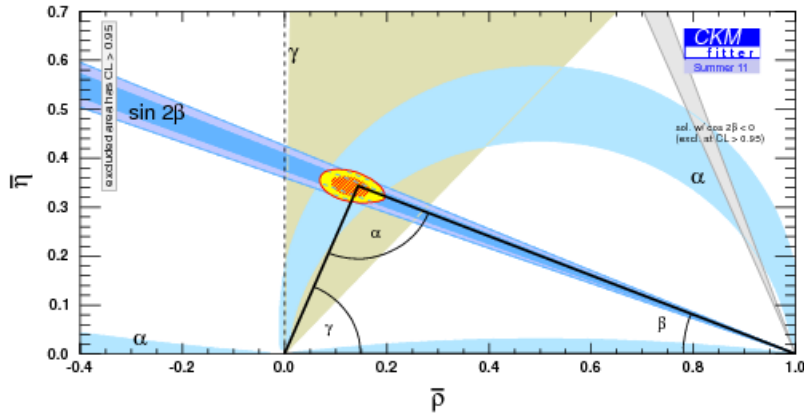


Figure 1.4: The constraints on the CKM unitarity triangle from direct measurements [34]. The red hashed region corresponds to the 68% confidence level on the apex position from the combined fit to these measurements; the yellow region with red boundary to the 95% confidence level. The superimposed triangle shows the result of the global UT fit including both indirect and direct measurements.

Angle β_s

Direct measurements of the angle β_s from $B_s^0 \rightarrow J/\psi(\mu^+\mu^-)\phi(K^+K^-)$ decays have been carried out at CDF [44, 45], DØ [46, 47] and LHCb [48]. In the SM, the \mathcal{CP} -violating phase of this decay $\phi_s^{J/\psi\phi} \approx -2\beta_s$ [49] and β_s is expected to be small; deviations from this equality may indicate contributions from NP phenomena. The analyses include measurement of other parameters such as $\Delta\Gamma_s$, the difference in the partial widths between the heavy and light B_s^0 states, which can also be affected by NP contributions. Figure 1.5 shows the constraints in the $\phi_s^{J/\psi\phi}$ - $\Delta\Gamma_s$ plane from the most recent CDF,

DØ and LHCb measurements, along with the SM prediction. It can be seen that these measurements are all consistent with the SM. The current average value of β_s from published CDF [44] and DØ [46] measurements, not including the LHCb measurement and without external constraints, is [50]

$$\beta_s = (0.39^{+0.18}_{-0.14}) \text{ rad} \quad \text{or} \quad \beta_s = (1.18^{+0.14}_{-0.18}) \text{ rad}.$$

A further measurement of β_s has been performed at LHCb using the decay $B_s^0 \rightarrow J/\psi(\mu^+\mu^-)f_0(980)(\pi^+\pi^-)$ [51]; the combined result from the two LHCb measurements is $\phi_s = (0.03 \pm 0.16 \pm 0.07)$ rad, where the first error is statistical and the second systematic [52].

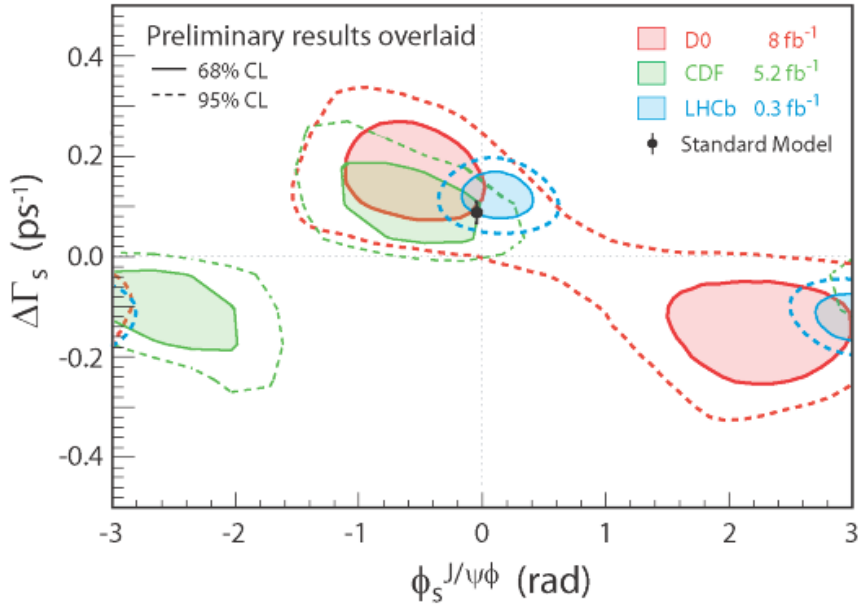


Figure 1.5: The constraints on B_s^0 parameters $\phi_s^{J/\psi\phi}$ and $\Delta\Gamma_s$.

Combined indirect and direct measurements

Combining the indirect and direct constraints on the UT gives the fit shown in Figure 1.6. The fitted apex position is [34]

$$\bar{\rho} = 0.144^{+0.023}_{-0.026}, \quad \bar{\eta} = 0.343^{+0.015}_{-0.014}.$$

The current global fitted values of the other Wolfenstein parameters are $A = 0.801^{+0.026}_{-0.014}$ and $\lambda = 0.22539^{+0.00062}_{-0.00095}$ [34].

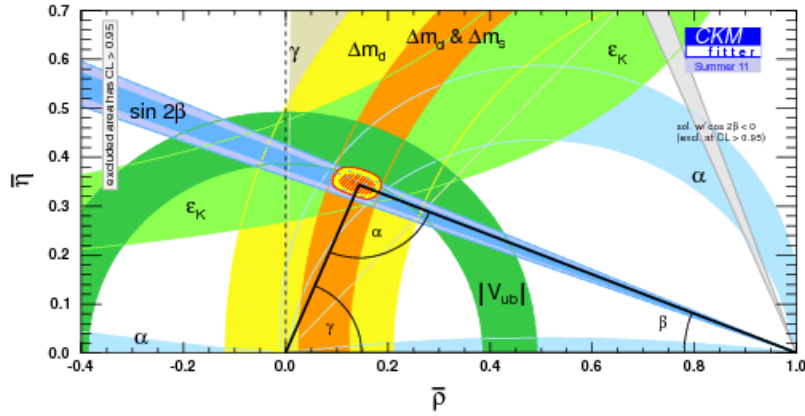


Figure 1.6: The constraints on the CKM unitarity triangle, combining indirect and direct measurements [34]. The red hashed region corresponds to the 68% confidence level on the apex position from the global fit; the yellow region with red boundary to the 95% confidence level.

Current measurements are consistent with SM expectations, although the constraints are not precise enough to rule out the presence of NP beyond the SM in loop processes. There is some tension between the current measured values and values predicted from the full SM UT fit for the branching ratio of the decay $B^+ \rightarrow \tau^+ \nu_\tau$ and for $\sin(2\beta)$ [53]; LHCb will provide increased precision to the β measurement in particular.

1.5 The time-independent measurement of γ from $B \rightarrow DK^{(*)}$ decays

The CKM angle γ can be measured directly in tree-level Feynman diagram processes such as $B \rightarrow DK^{(*)}$ decays, where D indicates a D^0 or \bar{D}^0 meson. These time-integrated measurements allow benchmarking of the SM value because the processes have no penguin loop contributions; the largest correction to them is expected to come from neutral D mixing, but this should lead to a very small correction on γ [54] and is normally neglected. \mathcal{CP} -violation in D meson decays is also neglected [55].

In charged B modes, there are two contributing SM tree diagrams, as shown in Figure 1.7. One is CKM favoured and colour favoured (Figure 1.7(a)), the other is CKM suppressed and colour suppressed (Figure 1.7(b)). W bosons do not carry colour charge and mesons are colour singlets, meaning that in Figure 1.7(a) the quarks from

the boson decay (s and \bar{u}) are unconstrained in colour. In Figure 1.7(b), however, colour suppression arises due to the internal W decay; the colours of the quarks from the boson (\bar{c} and s) are constrained by the colour of the spectator quark. Neutral B modes have two contributing colour suppressed SM tree diagrams, one CKM favoured (Figure 1.8(a)) and one CKM suppressed (Figure 1.8(b)).

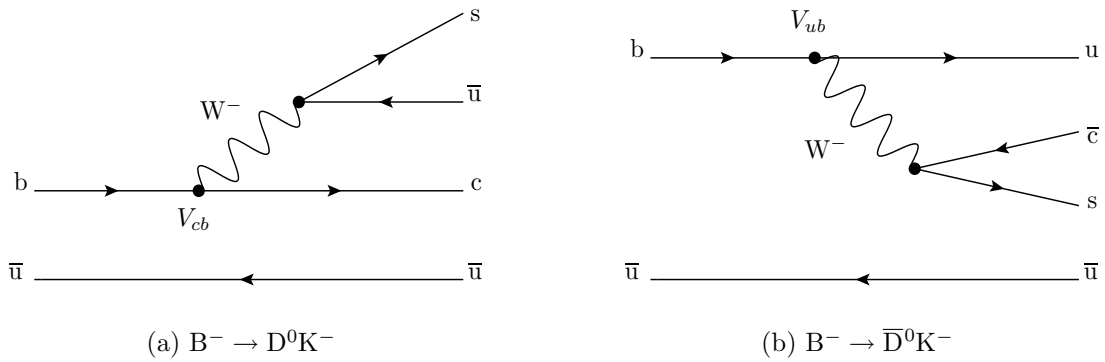


Figure 1.7: The two contributing tree-level Feynman diagrams for $B^- \rightarrow DK^-$. There are corresponding diagrams for B^+ . Figure 1.7(a) shows the colour favoured and CKM favoured contribution; the colour suppressed and CKM suppressed contribution is shown in Figure 1.7(b).

Methods using $B \rightarrow DK^{(*)}$ decays to measure γ exploit the fact that γ is the weak phase difference between the CKM matrix elements V_{ub} and V_{cb} . In particular, the amplitudes of $B \rightarrow DK^{(*)}$ decays are sensitive to γ due to interference between the tree diagrams when D^0 or \bar{D}^0 decays to the same final state f . For two arbitrary processes with the same initial and final states, the decay rate via amplitudes $A_1 e^{i\phi}$ and A_2 is proportional to

$$|A_1 e^{i\phi} + A_2|^2 = A_1^2 + A_2^2 + 2A_1 A_2 \cos \phi \quad (1.63)$$

and so the relative phase between the amplitudes, ϕ , can be extracted from the interference term.

The amplitudes of $B^\pm \rightarrow DK^\pm$ decays can be defined as

$$A_{b \rightarrow c} = A_B e^{i\delta_c} \quad (1.64)$$

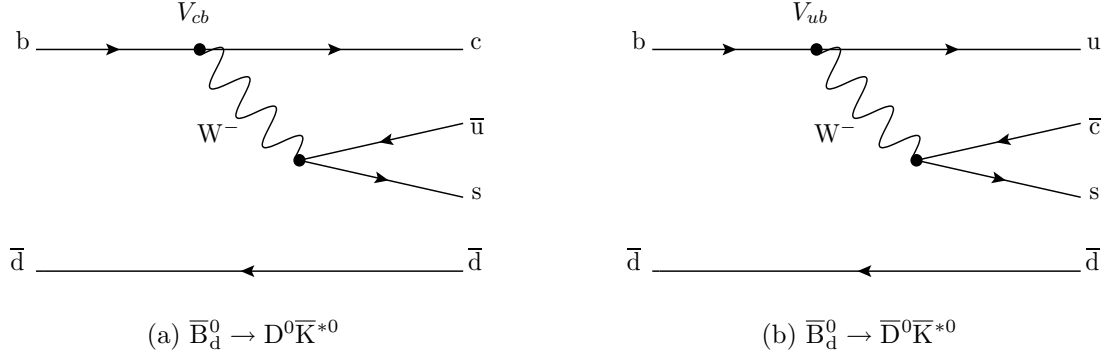


Figure 1.8: The two contributing tree-level Feynman diagrams for $\bar{B}_d^0 \rightarrow D\bar{K}^{*0}$. There are corresponding diagrams for B_d^0 . Figure 1.8(a) shows the colour suppressed and CKM favoured contribution; the colour suppressed and CKM suppressed contribution is shown in Figure 1.8(b).

for the $B^- \rightarrow D^0 K^-$ and $B^+ \rightarrow \bar{D}^0 K^+$ decays and

$$\begin{aligned}
 A_{b \rightarrow u} &= A_{b \rightarrow c} \cdot \frac{A_{b \rightarrow u}}{A_{b \rightarrow c}} \\
 &= A_B e^{i\delta_c} \left| \frac{A_{b \rightarrow u}}{A_{b \rightarrow c}} \right| \frac{e^{\pm i\gamma} e^{i\delta_u}}{e^{i\delta_c}} \\
 &= A_B r_B e^{\pm i\gamma} e^{i\delta_u}
 \end{aligned} \tag{1.65}$$

for the $B^- \rightarrow \bar{D}^0 K^-$ and $B^+ \rightarrow D^0 K^+$ decays, where γ is the \mathcal{CP} -violating weak interaction phase and δ_c and δ_u are the respective strong phases of the amplitudes. $\delta_B = \delta_u - \delta_c$ is the strong phase difference between the decays and r_B is the magnitude of the ratio of the amplitudes. The ratio of the amplitudes is therefore

$$\frac{A_{b \rightarrow u}}{A_{b \rightarrow c}} = r_B e^{i(\delta_B \pm \gamma)}. \tag{1.66}$$

For the full $B \rightarrow D(f)K^{(*)}$ decay chain, the $D \rightarrow f$ decay must also be considered. Irrespective of the $D \rightarrow f$ decay, however, all $B^\pm \rightarrow D(f)K^\pm$ channels have the three parameters γ , r_B and δ_B in common, allowing a combined measurement of γ from many channels. For neutral B decays the parameters r_{B^0} and δ_{B^0} are analogous to r_B and δ_B for the charged B case. The sensitivity to γ is affected by the ratio of the magnitudes of the amplitudes, r_B , with the error on γ increasing as r_B decreases. In the $B^\pm \rightarrow DK^\pm$ case,

$\delta_B = (112_{-13}^{+12})^\circ$ [34] and in the neutral B case, δ_{B^0} is currently poorly constrained [56]. r_B can be written as

$$r_B = \left| \frac{A(B^- \rightarrow \bar{D}^0 K^-)}{A(B^- \rightarrow D^0 K^-)} \right| = \left| \frac{A(B^+ \rightarrow D^0 K^+)}{A(B^+ \rightarrow \bar{D}^0 K^+)} \right| = \left| \frac{V_{ub}^* V_{cs}}{V_{cb}^* V_{us}} \right| f_c^B \quad (1.67)$$

in the charged B case and r_{B^0} can be written as

$$r_{B^0} = \left| \frac{A(\bar{B}_d^0 \rightarrow \bar{D}^0 \bar{K}^{*0})}{A(\bar{B}_d^0 \rightarrow D^0 \bar{K}^{*0})} \right| = \left| \frac{A(B_d^0 \rightarrow D^0 K^{*0})}{A(B_d^0 \rightarrow \bar{D}^0 K^{*0})} \right| = \left| \frac{V_{ub}^* V_{cs}}{V_{cb}^* V_{us}} \right| f_c^{B^0} \quad (1.68)$$

in the neutral B_d^0 case. f_c^B and $f_c^{B^0}$ are colour factors equal to the ratio of the colour suppressed to colour favoured contributions, $f_c^B \approx 0.3$ and $f_c^{B^0} \approx 0.8$ [57–60]. The best fit value to the experimental measurements of r_B in $B^\pm \rightarrow DK^\pm$ decays is 0.107 ± 0.010 [34]; r_{B^0} has been measured as < 0.55 at 95% confidence level [56]. The ratio $\left| \frac{V_{ub}^* V_{cs}}{V_{cb}^* V_{us}} \right|$ is approximately equal to the absolute values of the CKM parameters, given by $\sqrt{\rho^2 + \eta^2}$.

Several methods with different D decay final states are used to make time-independent γ measurements in $B \rightarrow DK^{(*)}$ channels, including

- the Gronau, London and Wyler (GLW) method;
- the Atwood, Duniety and Soni (ADS) method; and
- the Giri, Grossman, Soffer and Zupan (GGSZ or Dalitz) method.

These three methods will be summarised in the following sections.

1.5.1 The GLW method

The GLW method [61, 62], which has been employed at Belle, BaBar, CDF and LHCb, uses D decays to \mathcal{CP} eigenstates such as $D \rightarrow K^+ K^-$, $D \rightarrow \pi^+ \pi^-$ and $D \rightarrow K_S^0 \pi^0$ to measure γ .

The \mathcal{CP} -even (+) and \mathcal{CP} -odd (−) eigenstates can be defined as linear superpositions

of the mass eigenstates

$$D_{\mathcal{CP}\pm} = \frac{D^0 \pm \bar{D}^0}{\sqrt{2}}. \quad (1.69)$$

This means that for the charged B case, the decay amplitudes can be written in the form

$$\begin{aligned} A(B^+ \rightarrow D_{\mathcal{CP}\pm} K^+) &= \frac{1}{\sqrt{2}} (A(B^+ \rightarrow D^0 K^+) \pm A(B^+ \rightarrow \bar{D}^0 K^+)) \\ &= \frac{1}{\sqrt{2}} (|A(B^+ \rightarrow D^0 K^+)| e^{i\gamma} e^{i\delta} \pm |A(B^+ \rightarrow \bar{D}^0 K^+)| e^{i\bar{\delta}}) \end{aligned} \quad (1.70)$$

and

$$\begin{aligned} A(B^- \rightarrow D_{\mathcal{CP}\pm} K^-) &= \frac{1}{\sqrt{2}} (A(B^- \rightarrow D^0 K^-) \pm A(B^- \rightarrow \bar{D}^0 K^-)) \\ &= \frac{1}{\sqrt{2}} (|A(B^- \rightarrow D^0 K^-)| e^{i\bar{\delta}} \pm |A(B^- \rightarrow \bar{D}^0 K^-)| e^{-i\gamma} e^{i\delta}) \end{aligned} \quad (1.71)$$

assuming that the decay proceeds via a single weak phase. $\delta_B = \delta - \bar{\delta}$ is the strong phase difference between the decays.

Assuming there is no \mathcal{CP} -violation in neutral D mixing [54],

$$A(B^+ \rightarrow \bar{D}^0 K^+) = A(B^- \rightarrow D^0 K^-) \quad (1.72)$$

and

$$A(B^+ \rightarrow D^0 K^+) = e^{2i\gamma} A(B^- \rightarrow \bar{D}^0 K^-). \quad (1.73)$$

Two triangles can be constructed in the complex plane using the amplitudes of Equations 1.70 and 1.71 and the conditions of Equations 1.72 and 1.73. These triangles show the relationship between γ and the decay amplitudes. Figure 1.9 shows the two triangles for the \mathcal{CP} -even eigenstates; similar triangles can also be drawn for the \mathcal{CP} -odd eigenstates.

There are four \mathcal{CP} asymmetries which can be measured experimentally to determine

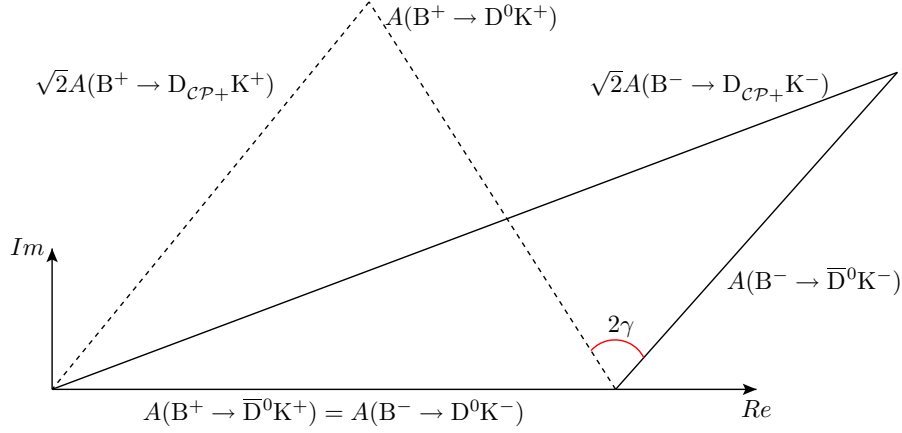


Figure 1.9: The triangles formed by the \mathcal{CP} -even eigenstate GLW amplitudes in the complex plane, showing their relationship to the CKM angle γ .

γ , r_B and δ_B . These are

$$\begin{aligned} R_{\mathcal{CP}\pm} &= 2 \frac{\Gamma(B^- \rightarrow D_{\mathcal{CP}\pm} K^-) + \Gamma(B^+ \rightarrow D_{\mathcal{CP}\pm} K^+)}{\Gamma(B^- \rightarrow D^0 K^-) + \Gamma(B^+ \rightarrow \bar{D}^0 K^+)} \\ &= 1 + r_B^2 \pm 2r_B \cos \gamma \cos \delta_B \end{aligned} \quad (1.74)$$

and

$$\begin{aligned} A_{\mathcal{CP}\pm} &= \frac{\Gamma(B^- \rightarrow D_{\mathcal{CP}\pm} K^-) - \Gamma(B^+ \rightarrow D_{\mathcal{CP}\pm} K^+)}{\Gamma(B^- \rightarrow D_{\mathcal{CP}\pm} K^-) + \Gamma(B^+ \rightarrow D_{\mathcal{CP}\pm} K^+)} \\ &= \frac{\pm 2r_B \sin \gamma \sin \delta_B}{R_{\mathcal{CP}\pm}}. \end{aligned} \quad (1.75)$$

The BaBar [63], Belle [64], CDF [65] and LHCb [66] measurements in the \mathcal{CP} -even decays $B^\pm \rightarrow D(K^+K^-, \pi^+\pi^-)K^\pm$, and the BaBar [63] and Belle [64] measurements in the \mathcal{CP} -odd decays $B^\pm \rightarrow D(K_S^0\pi^0, K_S^0\phi, K_S^0\omega, K_S^0\eta)K^\pm$, give average values for the \mathcal{CP} asymmetries of [50]

$$\begin{aligned} R_{\mathcal{CP}+} &= 1.11 \pm 0.06, \quad A_{\mathcal{CP}+} = 0.27 \pm 0.04, \\ R_{\mathcal{CP}-} &= 1.10 \pm 0.07 \text{ and } A_{\mathcal{CP}-} = -0.11 \pm 0.05, \end{aligned}$$

where the errors include statistical and systematic uncertainties.

BaBar and Belle have made other GLW asymmetry measurements with $B^\pm \rightarrow D^{(*)}K^{\pm(*)}$ decays; the results are summarised in reference [50].

The value of γ extracted using the GLW method has several ambiguities [67]. The BaBar measurement of [63] is used to place loose constraints on γ .

1.5.2 The ADS method

The ADS method [68–70] is applied to modes where the D meson decays to a non- \mathcal{CP} eigenstate, such as $D \rightarrow K^+\pi^-\pi^0$ and $D \rightarrow K^\pm\pi^\mp$. The full B decay can take one of two routes as shown in Figure 1.10; one is via the favoured $b \rightarrow c$ decay followed by a doubly Cabibbo suppressed $D^0 \rightarrow f$ decay and the alternative path is via the suppressed $b \rightarrow u$ decay followed by a Cabibbo favoured $\bar{D}^0 \rightarrow f$ decay. The two interfering amplitudes from the different decay paths are comparable in size, meaning that large interference effects are possible. This maximises the possible sensitivity to γ .

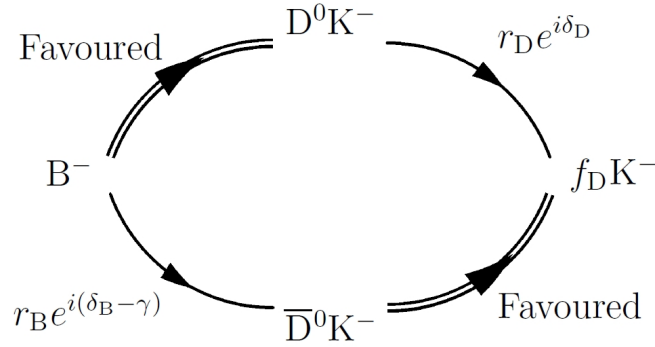


Figure 1.10: B^- decay modes used in the ADS method to maximise sensitivity to γ .

Two ADS \mathcal{CP} asymmetries, similar to those used in the GLW method, are defined as

$$\begin{aligned} R_{ADS} &= \frac{\Gamma(B^- \rightarrow fK^-) + \Gamma(B^+ \rightarrow \bar{f}K^+)}{\Gamma(B^- \rightarrow \bar{f}K^-) + \Gamma(B^+ \rightarrow fK^+)} \\ &= r_B^2 + r_D^2 + 2r_B r_D \cos \gamma \cos(\delta_B + \delta_D) \end{aligned} \quad (1.76)$$

and

$$\begin{aligned} A_{ADS} &= \frac{\Gamma(B^- \rightarrow fK^-) - \Gamma(B^+ \rightarrow \bar{f}K^+)}{\Gamma(B^- \rightarrow fK^-) + \Gamma(B^+ \rightarrow \bar{f}K^+)} \\ &= \frac{2r_B r_D \sin \gamma \sin(\delta_B + \delta_D)}{R_{ADS}}, \end{aligned} \quad (1.77)$$

where r_D is the ratio between the suppressed and favoured D decays and δ_D is the strong phase difference between them. These parameters have been measured for $D \rightarrow K\pi$ decays, giving values of $r_D = (5.78 \pm 0.08)\%$ and $\delta_D(21.9_{-12.4}^{+11.3})^\circ$ [50]. In order to allow the system, which has three unknown variables (r_B , δ_B and γ), to be overconstrained and a value for γ to be extracted, measurements of R_{ADS} and A_{ADS} must be made for two D decays to distinct non- \mathcal{CP} eigenstate final states. Alternatively, ADS rates from one D decay can be used in conjunction with rates from the GLW method to overconstrain the system in a joint ADS/GLW analysis [55].

Current ADS sensitivities to γ are poor due to the suppressed modes used in the method. Belle [71], BaBar [72], CDF [73] and LHCb [74] have observed the suppressed modes and made consistent measurements of R_{ADS} and A_{ADS} in the decay $B^\pm \rightarrow D(K\pi)K^\pm$, giving average values [50]

$$R_{ADS} = 0.0160 \pm 0.0027 \text{ and}$$

$$A_{ADS} = -0.46 \pm 0.13,$$

where the errors include statistical and systematic uncertainties.

BaBar and Belle have also made ADS asymmetry measurements using $B^\pm \rightarrow D^{(*)}(K\pi)K^{\pm(*)}$ decays and measurements of $B^\pm \rightarrow D(K\pi\pi^0)K^\pm$ and $B_d^0 \rightarrow D(K\pi, K\pi\pi^0, K\pi\pi\pi)K^*(892)^0$ decays have been made by BaBar. The results are summarised in reference [50].

1.5.3 The GGSZ (Dalitz) method

Multi-body D decays such as $D \rightarrow K_S^0\pi^+\pi^-$ and $D \rightarrow K_S^0K^+K^-$ are studied using the GGSZ, or Dalitz, method [75]. This method has several advantages over the GLW and ADS methods:

- it uses both \mathcal{CP} and flavour eigenstate final states as the whole resonant sub-structure of the decay is analysed simultaneously;
- the multi-body D decays concerned have higher branching fractions than those used in the GLW and ADS analyses; and
- the GGSZ method gives only a two-fold ambiguity in γ , $\gamma \rightarrow \gamma + \pi$.

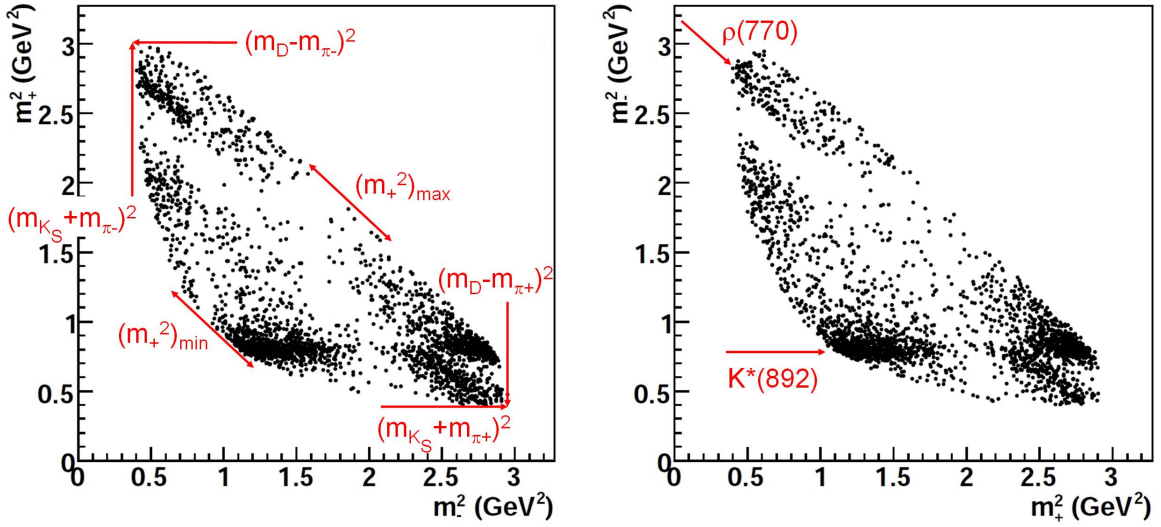
In the $D \rightarrow K_S^0 \pi^+ \pi^-$ decay, the three-body D decay amplitude can be written as

$$f(m_{\pm}^2, m_{\mp}^2) = A(D \rightarrow K_S^0(p_0) \pi^+(p_+) \pi^-(p_-)) \quad (1.78)$$

where m^2 , the invariant mass squared, is a function of the four-momenta p_0 , p_+ and p_- of the K_S^0 , π^+ and π^- daughters respectively,

$$m_{\pm}^2 = (p_0 + p_{\pm})^2. \quad (1.79)$$

Figure 1.11 shows B^+ and B^- Dalitz plots for simulated $B^{\pm} \rightarrow D(K_S^0 \pi^+ \pi^-) K^{\pm}$ decay candidates. Each point in the Dalitz plane, m_+^2 versus m_-^2 , represents a single $B^{\pm} \rightarrow D(K_S^0 \pi^+ \pi^-) K^{\pm}$ decay, with the plot boundary coming from the kinematic constraints of the decay, as shown in Figure 1.11(a).



(a) $B^+ \rightarrow D(K_S^0 \pi^+ \pi^-) K^+$

(b) $B^- \rightarrow D(K_S^0 \pi^+ \pi^-) K^-$

Figure 1.11: The Dalitz plots for $B^{\pm} \rightarrow D(K_S^0 \pi^+ \pi^-) K^{\pm}$. The red arrows in Figure 1.11(a) indicate the kinematic constraints on the distribution; for a given value of m_-^2 , the range of m_+^2 ($(m_+^2)_{\min}$ to $(m_+^2)_{\max}$) is determined by its values when the momenta of the K_S^0 and π^+ are antiparallel or parallel. The dominant resonances $K^*(892)$ and $\rho(770)$ can be seen in Figure 1.11(b). The Dalitz plots are taken from reference [76] and annotated.

In a general three-body decay $A \rightarrow xyz$, the decay can be modelled as proceeding via two-body intermediate states, for example $A \rightarrow I_{res} z$, $I_{res} \rightarrow xy$ where I_{res} is an intermediate state. The Dalitz plot from $A \rightarrow xyz$ decays will therefore show bands

in density centred around the invariant masses of the possible intermediate states. An example of this for the $D \rightarrow K_S^0 \pi^+ \pi^-$ decay is the $K^*(892)$ resonance, which appears via the process $D \rightarrow K^*(892)^\pm (K_S^0 \pi^\pm) \pi^\mp$ and is indicated in Figure 1.11(b). The spins and parities of the intermediate resonances cause the bands in the Dalitz distributions to have characteristic patterns [77]. In Figure 1.11 the differences in occupancy between the Dalitz plots from B^+ events and B^- events due to the effects of \mathcal{CP} -violation can be seen, in particular in the regions at the top left, bottom left and bottom right of the kinematically-allowed region.

The distributions of B^+ and B^- candidate decays in the Dalitz plane are described by probability density functions $S_+(m_+^2, m_-^2)$ and $S_-(m_-^2, m_+^2)$ respectively, which can be found from Equations 1.64, 1.65 and 1.78,

$$S_+(m_+^2, m_-^2) = |f(m_+^2, m_-^2) + r_B e^{i(\delta_B + \gamma)} f(m_-^2, m_+^2)|^2 \quad (1.80)$$

$$S_-(m_-^2, m_+^2) = |f(m_-^2, m_+^2) + r_B e^{i(\delta_B - \gamma)} f(m_+^2, m_-^2)|^2. \quad (1.81)$$

In these expressions, the first terms arise from the CKM favoured and colour favoured decays (Figure 1.7(a)) and the second terms from the CKM suppressed and colour suppressed decays (Figure 1.7(b)).

Fitting $S_+(m_+^2, m_-^2)$ and $S_-(m_-^2, m_+^2)$ simultaneously over the Dalitz plane allows γ , r_B and δ_B to be extracted. The amplitude for the $D \rightarrow K_S^0 \pi^+ \pi^-$ decay, $f(m_\pm^2, m_\mp^2)$, must be taken into account, either by using a binned model-independent approach [75, 78] or by using an unbinned model-dependent method, as described in reference [79].

Both Belle and BaBar have used the GGSZ model-dependent method to extract γ . A BaBar measurement with $B_d^0 \rightarrow D(K_S^0 \pi^+ \pi^-) K^{*0}$ decays gives a loose constraint on γ [80]. The current best measurements with $B^\pm \rightarrow D^{(*)}(K_S^0 \pi^+ \pi^-, K_S^0 K^+ K^-) K^{\pm(*)}$ decays are

$$\gamma = (78.4_{-11.6}^{+10.8} \pm 3.6 \pm 8.9)^\circ$$

at Belle [81] and

$$\gamma = (68 \pm 14 \pm 4 \pm 3)^\circ$$

at BaBar [82], where the first error is statistical, the second is systematic and the third is the error due to the model description of the Dalitz plot amplitude. Belle have also

performed a model-independent GGSZ measurement of γ with $B^\pm \rightarrow D(K_S^0 \pi^+ \pi^-)K^\pm$ decays only, extracting the value [83]

$$\gamma = (77.3_{-14.9}^{+15.1} \pm 4.2 \pm 4.3)^\circ,$$

where the first error is statistical, the second is systematic and the third is the error due to the input of CLEO-c strong phase measurements [84].

1.5.4 Combined time-independent γ measurement

Combining direct tree-level measurements from GLW, ADS and GGSZ analyses of $B \rightarrow D^{(*)}K^{(*)}$ decays gives [34]

$$\gamma = (68_{-11}^{+10})^\circ$$

with the fit result shown in Figure 1.12.

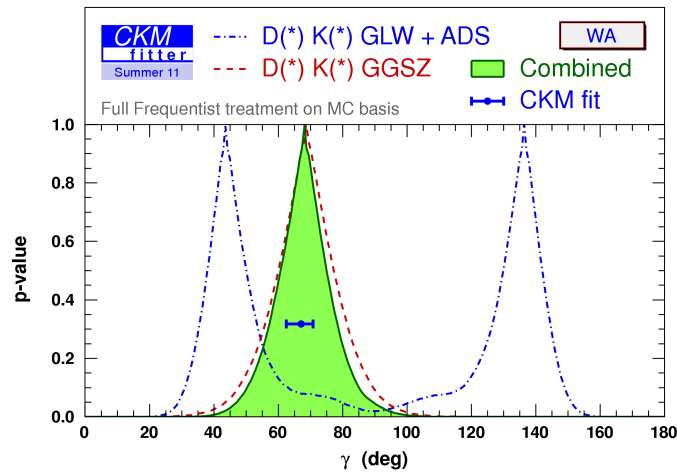


Figure 1.12: The global fit to direct measurements of the CKM angle γ [34].

At LHCb, the sensitivity to γ has been estimated from a global fit using the $B \rightarrow DK^{(*)}$ decay channels; for an integrated luminosity of 2 fb^{-1} at $\sqrt{s} = 14 \text{ TeV}$ the expected sensitivity is $3.9^\circ - 5.1^\circ$ [55, 85] using both time-independent and time-dependent measurements.

1.6 Summary

\mathcal{CP} -violation is vital in explaining the matter-antimatter imbalance in the Universe, as it allows for a difference between the interactions of matter and antimatter. It was first seen in the neutral kaon system and has been experimentally observed more recently in the B-meson system.

\mathcal{CP} -violation can be accommodated in the SM as an irreducible complex phase in the CKM matrix, however the amount of \mathcal{CP} -violation in the SM is not large enough to account for the observed matter-antimatter asymmetry in the Universe. The observed baryon asymmetry of the Universe is $(n_B - n_{\bar{B}})/n_\gamma \approx n_B/n_\gamma \approx 10^{-10}$ [86], in contrast to the predicted value from the Big Bang model assuming no initial asymmetry, $n_B/n_\gamma \approx 10^{-18}$ [86]. The amount of SM \mathcal{CP} -violation in the early Universe is at least eight orders of magnitude too small to account for the observed asymmetry value [87]. This is currently one of the most puzzling topics in particle physics and cosmology and the search for sources of \mathcal{CP} -violation from new physics theories beyond the SM has become a key area of research. The heavy flavour sector is the ideal area in which to perform this search as precision SM measurements of \mathcal{CP} parameters as well as NP measurements can be made.

γ is the least well-measured of the CKM angles. A precision measurement of this angle using SM processes is required in order to overconstrain the UT and to provide a SM benchmark against which other measurements, which may include NP contributions, can be compared. The current combined best fit value of $\gamma = (68_{-11}^{+10})^\circ$ from direct measurements is dominated by B-factory results, but the LHC is now providing the much higher statistics required to greatly reduce this error.

Chapter 2

The LHCb experiment at the LHC

The Large Hadron Collider beauty (LHCb) experiment at CERN is the only dedicated heavy flavour physics experiment at the Large Hadron Collider (LHC). Operation of both the LHC and the experiment began in late 2009. Section 2.1 of this chapter gives an overview of the LHC accelerator and Section 2.2 contains details of heavy flavour production at the LHC, a discussion of b-hadron decays and a description of the LHCb detector. Detector control, monitoring and data flow are described in Section 2.3 and the LHCb software is discussed in Section 2.4.

2.1 The Large Hadron Collider

The LHC, conceived in the 1980s, is a proton-proton collider now installed and operating in the 27 km circular tunnel that previously housed the Large Electron-Positron (LEP) collider. The LHC ring is a synchrotron accelerator [88–90], using 1232 superconducting dipole magnets (Figure 2.1) with a nominal magnetic field strength of 8.33 T to bend two counter-rotating proton beams around the ring. The dipole magnets are cooled with liquid helium, allowing an operating temperature of 1.9 K. Other magnets, for example quadrupoles, are used to optimise the particle trajectories and focus the beam.

Figure 2.2 shows a schematic of the LHC beam acceleration and injection complex [91]. Protons are obtained from a hydrogen duoplasmatron source and are initially accelerated in a linear accelerator to an energy of 50 MeV [92, 93]. They are then injected into the Proton-Synchrotron-Booster (PSB) complex and accelerated to 1.4 GeV in one of the PSB’s four rings. Each of these rings is one quarter of the circumference of

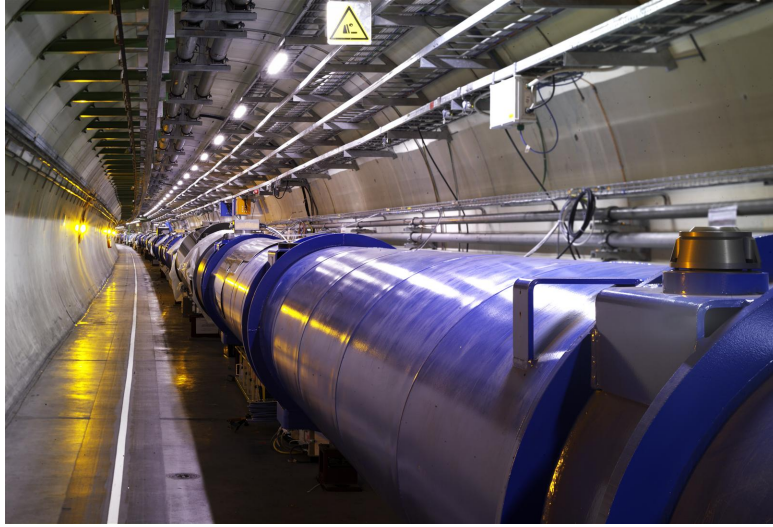


Figure 2.1: An LHC dipole magnet within the accelerator tunnel.

the Proton-Synchrotron (PS) ring and accelerates one proton bunch. The bunches are transferred into the PS, where they are divided, accelerated to an energy of 25 GeV and divided again to form the nominal LHC 25 ns bunch train. The splitting process also allows for the creation of the time gaps in the beam structure which are required for ramp up of the PS extraction magnets. After transfer to the Super-Proton-Synchrotron (SPS), further acceleration to 450 GeV occurs, before the beam is finally injected into the LHC ring. The time to fill both LHC rings is ~ 16 min [90] and in nominal running will be followed by ~ 20 min of final proton acceleration to 7 TeV. Eight radiofrequency (RF) cavities per beam are used within the LHC to accelerate the particles to their final energy and to optimise the beam bunch structure in order to ensure high luminosity at the collision points.

The maximum possible number of bunches in a beam would be approximately 3600, however empty bunch buckets are inserted into the bunch train to allow transfer of the protons from the PS to the SPS. In nominal running conditions, each of the two final proton beams will be structured as 2808 bunches spaced at 25 ns intervals, with each bunch containing 1.15×10^{11} particles. Figure 2.3 shows the four points around the LHC ring, in the ATLAS [94], CMS [95], LHCb [96] and ALICE [97] detectors, where the beams are brought together to collide. The nominal LHC operating luminosity is $10^{34} \text{ cm}^{-2} \text{ s}^{-1}$ but at the LHCb interaction point a lower luminosity $\mathcal{O}(10^{32}) \text{ cm}^{-2} \text{ s}^{-1}$ is achieved by a local de-focussing of the beams [98], so that events are dominated by a single proton-proton interaction per bunch crossing.

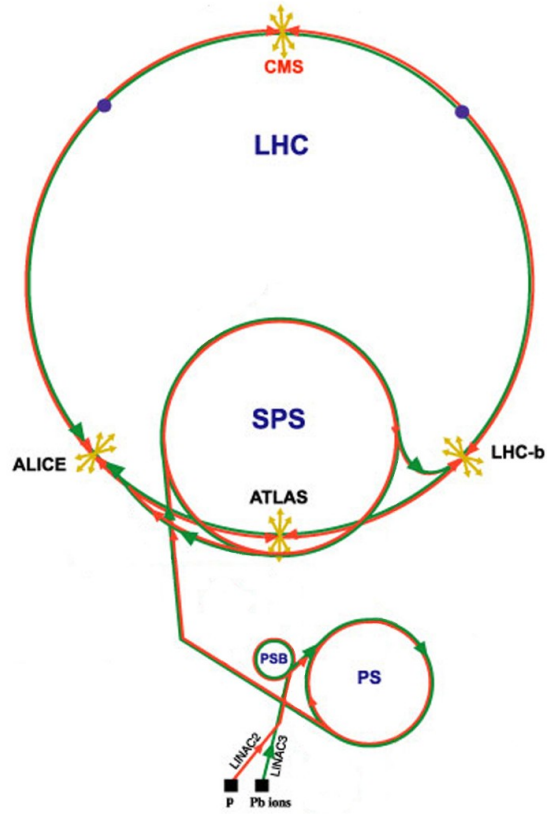


Figure 2.2: The LHC injector complex.

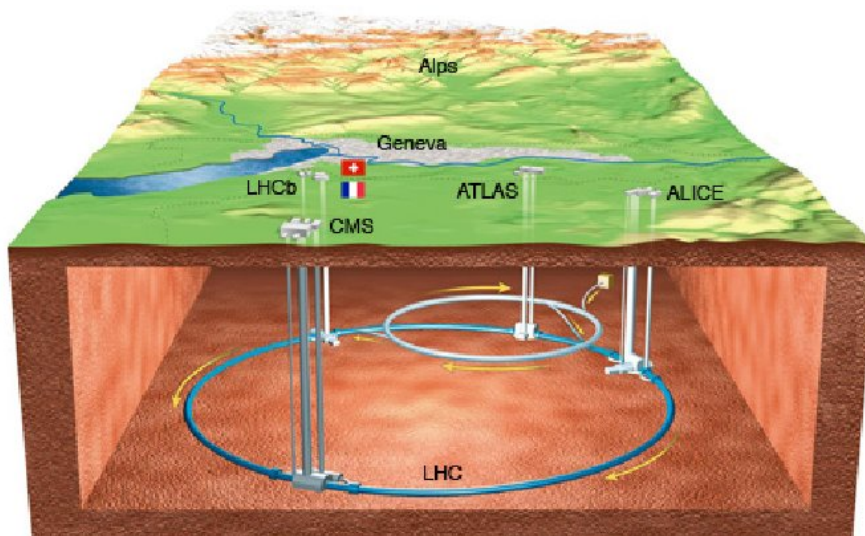


Figure 2.3: The LHC ring and the main experimental sites.

2.2 The LHCb experiment

The LHCb detector was primarily designed to make precision measurements of charge-parity (\mathcal{CP}) violating and rare heavy flavour decays (including those of B-mesons, Λ_b and D-mesons) and hence potentially find indirect evidence for NP beyond the Standard Model [98, 99]. The following sections detail the physics of heavy flavour production at the LHC, b-hadron decays and the consequences of these on the detector design. Overview descriptions of the individual subdetectors of LHCb are then given.

2.2.1 LHCb luminosity

At the nominal LHC luminosity of $10^{34} \text{ cm}^{-2} \text{ s}^{-1}$, LHCb would see, on average, $\mathcal{O}(10)$ inelastic proton-proton interactions per bunch crossing. The consequent detector occupancy would, however, be too high for acceptable readout, particularly in the tracking stations. Also, bunch crossings with multiple interactions are less suitable for b-tagging and lifetime analysis because of the ambiguities arising from multiple reconstructed proton-proton interaction vertices.

The probability of a given number of inelastic proton-proton interactions per bunch crossing as a function of luminosity is shown in Figure 2.4. The factors described above make it necessary for LHCb to run at a reduced nominal luminosity of $2 \times 10^{32} \text{ cm}^{-2} \text{ s}^{-1}$ [96], so that the number of single proton-proton interaction bunch crossings is maximised and the number of multiple interaction crossings is lowered. This is achieved by a local defocussing of the LHC beams at the interaction point. Running at lower luminosity has the additional benefit of reduced radiation damage to the detector components.

2.2.2 Heavy flavour production

The large inclusive $b\bar{b}$ production cross-section at the LHC centre-of-mass energy means that the LHC is the most intense source of b-hadrons in the world. Assuming an estimated 14 TeV cross-section of $500 \text{ } \mu\text{b}$ and the nominal LHCb luminosity of $2 \times 10^{32} \text{ cm}^{-2} \text{ s}^{-1}$, 10^{12} $b\bar{b}$ pairs will be produced per nominal data-taking year (10^7 s), giving a b-production rate of 100 kHz [96]. At e^+e^- colliders, such as PEP-II and KEK (for the BaBar and Belle experiments, respectively), the centre-of-mass energy of interactions is fixed. At a hadron collider such as the LHC, however, the parton distribution functions of the

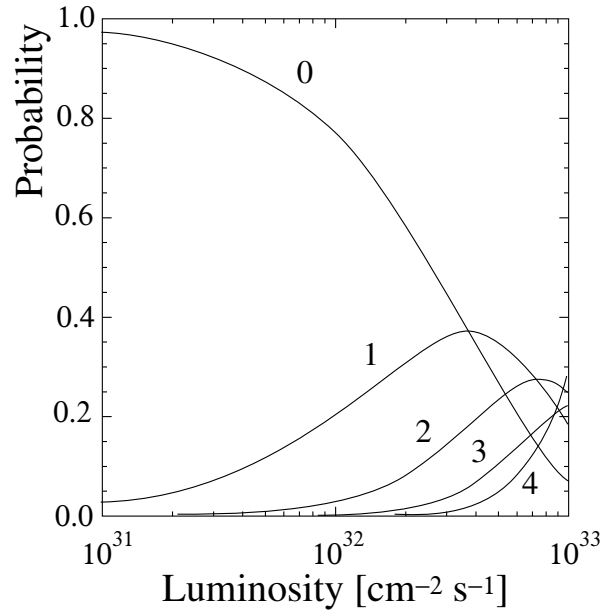


Figure 2.4: The proton-proton interaction probability as a function of LHC luminosity, assuming an inelastic proton-proton cross-section of 80 mb [98]. Curves are shown for zero, one, two, three and four interactions per bunch crossing.

protons mean that the interactions have a range of energies. The whole spectrum of b-hadrons is produced, with approximate fractions: B_d (40%), B_u (40%), B_s (10%) and b-baryons (10%) at the LHC [18].

The cross-section for b-quark production has been calculated to next-to-leading order (NLO) in perturbative QCD; perturbation theory can be used because the QCD scale (~ 1 GeV) is small compared to the b-quark mass. Three main processes, some of which are shown in Figure 2.5, are expected to dominate $b\bar{b}$ production at the LHC [100]:

- flavour creation in hard QCD scattering (gluon-gluon fusion, shown in Figure 2.5(a), and quark-antiquark annihilation, shown in Figure 2.5(b));
- gluon splitting in initial or final states (Figure 2.5(c)); and
- flavour excitation (a semi-hard process).

At NLO, the flavour excitation process, where the heavy quark is assumed to be already present in the colliding proton, is allowed. The Feynman diagrams for this process are not explicitly included in the cross-section calculation, however, because the net contribution from these diagrams is already included as a higher-order correction to the gluon-gluon fusion process [101]. Figure 2.6 shows the measured cross-section

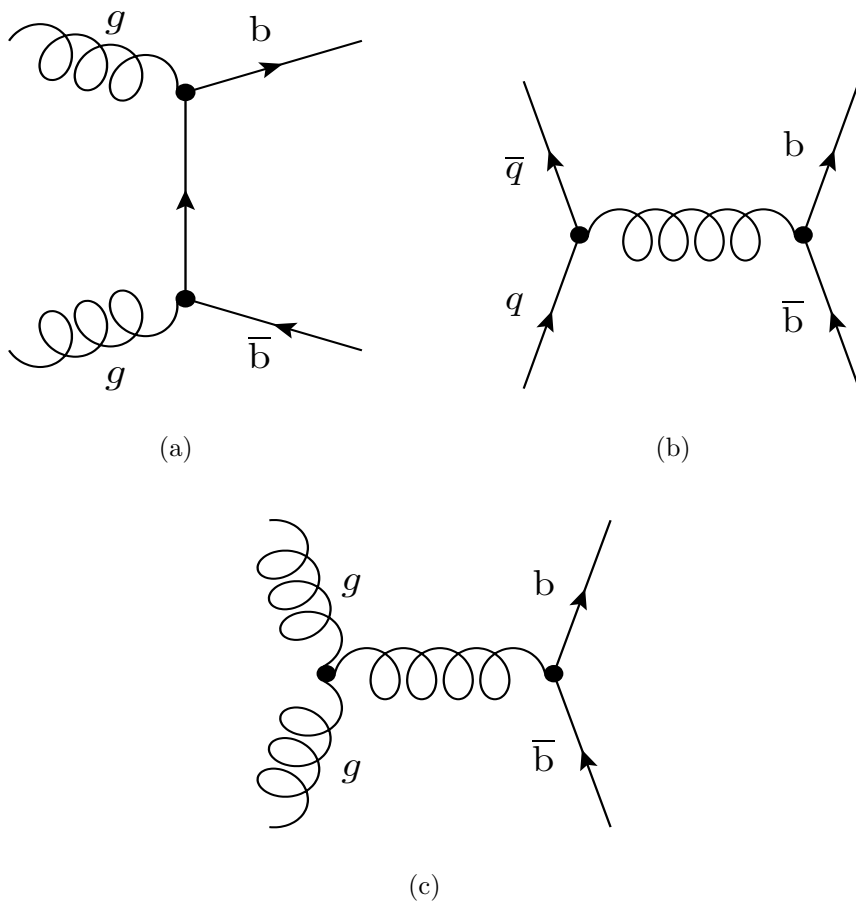


Figure 2.5: Examples of Feynman diagrams for dominant $b\bar{b}$ production processes. Figure 2.5(a) shows gluon-gluon fusion, Figure 2.5(b) shows quark-antiquark annihilation and Figure 2.5(c) shows gluon splitting.

$\sigma(\text{pp} \rightarrow \text{b}\bar{\text{b}}X)$ as a function of pseudorapidity from LHCb data at $\sqrt{s} = 7$ TeV [102]. Also shown for comparison are two predictions for the distribution using different parton distribution functions. It can be seen that the measured distribution is consistent with the predictions, both in normalisation and pseudorapidity-dependent shape.

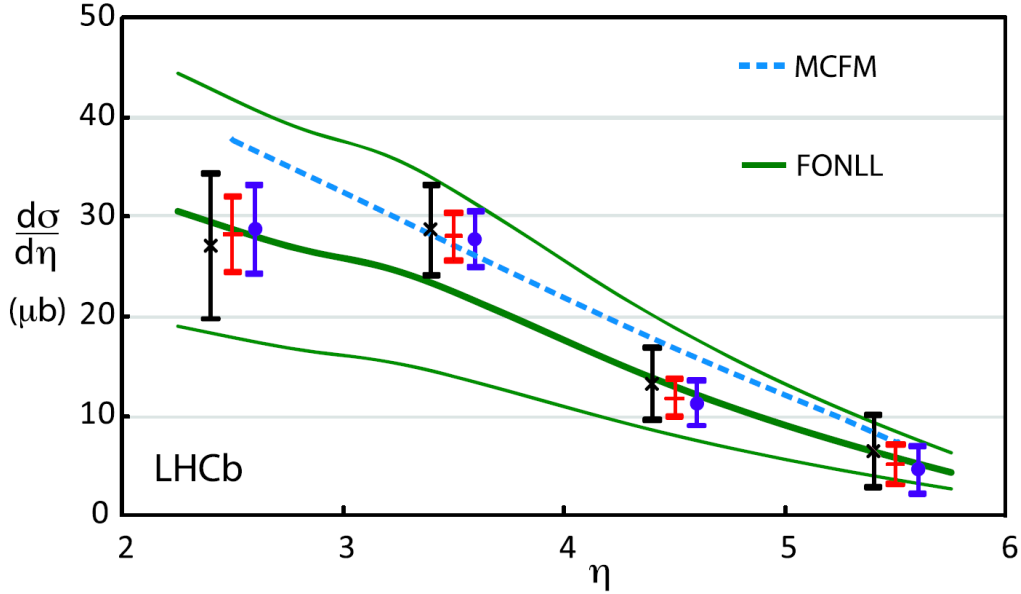


Figure 2.6: The measured cross-section $\sigma(\text{pp} \rightarrow \text{b}\bar{\text{b}}X)$ as a function of pseudorapidity from LHCb data at $\sqrt{s} = 7$ TeV [102]. The \times and \cdot data points indicate results from two independent data samples; the $+$ data points are the averages of these two results. The MCFM and FONLL predictions are also shown; the thin green lines indicate the theoretical uncertainties on the FONLL prediction.

As the rapidity difference between the b-quark and $\bar{\text{b}}$ -antiquark of a $\text{b}\bar{\text{b}}$ pair increases, the production cross-section decreases [103]. The quark and antiquark therefore have highly correlated polar angles with respect to the beam line. Also, the cross-section is suppressed as the transverse mass (the sum in quadrature of the b-quark mass and the transverse momentum, p_{T} , with respect to the beam line) of the system increases. These two effects mean that $\text{b}\bar{\text{b}}$ pairs are predominantly produced with both quarks in the forward direction or both in the backward direction, with similar rapidity and small p_{T} (see Figure 2.7).

The correlation in the direction of production has consequences for the LHCb detector design because the production of a b-quark within the detector acceptance means that the production of a corresponding $\bar{\text{b}}$ -antiquark also within the acceptance is highly likely. It is particularly important for b-tagging analyses where the flavour of a B-particle of interest is determined at production by measurement of the flavour of the other B-particle

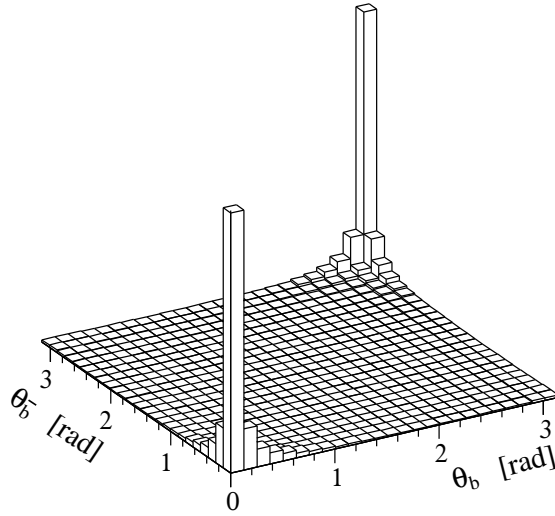


Figure 2.7: The simulated polar production angle with respect to the beam line (θ_b and $\theta_{\bar{b}}$) of b-hadrons at the LHC [98].

in the event, therefore requiring both of these particles to be within the acceptance.

The LHCb detector was designed as a single-arm forward spectrometer [96], due to the space constraints of the existing cavern and budgetary considerations. The correlation in $b\bar{b}$ pair production angles means that the loss in statistics due to reduced angular coverage is only a factor of two, however, and the increase in precision from using all of the available space for a single-arm detector outweighs this loss. The maximum angular acceptance of the detector is 300 mrad in the bending (horizontal) plane and 250 mrad in the non-bending (vertical) plane; the minimum acceptance is defined by the beam-pipe. A schematic of LHCb is shown in Figure 2.8^a and a photograph of the experimental cavern is shown in Figure 2.9. Most of the detector subsystems are divided into two halves which can be moved out separately to allow access to the beam-pipe and assembly and maintenance.

2.2.3 b-hadron decays

Tree-level weak decays of b-hadrons occur via the CKM-suppressed $b \rightarrow u$ and $b \rightarrow c$ quark transitions, because the CKM-favoured transition of $b \rightarrow t$ is kinematically forbidden due to the large top-quark mass ($m_t \sim 173 \text{ GeV}/c^2$ [18]). Hence, due to the

^aIn Figure 2.8, the y and z coordinate directions of the LHCb coordinate system are shown. LHCb uses a right-handed coordinate system, so that positive x goes into the page. The proton-proton interaction point is approximately at the position $x = y = z = 0$.

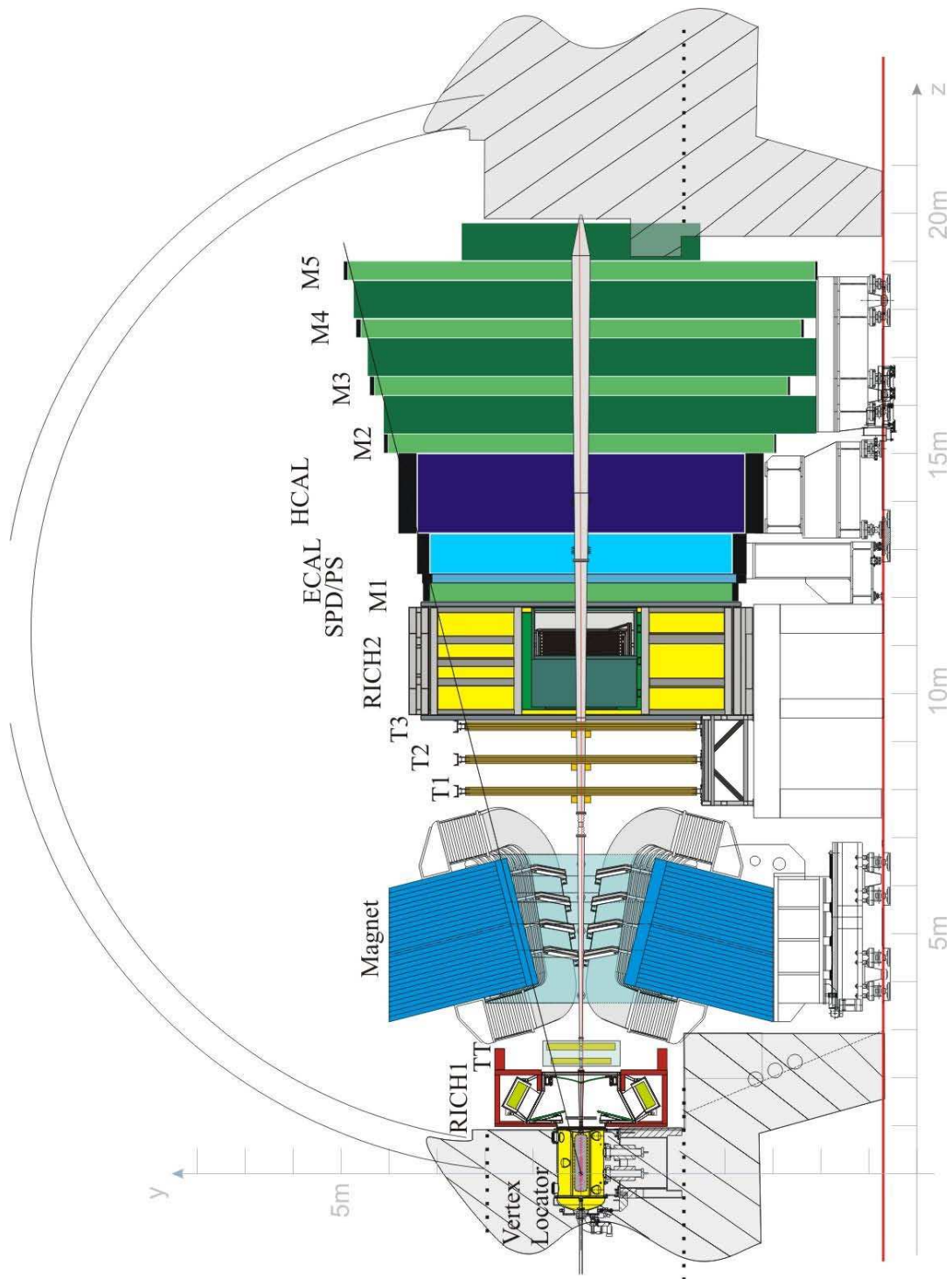


Figure 2.8: The LHCb detector [96]. The downstream direction is defined as the direction of increasing z coordinate, with the vertex locator (VELO) situated at $z = 0$. This is followed by the first charged particle identification (PID) subdetector (RICH1), the first tracking station (TT), then the magnet. Downstream of the magnet are the three tracking stations (T1-T3), the second PID subdetector (RICH2), the muon station M1, the calorimetry system (SPD/PS/ECAL/HCAL) and the muon stations M2-M5.

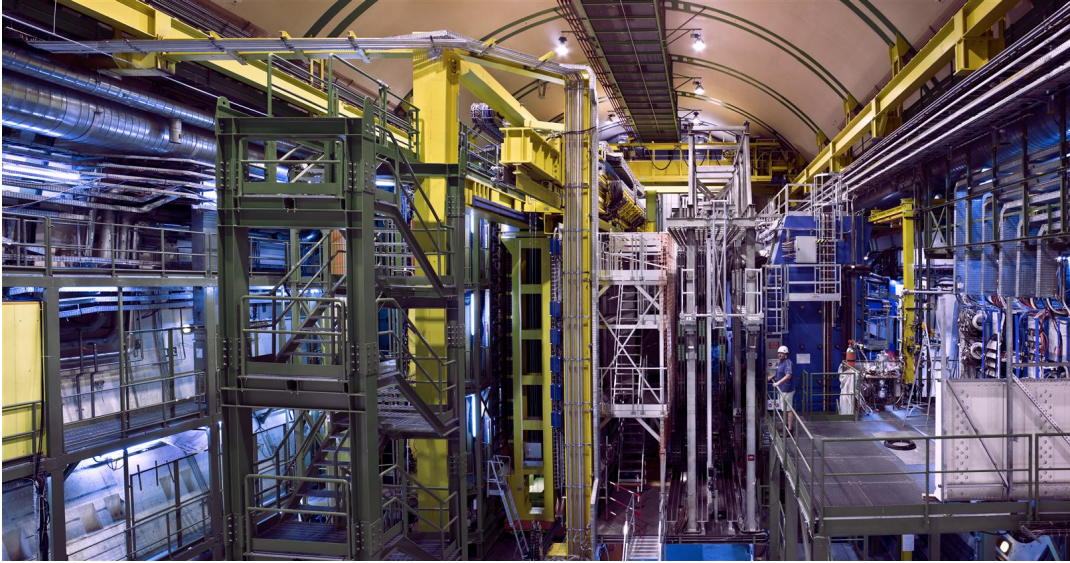


Figure 2.9: A photograph of the LHCb detector within the experimental cavern. The z coordinate increases from right to left.

small CKM factors for these inter-generation transitions ($|V_{ub}| = 3.501 \times 10^{-3}$ and $|V_{cb}| = 40.7 \times 10^{-3}$ [34]), B-mesons have long proper lifetimes, $\tau_b \sim \mathcal{O}(1)$ ps [18]. Typical b-hadron momenta at LHCb therefore give a decay length of ~ 1 cm [98]. The detector must be able to distinguish displaced decay vertices from primary proton-proton interaction vertices (PVs) because the displaced vertices are an excellent signature of b-hadron decays. The vertex locator (VELO) subdetector (Section 2.2.5) was designed for this function and allows for precise vertexing for B-meson lifetime studies.

The LHCb tracking system, described in Section 2.2.6, has been designed to measure the momenta of charged particles to high precision. This allows good mass resolution to be achieved, so that background can be reduced in the signal reconstructed mass region. In order to perform precise \mathcal{CP} -violation and rare B-decay analyses, the LHCb detector must be capable of reconstructing charged particle tracks, up to ~ 150 GeV/ c , with high efficiency.

Many of the decay modes under study have charged hadrons in the final state and so good particle identification (PID) is necessary to distinguish between them. The Ring Imaging Cherenkov (RICH) subdetectors, described in Section 2.2.8, provide crucial PID information, in particular for π^\pm and K^\pm separation. The calorimeters, described in Section 2.2.9, provide PID information for neutral particles and electrons, and the muon subdetectors (Section 2.2.10) provide muon PID. The identification of high p_T muons is important because, due to their penetrating power, they can provide a clean signal for

the trigger.

During nominal data-taking, the expected b-production rate at LHCb is 100 kHz [96]. The fraction of $b\bar{b}$ events with all of the decay products of at least one B-meson within LHCb detector acceptance is ~ 0.15 and the decays of interest typically have branching fractions less than $\mathcal{O}(10^{-3})$. A two-level trigger system, described in Section 2.2.11, is therefore necessary to select an enriched sample of events of interest from all proton-proton bunch crossings. The trigger has hardware and software stages to efficiently select events to be recorded for later detailed analysis.

The trigger and various subdetectors (VELO, tracking system, RICH subdetectors, calorimeters and muon subdetector) of LHCb, designed to meet the requirements detailed above, are described in the following sections.

2.2.4 Beam-pipe

The continuation of the LHC vacuum through the centre of LHCb is provided by the experiment beam-pipe, which is 19 m long [96]. This is the high rapidity region of the detector and so has large particle densities; any material seen by primary incident particles must have a minimal interaction length in order to avoid the production of secondary particles and a corresponding increase in detector occupancy. The beam-pipe mass and the presence of connecting bellows and flanges directly affects occupancy, particularly for the RICH subdetectors and the tracking chambers. The design and materials of the beam-pipe were therefore chosen to minimise these effects.

The beam-pipe is divided into four conical sections, with the three sections closest to the interaction point made of beryllium and the section furthest from the interaction point made of stainless steel. Beryllium was chosen for the sections in the occupancy sensitive region because of its high transparency to particles produced in proton-proton collisions. The first section of beam-pipe is 1 mm thick and runs from the VELO exit window, traversing RICH1 and the Tracker Turicensis (TT) and including a 25 mrad half-angle cone and a transition to the 10 mrad half-angle cone used in the other sections. The second and third sections, passing through the dipole magnet and through the Tracker, RICH2, M1 and part of ECAL respectively, have thicknesses varying from 1 mm to 2.4 mm as the diameter of the beam-pipe increases. The fourth section passes through the remaining parts of the calorimeter and muon systems and is 4 mm thick. It completes the 10 mrad cone and also provides another cone for the transition to the

final 60 mm aperture.

In order to allow independent commissioning and maintenance of the detector, the experiment beam vacuum is separated from the LHC vacuum with isolation valves at the cavern entrance and exit.

2.2.5 Vertex locator

The VELO detects tracks close to the proton-proton interaction point and is therefore a vital part of the LHCb tracking system. The information it provides is used to find the displaced secondary decay vertices which are a signature of heavy flavour decays [96, 104]. Good reconstruction of these vertices is necessary for b-tagging studies and to ensure the required signal-to-background ratios for reconstructed B-decays are achieved. A typical b-hadron momentum at LHCb gives a decay length of ~ 1 cm, so the VELO must provide resolution $\mathcal{O}(1 \text{ mm})$ on the position of the vertices. The VELO also extends upstream of the nominal interaction point, so that PVs can be reconstructed. Tracks from b-hadron decays typically have a large impact parameter with respect to the PV and this quantity is therefore a useful discriminating variable in the selection of decays; in order to calculate it, the position of the PV must be known accurately. If a track from the PV is misassigned to a secondary decay vertex, a B-decay will be reconstructed incorrectly to form a combinatoric background event. A further pair of dedicated tracking stations at the upstream end of the VELO provide information for the pile-up trigger, described in Section 2.2.11. The VELO also provides data for a fast track finding algorithm in the trigger.

The VELO consists of 21 tracking stations, each divided into two modules, as shown in Figure 2.10. The VELO modules upstream of the nominal interaction point are used to improve resolution on the PV position; an additional two stations for pile-up are also labelled as “VETO stations”. A short track extrapolation length from the first station to the PV leads to a better resolution on impact parameter measurements, so the innermost radius of the active sensor area should be as small as possible; however, the distance of closest safe approach to the beam line changes on injection into the LHC. During stable running, the closest allowed approach is 5 mm [96, 105], with active silicon at a distance of ~ 8 mm. During injection and beam acceleration, the RMS beam spot size increases; the two halves of the VELO have therefore been designed to retract by a distance of 3 cm [96, 105] to prevent damage. In order to cover the full azimuthal acceptance and to improve alignment, the geometry of the sensors is staggered so that the two halves of

each station overlap when the VELO is closed.

The silicon sensors are mounted onto support structures which, together with the associated readout electronics chips, are called modules; a photograph of three modules is seen in Figure 2.11. A cylindrical geometry is used for the sensors because it allows faster reconstruction of tracks and vertices for the trigger than rectilinear coordinates. Each module has two silicon sensors, one to measure radial coordinate (R-sensor) and one to measure azimuthal angles (ϕ -sensor).

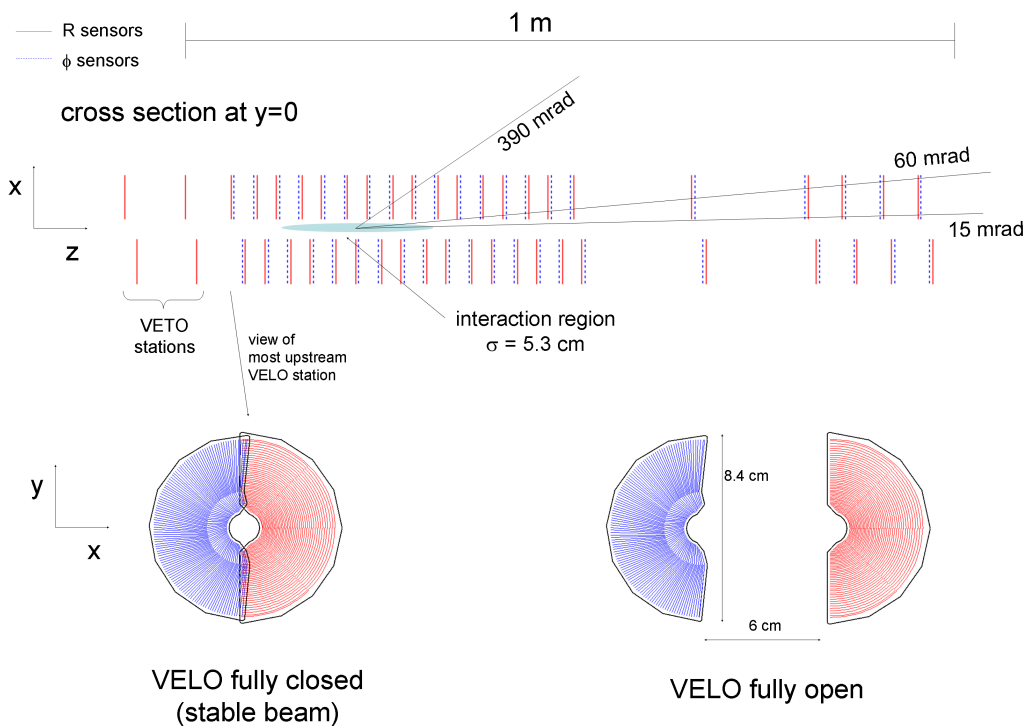


Figure 2.10: The LHCb VELO, as seen from above, showing the module layout [96]. A station consists of two modules, one in each half of the VELO.

The VELO is designed so that any track within LHCb angular acceptance should pass through at least three of its modules. The outer radius of the VELO sensors means that the spacing between modules in the central region must be less than 5 cm. The position of the most downstream module is determined by the inner angular acceptance of 15 mrad and the minimum distance of the sensors to the beam line.

In order to reduce the material seen by tracks and to allow the sensors to be as close to the beam as possible, the VELO is operated under vacuum. The VELO vacuum

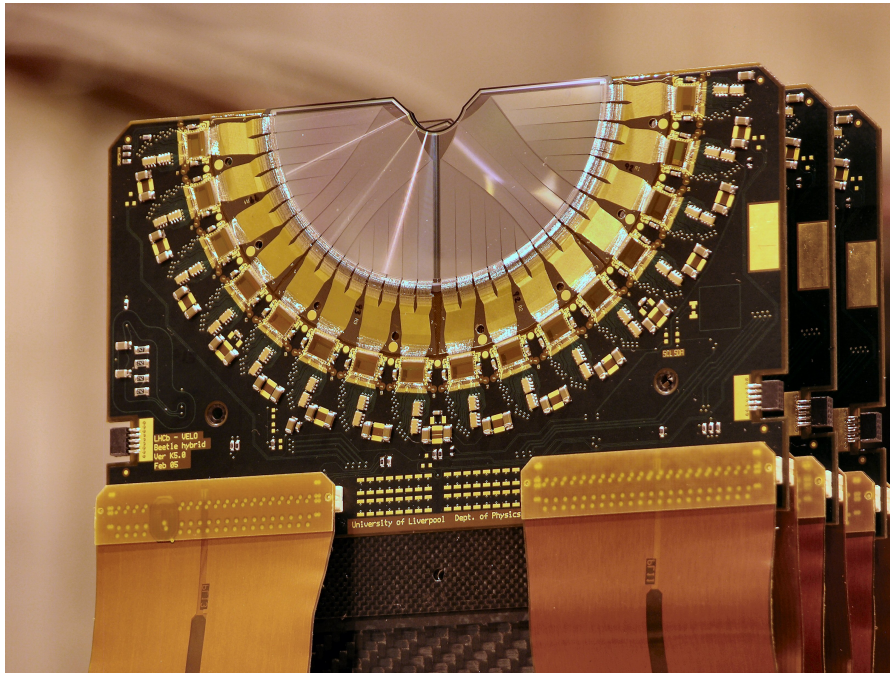


Figure 2.11: Three LHCb VELO modules.

enclosure acts like an extension to the LHC beam-pipe, however, to protect the LHC vacuum from outgassing of the modules, the two detector halves are placed inside thin aluminium vacuum boxes, called the RF boxes. The boxes also act as a shield, protecting the VELO from radiofrequency (RF) pickup from the LHC beams and protecting the beams from the effects of wake fields generated as they pass through the VELO structure. Figure 2.12 shows the arrangement of the modules along a section of the RF boxes around the beam line. The sections of RF box in this region are called the RF foil and are corrugated to allow overlap of the two VELO halves.

The VELO silicon sensors [96] are designed to read out orthogonal coordinates. Each sensor is an approximately semi-circular annulus with the outer radius of the active area equal to 42 mm. The overall size of a sensor is limited by the wafers used to produce it. The inner sensitive radius is ~ 8 mm, due to the space necessary for the RF foil and the 1 mm thick guard structures on the silicon, as well as the minimum safe distance from the beam line (5 mm). There are 2048 readout channels per sensor and the corresponding silicon strip layouts are shown in Figure 2.13. The R-sensors are divided into four sectors, each with 512 strips running concentrically. The segmentation into four regions minimizes occupancy and reduces strip capacitance. The strip pitch varies linearly from the inner edge (38 μm) to the outer edge (102 μm) in order to keep the strip occupancy approximately constant across the subdetector and to ensure that measurements along

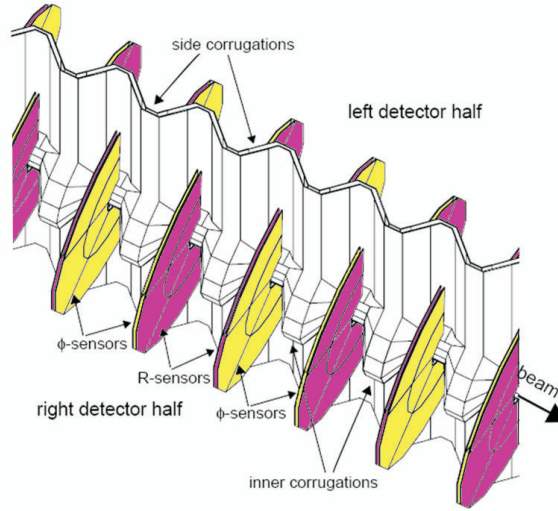


Figure 2.12: VELO modules positioned along the RF foil [96].

a track contribute to the impact parameter precision with equal weight. The ϕ -sensors are divided radially into two sections to reduce occupancy and to prevent too large a strip pitch at the outer edge. The strips in each section have different skews with respect to the radial direction: the inner section has 683 strips with angle 20° to the radial and the outer section has 1365 strips with angle -10° to the radial. In adjacent modules the ϕ -sensors have opposite skews with respect to each other, providing a stereo effect. The strip pitch at the innermost radius is $38\ \mu\text{m}$ and increases linearly to the boundary between the inner and outer sections. At the inner radius of the outer section, the strip pitch is $39\ \mu\text{m}$, approximately half of the pitch of the inner section strips at the boundary.

The VELO subdetector meets all of the requirements for vertex finding at LHCb. It presents an average of 17.5% of a radiation length of material to tracks within the detector acceptance, the largest contribution to this coming from the RF foil. Figure 2.14 shows the reconstructed PV resolution in 2010 data as a function of the number of tracks used to reconstruct the vertex. It can be seen that a 25 track resolution of $14\ \mu\text{m}$ in x , $13\ \mu\text{m}$ in y and $75\ \mu\text{m}$ in z was achieved. In early 2011, a 25 track resolution of $13.0\ \mu\text{m}$ in x , $12.5\ \mu\text{m}$ in y and $68.5\ \mu\text{m}$ in z was found, as shown in Figure 2.15. Figure 2.16 shows the impact parameter resolution achieved in 2010 and Figure 2.17 shows the same distributions for the early 2011 data. The expected parameterisation of these distributions from simulation is $\sigma_{IP} = 14\ \mu\text{m} + 35\ \mu\text{m}/p_T$, where p_T is measured in GeV/c [96].

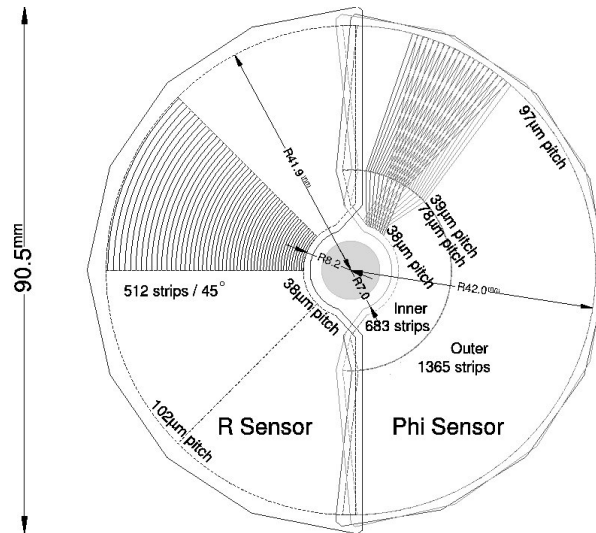


Figure 2.13: VELO silicon sensors, with some strips shown [96]. For the ϕ -sensor, strips on two adjacent modules are indicated so that the stereo angle can be seen.

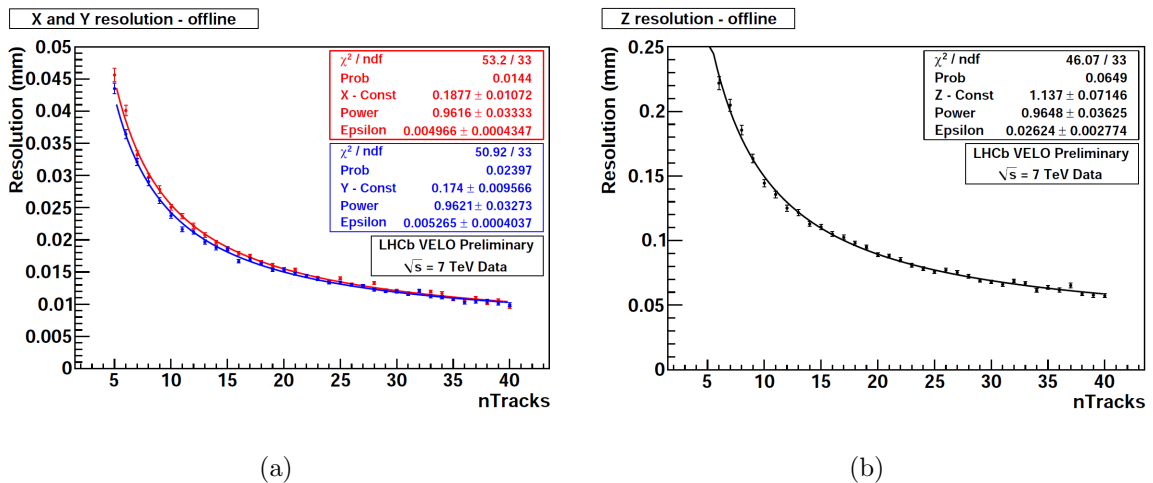


Figure 2.14: VELO PV resolution in 2010 data as a function of the number of tracks used to reconstruct the vertex [106].

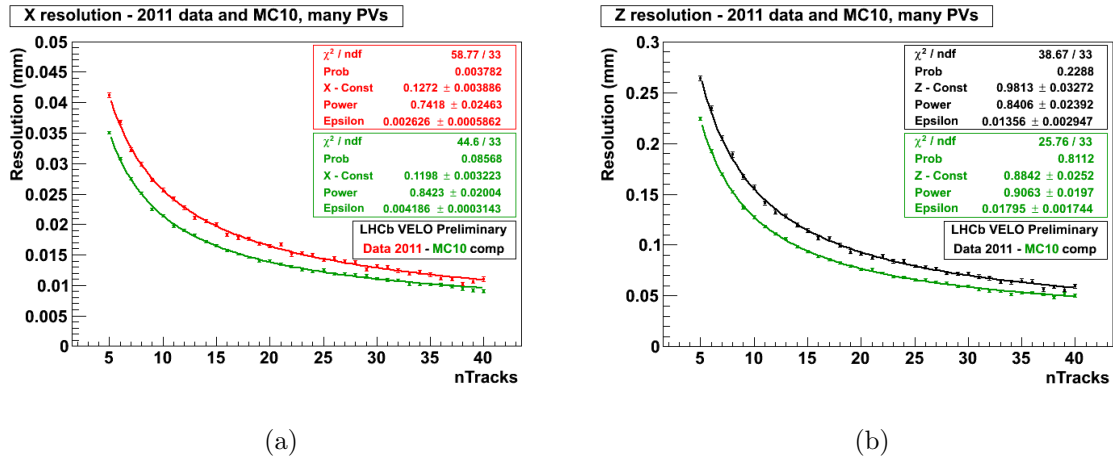


Figure 2.15: VELO PV resolution in 2011 data and simulation (MC10) as a function of the number of tracks used to reconstruct the vertex [107].

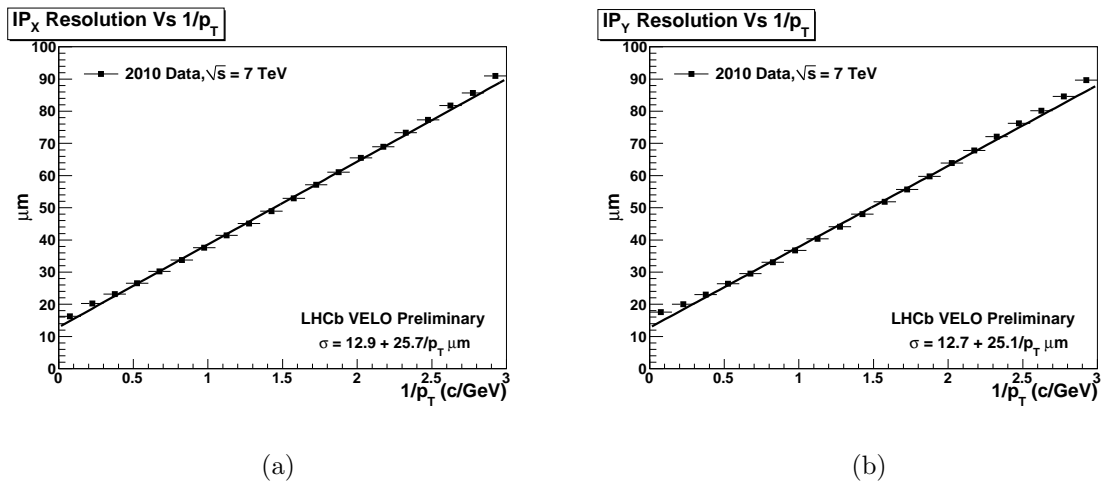


Figure 2.16: VELO impact parameter resolution in 2010 data as a function of inverse transverse momentum.

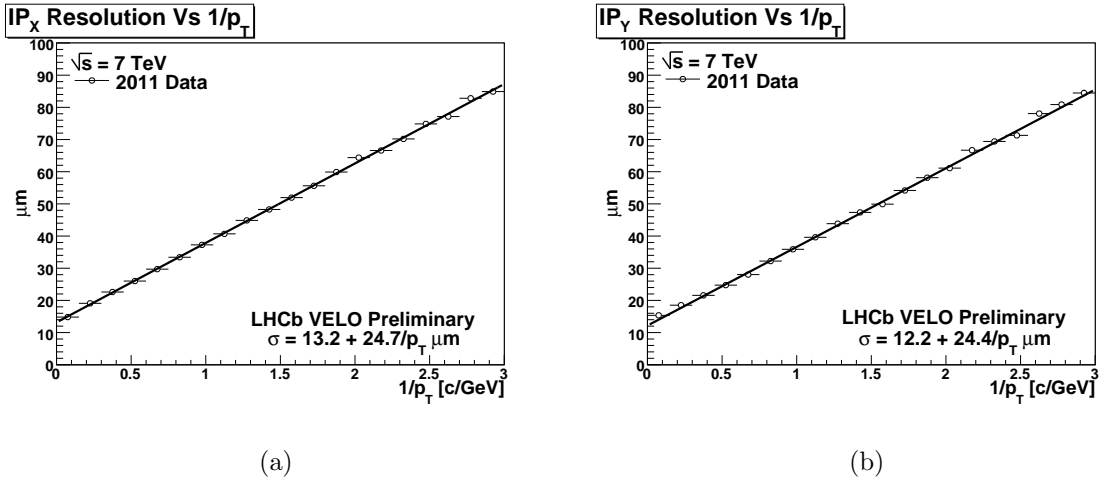


Figure 2.17: VELO impact parameter resolution in 2011 data as a function of inverse transverse momentum.

2.2.6 Tracking system

The LHCb tracking system consists of the VELO, the TT upstream of the dipole magnet and stations T1-T3 downstream of it [96, 99]. The overall aim of these subdetectors is to provide accurate spatial measurements of charged particle tracks and hence allow properties such as their momenta and impact parameters to be calculated. Figure 2.18 shows the event containing the first selected hadronic B decay candidate found in 2010 data, with all reconstructed tracks in the event indicated. The tracks used to reconstruct the B candidate are highlighted and labelled, as are the PV and the decay vertices.

The TT lies between the RICH1 subdetector and the dipole magnet and is used to reconstruct the tracks of low momentum particles which are swept out of acceptance by the magnet, and for the decay products of long-lived neutral particles such as the K_S^0 . The required single hit resolution of $\sim 50 \mu\text{m}$ and high particle flux mean that silicon detectors are used because they can have a granularity high enough to prevent large occupancies being problematic. The TT consists of four detection layers in a rectangular shape around the beam-pipe, approximately 150 cm in width and 130 cm in height in order to cover the full LHCb acceptance. Each detection layer consists of $\sim 10 \text{ cm} \times 9 \text{ cm}$ silicon microstrip sensors with a strip pitch of $\sim 180 \mu\text{m}$ which are bonded together to cover the required area. In the first and last of the four layers, the strips are arranged vertically in order to give position information in the bending plane. The second and third layers have strips arranged at $\pm 5^\circ$ to the vertical in order

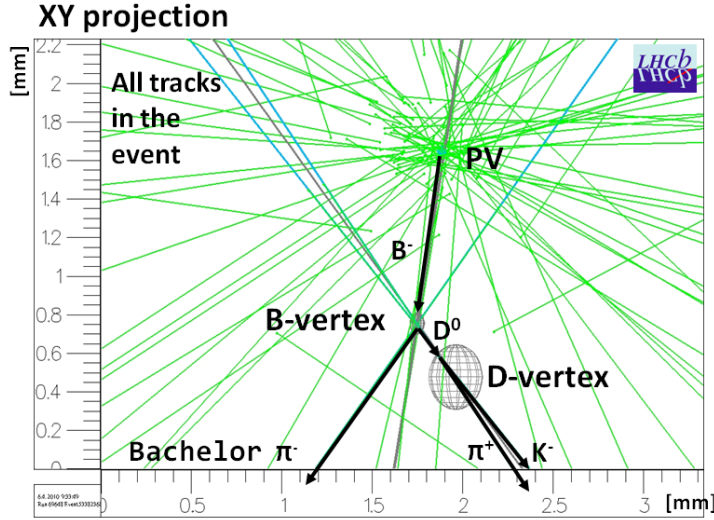


Figure 2.18: An event from 2010 data, showing all reconstructed tracks and the tracks used to reconstruct the first hadronic B decay candidate.

to provide stereo views for reconstruction in the non-bending plane.

The tracking stations (T-stations) T1-T3 are divided into two regions: the Inner Tracker (IT) and the Outer Tracker (OT). The IT covers the central region of each station and is cross-shaped around the beam-pipe, approximately 120 cm in width by 40 cm in height. The same hit position resolution as the TT is required for sufficient momentum resolution and this region receives the highest particle fluxes; therefore the same silicon microstrip technology as for the TT is used, arranged in the same four detection layer scheme at each station. The silicon sensors in the IT are $\sim 8 \text{ cm} \times 11 \text{ cm}$ with a strip pitch of $\sim 200 \mu\text{m}$. The IT only covers approximately 2% of the detector acceptance but it is estimated that 20% of tracks pass through it.

The OT covers the rest of the detector acceptance at tracking stations T1-T3, up to 300 mrad in the bending plane and 250 mrad in the non-bending plane. The particle flux is lower in this region and to cover it with silicon detector technology would be prohibitively expensive, so the OT is a drift-time subdetector using straw tube technology. Kapton tubes of diameter $\sim 5 \text{ mm}$ are filled with a gas mixture of Ar(70%) / CO₂(30%) and a thin gold-tungsten wire anode is placed down the centre axis of each tube. The maximum drift time across the tube is below 50 ns (two LHC bunch crossings). The tubes are arranged in modules, each consisting of two staggered layers of tubes. These

modules are assembled into four detection layers at each station, with the tubes in each layer vertical or at $\pm 5^\circ$ as described above for the TT/IT subdetectors.

Track reconstruction is based on track seeds, made from hits in the VELO (VELO-seeds) or hits in the T-stations (T-seeds). The full tracks are reconstructed from these seeds, adding in the information from the other tracking subdetectors. Reconstructed tracks fall into one of the following classes:

- **long tracks** : these traverse all of the tracking subdetectors. A VELO-seed is matched to hits in the TT and T-stations. They have the most precise momentum determination and are therefore the most important tracks for b-hadron decay reconstruction;
- **upstream tracks** : these traverse only the VELO and the TT station. They are typically low momentum tracks which are swept out of the detector acceptance by the magnet. They pass through RICH1, however, so may produce Cherenkov photons if their momentum is large enough, and they can be used to understand RICH1 backgrounds. They may also be used for flavour tagging or b-hadron decay reconstruction, although their momentum resolution is poor;
- **downstream tracks** : these traverse only the TT station and the T-stations. They are typically decay daughter particles from long-lived particles, such as K_S^0 ;
- **VELO tracks** : these are measured only in the VELO and so have large angles or are going backwards. They are useful for PV reconstruction; and
- **T tracks** : these are only measured in the T-stations. They are typically from secondary interactions but are used for RICH2 global pattern recognition.

The different types of track, in the context of the tracking system, are shown in Figure 2.19.

The nominal momentum resolution of the tracking system is $\Delta p/p = (0.35 - 0.55)\%$, depending on the track momentum [96]. During 2010, the tracking efficiency was found using a tag-and-probe method with $K_S^0 \rightarrow \pi^+\pi^-$ decays [108]. Figure 2.20 shows the long track efficiency measured from these decays in data as a function of track transverse momentum (p_T), with a comparison to Monte-Carlo (MC) simulation. It is above 95% for all tracks with a transverse momentum above 100 MeV/c.

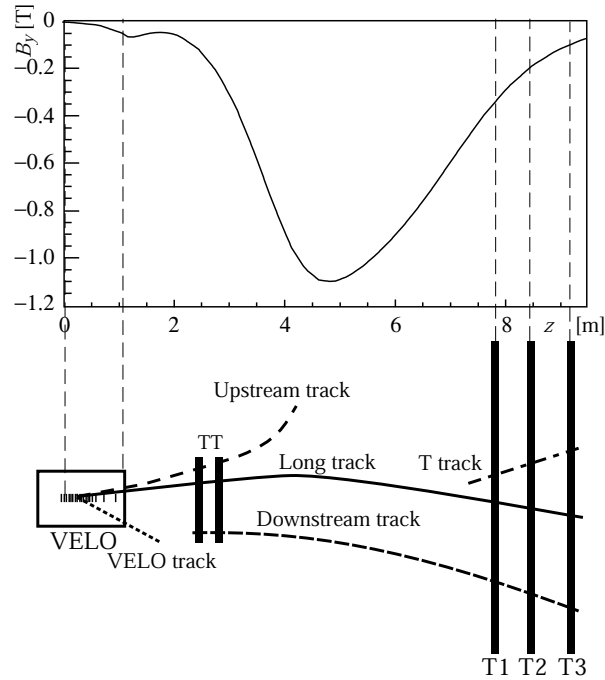


Figure 2.19: An illustration of track types and the tracking system subdetectors. The upper distribution shows the magnetic field component in the vertical direction (B_y) as a function of the z coordinate.

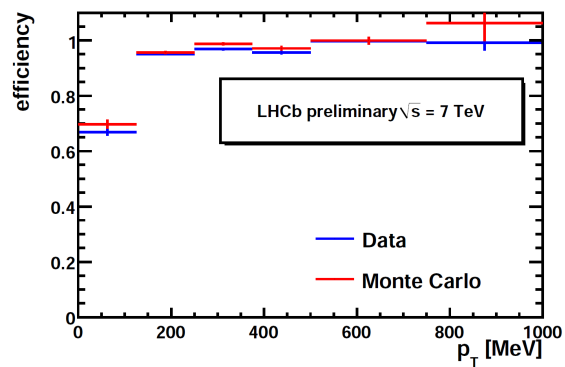


Figure 2.20: A comparison of the tracking efficiency from 2010 data and Monte-Carlo simulation as a function of transverse momentum (p_T) [108].

In 2011, the tracking efficiency was again found using a tag-and-probe method, but with $J/\psi \rightarrow \mu^+\mu^-$ decays [109]. Figure 2.21 shows the resulting long track efficiency as a function of momentum (p) and pseudorapidity (η) with a comparison to MC simulation; average efficiencies for long tracks are found to be above 96%.

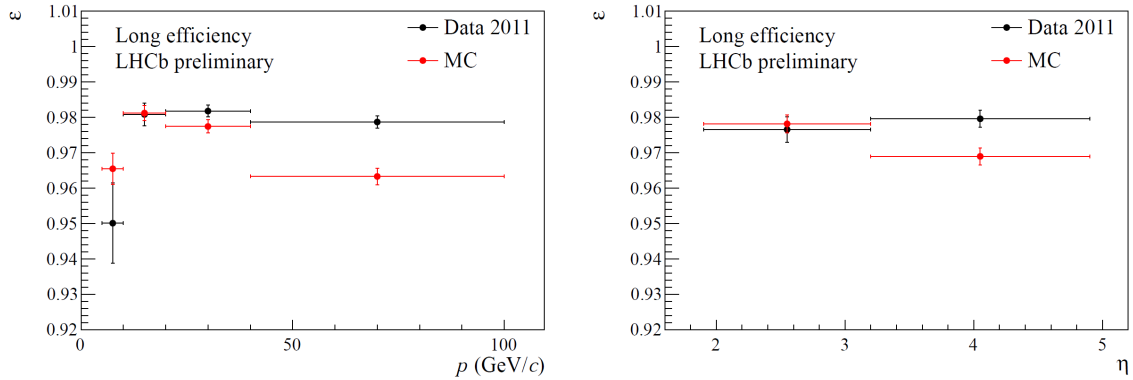


Figure 2.21: A comparison of the tracking efficiency from 2011 data and Monte-Carlo simulation as a function of momentum (p) and pseudorapidity (η) [109].

2.2.7 Dipole magnet

The LHCb dipole magnet (Figure 2.22) is positioned between the TT and T1 tracking stations. Its vertical magnetic field is used to provide bending for the measurement of the momenta of charged particles [96, 110]. In order to cover the full experimental acceptance, the magnet is required to have an aperture of at least ± 300 mrad in the horizontal plane and ± 250 mrad in the vertical plane. The magnet coils are tilted and offset to follow this acceptance, and the inner faces of the coils are placed 100 mm outside of it. For various physics analyses, such as the measurement of \mathcal{CP} asymmetries, it is important to control the systematic effects of the detector by periodically inverting the polarity of the magnetic field between two configurations (“magnet up” and “magnet down”). A warm magnet design was therefore chosen, as it allows for this due to the ability to ramp rapidly.

Upstream of the magnet, there is a low fringe magnetic field in the VELO and RICH1. In the VELO, a large field would prevent the use of a fast track finding algorithm in the trigger; RICH1 must also be in a low field so that charged particle tracks are not bent as they pass through the gas radiator and photon detector images are not distorted. To allow for the use of a simple, approximate p_T measurement in the trigger, however, a

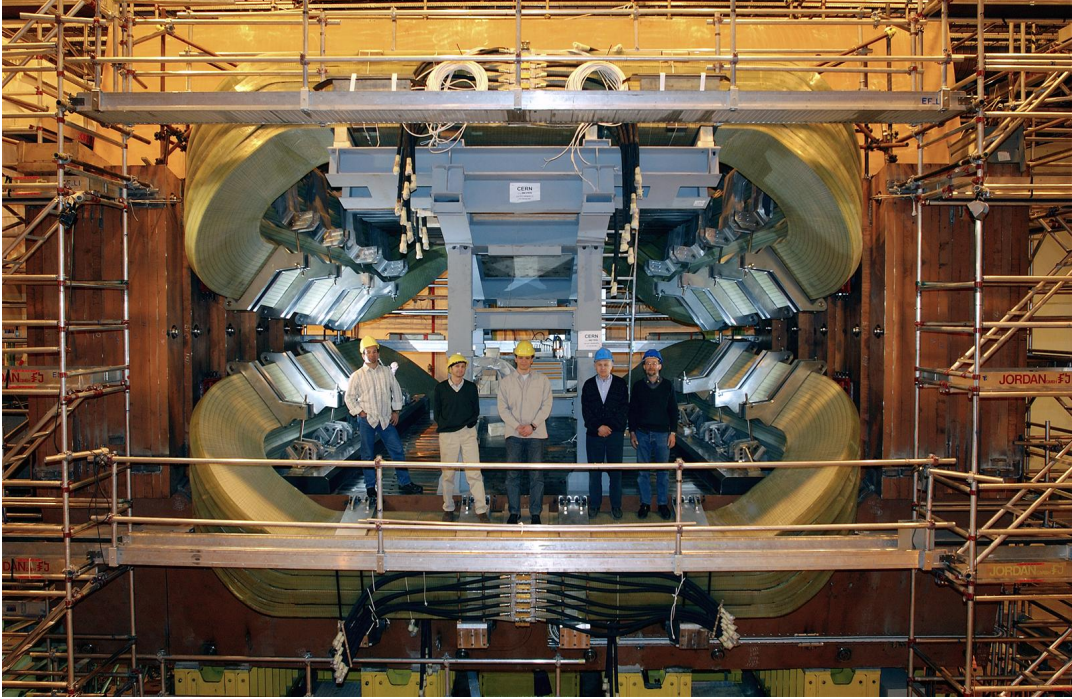


Figure 2.22: The LHCb dipole magnet, view from downstream position towards the interaction point.

small fringe field has been introduced upstream of the magnet between the VELO and TT [111, 112]. To achieve the required momentum resolution for tracks originating near the PV, the magnet must provide an integrated magnetic field of $\sim 4 \text{ Tm}$ for a track 10 m in length, with a peak field strength of 1.1 T. The magnetic field was mapped with an array of Hall probes and the measured on-axis vertical field, that is the vertical component of the field along the beam line, is shown in Figure 2.23 for both magnet polarities.

2.2.8 The RICH subdetectors and particle identification

RICH1 and RICH2 comprise the RICH system [96, 113], which is designed to identify charged particles over the momentum range $2 \text{ GeV}/c$ to more than $100 \text{ GeV}/c$. Particle identification (PID) is necessary to reduce background on selected final states; many physics analyses require good π^\pm and K^\pm separation in particular. For example, in the analysis of the decay $B^\pm \rightarrow \bar{D}^0/D^0(K_S^0\pi^+\pi^-)K^\pm$, separation between π^\pm and K^\pm allows identification of the control channel $B^\pm \rightarrow \bar{D}^0/D^0(K_S^0\pi^+\pi^-)\pi^\pm$. The polar angle and momentum coverage of RICH1 and RICH2 for tracks from MC simulated $B_d^0 \rightarrow \pi^+\pi^-$

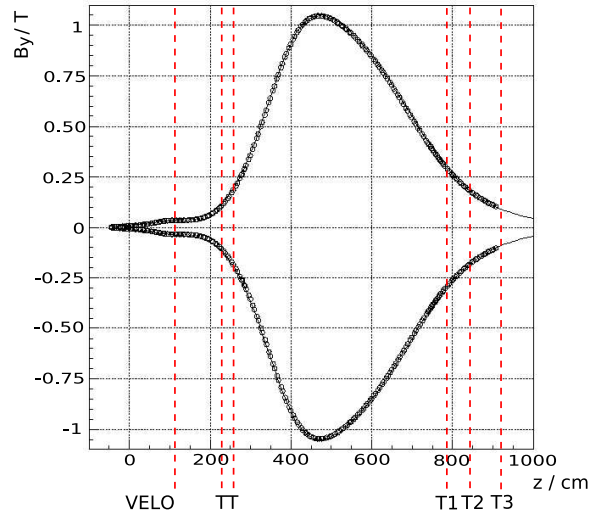


Figure 2.23: The measured on-axis field of the LHCb dipole magnet.

events is shown in Figure 2.24.

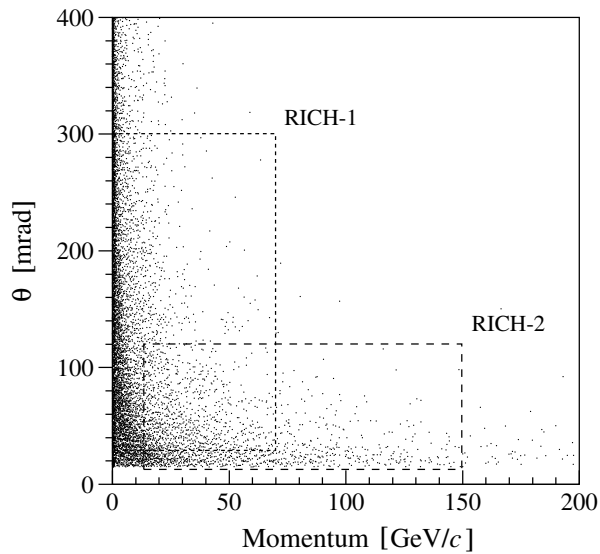


Figure 2.24: The polar angle and momentum coverage of the RICH subdetectors for all tracks from MC simulated $B_d^0 \rightarrow \pi^+ \pi^-$ events.

RICH1 uses aerogel and C_4F_{10} gas radiators which are optimised for low momentum tracks ($2 - 60 \text{ GeV}/c$) and covers the whole LHCb acceptance. It is situated immediately upstream of the dipole magnet in order to minimise the required active area and to detect particles which may be bent out of detector acceptance by the magnet. This means it must operate in the small fringe magnetic field which allows trigger p_T measurements between the VELO and TT. Material upstream of the tracking stations and within LHCb

acceptance will degrade the tracking resolution, so mirrors are used to reflect and focus any Cherenkov photons produced by a track onto planes of photon detectors situated outside of acceptance. A schematic side-view of RICH1 is shown in Figure 2.25.

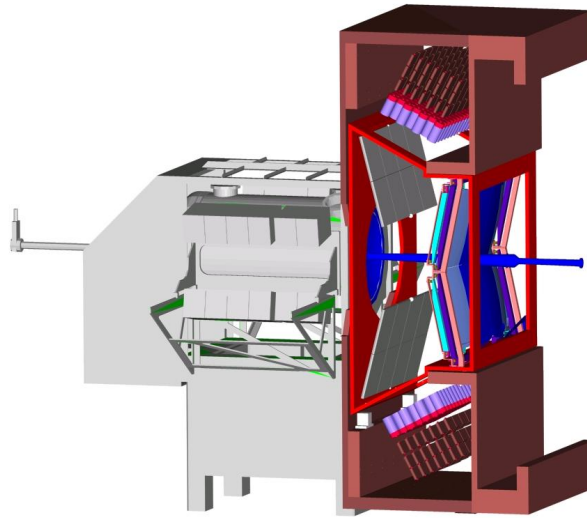


Figure 2.25: A schematic of the RICH1 subdetector, with the VELO to the left.

RICH2 is downstream of the T-stations and covers high momentum tracks, from $\sim 15 \text{ GeV}/c$ up to more than $100 \text{ GeV}/c$, with a reduced acceptance of up to 120 mrad horizontally and 100 mrad vertically. It is similar in design to RICH1 but uses only one radiator, CF_4 gas, and the optical layout is horizontal rather than vertical. In this case, the mirror system is also required to keep the length of RICH2 within the space available between the tracking stations and calorimeters. Figure 2.26 shows a photograph of RICH2 under construction.

Cherenkov radiation

As charged particles pass through radiator material they will emit photons of Cherenkov light if their speed through the medium is faster than the speed of light in it. At any point, the emission lies on an instantaneous cone formed by photons emitted at a constant angle, θ , to the particle track,

$$\cos \theta \simeq \frac{c}{vn}, \quad (2.1)$$



Figure 2.26: The RICH2 subdetector under construction, with the spherical mirrors and beam-pipe visible.

where c is the speed of light, v the speed of the particle and n is the refractive index of the radiator medium. This angle between the track and photon is known as the Cherenkov angle, and the azimuthal angle, Cherenkov ϕ , describes the position of the photon around the emission cone. Further discussion of Cherenkov emission can be found in Appendix A.

If the emitted photons were detected directly, a solid disc around the track would be seen as the particle randomly emits Cherenkov photons along the whole length of its track through the radiator. Instead, in both RICH1 and RICH2, the photons from a track are focussed into a ring by spherical mirrors and then reflected by additional flat mirrors onto the detector planes outside the acceptance of the radiators. The Cherenkov angle ϕ therefore describes the position of a photon around the detected ring. The frequency spectrum of the emitted radiation in the LHCb RICH system is in the far-visible and near-UV regions (wavelength range 200 – 600 nm [96]).

Radiators

The RICH system uses three radiators with different refractive indices to cover the necessary momentum range. RICH1 contains aerogel and a gas radiator, C_4F_{10} . Aerogel is a colloidal form of quartz (SiO_2) with refractive index $n = 1.030$ at $\lambda = 400$ nm [96]. It has a very low density but is still solid. It is arranged in 5 cm thick tiles to form a single panel at the front of the subdetector. The high refractive index provides coverage for low momentum particles, for example the K^\pm Cherenkov light production threshold

is $\sim 2 \text{ GeV}/c$. C_4F_{10} fills the remaining volume in RICH1, giving an effective radiator length of 95 cm. The gas has a refractive index of $n = 1.0014$ at $\lambda = 400 \text{ nm}$ [96] and provides a 3σ separation between π^\pm and K^\pm up to $\sim 50 \text{ GeV}/c$. RICH2 has one gaseous radiator, CF_4 , with an effective radiator length of 180 cm. It covers the momentum range above $\sim 15 \text{ GeV}/c$. At $\lambda = 400 \text{ nm}$ the refractive index of the gas is $n = 1.0005$.

Distributions of Cherenkov angle as a function of particle momentum show a band for each particle type in each radiator. The distributions for the three RICH radiators from simulated events are shown in Figure 2.27. It can be seen that in each radiator, Cherenkov photon production turns on at particular momentum threshold which is different for each particle type. At high momenta the Cherenkov angle for all types of particle tends to the same value in an effect known as saturation. Figure 2.28 shows the reconstructed Cherenkov angle as a function of track momentum for the two RICH gas radiators in 2010 data.

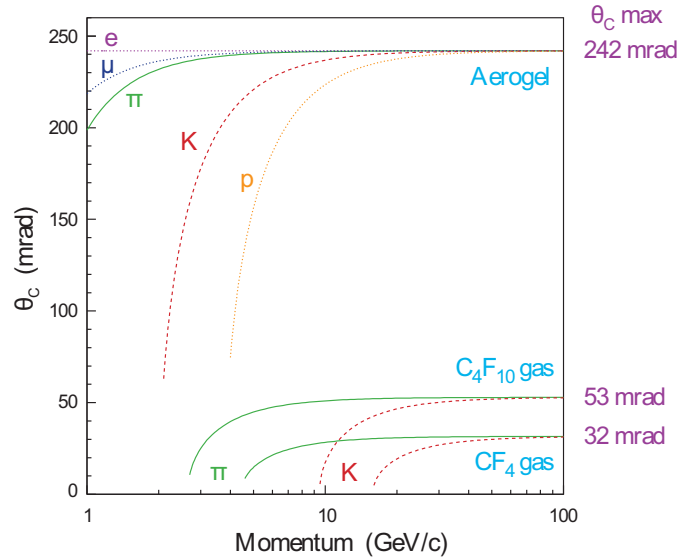


Figure 2.27: The Cherenkov angle as a function of particle momentum from simulation [96].

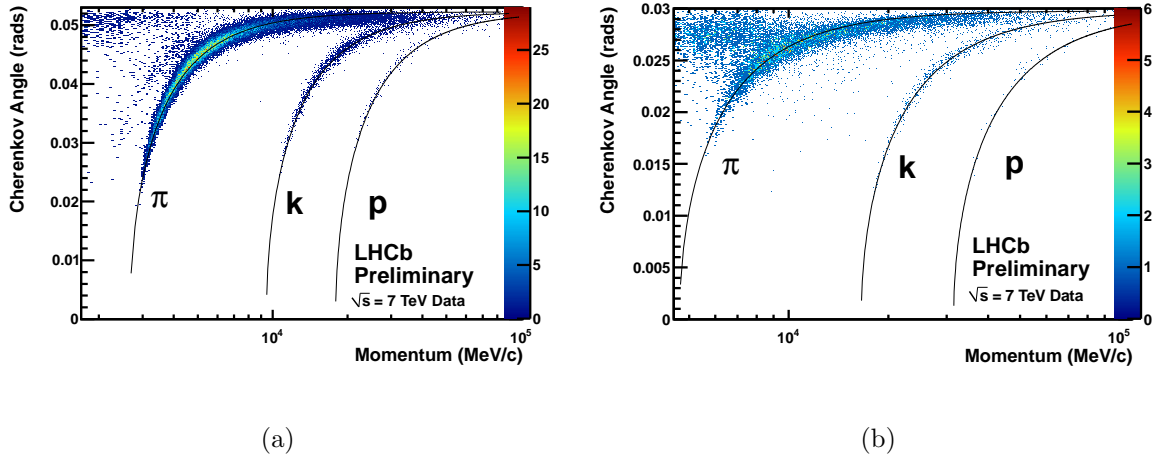


Figure 2.28: The Cherenkov angle in the RICH gas radiators as a function of particle momentum, 2010 data [114]. Figure 2.28(a) shows the distribution for the RICH1 gas radiator and Figure 2.28(b) shows the distribution for the RICH2 gas radiator.

Hybrid Photon Detectors

The RICH subdetectors use Hybrid Photon Detectors (HPDs) for detection of the spatial positions of Cherenkov photons [115–117]. The HPD is a vacuum photon detector, consisting of a ~ 40 mm radius vacuum tube with a 7 mm thick quartz entrance window and an encapsulated silicon pixel anode. Photoelectrons, produced by the interaction of photons with a thin S20 multi-alkali photocathode layer on the inner side of the quartz window, are accelerated by a ~ 20 kV potential difference onto a segmented silicon pixel array at the back of the tube. The optics of the applied electric field also cross-focus and demagnify the image by a factor of ~ 5 . This is illustrated in Figure 2.29, together with a photograph of an HPD. Photoelectrons accelerated through ~ 20 kV and incident on the anode typically produce ~ 5000 electron-hole pairs in the silicon. The spatial resolution of an HPD is $2.5 \text{ mm} \times 2.5 \text{ mm}$ at the photocathode and the time resolution for readout is 25 ns.

The HPDs are situated in four planes, two for each RICH subdetector, outside of the LHCb acceptance. As shown in Figure 2.30, they are arranged in a hexagonal close-packed array because their circular front apertures do not tessellate. Some of the total area is therefore not sensitive to photons as it lies between HPDs. Also, the intrinsic tube active area fraction of an HPD, due to the size of the anode pixel chip, is $\sim 80\%$. Taking both of these factors into account, the active-to-total area ratio is $\sim 64\%$. If

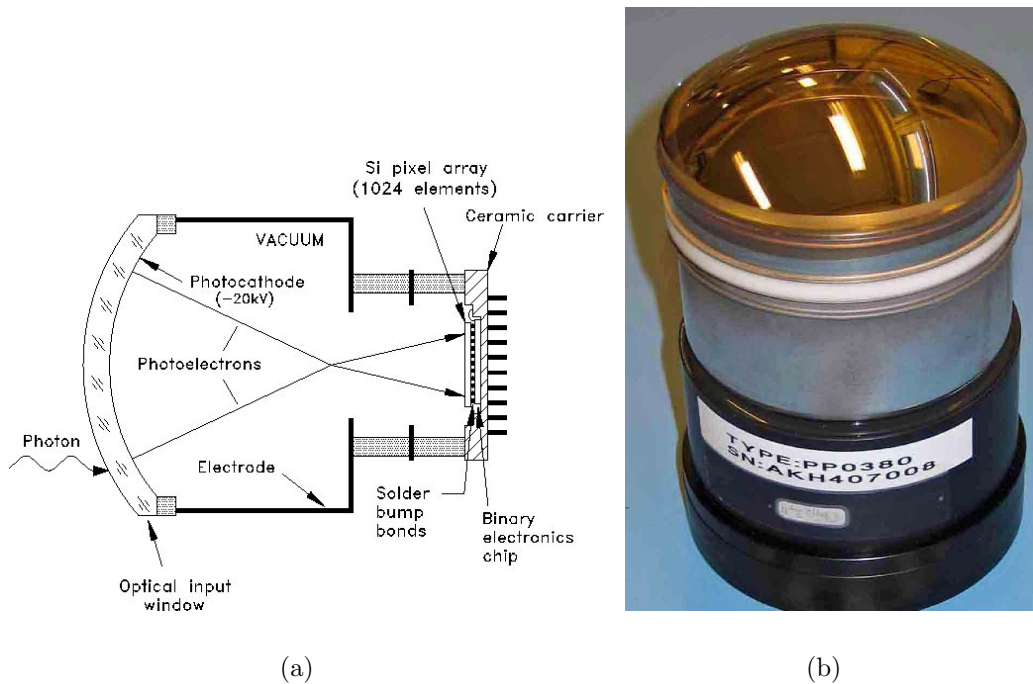


Figure 2.29: The HPD for the RICH subdetectors [96]. Figure 2.29(a) shows a schematic of an HPD with an example photoelectron acceleration trajectory. Figure 2.29(b) shows a photograph of an HPD.

an HPD is subjected to a magnetic field greater than a few mT, distortions are seen in the electron optics which affect efficiency and hence PID. Each HPD therefore has an individual 1 mm thick cylindrical μ -metal magnetic shield to protect against stray external fields up to 5 mT and both RICH subdetectors have large magnetic shielding boxes around the HPD planes to reduce the stray field from the dipole magnet to an acceptable level. Magnetic distortion corrections are also applied to the data at the reconstruction stage of processing [118].

RICH reconstruction software

Knowledge of the HPD photon hit point and the optics of the detector allows reconstruction of the Cherenkov emission angle for a given photon, under the assumption that it originated from a given track. This information is then used by the reconstruction software to carry out PID via a global log-likelihood method [119]; assuming a given type of particle for each track and using momentum and tracking measurements from other parts of the detector, the log-likelihood that all of the hits observed in the RICH



Figure 2.30: The arrangement of HPDs in the upper box of RICH1.

HPDs were produced by these tracks is maximised for a whole event. The maximisation is carried out strategically; particle type hypotheses are initially all set to be pion, as this is expected to be the most numerous type of track in LHCb, and the log-likelihood is calculated. The hypothesis for each track in turn is then changed to e^\pm , μ^\pm , K^\pm and proton, leaving the other track hypotheses unchanged. The log-likelihood is recalculated for each set of hypotheses, the change of hypothesis giving the largest increase in log-likelihood is identified and that track is set to that hypothesis. This process is repeated, changing all track hypotheses except the one set at the previous step, to find the next largest increase in log-likelihood; iteration continues until no further increase in log-likelihood can be found. The output of the RICH reconstruction is a best hypothesis and a set of $\Delta\log$ -likelihoods, or ΔLL s, for each track. Each gives the probability of it being one hypothesis rather than another; for example, $\Delta LL(K-\pi) = \ln \left(\frac{\text{likelihood of particle being a K}}{\text{likelihood of particle being a } \pi} \right)$. The global method is preferred in high multiplicity (many ring) environments, such as the LHCb RICH system, because it accounts for track “background” which is actually composed of Cherenkov photons from other tracks [120].

The performance of the RICH system in 2010 and 2011 has been found using tracks from clean samples of $K_S^0 \rightarrow \pi^+\pi^-$, $\Lambda \rightarrow p\pi^-$, $\phi \rightarrow K^+K^-$ and $D^*(2010)^\pm \rightarrow D^0/\bar{D}^0(K\pi)\pi^\pm$ decays [121], selected without use of PID information. Figure 2.31 shows the RICH system performance for K/π identification with 2010 data and early 2011 data.

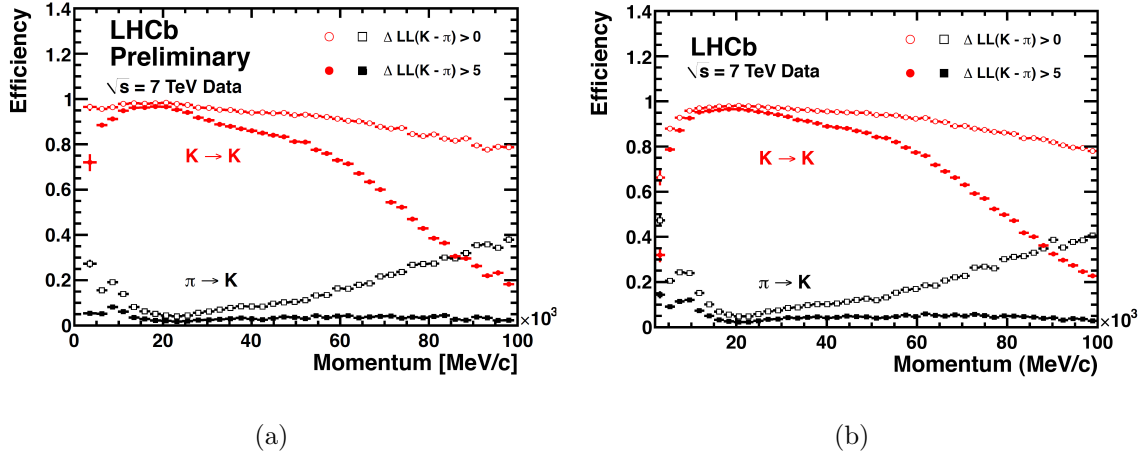


Figure 2.31: The RICH system performance in 2010 data (Figure 2.31(a)) and early 2011 data (Figure 2.31(b)) [122]. The efficiency for identifying kaons as a function of the track momentum is shown in red. The misidentification rate of calibration pions identified as kaons is shown in black. The open and closed symbols show the distributions after two different ΔLL criteria have been applied to the calibration tracks.

2.2.9 Calorimeters

The LHCb calorimeter system provides information for the hardware trigger and identifies and measures the energies and positions of both charged (electrons, hadrons) and neutral (photons, π^0) particles. It includes four consecutive sections: the scintillator pad detector (SPD) and preshower (PS), followed by the electromagnetic (ECAL) and hadronic (HCAL) calorimeters [96, 123]. Neutral particles leave no information in the rest of the detector, so the accurate reconstruction of π^0 s and prompt photons in the calorimeters is essential for flavour tagging and the study of some b-hadron decays. The calorimeters are located downstream of the first muon station and cover the complete $300 \text{ mrad} \times 250 \text{ mrad}$ LHCb acceptance, except for a central region of $25 \text{ mrad} \times 25 \text{ mrad}$ around the beam-pipe, the size of which is determined by acceptable radiation dose levels.

The SPD/PS subdetectors consist of two planes of scintillator pads on either side of a 15 mm thick lead converter plate. The information they provide is used to validate the electromagnetic nature of the ECAL showers. Only charged particles will interact with the scintillator of the SPD, the most upstream part of the calorimeter system, allowing a distinction to be made between high E_T electrons and high E_T photons and

π^0 s, where E_T is defined as the sum in quadrature of particle mass and p_T . This is vital for accurate low-level electron trigger information. The lead converter allows the PS to perform charged pion background rejection. The thickness of the plate corresponds to ~ 2.5 radiation lengths for electrons, however only $\mathcal{O}(1\%)$ of pions interact with this thickness of lead as they pass through it [124].

The ECAL requires good energy resolution, fast response time and fine transverse segmentation for efficient π^0 reconstruction and discrimination between electrons and hadrons with overlapping photon showers. It has a depth of 25 radiation lengths and is a sampling calorimeter constructed from “shashlik” technology [125], that is individual modules made of 4 mm thick scintillator tiles interspersed with 2 mm thick lead absorber plates (see Figure 2.32). Light is collected by wavelength-shifting (WLS) fibres embedded in the tiles. The fibres absorb scintillation light produced by charged particles traversing the tiles and then re-emit it as light to be measured by photon detectors outside of LHCb acceptance. This technology allows for a test-beam data energy resolution of [96]

$$\frac{\sigma(E)}{E} = \frac{(8.5 - 9.5)\%}{\sqrt{E}} \oplus 0.8\%, \quad (2.2)$$

where E is measured in GeV.

In order to match detector occupancy, the segmentation of the SPD, PS and ECAL is different in three lateral regions, with the segmentations used in the SPD and PS scaled depending on the z coordinate so that they match the ECAL segmentation projectively. This allows for faster and simpler energy reconstruction in the trigger [126].

The main purpose of the HCAL is to provide information for the low-level hadron trigger, so it requires a fast response time but not a particularly high energy resolution. Due to this and space constraints, it is 5.6 hadron interaction lengths deep, so that hadronic showers may not be fully contained within the calorimeter. The HCAL is constructed from similar technology to the ECAL. Scintillating tiles, with one edge parallel to the beam line, are sandwiched between steel absorber plates; alternate layers consist of tiles and the steel absorber or steel only (see Figure 2.32). The scintillation light is transmitted to photon detectors by WLS fibres, which are attached to the tile edge. With this arrangement, the energy resolution of the HCAL from test-beam data is [96]

$$\frac{\sigma(E)}{E} = \frac{(69 \pm 5)\%}{\sqrt{E}} \oplus (9 \pm 2)\%, \quad (2.3)$$

where E is measured in GeV. The HCAL has only two regions of different segmentation, with larger cell sizes, due to the dimensions of hadronic showers.

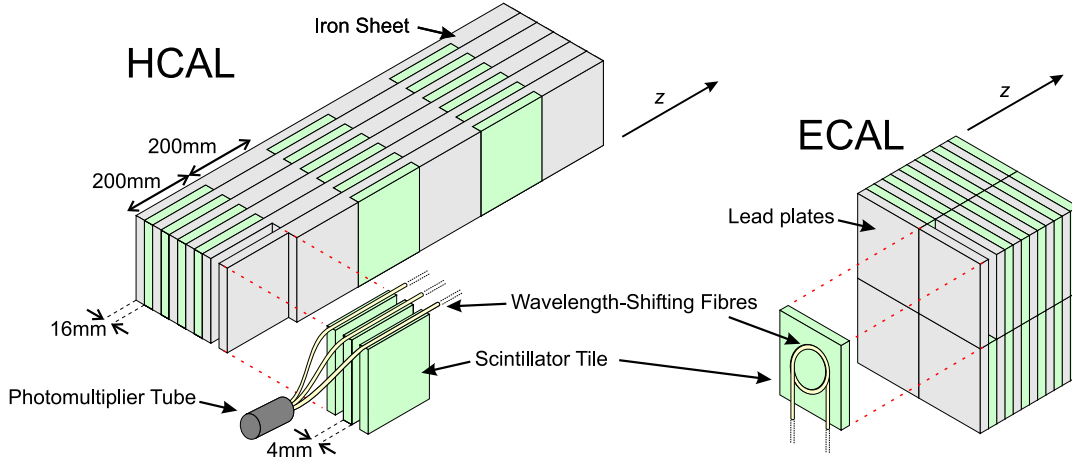


Figure 2.32: The internal structure of the LHCb HCAL and ECAL, showing scintillator tiles, absorber plates and WLS readout fibres.

Before the start of proton-proton collisions at the LHC, initial calibration and time alignment of the calorimeters was performed using cosmic rays [127]. The performance of the calorimeter system during 2010 and early 2011 is summarised in reference [128]. Calibration of the ECAL is carried out using the π^0 mass peak reconstructed from pairs of photons and HCAL calibration is performed using a radioactive source scan (^{137}Cs); the procedures are detailed in reference [129]. Figure 2.33 shows the invariant mass distributions of some resonances reconstructed from varying amounts of 2010 data using calorimeter information.

2.2.10 Muon system

The muon system provides identification of penetrating muons from b-hadron decays for the High Level Trigger and offline analysis, and for low-level trigger information [96]. Many of the studied \mathcal{CP} -violating and rare decay modes at LHCb contain muons and so the muon trigger is an important part of the trigger scheme. The inner acceptance of the muon system is 20 (16) mrad in the bending (non-bending) plane and the outer boundary is 306 (258) mrad. This matches the rest of the LHCb detector acceptance.

The muon system consists of detectors at station M1 before the calorimeters and stations M2-M5 after; M1 is used primarily to provide an improved p_T measurement

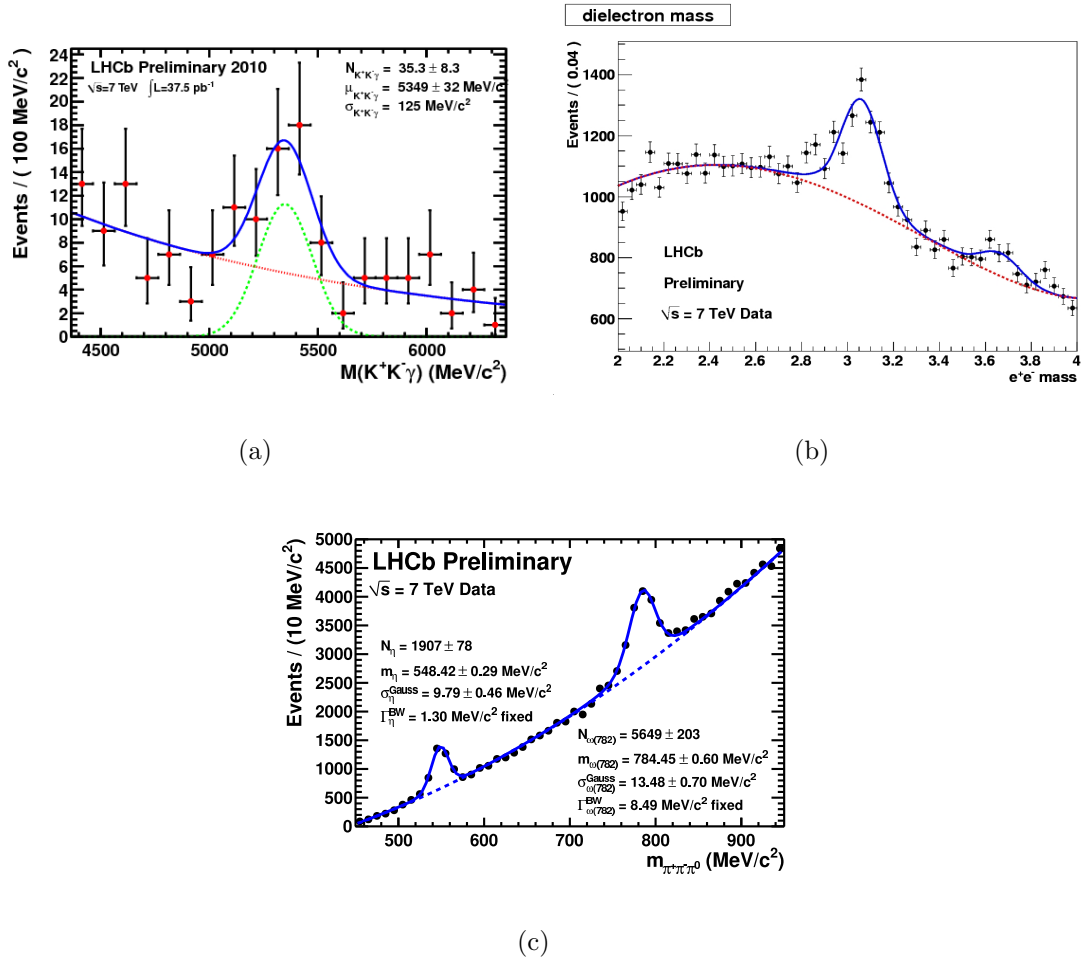


Figure 2.33: Invariant mass distributions from 2010 data using calorimeter information. Figure 2.33(a) shows the distribution for $B_s^0 \rightarrow \phi\gamma$ decays, Figure 2.33(b) shows the distribution for $J/\psi/\psi(2S) \rightarrow e^+e^-$ decays and Figure 2.33(c) shows the distribution for $\eta/\omega \rightarrow \pi^+\pi^-\pi^0$ decays.

for muons that are detected in the other stations. M2-M5 are the most downstream parts of the LHCb detector and are interleaved with 80 cm thick iron absorbers to select penetrating muons. The minimum momentum for a muon to cross all five stations is $\sim 6\text{ GeV}/c$. The physical sizes of the stations are projective, as they are determined by the angular acceptance requirement, so the sizes increase with downstream distance from the interaction point. Each station is divided into four regions (R1-R4), centred on the beam-pipe, with R1 innermost. A side view of the system, with region division indicated, is shown in Figure 2.34. The linear dimensions and the spatial segmentations of the regions are in the ratio 1:2:4:8 (R1-R4) so that the particle flux and channel occupancy are roughly the same for each of the regions of a given station. Spatial

resolution worsens towards the outer acceptance boundary but it is in any case limited by the increase in multiple scattering at large angles.

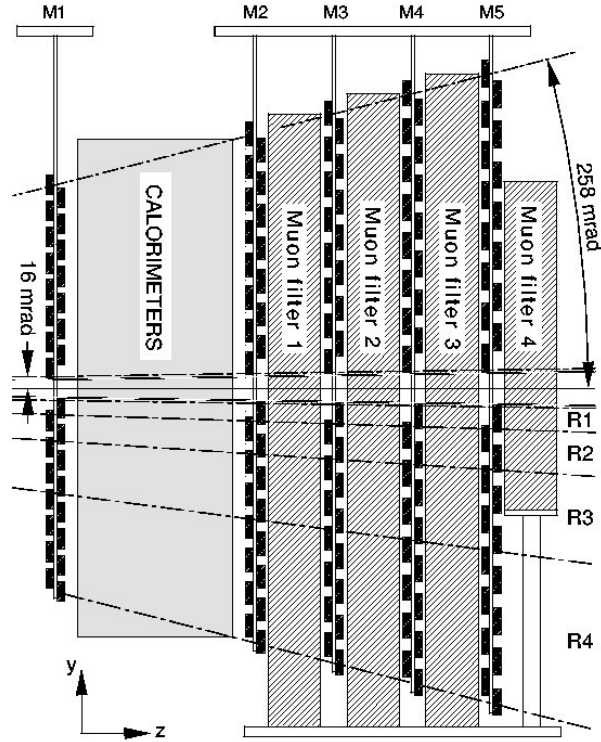


Figure 2.34: The muon system, from the side, with regions R1-R4 indicated [96].

Two types of detector technology are used in the muon stations. The inner region (R1) of M1 is constructed from triple Gas-Electron-Multiplier (triple-GEM) detectors [130] because this area is subjected to the highest particle fluxes. The rest of M1 and M2-M5 consist of multi-wire proportional chambers (MWPCs) [131]. In M2-M5 these have four equal 5 mm gas gaps with anode wires at the centre of each gap, an applied voltage of ~ 2.8 kV and an Ar/CO₂/CF₄ [132] mixture flowing through the gas gaps in series. A muon crossing a gas gap produces electrons which are accelerated towards the anode wires and undergo gas amplification near them. The four gaps are arranged into two sensitive layers of independent readout: two adjacent gaps have their readout electrodes hardwired together in OR to create a double gap layer. This improves the trigger efficiency and time resolution of readout. In order to minimise material in front of the ECAL, M1 has only two gas gaps, which are read out independently.

Different readout schemes are used in different MWPCs, depending on their distance from the beam-pipe. In R4, the outermost region containing the most chambers, the

required spatial resolution is relatively modest, and so the readout pads consist of adjacent anode wires grouped together. This is the safest and simplest readout method, but as the wires are vertically aligned the horizontal resolution is limited by the anode wire spacing (2.5 mm) and the vertical resolution by the chamber size (20 – 30 cm). In the rest of the MWPCs, pads are etched onto the cathode planes of the chambers. Simple cathode or anode readout cannot be used for the inner regions R1 and R2 in stations M2 and M3 because the required horizontal spatial resolution would mean unfeasibly small logical pad sizes. Therefore, a combination of wire and pad readout is used (see Figure 2.35). This allows horizontal resolution to be defined by the anode wires and vertical resolution by the cathode pad size. In the remaining MWPC regions of the muon system, cathode pad readout alone is used. In some areas of the system, constraints on noise level and dead-time of the front-end electronics mean that the physical size of the readout pads is smaller than the required spatial resolution. In these cases, up to four physical pads are logically OR-ed together to form one logical pad.

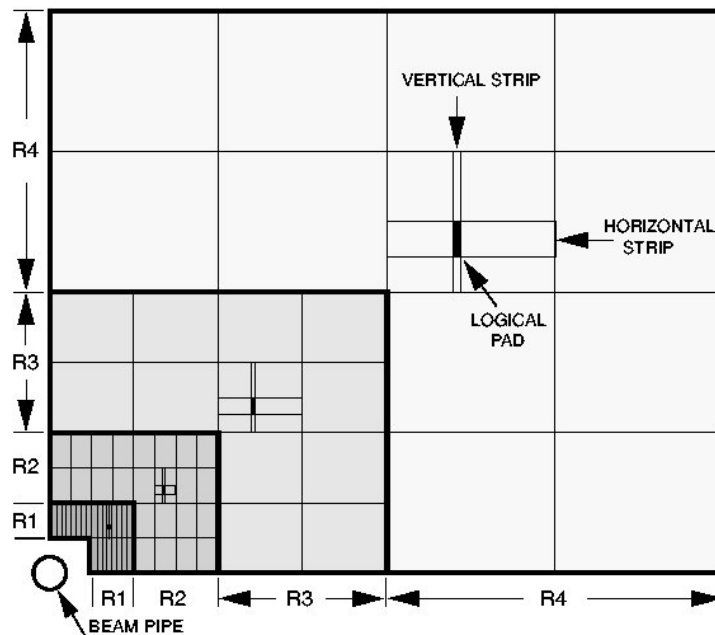


Figure 2.35: The sectors of one quadrant of muon stations M2 and M3, seen from the front [96]. The intersection of a cathode pad and anode wires to form a logical readout pad is shown. A sector of region R1 (R2, R3, R4) contains 8 (4, 4, 4) horizontal strips and 6 (12, 24, 24) vertical strips.

Triple-GEM detectors consist of three perforated gas electron multiplier foils between an anode and a cathode plane; the drift gap between foils is also filled with an Ar/CO₂/CF₄ gas mixture, but of a different composition ratio to that used in the MW-

PCs. An ionisation electron, produced in the gap between the cathode and the first foil, is attracted through the successive foils by electric fields. It is multiplied as it passes through each foil, before drifting to the anode plane for pad readout. Triple-GEM detectors give good time and spatial resolution whilst being fairly robust against radiation damage. In M1 R1, two superimposed triple-GEMs logically OR-ed together are used.

The muon system was initially spatially and time aligned using cosmic rays [133]. In proton-proton collision data, muon identification efficiency has been estimated with a tag-and-probe method using $J/\psi \rightarrow \mu^+\mu^-$ decays. The misidentification rate for pions was estimated with $K_S^0 \rightarrow \pi^+\pi^-$ decays and for protons and pions with $\Lambda \rightarrow p\pi^-$ decays [134–136]. Figure 2.36 shows Υ resonances in the reconstructed dimuon invariant mass distribution from 2010 data.

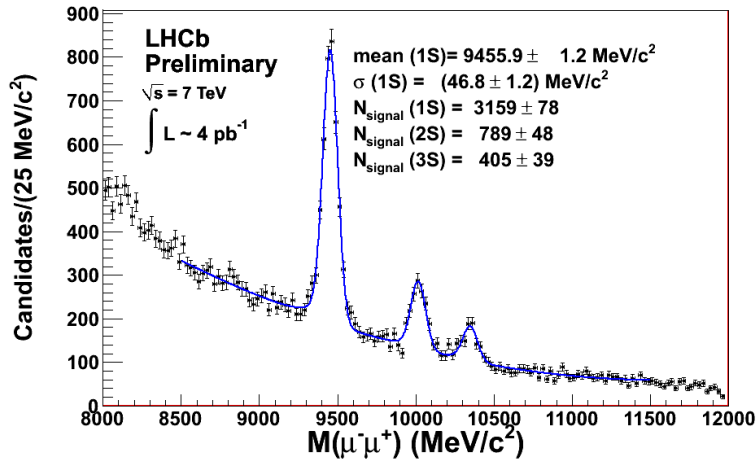


Figure 2.36: The dimuon mass spectrum from 2010 data, showing Υ resonances.

2.2.11 LHCb trigger system

Only a tiny fraction of LHC bunch crossings produce $b\bar{b}$ pairs and decays of interest in physics analyses typically have branching fractions less than $\mathcal{O}(10^{-3})$. Also, the fraction of $b\bar{b}$ events with all of the decay products of at least one B-meson within LHCb detector acceptance is ~ 0.15 [96]. Therefore, an efficient trigger system is vital in order to only store data from events of interest. The huge reduction in event rate from the bunch crossing frequency is obtained using a two-level trigger system [96, 137].

The LHCb trigger exploits the presence of displaced secondary decay vertices (due to the long b-hadron lifetime) and high p_T daughter particles (allowed due to the large invariant masses of b-hadrons) in order to select b-hadron events. Level-0 (L0) and the High Level Trigger (HLT) form the two stages of the trigger. L0 is a hardware trigger which uses information from specific parts of the detector and custom front-end electronics. Events which pass L0 are fully read out from the whole detector and passed to the HLT, a software trigger, for further processing. The trigger has been designed so that it has the maximum efficiency for passing events which would be selected for physics analysis using the full event reconstruction, whilst maintaining strong background rejection. The L0 and HLT steps will be discussed in further detail below.

Level-0 trigger

The L0 trigger is synchronised with the LHC bunch crossing frequency and has a maximum output rate of 1 MHz [138]. It is implemented in three discrete hardware components, processing information from the pile-up, calorimeters and muon subdetectors. The L0 Decision Unit (L0DU) combines the information from the different systems and makes the final L0 decision. The full detector information for an event is not read out from the front-end electronics until the L0DU has accepted it, so data from subdetectors must be stored in memory buffers until the decision is made [139]. In LHCb the storage time is fixed to be 4 μs and includes time-of-flight, cable delays and delays in the front-end electronics, leaving 2 μs for the trigger decision processing [111].

The pile-up system consists of two R-sensor VELO planes, upstream of the interaction point, which allows an estimate of the number of proton-proton primary interactions in a given bunch crossing to be made.

The L0 calorimeter trigger is designed to select tracks with high E_T deposits in the calorimeters and to identify the highest E_T photon, electron, π^0 and hadron candidate particles. In the ECAL and HCAL, high energy clusters are found by summing the E_T in each 2×2 cell cluster and then selecting the clusters with the largest E_T . This cluster size is chosen because it contains most of the energy deposit for a track but avoids overlap with deposits from neighbouring tracks. Information from the PS and SPD is then added in order to identify the type of particle as photon, electron, π^0 or hadron. The highest E_T candidate for each particle type is passed to the L0DU, along with the total E_T in the HCAL and the total charged track multiplicity in the SPD. The total HCAL E_T information is used to reject events without visible interactions and the SPD

multiplicity is used to reject events with many charged tracks [96].

The L0 muon trigger is designed to select high p_T muon candidates with hits in each of the five muon stations. The hits must lie on a straight line which points towards the proton-proton interaction point [96, 140, 141]. The position of the hits in the first two muon stations allows the determination of the p_T of the candidate. Each quadrant of the detector is treated separately, so that the two highest p_T muon candidates from each quadrant are sent to the L0DU.

The information from the three systems is passed to the L0DU which then applies p_T , E_T or multiplicity requirements as necessary. If required, the L0DU can be reprogrammed to allow a change in trigger thresholds [142]. A logical OR of the individual system decisions is made and the resulting decision is sent to the Readout Supervisor (see Section 2.3). The Readout Supervisor takes the final decision to broadcast a L0-accept or L0-reject for an event.

High Level Trigger

The High Level Trigger is a software trigger implemented in C⁺⁺ and is split into two stages, HLT1 and HLT2. It has access to the full event information read out from the LHCb detector. The trigger runs on processing nodes in an online computing farm, called the Event Filter Farm (EFF).

The HLT1 stage uses a partial reconstruction of the data to allow access to event objects such as tracks. During early and mid-2010, the HLT1 trigger consisted of an L0 decision confirmation scheme, as detailed in references [96, 143]. Later in the year, during the period when the majority of the integrated luminosity for that year was recorded, the approach of the HLT1 was changed [144, 145]. The new strategy was also used in 2011. The updated HLT1 trigger is composed of a set of inclusive trigger “lines” whose decisions are combined in a logical OR to give the final HLT1 decision. There are approximately 20 lines, of which about 15 are intended for use in physics analysis; the rest are minimum-bias type triggers. Each of the trigger lines used in physics analysis requires the presence of one or two tracks (single or dimuons, single electrons, single hadrons) which fulfil certain criteria, for example high transverse momentum and good χ^2 per degree of freedom for the track fit. HLT1 has a maximum output rate of ~ 40 kHz.

At the HLT2 stage, there are many ($\mathcal{O}(100)$) lines, with each line triggering on the presence of an inclusive decay signature or exclusive c- and b-hadron candidates. In each

line, reconstruction and selection of the signature or candidate is performed in as similar a way as possible to that performed on the fully reconstructed data. Any differences in approach are due to limitations from computing time requirements; for example RICH PID information is usually not used. The logical OR of the line decisions is taken to give the final HLT2 decision; the maximum output rate of HLT2 is $\sim 2 - 3$ kHz.

The trigger is configured using a unique hexadecimal Trigger Configuration Key (TCK); for example, setting *0x002e002a* was used in 2010. The TCK setting defines the sequence of lines included in the trigger and what thresholds and selection criteria are used for each line. It is therefore possible to pinpoint exact trigger conditions for individual events in data and to reproduce the trigger on MC simulated events.

In order to have well-defined data samples, events passing specific trigger lines are used in physics analyses. Two further trigger selection categories, TOS and TIS, are also often used. The categories are defined as follows:

- TOS (Trigger On Signal): the signal candidate or one or its constituent parts triggered the event; and
- TIS (Trigger Independent of Signal): the event was triggered independently of the presence of the signal candidate.

Candidates which are TOS will be affected by the trigger line under consideration, for example they may have an implicit lifetime bias, which may or may not need to be accounted for in a physics analysis. TIS candidates should be unbiased by the trigger. Candidates can be classified as TIS with respect to specific trigger lines, or with respect to all lines (“global” TIS).

For studies of hadronic decays in 2010 and 2011 data, certain trigger lines are typically used at each stage of the trigger process:

- L0 Hadron: this requires the presence of a hadron candidate with high transverse energy in the calorimeters. An SPD multiplicity requirement is also applied to reject events with many charged tracks;
- HLT1 1Track: this line is based upon the premise that any b-hadron decay will contain at least one well-fitted track with high transverse momentum and separation from the proton-proton interaction point [146, 147]. If a track passing the criteria is present in the event, the event passes the trigger; and

- HLT2 Topological: these lines take advantage of the typical topology of b-hadron decays. They reconstruct b-hadron candidates from two, three or four well-fitted tracks with high separation from the proton-proton interaction point and high transverse momenta. The candidates must have a large flight distance and a mass lying within a certain range. A mass correction based on missing transverse momentum is applied to the candidate, so that tracks from the full decay can be missed in the reconstruction; for example the decay $B \rightarrow D(K_S^0 \pi^+ \pi^-) K^\pm$, where there are five tracks in the final state, can pass the 2-body Topological trigger. In 2010 the Topological trigger used a “cut-based” selection, with selection criteria applied to the individual candidate components [148]. In 2011, a multivariate Boosted Decision Tree approach was used [147].

2.3 Detector control, monitoring and data flow

The Experiment Control System (ECS) performs control and monitoring of the operational state of the LHCb detector [96, 149]. This includes, for example, Data Acquisition (DAQ), as well as more typical detector properties such as temperature and pressure. Due to its hierarchical structure, the ECS can be partitioned to allow independent operation of subdetectors for commissioning or calibration purposes. The control and data paths are separated to ensure system reliability and the possibility of recovery after errors without physical hardware interventions. The Timing and Fast Control (TFC) system distributes the LHC beam-synchronous clock, L0 trigger, synchronous resets and fast control commands and is therefore important in all stages of LHCb data readout [96, 149]. The main part of the system, the Readout Supervisor, implements the interface between the LHCb trigger system and the data readout chain and so ensures data is kept synchronous. It can also produce auto-triggers for subdetector calibration and tests, and controls the trigger as the load on the readout system changes. If there is danger of a front-end electronics data buffer overflow, the L0 trigger decision can be overridden and throttling applied. The Readout Supervisor also balances workload in the online computing farm (the EFF) by selecting and broadcasting events to send to the processing nodes. The different stages of the LHCb HLT are run on each of the EFF processing nodes. Events containing raw data from the whole detector are passed to the farm at the L0 trigger output rate. All of the information for an event is passed to a single node, which then runs the trigger algorithms. The quality of acquired data is checked on a separate online monitoring farm where special algorithms are run on HLT

accepted events.

The full HLT output is transferred away from the EFF. The raw detector data is reconstructed and saved in SDST file format, which contains reconstruction information but not the full raw event information. Physics preselections (“stripping” selections) are applied to the SDST events using DaVinci (see below) and the selected events are used to produce smaller datasets which can be feasibly analysed by an individual. These final datasets are in DST file format, which includes both the reconstruction information and the full raw event information. The raw data is also stored long-term on tape. Re-processing, that is restripping of reconstructed events or full reconstruction and restripping of the raw data, occurs once or twice per year as more accurate detector description parameters become available and the physics preselections are refined [150].

2.4 LHCb software and Monte-Carlo simulation

The LHCb software framework [151] is structured as a set of projects built upon Gaudi [152], an experiment independent event data processing framework. Gaudi is an object-oriented C++ architecture that provides common functions needed by all of the various projects, such as data access, histogram plotting and messaging, but does not perform processing tasks on its own. Tasks are carried out by algorithms and tools within the various CMT packages of the projects and are implemented separately from data storage objects. This allows the change, replacement or addition of algorithms as often as required, without repetition of data storage. The use of the Gaudi framework for all applications means that the LHCb software is well suited to use on a distributed computing system; in particular reconstruction and analysis jobs can be run on the LHC Computing Grid (LCG) [153] which has significant storage and computing power world wide. The GANGA project [154] provides the LCG job submission interface and the LHCb DIRAC project [155, 156] contains the necessary tools to perform workload management.

2.4.1 Monte-Carlo event simulation

Monte-Carlo (MC) simulated events are used to study the performance of the detector and to carry out physics analyses. MC simulation is carried out by two LHCb applications (Gauss [157] and Boole [158]) and requires three steps:

- **Event generation (in Gauss)** : simulation of proton-proton interactions and scattering processes are carried out using PYTHIA [159]. The package has been tuned to account for LHC beam effects such as beam cross-section and decreasing luminosity throughout a run and also to produce multiplicities at low energies. The outgoing hadrons from the PYTHIA simulation are then decayed using Evt-Gen [160], developed by the BaBar experiment to specifically handle the decays of b-hadrons, and modified for use in LHCb.
- **Detector simulation (in Gauss)** : after event generation, the simulation of the interaction of the generated particles with the detector is carried out using the GEANT4 toolkit [161, 162]. The detector simulation step includes, for example, Cherenkov photon production in the RICH subdetectors and energy deposits in silicon detectors.
- **Detector digitisation (in Boole)** : Boole takes the information from the detector simulation and models the detector response to the particle interactions, simulating the effects of readout electronics and L0 trigger hardware. This includes noise, cross-talk, zero-suppression routines and spill-over from previous bunch crossings. This is the final step in the simulation process as the format of the MC events after detector digitisation is identical to that of real data.

2.4.2 HLT (software trigger)

The HLT (software trigger) is run by a project called Moore [163]. As well as running on LHCb data during proton-proton collisions, Moore can run on MC simulated events after the Boole digitisation step. It can be used in two modes: in rejection mode, only events that pass the trigger lines are output. In pass through or flagging mode, all events are output and the pass/fail information for all of the trigger lines is added to each event.

2.4.3 Event reconstruction and analysis

Event reconstruction is designed to run identically on MC simulation and real data. Any extra MC information is processed separately from information present for real data and then matching of reconstructed quantities with MC truth values is carried out. The LHCb reconstruction project is called Brunel [164] and it performs the reconstruction of

events passed to it in raw readout format. This includes track reconstruction algorithms and particle identification for the tracks found in the RICH, muon and calorimeter subdetectors. Pattern recognition algorithms are used to reconstruct tracks from the detector response; a precise set of tracks is then passed to the PID routines for processing.

The LHCb physics analysis software, DaVinci [165], performs final event reconstruction, that is decay vertex reconstruction and assignment of particular particle hypotheses to reconstructed tracks. Extrapolation and vertexing routines are used to follow the decay trees of unstable particles through the detector. Particles and decays of interest for physics and calibration studies are finally selected and studied using dedicated algorithms.

Panoramix [166], the LHCb event display software, can be used to visualise the detector geometry or to inspect MC simulated or data events.

2.5 2010 and 2011 data-taking

Proton-proton collisions started at the LHC in late 2009 at a centre-of-mass energy $\sqrt{s} = 0.9$ TeV. In March 2010, the first proton-proton collisions at a centre-of-mass energy of $\sqrt{s} = 7$ TeV were recorded, and collisions continued at this energy until October 2010. During this period, LHCb recorded 37.66 pb^{-1} of the 42.15 pb^{-1} of integrated luminosity delivered by the LHC, as shown in Figure 2.37.

A large proportion of the data taken in this period had an average number of visible proton-proton interactions per bunch crossing (μ) higher than the nominal LHCb value of < 1 . The peak value of μ occurs at the start of an LHC fill, immediately after the LHC beams have been repopulated with protons and collisions have restarted. As can be seen in Figures 2.38 and 2.39, the peak μ increased steadily throughout the year (increasing LHC fill number) as the instantaneous luminosity increased. The negative effects of higher μ data-taking include higher detector occupancy and a faster rate of radiation damage to the subdetectors.

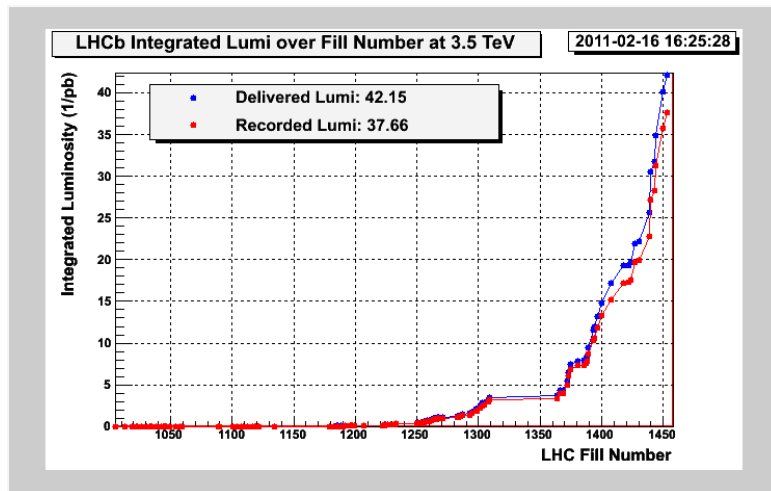


Figure 2.37: The integrated luminosity delivered to and recorded by LHCb in 2010 proton-proton collisions.

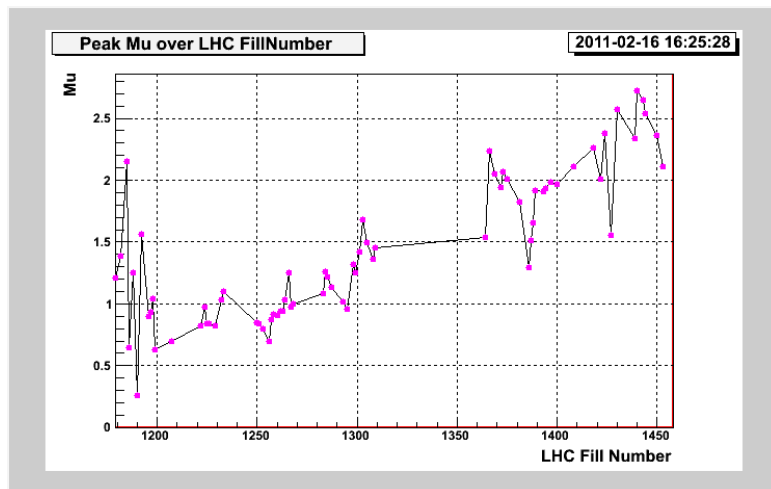


Figure 2.38: The peak μ per LHC fill at LHCb in 2010.

A second period of proton-proton collision data-taking started in April 2011 and continued until October 2011. During this period, 1.1067 fb^{-1} of the 1.2195 fb^{-1} of integrated luminosity delivered to LHCb by the LHC was recorded, as shown in Figure 2.40. The inefficiency in recorded luminosity was dominated by readout dead time and the time taken for the VELO to be closed after injection and acceleration of the proton beams. Figure 2.41 shows the peak μ during the LHC fills of this period. It can be seen that the peak μ values were still higher than the nominal LHCb value, but in general slightly lower than in 2010. As can be seen in Figure 2.42, the peak instantaneous luminosity per LHC fill was higher than the LHCb nominal value of $2 \times 10^{32} \text{ cm}^{-2} \text{ s}^{-1}$ for the majority of this period.

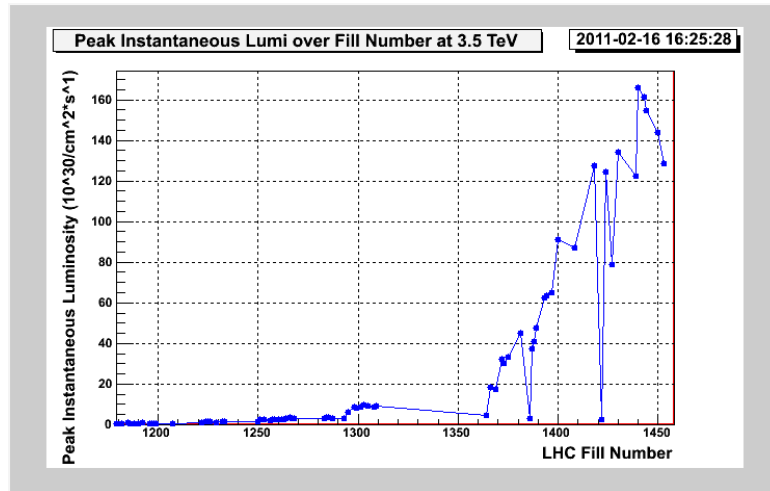


Figure 2.39: The peak instantaneous luminosity per LHC fill at LHCb in 2010.

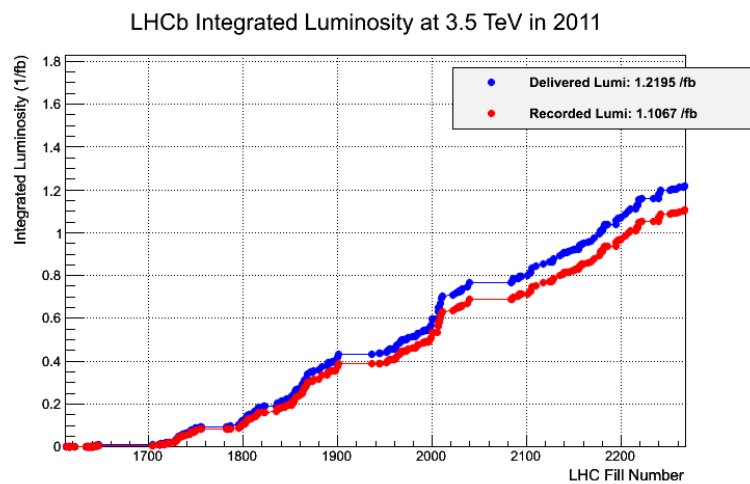


Figure 2.40: The integrated luminosity delivered to and recorded by LHCb in 2011 proton-proton collisions.

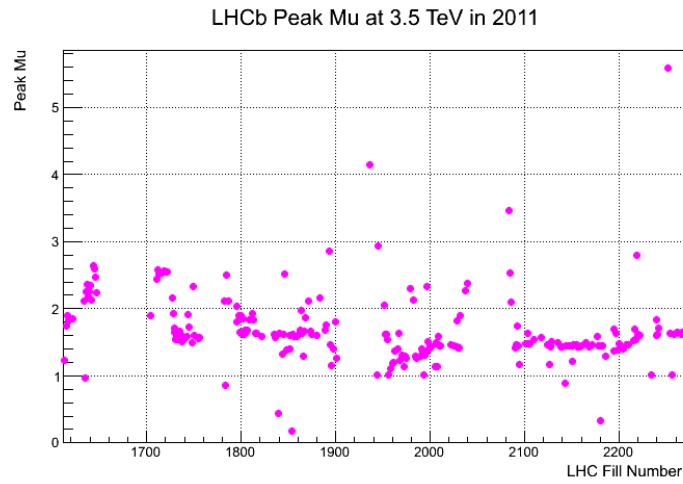


Figure 2.41: The peak μ per LHC fill at LHCb in 2011.

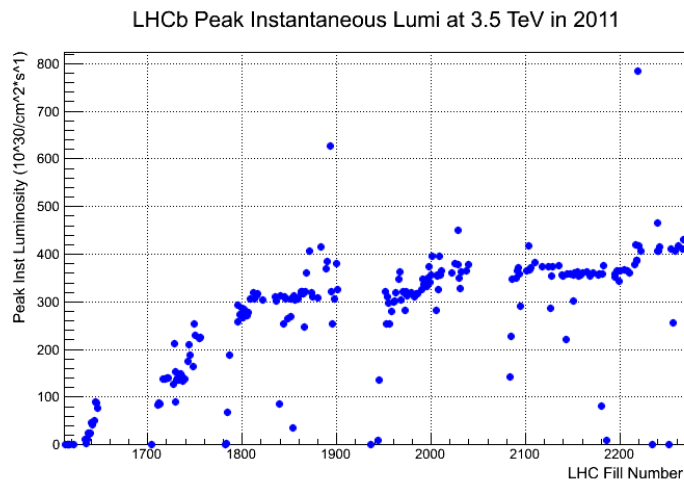


Figure 2.42: The peak instantaneous luminosity per LHC fill at LHCb in 2011.

2.6 Summary

The LHCb experiment is one of the four large experimental detectors at the LHC at CERN. The subdetector designs and trigger of LHCb have been optimised for studies of b-hadron decays; high numbers of these decays have been produced in LHC proton-proton collisions since 2009. In 2010, LHCb recorded an integrated luminosity of 37.66 pb^{-1} at $\sqrt{s} = 7 \text{ TeV}$, and in 2011 an integrated luminosity of 1.1067 fb^{-1} was recorded at the same proton-proton collision energy. The performance of the subdetectors in $\sqrt{s} = 7 \text{ TeV}$ data recorded in 2010 and 2011 has been investigated; all subdetectors were operational for the data used in the analysis presented in this thesis.

Chapter 3

$B^\pm \rightarrow D(K_S^0 \pi^+ \pi^-) K^\pm$ candidate reconstruction and selection

This chapter describes the event reconstruction and optimisation of the selection criteria used to separate $B^\pm \rightarrow D(K_S^0 \pi^+ \pi^-) K^\pm$ signal candidates from background. D represents either a D^0 or \bar{D}^0 meson. As described in Chapter 1, $B^\pm \rightarrow D(K_S^0 \pi^+ \pi^-) K^\pm$ decays can be used to measure the CKM angle γ via the GGSZ (Dalitz) method; the topologically similar decays $B^\pm \rightarrow D(K_S^0 \pi^+ \pi^-) \pi^\pm$ are an important control channel in the analysis.

The topology and reconstruction of $B^\pm \rightarrow D(K_S^0 \pi^+ \pi^-) K^\pm$ decays is detailed in Section 3.1, followed by a summary of the MC event samples (Section 3.2) used to optimise the signal selection. Descriptions of selection variables which can be used to discriminate between signal and background decays are given in Section 3.3. The selection optimisation procedure is then described in Section 3.4, followed by the results of the procedure (Section 3.5), the final selection criteria and expected annual event yield (Section 3.6).

3.1 $B^\pm \rightarrow D(K_S^0 \pi^+ \pi^-) K^\pm$ reconstruction

A schematic of the topology of a $B^\pm \rightarrow D(K_S^0 \pi^+ \pi^-) K^\pm$ signal decay is shown in Figure 3.1. Each proton-proton collision in LHCb forms a PV which is reconstructed from all of the tracks in the event which have been reconstructed by the VELO subdetector. A B^\pm meson coming from the PV will travel a short distance and then decay to form a displaced secondary vertex; the comparatively long B^\pm lifetime of (1.641 ± 0.008) ps [18] gives a B^\pm flight distance of ~ 1 cm, so that the secondary vertex also lies within the

VELO. At the secondary vertex, a D meson and a bachelor K^\pm meson are produced. The D meson has a lifetime of (0.4101 ± 0.0015) ps [18], meaning that it results in a further, tertiary vertex where it decays to $K_S^0\pi^+\pi^-$. Finally, the K_S^0 from the D meson travels through the detector and then decays; in LHCb only the decay $K_S^0 \rightarrow \pi^+\pi^-$ is reconstructed. Due to the long lifetime of the K_S^0 , its daughter pion tracks can be either upstream or long tracks if the K_S^0 decays within the VELO or downstream tracks if the decay occurs further downstream in the detector. The different track types are described in detail in Section 2.2.6; long tracks have information from all of the tracking subdetectors, but upstream and downstream tracks do not. In this analysis, each K_S^0 candidate is reconstructed using either a long-long (LL) or a downstream-downstream (DD) pair of pion daughters. Other daughter track combinations are possible but are not considered here; for example an upstream-upstream combination would have a poor K_S^0 vertex resolution, and long-downstream/downstream-long combinations have a very high background. The D and B^\pm meson candidates reconstructed using the LL and DD K_S^0 candidates are also labelled with LL and DD throughout this thesis, in order to differentiate between the two sets of candidates.

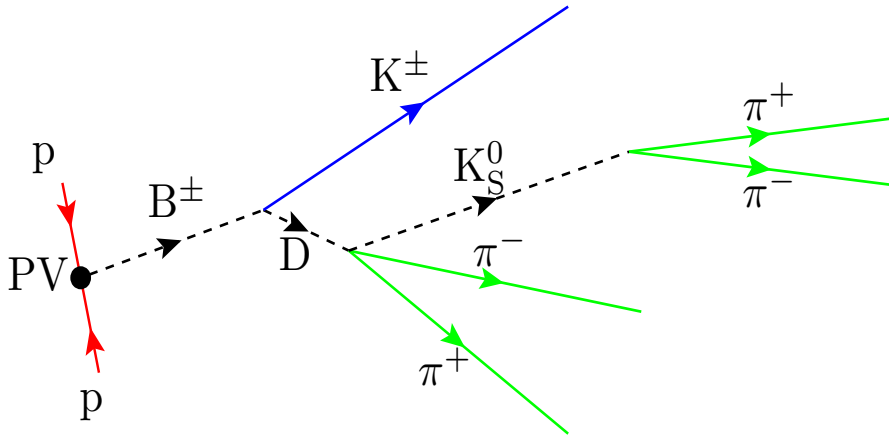


Figure 3.1: The topology of the decay $B^\pm \rightarrow D(K_S^0\pi^+\pi^-)K^\pm$ (not to scale).

3.2 Monte-Carlo event samples

The MC simulation samples used in the optimisation of the candidate selection criteria were produced using the software described in Section 2.4.1 as part of the MC09 MC production. At the time of the selection optimisation the LHC had not yet started colliding protons and the planned centre-of-mass energy of the 2010-2011 LHC collisions had

not been chosen. Therefore, the MC09 production used the “best guess” proton-proton collision energy of $\sqrt{s} = 10$ TeV. The GEANT4 detector description for the MC09 production was significantly improved compared to that used in the DC06 production (events from the DC06 production were used for the studies of Chapter 2).

The specific MC09 samples used for the optimisation are shown in Table 3.1. Events containing $B^\pm \rightarrow D(K_S^0 \pi^+ \pi^-) K^\pm$ signal decays were simulated and reconstructed with the LHCb geometric acceptance requirement applied. This requires that all of the particles of the decay are within the LHCb detector acceptance and it has an efficiency, $\epsilon_{acceptance}$, known as the generator factor. The equivalent signal sample size is therefore equal to (generated sample size)/(generator factor) events. Each simulated event in the MC signal sample contained at least one $B^\pm \rightarrow D(K_S^0 \pi^+ \pi^-) K^\pm$ decay, with the $D \rightarrow K_S^0 \pi^+ \pi^-$ part of the decay generated without a decay amplitude model applied; in other words the whole possible phase space was filled with equal probability. The predominant generic background to the signal decays arises from other b-hadron decays. A large sample of “inclusive $b\bar{b}$ ” events was therefore used as the background sample for the optimisation. Each event in this sample has at least one b-hadron decaying within the LHCb detector acceptance.

Reconstructed candidate case	MC sample	Generated sample size	Generator factor, $\epsilon_{acceptance}$	Equivalent sample size
LL	Signal	975059	0.174 ± 0.001	5616699
LL	Inclusive $b\bar{b}$	20825843	0.435 ± 0.006	47875501
DD	Signal	1392995	0.174 ± 0.001	8024165
DD	Inclusive $b\bar{b}$	25143769	0.435 ± 0.006	57801768

Table 3.1: The sizes of MC samples used in the optimisation of the signal event selection.

3.3 Selection variables and the signal preselection

The variables used to differentiate signal $B^\pm \rightarrow D(K_S^0 \pi^+ \pi^-) K^\pm$ decays from background include:

- the *impact parameter* (IP) χ^2 of a track or candidate with respect to the PV. The

impact parameter is the perpendicular distance from the PV to the extrapolated momentum vector of that track or candidate. The IP χ^2 is calculated by projecting the particle to the position of closest approach to the PV and re-fitting the vertex. Daughter tracks from B decays have large impact parameter χ^2 s as they originate from secondary or higher vertices. B candidates have a small impact parameter χ^2 as they originate from the PV;

- the reconstructed candidate *mass*, which is compared to the measured global average value from the PDG [18]. A window around the average value is defined in order to select signal candidates;
- the decay *vertex* χ^2 *per degree of freedom (d.o.f.)*, which is a measure of the goodness of fit of a decay vertex. A small vertex $\chi^2/\text{d.o.f.}$ means that the vertex is well-constrained;
- the *flight distance (FD)* χ^2 , which is calculated for a candidate by adding all of the tracks from its reconstructed decay vertex to the PV and recalculating the vertex χ^2 . The FD χ^2 is large for true B candidates as they are long-lived and the tracks from the B decay do not form a good vertex with the PV tracks. This variable can also be used for B daughters such as the K_S^0 in $B^\pm \rightarrow D(K_S^0 \pi^+ \pi^-) K^\pm$. Again, the χ^2 is calculated between tracks from the PV and the decay vertex of the candidate particle;
- the Δ log-likelihoods, or ΔLL s, constructed from the PID log-likelihoods. For example, a cut of $\Delta LL(K - \pi) > 0.0$ means that the track is more likely to be a K than a π ;
- the direction cosine, or *DIRA*. If a candidate is correctly reconstructed, its momentum vector and the vector between its reconstructed production and decay points will be closely aligned. The DIRA is the cosine of the angle between the momentum and direction vectors and for a well-reconstructed candidate should peak at 1;
- the *track* $\chi^2/\text{d.o.f.}$ is a measure of the quality of fit of a track. This variable is useful for removing poorly-reconstructed tracks. A low track $\chi^2/\text{d.o.f.}$ corresponds to a good track fit; and
- the transverse momentum, p_T , is the component of the particle's momentum in the plane perpendicular to the direction of the proton beams. Due to the large mass of the B, its daughters tend to have high transverse momenta.

$B^\pm \rightarrow D(K_S^0 \pi^+ \pi^-) K^\pm$ candidates with either a LL or DD K_S^0 daughter were reconstructed from the MC event samples of Table 3.1 using DaVinci. A loose preselection of some of the variables listed above was applied to the reconstructed candidates, thereby reducing the number of candidates processed during the full optimisation. The variables used in the preselection were:

- the impact parameter χ^2 with respect to the PV of the daughter π from the K_S^0 ;
- the mass, vertex $\chi^2/\text{d.o.f.}$ and flight distance χ^2 from the PV of the K_S^0 ;
- the impact parameter χ^2 with respect to the PV of the daughter π from the D;
- the mass and vertex $\chi^2/\text{d.o.f.}$ of the D;
- the impact parameter χ^2 with respect to the PV and $\Delta LL(K - \pi)$ of the bachelor K^\pm ; and
- the mass, vertex $\chi^2/\text{d.o.f.}$, impact parameter χ^2 with respect to the PV and pointing angle (DIRA) of the B^\pm .

The preselection criteria are shown in Table 3.2 and were chosen with the aim of very loosely selecting B^\pm candidates in the signal channel and background candidates with signal-like characteristics.

Particle	Preselection criteria, LL candidates	Preselection criteria, DD candidates
K_S^0 daughter π	IP χ^2 (PV) > 6.25	IP χ^2 (PV) > 6.25
K_S^0	$ \text{mass} - 497.61 < 50.0 \text{ MeV}/c^2$ vertex $\chi^2/\text{d.o.f.} < 16.0$ FD χ^2 (PV) > 4.0	$ \text{mass} - 497.61 < 80.0 \text{ MeV}/c^2$ vertex $\chi^2/\text{d.o.f.} < 16.0$ FD χ^2 (PV) > 4.0
D daughter π	IP χ^2 (PV) > 6.25	IP χ^2 (PV) > 6.25
D	$ \text{mass} - 1864.8 < 100.0 \text{ MeV}/c^2$ vertex $\chi^2/\text{d.o.f.} < 16.0$	$ \text{mass} - 1864.8 < 100.0 \text{ MeV}/c^2$ vertex $\chi^2/\text{d.o.f.} < 16.0$
Bachelor K^\pm	IP χ^2 (PV) > 6.25 $\Delta LL(K - \pi) > -5.0$	IP χ^2 (PV) > 6.25 $\Delta LL(K - \pi) > -5.0$
B^\pm	$ \text{mass} - 5279.2 < 500.0 \text{ MeV}/c^2$ vertex $\chi^2/\text{d.o.f.} < 16.0$ IP χ^2 (PV) < 36.0 DIRA > 0.99975	$ \text{mass} - 5279.2 < 500.0 \text{ MeV}/c^2$ vertex $\chi^2/\text{d.o.f.} < 16.0$ IP χ^2 (PV) < 36.0 DIRA > 0.99975

Table 3.2: The preselection criteria applied to the signal and background MC B^\pm candidates.

No trigger selection was included in the preselection step because the LHCb trigger was not well-defined at the time of optimisation. The preselected B^\pm candidates were saved for use as input for the optimisation algorithm; the preselected sample sizes were 55995 (69034) signal candidates and 264638 (110878) inclusive $b\bar{b}$ candidates in the LL (DD) samples.

3.4 Optimisation of the $B^\pm \rightarrow D(K_S^0 \pi^+ \pi^-) K^\pm$ candidate selection

An optimisation algorithm [167] was used to carry out an automated optimisation of the signal selection criteria. The preselected MC candidates in Section 3.3 were used as the input signal and background samples; the optimisation was performed separately for the LL and DD B^\pm candidates as the available track information and decay topology were different in the two cases.

The optimisation algorithm varied rectangular criteria (“cuts”) in order to maximise the metric $\frac{S}{\sqrt{S+B}}$, where S is the yield of signal candidates and B is the yield of background candidates. The signal and background candidate yields were normalised to an integrated luminosity of 2 fb^{-1} , corresponding to the expected nominal year of data-taking at LHCb (10^7 sec at an instantaneous luminosity of $2 \times 10^{32} \text{ cm}^{-2} \text{ s}^{-1}$). The assumed $b\bar{b}$ cross-section at $\sqrt{s} = 10 \text{ TeV}$ was $\sigma_{10\text{TeV}} = 336 \text{ }\mu\text{b}$. This value was calculated by taking the ratio of cross-sections at $\sqrt{s} = 10 \text{ TeV}$ and $\sqrt{s} = 14 \text{ TeV}$ from PYTHIA and then multiplying by $500 \text{ }\mu\text{b}$, the value which had been assumed for the cross-section in previous $\sqrt{s} = 14 \text{ TeV}$ physics studies. Using $\sigma_{10\text{TeV}} = 336 \text{ }\mu\text{b}$ gives a yield of 0.672×10^{12} $b\bar{b}$ pairs produced in a 2 fb^{-1} nominal year.

The signal yield, S , was calculated as follows:

$$S = 2 \times N_{b\bar{b}} \cdot f(b \rightarrow B^\pm) \cdot \text{Br}(B^\pm \rightarrow DK^\pm) \cdot \text{Br}(D \rightarrow K_S^0 \pi^+ \pi^-) \cdot \text{Br}(K_S^0 \rightarrow \pi^+ \pi^-) \cdot \epsilon_{sig,acceptance} \cdot \epsilon_{sig,sel} \quad (3.1)$$

where $N_{b\bar{b}} = 0.672 \times 10^{12}$, $\epsilon_{sig,acceptance}$ is the generator factor for the MC signal sample and the B^\pm hadronisation fraction and the branching fractions are given in Table 3.3.

The selection efficiency of the signal, $\epsilon_{sig,sel}$, is given by

$$\epsilon_{sig,sel} = \frac{\text{number of signal candidates passing selection}}{\text{generated signal sample size}}, \quad (3.2)$$

where the generated signal sample size is shown in Table 3.1.

Process	Hadronisation/branching fraction
$f(b \rightarrow B^\pm)$	$(40.3 \pm 1.1)\%$
$\text{Br}(B^\pm \rightarrow DK^\pm)$	$(3.68 \pm 0.33) \times 10^{-4}$
$\text{Br}(D \rightarrow K_S^0\pi^+\pi^-)$	$(2.81 \pm 0.15)\%$
$\text{Br}(K_S^0 \rightarrow \pi^+\pi^-)$	$(69.20 \pm 0.05)\%$

Table 3.3: The signal branching fractions and B^\pm hadronisation fraction, taken from reference [18]. $\text{Br}(B^\pm \rightarrow DK^\pm)$ does not include the CKM suppressed $B^+ \rightarrow D^0(K_S^0\pi^+\pi^-)K^+$ and $B^- \rightarrow \bar{D}^0(K_S^0\pi^+\pi^-)K^-$ decay modes.

Similarly, the background yield is given by,

$$\begin{aligned} B &= N_{b\bar{b}} \cdot \epsilon_{bkg,acceptance} \cdot \epsilon_{bkg,sel} \\ &= 0.672 \times 10^{12} \times \epsilon_{bkg,acceptance} \cdot \epsilon_{bkg,sel} \end{aligned} \quad (3.3)$$

where $\epsilon_{bkg,sel}$ is the selection efficiency for the background, given by

$$\epsilon_{bkg,sel} = \frac{\text{number of background candidates passing selection}}{\text{generated background sample size}}, \quad (3.4)$$

$\epsilon_{bkg,acceptance}$ is the generator factor for the MC background sample and the generated background sample size is shown in Table 3.1.

The background candidates were divided into two categories: the low-mass backgrounds (for example from $B^\pm \rightarrow D^*(2007)^0K^\pm$ decays), which peak in the reconstructed B^\pm candidate mass distribution at masses below the global average B^\pm mass, and the combinatoric backgrounds, which are flat in B^\pm mass. The low-mass background candidates were counted in the same way as signal candidates, with weight 1 if they had mass lying within the signal B^\pm mass window. In order to make best use of the available statistics, combinatoric background candidates were counted with weight 0.1 if they had mass lying within an extended B^\pm mass window of width $10\times$ the signal window.

The two contributions were then summed to give the number of background candidates passing the selection of Equation 3.4.

The metric $\frac{S}{\sqrt{S+B}}$ was maximised using the optimisation algorithm, which performed the following steps:

- the available cut values and the starting cut value for each variable were specified at the start of each optimisation procedure;
- the value of the metric for the starting cut values was calculated and recorded as the overall maximum metric;
- the available cut values for the first variable were stepped through sequentially and the metric was calculated when each of the cut values was applied. The cut values for all other variables were set to their initial values during this procedure. The variable under consideration, the maximum metric possible for that variable and the variable cut value corresponding to the maximum metric were recorded. The maximum metric for this first variable was recorded as the temporary maximum metric;
- the possible cuts for each of the remaining variables were stepped through in the same manner. For each of these subsequent variables, the maximum metric possible for the variable was compared to the temporary maximum metric and if it was larger it was saved as the new temporary maximum. The variable and cut value which corresponded to the new temporary maximum were also stored. During the step through of a given variable, the other variables all had their cuts set to their initial values;
- once all variables had been considered, a single iteration was complete. At this point, the temporary maximum metric from the iteration was equal to the largest possible metric achievable by changing the cut value of one variable and leaving the others unchanged;
- the temporary maximum metric was compared to the overall maximum metric. If the temporary maximum metric was larger than the current overall maximum metric, the cut value for the variable corresponding to the temporary maximum was moved one step towards the cut value which gave the maximum. This cut value replaced the initial value as the default cut to be used when other variables were being considered. The metric calculated with this changed cut, not the temporary maximum metric, became the new overall maximum metric;

- the iterations over all of the variables were repeated until no increase in the metric could be achieved.

The algorithm considered the variables listed in Table 3.4.

Particle	Variables
K_S^0 daughter π	$\Delta LL(\pi - K)$ impact parameter χ^2 with respect to the PV track $\chi^2/\text{d.o.f.}$
K_S^0	vertex $\chi^2/\text{d.o.f.}$ flight distance χ^2 from the PV
D daughter π	impact parameter χ^2 with respect to the PV track $\chi^2/\text{d.o.f.}$ $\Delta LL(\pi - K)$
D	vertex $\chi^2/\text{d.o.f.}$ flight distance χ^2 from the PV
Bachelor K^\pm	$\Delta LL(K - \pi)$ $\Delta LL(K - p)$ track $\chi^2/\text{d.o.f.}$ impact parameter χ^2 with respect to the PV p_T
B^\pm	flight distance χ^2 from the PV vertex $\chi^2/\text{d.o.f.}$ impact parameter χ^2 with respect to the PV DIRA p_T

Table 3.4: The variables considered by the optimisation algorithm.

The mass windows for the composite B^\pm , D and K_S^0 meson candidates were fixed to be $\pm 3\sigma$ around the measured global average [18], where σ was taken from a Gaussian fit to the true mass distributions from the preselected signal events. Figures 3.2, 3.3 and 3.4 show the mass distributions and fits. Fixed upper momentum requirements of 100 GeV/c were applied to the bachelor kaon and all of the pions, corresponding to the upper momentum limit of the capability of the RICH system to differentiate between π and K hypotheses.

It was not possible to ascertain if the set of optimal criteria identified from a given starting point or with given available cut values was unique in maximising the metric value. Therefore, the optimisation procedure was repeated many times with different cut starting points and different available values for the cuts, with the aim of identifying as many degenerate solutions as possible if they were present. On convergence of the algorithm, if a cut for a particular variable had been placed at the minimum or maximum allowed value, the whole procedure was repeated with a lower or higher set of available cut values for that variable respectively, up to the bound placed by the preselection criteria. Initially, large step sizes were used between the available cut values for each variable. Once robust convergence had been achieved, however, the step size between available values was reduced. During optimisation, the testing of all possible cut values for all variables at each iteration minimised the dependence on the order in which correlated variables were considered.

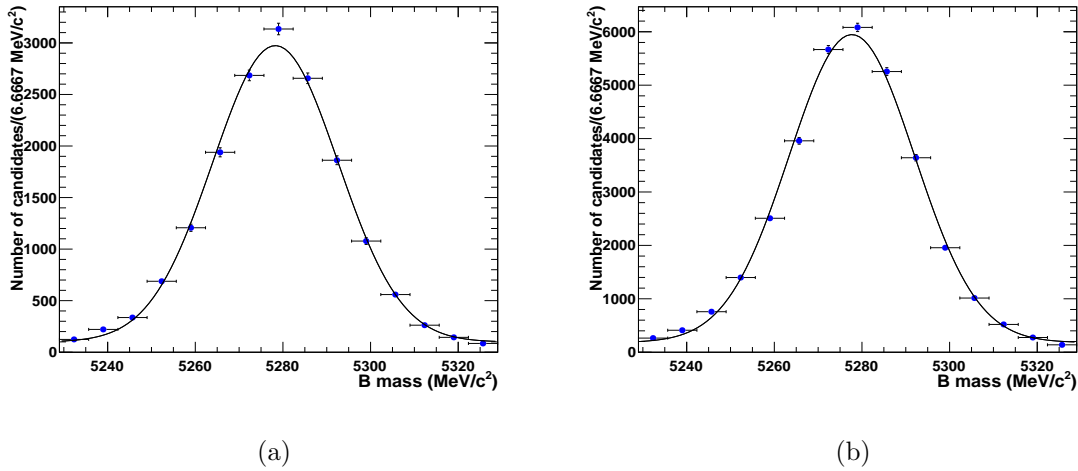


Figure 3.2: The mass distributions for LL (Figure 3.2(a)) and DD (Figure 3.2(b)) true B^\pm candidates from $B^\pm \rightarrow D(K_S^0 \pi^+ \pi^-) K^\pm$ MC. The lines are the results of Gaussian fits to the distributions, with fitted σ s of $14.3 \text{ MeV}/c^2$ (LL) and $14.3 \text{ MeV}/c^2$ (DD).

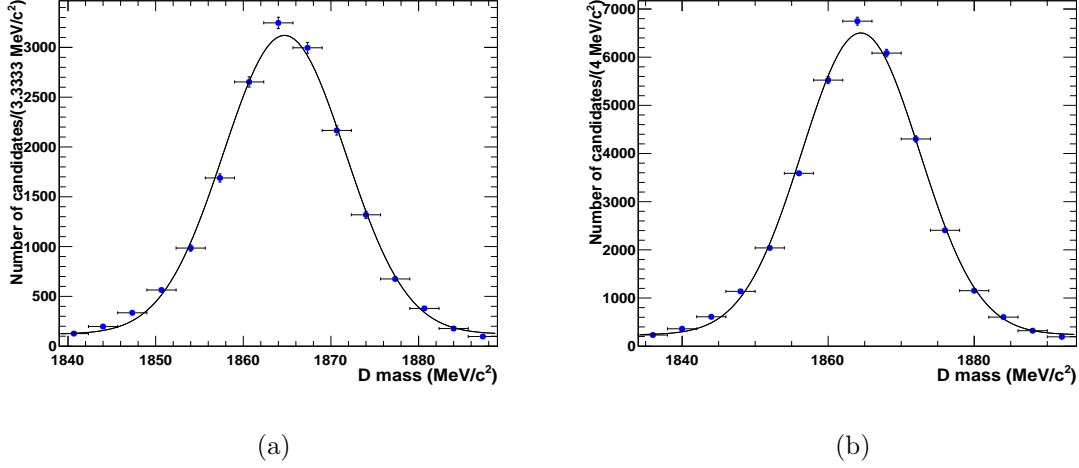


Figure 3.3: The mass distributions for LL (Figure 3.3(a)) and DD (Figure 3.3(b)) true D candidates from $B^\pm \rightarrow D(K_S^0 \pi^+ \pi^-) K^\pm$ MC. The lines are the results of Gaussian fits to the distributions, with fitted σ s of 7.0 MeV/c² (LL) and 8.1 MeV/c² (DD).

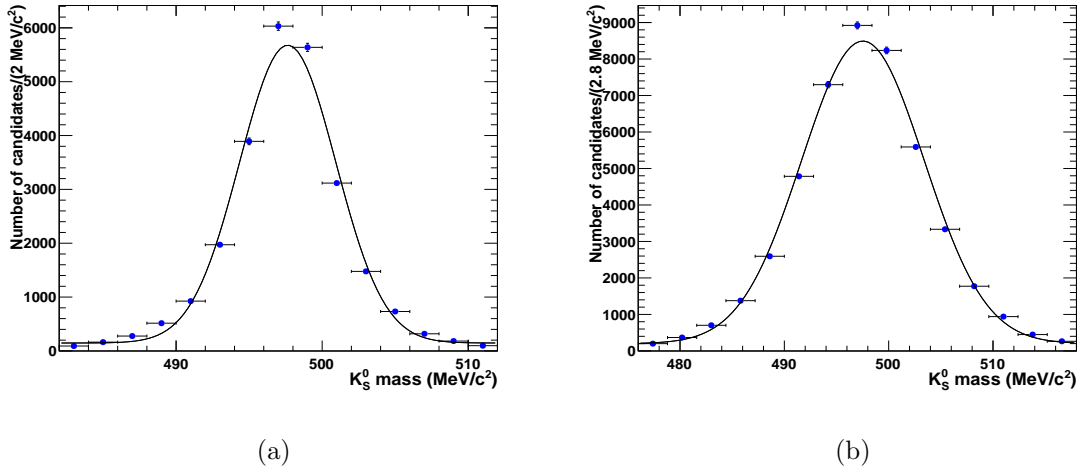


Figure 3.4: The mass distributions for LL (Figure 3.4(a)) and DD (Figure 3.4(b)) true K_S⁰ candidates from $B^\pm \rightarrow D(K_S^0 \pi^+ \pi^-) K^\pm$ MC. The lines are the results of Gaussian fits to the distributions, with fitted σ s of 3.3 MeV/c² (LL) and 5.9 MeV/c² (DD).

3.5 Selection optimisation results

The results of the optimisation of the selections for $B^\pm \rightarrow D(K_S^0 \pi^+ \pi^-) K^\pm$ signal decays with LL and DD K_S^0 are summarised in Tables 3.5 and 3.6 respectively.

For the LL candidate selection optimisation, it was found that the algorithm converged to three different sets of criteria with the same value for the metric, $\frac{S}{\sqrt{S+B}} = 69.7 \pm 0.4$. Almost the same selection variables were chosen by the algorithm in all three cases but with slightly different final criteria values. Although the LHCb trigger was not finalised at the time of optimisation, the trigger selections typically take advantage of the displaced secondary B decay vertex. Therefore, the sets of criteria (B and C) in Table 3.5 with a flight distance χ^2 requirement on the B^\pm candidate were better aligned with the expected trigger requirements than set A . Criteria set B was chosen as the final selection because the B^\pm flight distance χ^2 requirement of set C was potentially very harsh. The selection passed 6841 signal candidates and no background candidates from the preselected samples. The signal selection efficiency for LL candidates was therefore $\epsilon_{sig,sel} = (7.02 \pm 0.08) \times 10^{-3}$.

Particle	Criteria set A	Criteria set B	Criteria set C
K_S^0 daughter π	IP χ^2 (PV) > 16.0 $p < 100.0$ GeV/c track $\chi^2/\text{d.o.f.} < 25.0$	IP χ^2 (PV) > 9.0 $p < 100.0$ GeV/c	IP χ^2 (PV) > 16.0 $p < 100.0$ GeV/c
K_S^0	$ \text{mass} - 497.61 < 15.0$ MeV/ c^2 vertex $\chi^2/\text{d.o.f.} < 16.0$ FD χ^2 (PV) > 4.0	$ \text{mass} - 497.61 < 15.0$ MeV/ c^2 vertex $\chi^2/\text{d.o.f.} < 16.0$ FD χ^2 (PV) > 4.0	$ \text{mass} - 497.61 < 15.0$ MeV/ c^2 vertex $\chi^2/\text{d.o.f.} < 16.0$ FD χ^2 (PV) > 4.0
D daughter π	IP χ^2 (PV) > 25.0 $p < 100.0$ GeV/c $\Delta LL(\pi - K) > -7.5$	IP χ^2 (PV) > 25.0 $p < 100.0$ GeV/c $\Delta LL(\pi - K) > -10.0$	IP χ^2 (PV) > 25.0 $p < 100.0$ GeV/c $\Delta LL(\pi - K) > -10.0$
D	$ \text{mass} - 1864.8 < 25.0$ MeV/ c^2 vertex $\chi^2/\text{d.o.f.} < 4.0$ $\Delta LL(K - \pi) > -1.0$ $\Delta LL(K - p) > 1.0$ $p < 100.0$ GeV/c IP χ^2 (PV) > 9.0 $p_T > 250.0$ MeV/c	$ \text{mass} - 1864.8 < 25.0$ MeV/ c^2 vertex $\chi^2/\text{d.o.f.} < 4.0$ $\Delta LL(K - \pi) > -3.0$ $\Delta LL(K - p) > -10.0$ $p < 100.0$ GeV/c IP χ^2 (PV) > 16.0 $p_T > 1.0$ GeV/c	$ \text{mass} - 1864.8 < 25.0$ MeV/ c^2 vertex $\chi^2/\text{d.o.f.} < 4.0$ $\Delta LL(K - \pi) > -3.0$ $\Delta LL(K - p) > -10.0$ $p < 100.0$ GeV/c IP χ^2 (PV) > 16.0 $p_T > 500.0$ MeV/c
Bachelor K^\pm	$ \text{mass} - 5279.2 < 50.0$ MeV/ c^2 vertex $\chi^2/\text{d.o.f.} < 6.25$ IP χ^2 (PV) < 25.0 DIRA > 0.99999	$ \text{mass} - 5279.2 < 50.0$ MeV/ c^2 FD χ^2 (PV) > 169.0 vertex $\chi^2/\text{d.o.f.} < 6.25$ IP χ^2 (PV) < 9.0 DIRA > 0.99999	$ \text{mass} - 5279.2 < 50.0$ MeV/ c^2 FD χ^2 (PV) > 225.0 vertex $\chi^2/\text{d.o.f.} < 6.25$ IP χ^2 (PV) < 9.0 DIRA > 0.99999
B^\pm	-	-	-

Table 3.5: The optimised selection criteria for LL candidates. "-" indicates that the optimised criteria do not include a cut on the given variable within the allowed phase space.

For the DD candidate selection optimisation, the algorithm converged to two sets of criteria with the same metric value, $\frac{S}{\sqrt{S+B}} = 79.2 \pm 0.3$. The set of criteria labelled criteria set B in Table 3.6 was chosen for the final DD candidate selection, again as it was best aligned with expected trigger requirements. The selection passed 12996 signal candidates and no background candidates from the preselected samples. The signal selection efficiency for DD candidates was therefore $\epsilon_{sig,sel} = (9.33 \pm 0.08) \times 10^{-3}$.

Particle	Criteria set A	Criteria set B
K_S^0 daughter π	$\Delta LL(\pi - K) > 0.0$ IP χ^2 (PV) > 6.25 $p < 100.0$ GeV/c track $\chi^2/\text{d.o.f.} < 4.0$	$\Delta LL(\pi - K) > 2.5$ IP χ^2 (PV) > 6.25 $p < 100.0$ GeV/c -
K_S^0	$ \text{mass} - 497.61 < 21.0$ MeV/ c^2 vertex $\chi^2/\text{d.o.f.} < 16.0$ FD χ^2 (PV) > 4.0	$ \text{mass} - 497.61 < 21.0$ MeV/ c^2 vertex $\chi^2/\text{d.o.f.} < 16.0$ FD χ^2 (PV) > 4.0
D daughter π	IP χ^2 (PV) > 16.0 $p < 100.0$ GeV/c $\Delta LL(\pi - K) > 2.5$	IP χ^2 (PV) > 16.0 $p < 100.0$ GeV/c $\Delta LL(\pi - K) > 2.5$
D	$ \text{mass} - 1864.8 < 30.0$ MeV/ c^2 vertex $\chi^2/\text{d.o.f.} < 16.0$	$ \text{mass} - 1864.8 < 30.0$ MeV/ c^2 vertex $\chi^2/\text{d.o.f.} < 16.0$
Bachelor K^\pm	$\Delta LL(K - \pi) > 2.5$ $\Delta LL(K - p) > -1.0$ $p < 100.0$ GeV/c IP χ^2 (PV) > 6.25 $p_T > 250.0$ MeV/c track $\chi^2/\text{d.o.f.} < 9.0$	$\Delta LL(K - \pi) > -1.0$ $\Delta LL(K - p) > -5.0$ $p < 100.0$ GeV/c IP χ^2 (PV) > 6.25 $p_T > 500.0$ MeV/c -
B^\pm	- vertex $\chi^2/\text{d.o.f.} < 9.0$ IP χ^2 (PV) < 16.0 DIRA > 0.99995	$ \text{mass} - 5279.2 < 50.0$ MeV/ c^2 FD χ^2 (PV) > 100.0 vertex $\chi^2/\text{d.o.f.} < 9.0$ IP χ^2 (PV) < 16.0 DIRA > 0.9999

Table 3.6: The optimised selection criteria for DD candidates. "-" indicates that the optimised criteria do not include a cut on the given variable within the allowed phase space.

Figures 3.5–3.19 show the distributions of the variables used in the candidate selections, comparing background and signal preselected candidates. The final optimised cut value is indicated on each of the figures with a black line and an arrow to show the region selected. In certain cases, such as that shown in Figure 3.7, the optimal cut value was placed at the value imposed by the preselection criteria applied to the candidates. This indicated that the metric was not sensitive to more stringent requirements on these variables. Studies of topologically similar B decays indicate that the application of loose requirements on these variables is necessary, however, in order to reduce the level of combinatoric background. These cut values were therefore included as part of the optimised criteria.

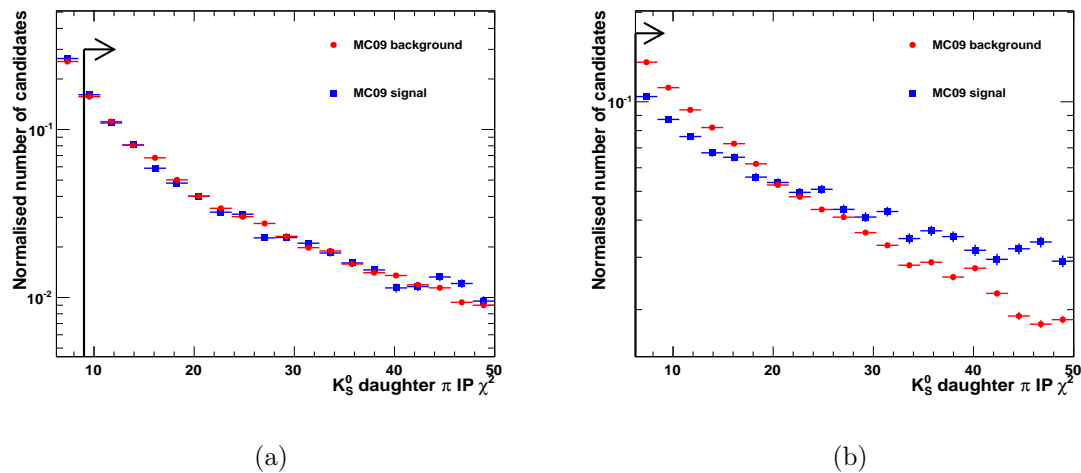


Figure 3.5: The IP χ^2 (PV) distributions for LL (Figure 3.5(a)) and DD (Figure 3.5(b)) K_S^0 daughter π in preselected MC events.

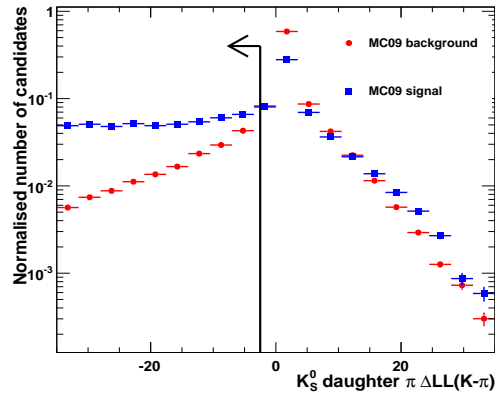
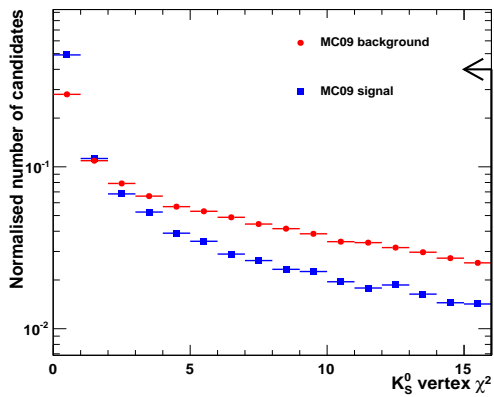
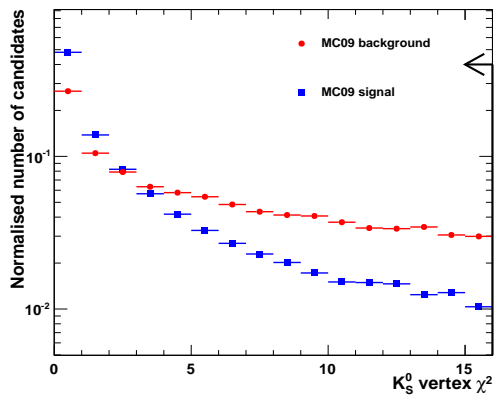


Figure 3.6: The $\Delta LL(K - \pi)$ distributions for K_S^0 daughter π in preselected DD MC events.



(a)



(b)

Figure 3.7: The vertex χ^2 distributions for LL (Figure 3.7(a)) and DD (Figure 3.7(b)) K_S^0 candidates in preselected MC events.

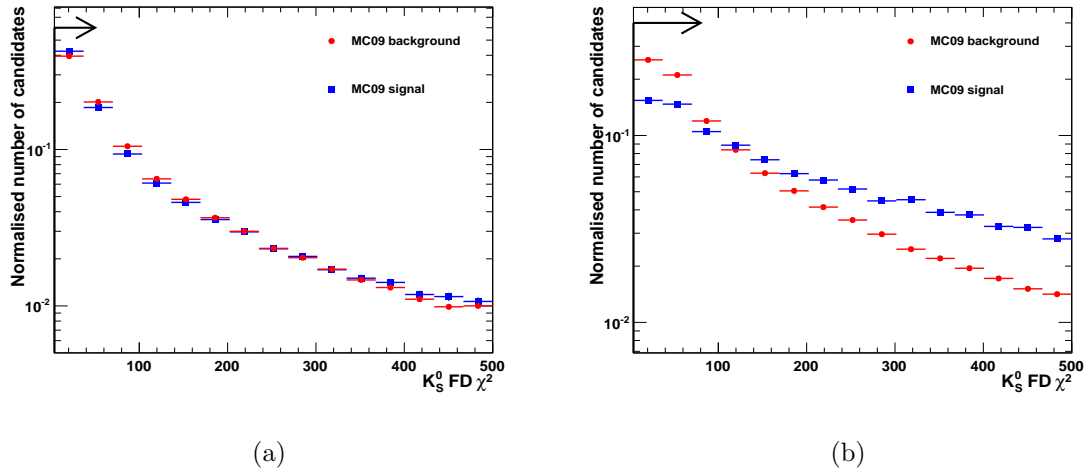


Figure 3.8: The FD χ^2 (PV) distributions for LL (Figure 3.8(a)) and DD (Figure 3.8(b)) K_S^0 candidates in preselected MC events.

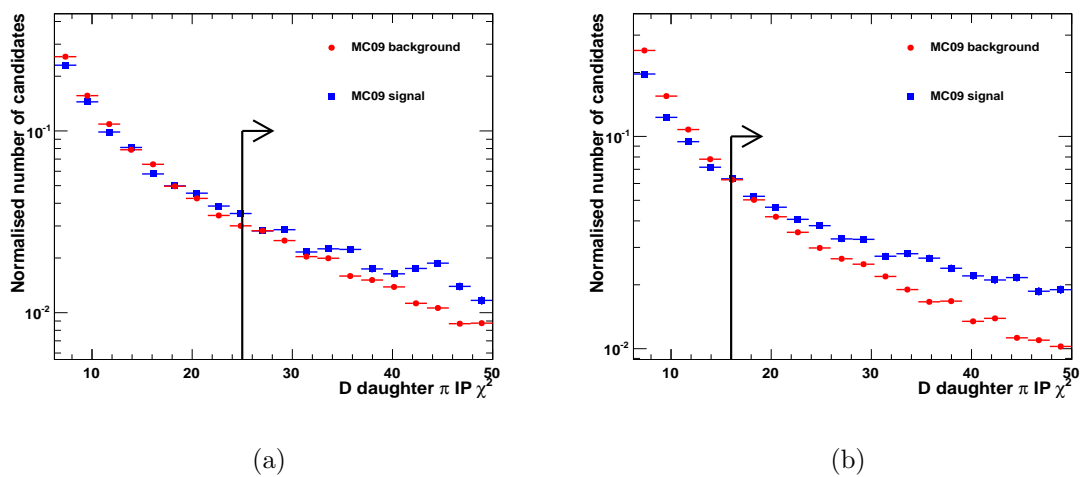


Figure 3.9: The IP χ^2 (PV) distributions for LL (Figure 3.9(a)) and DD (Figure 3.9(b)) D daughter π in preselected MC events.

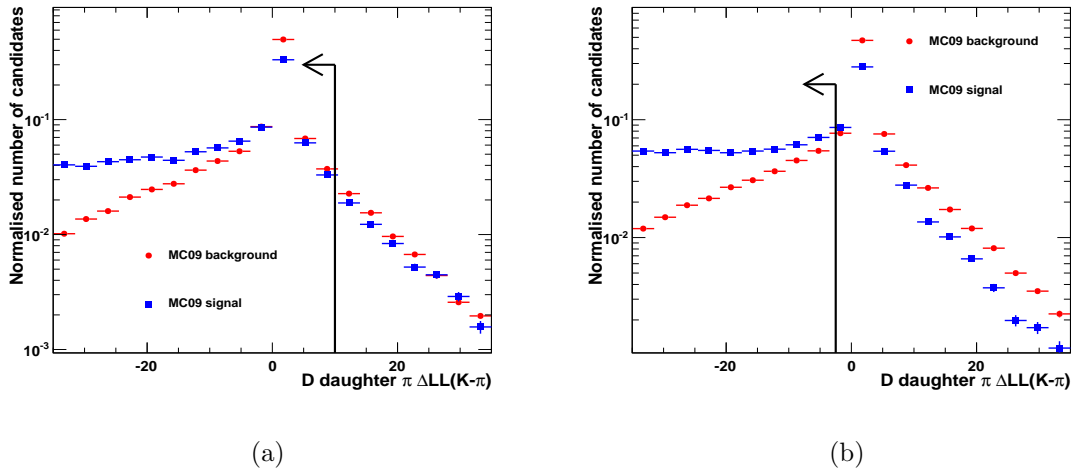


Figure 3.10: The $\Delta LL(K - \pi)$ distributions for LL (Figure 3.10(a)) and DD (Figure 3.10(b)) D daughter π in preselected MC events.

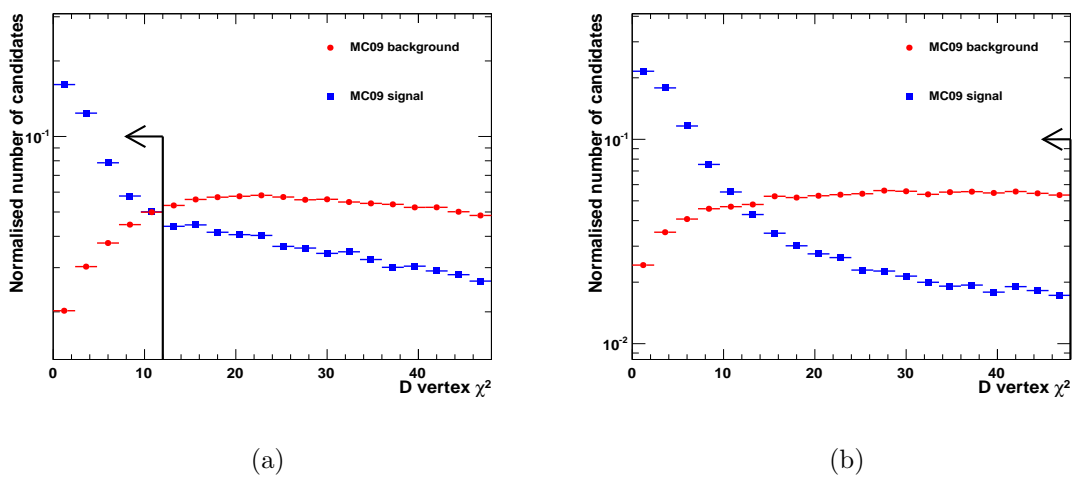


Figure 3.11: The vertex χ^2 distributions for LL (Figure 3.11(a)) and DD (Figure 3.11(b)) D candidates in preselected MC events.

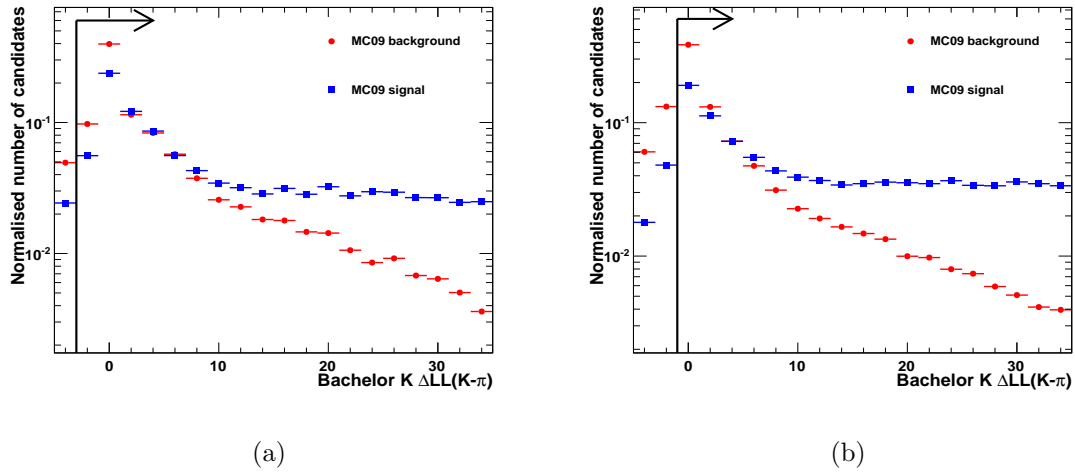


Figure 3.12: The $\Delta LL(K - \pi)$ distributions for the bachelor K^\pm in LL (Figure 3.12(a)) and DD (Figure 3.12(b)) preselected MC events.

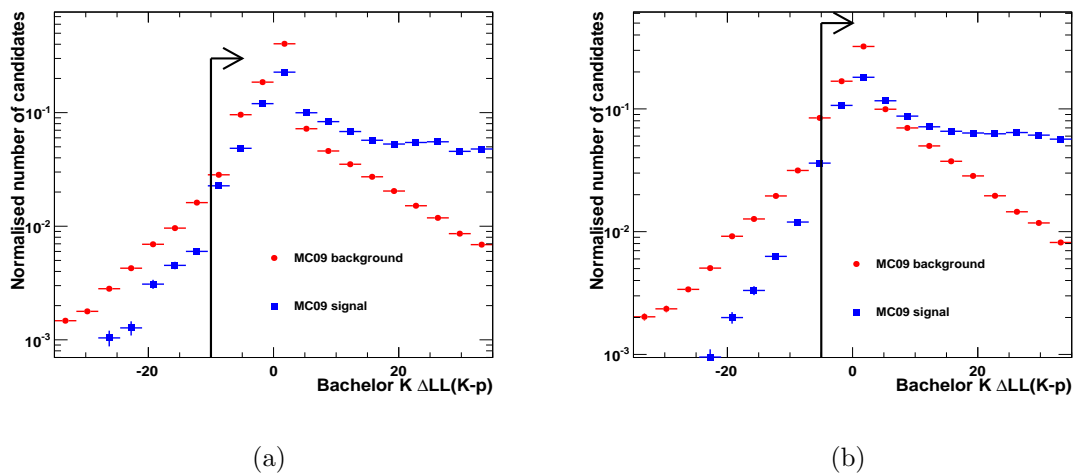


Figure 3.13: The $\Delta LL(K - p)$ distributions for the bachelor K^\pm in LL (Figure 3.13(a)) and DD (Figure 3.13(b)) preselected MC events.

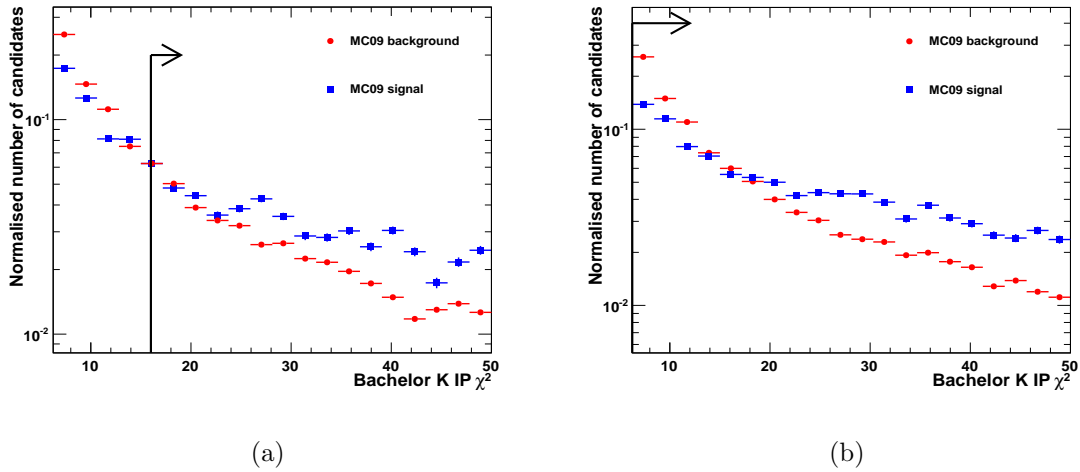


Figure 3.14: The IP χ^2 (PV) distributions for the bachelor K^\pm in LL (Figure 3.14(a)) and DD (Figure 3.14(b)) preselected MC events.

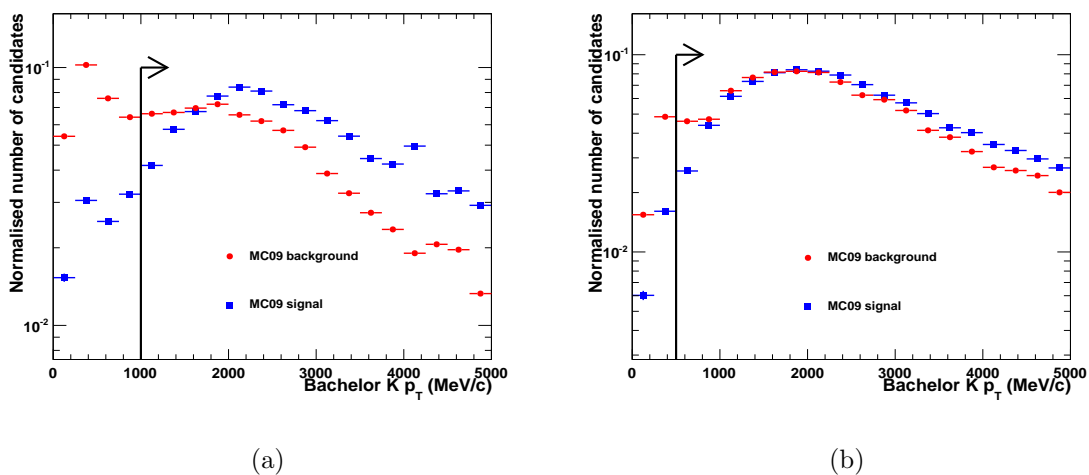


Figure 3.15: The p_T distributions for the bachelor K^\pm in LL (Figure 3.15(a)) and DD (Figure 3.15(b)) preselected MC events.

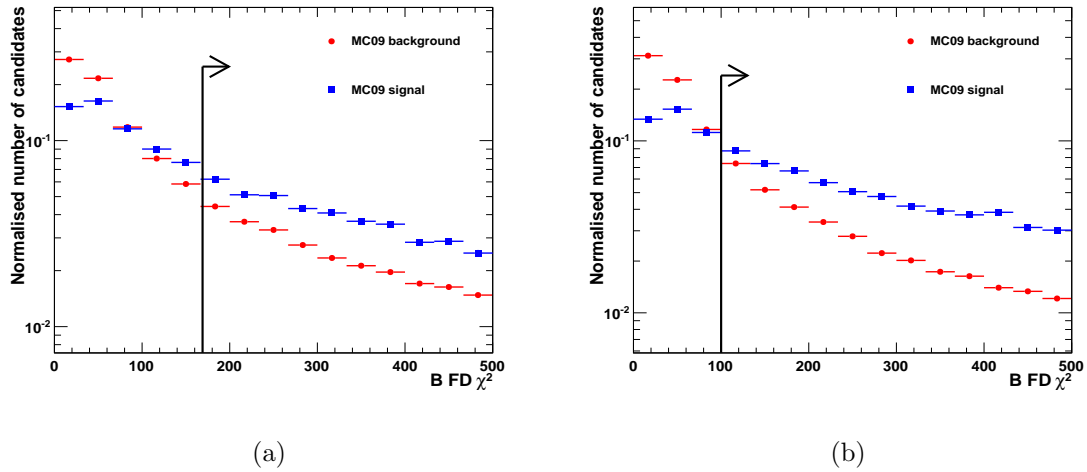


Figure 3.16: The FD χ^2 (PV) distributions for LL (Figure 3.16(a)) and DD (Figure 3.16(b)) B^\pm candidates in preselected MC events.

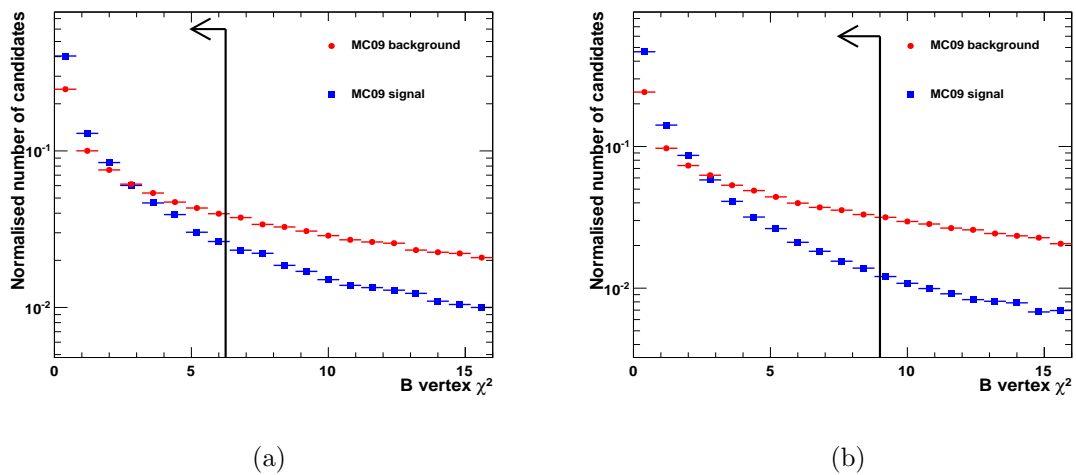


Figure 3.17: The vertex χ^2 distributions for LL (Figure 3.17(a)) and DD (Figure 3.17(b)) B^\pm candidates in preselected MC events.

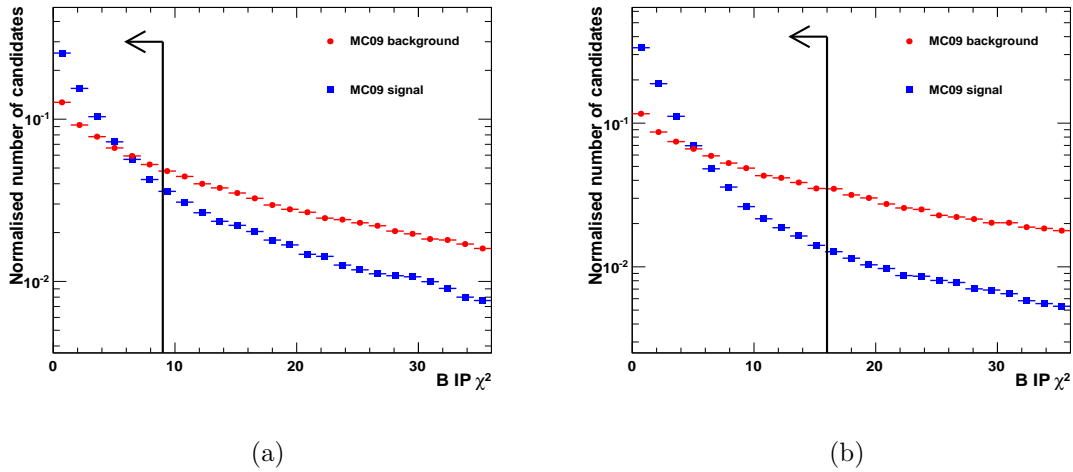


Figure 3.18: The IP χ^2 (PV) distributions for LL (Figure 3.18(a)) and DD (Figure 3.18(b)) B^\pm candidates in preselected MC events.

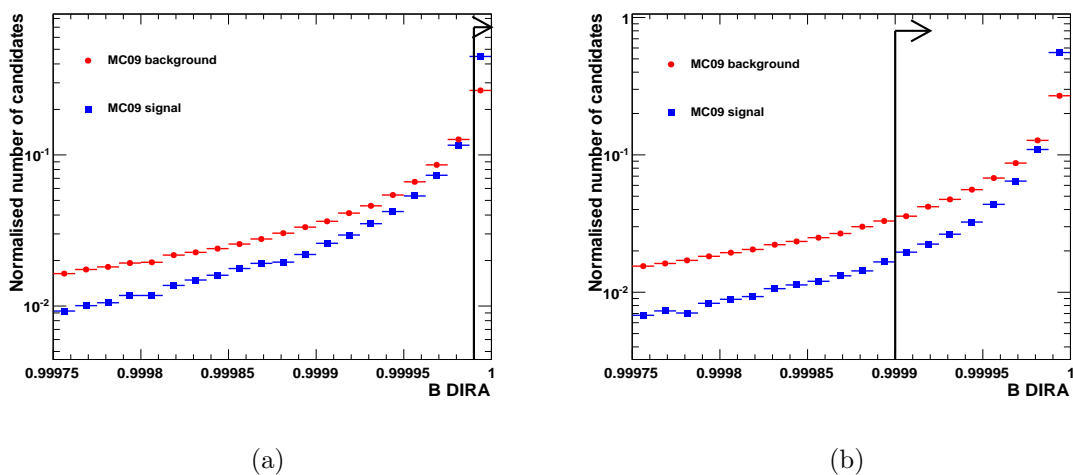


Figure 3.19: The DIRA distributions for LL (Figure 3.19(a)) and DD (Figure 3.19(b)) B^\pm candidates in preselected MC events.

3.6 Estimated candidate yields

Yield calculations were performed as described in Section 3.4. The criteria shown in Tables 3.5 and 3.6 gave estimated signal yields of $S = 4721 \pm 57$ LL candidates and $S = 6277 \pm 55$ DD candidates for an integrated luminosity of 2 fb^{-1} , where the errors are statistical.

For inclusive $b\bar{b}$ background candidates, upper limits were calculated for the 2 fb^{-1} yields because no candidates from the MC sample passed the selection. For the low-mass backgrounds, no candidates passed within the $\pm 50 \text{ MeV}/c^2$ B^\pm signal mass window. Poisson statistics were assumed, leading to an upper limit of < 2.30 expected candidates at 90% confidence level [18] in the mass window. This corresponds to an upper limit on the background candidate yield of < 32284 (< 26740) for the LL (DD) selection with an integrated luminosity of 2 fb^{-1} . For the combinatoric flat backgrounds, no candidates passed within the $\pm 500 \text{ MeV}/c^2$ B^\pm mass window. Again assuming Poisson statistics, this corresponds to an upper limit of < 3228 (< 2674) candidates for the LL (DD) background yields in the signal $\pm 50 \text{ MeV}/c^2$ B^\pm mass window with an integrated luminosity of 2 fb^{-1} . These limits were constrained by the size of the available MC background sample; lower values may have been found with a larger size sample.

3.7 Summary

The selection of $B^\pm \rightarrow D(K_S^0 \pi^+ \pi^-) K^\pm$ signal decay candidates was optimised on MC using an algorithm which maximised the metric $\frac{S}{\sqrt{S+B}}$. The resulting selection produced signal selection efficiencies of $\epsilon_{sig,sel} = (7.02 \pm 0.08) \times 10^{-3}$ for LL candidates and $\epsilon_{sig,sel} = (9.33 \pm 0.08) \times 10^{-3}$ for DD candidates. The corresponding yields were 4721 ± 57 LL and 6277 ± 55 DD B^\pm candidates, without any trigger applied, for an integrated luminosity of 2 fb^{-1} . Upper limits were placed on the number of expected candidates from inclusive $b\bar{b}$ decays in the signal mass window; for low-mass backgrounds the limits were < 32284 (< 26740) LL (DD) candidates and for combinatoric type backgrounds, the limits were < 3228 (< 2674) LL (DD) candidates.

Chapter 4

A measurement of the ratio of branching fractions $\text{Br}(B^\pm \rightarrow DK^\pm) / \text{Br}(B^\pm \rightarrow D\pi^\pm)$ using 2010 data

This chapter describes the measurement of the ratio of branching fractions $\text{Br}(B^\pm \rightarrow DK^\pm) / \text{Br}(B^\pm \rightarrow D\pi^\pm)$ using the decays $B^\pm \rightarrow D(K_S^0\pi^+\pi^-)K^\pm$ and $B^\pm \rightarrow D(K_S^0\pi^+\pi^-)\pi^\pm$ and approximately 36.5 pb^{-1} of $\sqrt{s} = 7 \text{ TeV}$ data collected by LHCb during 2010.

The measurement of the ratio of branching fractions $\text{Br}(B^\pm \rightarrow DK^\pm) / \text{Br}(B^\pm \rightarrow D\pi^\pm)$ with the decays $B^\pm \rightarrow D(K_S^0\pi^+\pi^-)K^\pm$ and $B^\pm \rightarrow D(K_S^0\pi^+\pi^-)\pi^\pm$ establishes many of the necessary analysis components, for example detailed background studies, for the measurement of γ at LHCb using these decays. The decay channels $B^\pm \rightarrow D\pi^\pm$ are important control channels for $B^\pm \rightarrow DK^\pm$ decays, having almost identical topologies but much higher branching fractions. They are far less sensitive to the CKM angle γ than $B^\pm \rightarrow DK^\pm$ decays, with a ratio of decay amplitude magnitudes of [50]

$$\left| \frac{A(B^- \rightarrow \bar{D}^0\pi^-)}{A(B^- \rightarrow D^0\pi^-)} \right| = \left| \frac{A(B^+ \rightarrow D^0\pi^+)}{A(B^+ \rightarrow \bar{D}^0\pi^+)} \right| \approx 0.01, \quad (4.1)$$

compared to the value of $r_B = 0.107 \pm 0.010$ [34] for $B^\pm \rightarrow DK^\pm$ decays. They can therefore be used to constrain acceptance effects such as the decay selection efficiency across the Dalitz plane in a GGSZ analysis (Section 1.5.3).

The ratio $\text{Br}(B^\pm \rightarrow DK^\pm) / \text{Br}(B^\pm \rightarrow D\pi^\pm)$ has been measured at Belle [168], BaBar [169] and CLEO [170] using various two- and four-body charged track D decays;

the average value is $(7.6 \pm 0.6)\%$ [18]. There is some spread between the results from the different experiments, as can be seen in the likelihood curve shown in Figure 4.1. Preliminary measurements have also been performed at LHCb using two- and four-body D decays [66] and the same 2010 data set as considered in this chapter. These decays have higher candidate statistics in this data set than the $B^\pm \rightarrow D(K_S^0\pi^+\pi^-)K^\pm$ and $B^\pm \rightarrow D(K_S^0\pi^+\pi^-)\pi^\pm$ decays. The nature of the reconstructed D decays used for both the global average value and the other LHCb measurements lead to the contributions to the measured branching fraction ratio from the suppressed $B^+ \rightarrow D^0h$ and $B^- \rightarrow \bar{D}^0h$ decays being different from the contributions in the $B^\pm \rightarrow D(K_S^0\pi^+\pi^-)h$ decay case considered in this thesis.

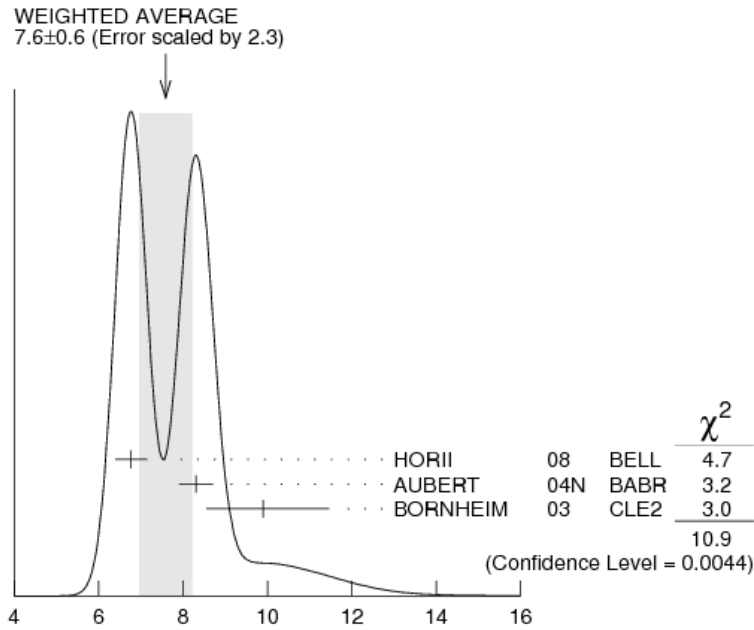


Figure 4.1: The likelihood curve for the ratio of branching fractions, $\text{Br}(B^\pm \rightarrow DK^\pm) / \text{Br}(B^\pm \rightarrow D\pi^\pm)$ [18]. The values of the ratio are equal to the values indicated on the horizontal axis multiplied by 10^{-2} .

4.1 Introduction

The ratio of branching fractions is given by

$$\frac{\text{Br}(B^\pm \rightarrow DK^\pm)}{\text{Br}(B^\pm \rightarrow D\pi^\pm)} = \frac{N_{B^\pm \rightarrow DK^\pm}^{\text{signal}}}{N_{B^\pm \rightarrow D\pi^\pm}^{\text{signal}}} \cdot \frac{\epsilon_{B^\pm \rightarrow D\pi^\pm}}{\epsilon_{B^\pm \rightarrow DK^\pm}}, \quad (4.2)$$

where $N_{B^\pm \rightarrow Dh}^{\text{signal}}$ is the number of candidates of the decay $B^\pm \rightarrow D(K_S^0 \pi^+ \pi^-)h$ (h denoting a bachelor K^\pm or π^\pm) and $\epsilon_{B^\pm \rightarrow Dh}$ is the total efficiency for $B^\pm \rightarrow D(K_S^0 \pi^+ \pi^-)h$. The total efficiency combines the detector acceptance, trigger, stripping, decay reconstruction and selection and can be written as products of the individual efficiencies,

$$\epsilon_{B^\pm \rightarrow D\pi^\pm} = \epsilon_{B^\pm \rightarrow D\pi^\pm}^{\text{acceptance}} \cdot \epsilon_{B^\pm \rightarrow D\pi^\pm}^{\text{reco}} \cdot \epsilon_{B^\pm \rightarrow D\pi^\pm}^{\text{trigger}} \cdot \epsilon_{B^\pm \rightarrow D\pi^\pm}^{\text{stripping}} \cdot \epsilon_{B^\pm \rightarrow D\pi^\pm}^{\text{sel}} \quad (4.3)$$

$$\epsilon_{B^\pm \rightarrow DK^\pm} = \epsilon_{B^\pm \rightarrow DK^\pm}^{\text{acceptance}} \cdot \epsilon_{B^\pm \rightarrow DK^\pm}^{\text{reco}} \cdot \epsilon_{B^\pm \rightarrow DK^\pm}^{\text{trigger}} \cdot \epsilon_{B^\pm \rightarrow DK^\pm}^{\text{stripping}} \cdot \epsilon_{B^\pm \rightarrow DK^\pm}^{\text{sel}} \quad (4.4)$$

with each of the individual efficiencies being measured with respect to the previous one in the product. $\epsilon_{B^\pm \rightarrow Dh}^{\text{sel}}$ can be further decomposed into the product of the efficiencies from kinematic and PID selection criteria,

$$\epsilon_{B^\pm \rightarrow Dh}^{\text{sel}} = \epsilon_{B^\pm \rightarrow Dh}^{\text{sel,kin}} \cdot \epsilon_{B^\pm \rightarrow Dh}^{\text{sel,PID}}. \quad (4.5)$$

It is only necessary to find $\epsilon_{B^\pm \rightarrow Dh}^{\text{sel,PID}}$ for the bachelor hadron as the PID requirements placed on the other particles in the decay are identical in both sets of decays and the respective efficiencies will therefore cancel in the ratio. Similarly, the reconstruction, trigger, stripping and kinematic selection efficiencies for the $D \rightarrow K_S^0 \pi^+ \pi^-$ parts of the decays should cancel in the ratio. They have been included in the individual efficiency determinations in this analysis, however, for practical reasons.

The following sections of this chapter describe the selection of the two decay modes (Section 4.2), the mass fit to the data to extract the signal yields (Section 4.3), calculation of the branching fraction ratio (Sections 4.4 and 4.5) and, finally, the systematic uncertainties on the measurement (Section 4.6). The final result is given in Section 4.7.

4.2 Decay selection criteria

During 2010, proton-proton collision data were recorded in both dipole magnet up ($\int \mathcal{L} dt = (18.0 \pm 1.8) \text{ pb}^{-1}$) and magnet down ($\int \mathcal{L} dt = (18.5 \pm 1.85) \text{ pb}^{-1}$) field configurations. The data were processed and recorded as detailed in Chapter 2. At the central stripping stage, $B^\pm \rightarrow D(K_S^0 \pi^+ \pi^-) \pi^\pm$ and $B^\pm \rightarrow D(K_S^0 \pi^+ \pi^-) K^\pm$ candidates were reconstructed in the data using DaVinci with either a LL or DD K_S^0 daughter. The selection criteria given in Table 4.1 were applied at the stripping stage and the candidates were saved to the centrally stored DSTs. These criteria were, in the most part, slightly less stringent than the optimised selection criteria described in Chapter 3. The mass windows were larger to allow for the study of backgrounds in the mass sidebands and a difference in detector mass resolution compared to MC. Some additional criteria were applied, including a requirement of fewer than 240 reconstructed tracks in the event, removing events with high detector occupancy. A further momentum requirement, $p > 2.0 \text{ GeV}/c$, was applied to all of the pions and kaons in the decay in order to match the lower momentum bound of efficient $K - \pi$ separation in the RICH detectors. Finally, all long (downstream) tracks had a track fit quality requirement of track $\chi^2/\text{d.o.f.} < 5.0$ (< 10.0) applied to them to remove poorly-reconstructed tracks.

Particle	LL candidate criteria	DD candidate criteria
K_S^0 daughter π	- IP χ^2 (PV) > 6.25 $p > 2.0$ GeV/c $p < 100.0$ GeV/c track $\chi^2/\text{d.o.f.} < 5.0$	$\Delta LL(\pi - K) > 0.0$ IP χ^2 (PV) > 4.0 $p > 2.0$ GeV/c $p < 100.0$ GeV/c track $\chi^2/\text{d.o.f.} < 10.0$
K_S^0	$ \text{mass} - 497.61 < 30.0$ MeV/c ² vertex $\chi^2/\text{d.o.f.} < 18.0$ FD χ^2 (PV) > 4.0	$ \text{mass} - 497.61 < 42.0$ MeV/c ² vertex $\chi^2/\text{d.o.f.} < 18.0$ FD χ^2 (PV) > 4.0
D daughter π	IP χ^2 (PV) > 9.0 $p > 2.0$ GeV/c $p < 100.0$ GeV/c track $\chi^2/\text{d.o.f.} < 5.0$	IP χ^2 (PV) > 9.0 $p > 2.0$ GeV/c $p < 100.0$ GeV/c track $\chi^2/\text{d.o.f.} < 5.0$
D	$ \text{mass} - 1864.8 < 50.0$ MeV/c ² vertex $\chi^2/\text{d.o.f.} < 6.25$	$ \text{mass} - 1864.8 < 60.0$ MeV/c ² vertex $\chi^2/\text{d.o.f.} < 16.0$
Bachelor K^\pm or π^\pm	IP χ^2 (PV) > 12.25 $p > 2.0$ GeV/c $p < 100.0$ GeV/c $p_T > 1.0$ GeV/c track $\chi^2/\text{d.o.f.} < 5.0$	IP χ^2 (PV) > 4.0 $p > 2.0$ GeV/c $p < 100.0$ GeV/c $p_T > 500.0$ MeV/c track $\chi^2/\text{d.o.f.} < 5.0$
B^\pm	$ \text{mass} - 5279.2 < 500.0$ MeV/c ² FD χ^2 (PV) > 156.25 vertex $\chi^2/\text{d.o.f.} < 9.0$ IP χ^2 (PV) < 12.25 DIRA > 0.9999	$ \text{mass} - 5279.2 < 500.0$ MeV/c ² FD χ^2 (PV) > 90.25 vertex $\chi^2/\text{d.o.f.} < 12.25$ IP χ^2 (PV) < 18.0 DIRA > 0.99985
-	Number of tracks in event < 240	Number of tracks in event < 240

Table 4.1: The stripping selections for LL and DD B^\pm candidates in 2010 data.

DaVinci was then used to access and filter the saved candidates, applying further selection criteria to them. The final, overall candidate selection criteria were almost identical to the optimised selections shown in Tables 3.5 and 3.6; the differences being:

- the requirement of fewer than 240 tracks per event;
- the additional momentum requirement, $p > 2.0 \text{ GeV}/c$, applied to all pions and kaons;
- the requirement on long tracks of track $\chi^2/\text{d.o.f.} < 5.0$ and on downstream tracks of track $\chi^2/\text{d.o.f.} < 10.0$;
- the PID requirements on the bachelor pion and kaon were replaced with $\Delta LL(K - \pi) < 0.0$ and $\Delta LL(K - \pi) > 0.0$, respectively. No $\Delta LL(K - p)$ requirements were made; and
- B^\pm candidates were reconstructed in a mass window $\pm 500 \text{ MeV}/c^2$ around the global average value [18].

The detector description and conditions used to filter the B^\pm candidates were identical to those used to initially process the data.

Trigger decision criteria were also applied in order to obtain well-defined samples of candidates with systematic errors which would cancel in the ratio of branching fractions. Candidates were required to pass the combined logical criteria

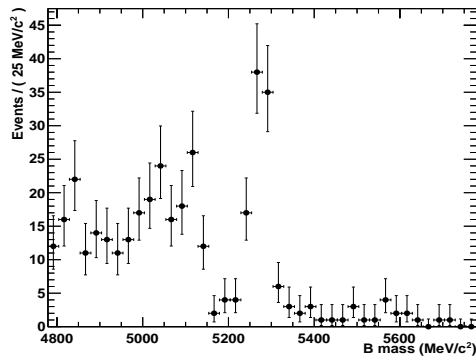
$$\begin{aligned}
 & ((\text{L0 Hadron TOS}) \text{ OR } (\text{L0 Global TIS})) \text{ AND} \\
 & ((\text{HLT1 1Track TOS}) \text{ OR } (\text{HLT1 Global TIS})) \text{ AND} \\
 & ((\text{HLT2 Topological 2-body TOS}) \text{ OR } (\text{HLT2 Topological 3-body TOS}) \text{ OR } (\text{HLT2 Global TIS}))
 \end{aligned}
 \tag{4.6}$$

where the categories triggered on signal (TOS) and triggered independent of signal (TIS) are described in detail in Chapter 2. The data were recorded over a period of several months and during this time the trigger settings were altered, although a few settings were dominant.

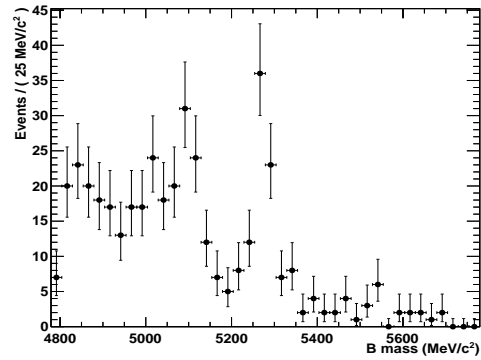
In cases where multiple B^\pm candidates were reconstructed and selected in a single event, the candidate with the largest value of B^\pm flight distance χ^2 from the PV was retained and the other candidates discarded. It was found that the B^\pm candidates in

these events were within a few MeV/c^2 in reconstructed mass and were therefore most likely differently reconstructed versions of a single real decay.

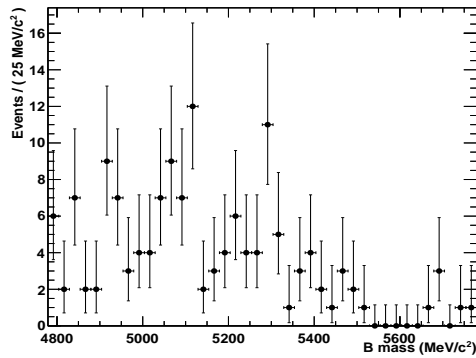
The resulting $B^\pm \rightarrow D(K_S^0\pi^+\pi^-)h$ candidate mass distributions, combining the magnet up and the magnet down data, are shown in Figure 4.2. All candidates in these distributions pass the full selection, including the combined trigger and stripping as detailed above. In the $B^\pm \rightarrow D\pi^\pm$ distributions, clear signal mass peaks can be seen near the global average B^\pm mass of $(5279.2 \pm 0.3) \text{ MeV}/c^2$ [18]; in the $B^\pm \rightarrow DK^\pm$ cases the statistics are much lower. In particular, the DD $B^\pm \rightarrow DK^\pm$ mass distribution (Figure 4.2(d)) does not show a clear signal peak and would therefore be difficult to fit. For this reason, only the LL $B^\pm \rightarrow D\pi^\pm$ and LL $B^\pm \rightarrow DK^\pm$ candidates were used in the calculation of the ratio of branching fractions and it is these that will be discussed in the rest of this chapter.



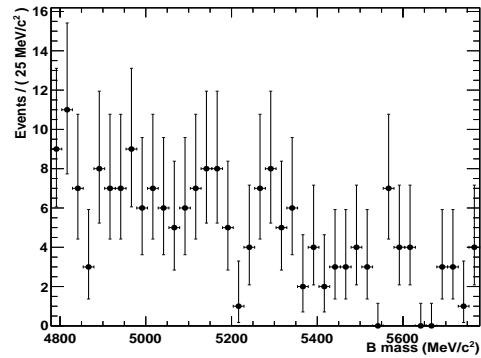
(a)



(b)



(c)



(d)

Figure 4.2: The $B^\pm \rightarrow D(K_S^0 \pi^+ \pi^-)h$ candidate mass distributions from 36.5 pb^{-1} of 2010 data. Figure 4.2(a) shows the $B^\pm \rightarrow D\pi^\pm$ LL distribution, Figure 4.2(b) the $B^\pm \rightarrow D\pi^\pm$ DD distribution, Figure 4.2(c) shows the $B^\pm \rightarrow DK^\pm$ LL distribution and Figure 4.2(d) the $B^\pm \rightarrow DK^\pm$ DD distribution.

4.3 Mass fit

In order to evaluate the yield of $B^\pm \rightarrow D\pi^\pm$ candidates and the ratio of yields of Equation 4.2, $N_{B^\pm \rightarrow DK^\pm}^{signal} / N_{B^\pm \rightarrow D\pi^\pm}^{signal}$, the two mass distributions of Figures 4.2(a) and 4.2(c) were fitted simultaneously with an extended unbinned likelihood fit using the RooFit software toolkit [171]. The distributions were not separated into magnet up and down subsets due to lack of statistics. The fit expression used for the mass distributions is detailed below, preceded by a description of the backgrounds considered and the signal and background component probability distribution functions (PDFs).

4.3.1 Signal and background fits to Monte-Carlo

In late 2010, further MC simulation was performed (see Section 2.4.1) as part of the MC10 production; this simulation used a proton-proton collision energy of $\sqrt{s} = 7$ TeV, an average number of proton-proton interactions per bunch crossing of 2.5 and an updated detector description so that it matched the majority of the data recorded by LHCb during 2010 as closely as possible. The MC10 samples were produced with the LHCb dipole magnet in both up and down field configurations, and the kinematic description of the decays and their reconstruction in the MC were in reasonably good agreement with the data (see Appendix C), except for the PID performance [121]. The different background and signal contributions to the mass distribution fit of the data were evaluated with samples from this simulation; MC truth information was used to separate candidates into the different possible categories. In all cases, multiple candidates in a single event were removed in the same way as for data. Candidates from magnet up and down MC samples were summed with equal weights to give the overall distributions.

In order to find appropriate PDFs for the signal mass distributions, $B^\pm \rightarrow D(K_S^0\pi^+\pi^-)\pi^\pm$ and $B^\pm \rightarrow D(K_S^0\pi^+\pi^-)K^\pm$ LL candidates were reconstructed and selected, using the full selection including trigger and stripping, from approximately 3M (1.5M magnet up, 1.5M magnet down) MC10 $B^\pm \rightarrow D(K_S^0\pi^+\pi^-)h$ signal events. As for the MC09 production, in the MC10 samples the $D \rightarrow K_S^0\pi^+\pi^-$ specific decay was generated according to phase space and a decay amplitude model was not applied. The candidate mass distributions were fitted with a sum of a Gaussian and a Crystal Ball PDF [172] with a low-mass tail,

CB ,

$$CB(M|\mu, \sigma, \alpha, n) = \begin{cases} \frac{\left(\frac{n}{|\alpha|}\right)^n \cdot \exp\left(-\frac{1}{2}|\alpha|^2\right)}{\left(n/|\alpha| - |\alpha| - \frac{M-\mu}{\sigma}\right)^n} & \frac{M-\mu}{\sigma} \leq -|\alpha| \\ \exp\left(-\frac{1}{2}\left(\frac{M-\mu}{\sigma}\right)^2\right) & \frac{M-\mu}{\sigma} > -|\alpha| \end{cases} \quad (4.7)$$

where M is the mass of the $B^\pm \rightarrow Dh$ candidates, μ is the Gaussian mean, σ is the Gaussian width and α and n are parameters describing the low-mass tail. The Crystal Ball and Gaussian were constrained to have the same mean in each of the fits. The Crystal Ball low-mass tail accounts for radiative losses to the final state tracks and also resolution effects; the Gaussian part of the Crystal Ball also provides a resolution effect on the high mass side of the peak. The resulting distributions are shown in Figure 4.3.

The potential backgrounds to the signal $B^\pm \rightarrow D(K_S^0\pi^+\pi^-)h$ decays can be classified into the following categories [79]:

1. phase-space combinatoric background: a fake D (with at least one fake final state particle) combined with a true or fake bachelor h .
2. cross-feed background: a true $D \rightarrow K_S^0\pi^+\pi^-$ candidate combined with a true bachelor h originating from the same B^\pm , but the h is misidentified as the other case of π/K .
3. Dh -random background: a true $D \rightarrow K_S^0\pi^+\pi^-$ candidate combined with a true or fake bachelor h originating from a different b-hadron or the underlying event. Example decays include $B^\pm \rightarrow D\pi^\pm$ where the D has been paired with a π^\pm from the PV.
4. D^* background: a true $D \rightarrow K_S^0\pi^+\pi^-$ originating from the D^* in a $B \rightarrow D^*X$ decay, combined with a true or fake h from the same B. Example decays include: $B_d^0 \rightarrow \bar{D}^*(2007)^0(\bar{D}^0\gamma)K^*(892)^0(K\pi)$, $B \rightarrow D^*K$, and $B \rightarrow D^*\rho$.
5. Dh -signal background: a true $D \rightarrow K_S^0\pi^+\pi^-$ candidate, originating either directly or indirectly from a B, combined with a true or fake h from the same B (excluding the D^* and cross-feed backgrounds). Example decays include $B^\pm \rightarrow D\mu^\pm\nu$ where the μ is misidentified as h and $B \rightarrow D\rho$ where a daughter of the ρ is used as the bachelor.
6. non-resonant background: a true $B^\pm \rightarrow Dh$ decay, but the true D decay is to the four-body final state $\pi\pi\pi\pi$; the decay is reconstructed as $D \rightarrow K_S^0\pi^+\pi^-$. This

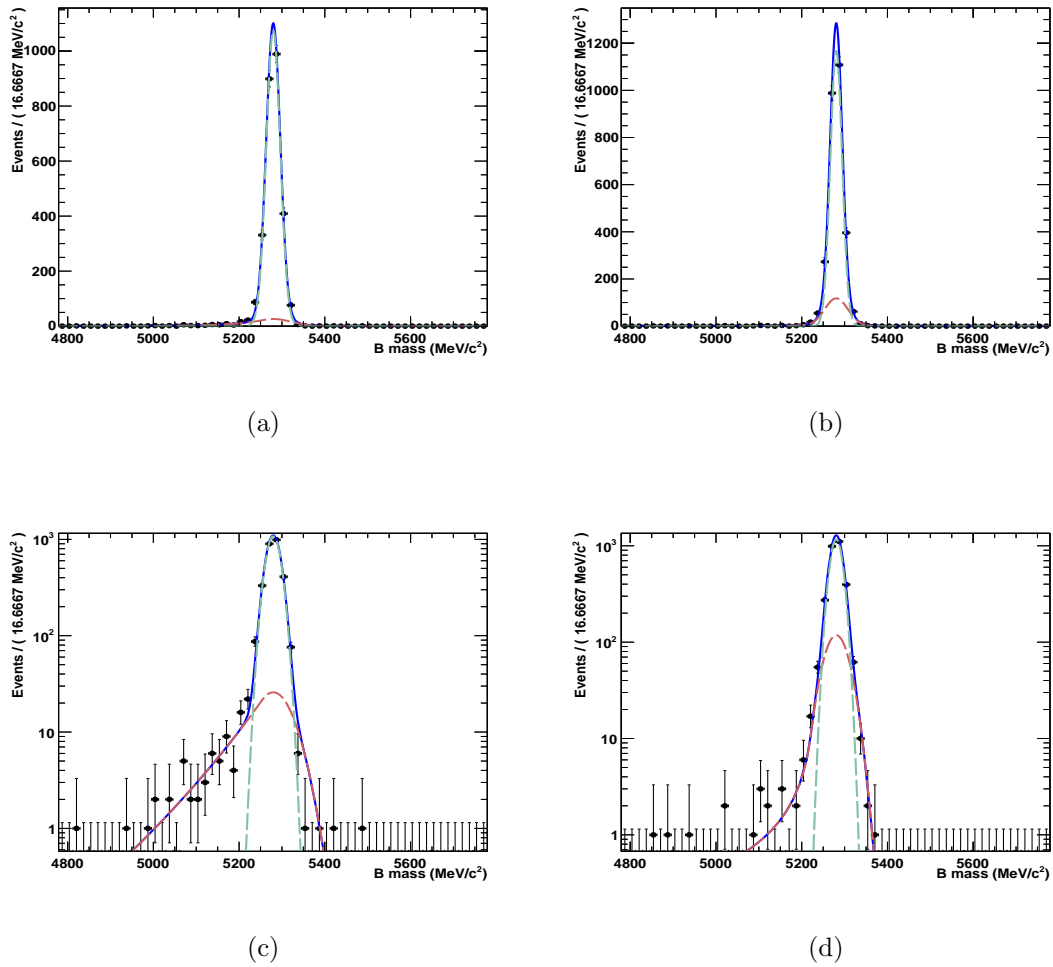


Figure 4.3: The signal $B^\pm \rightarrow D(K_S^0 \pi^+ \pi^-) h$ candidate mass distributions from MC. Figure 4.3(a) shows the $B^\pm \rightarrow D\pi^\pm$ signal distribution and Figure 4.3(b) shows the $B^\pm \rightarrow DK^\pm$ signal distribution. Figures 4.3(c) and 4.3(d) show the same $B^\pm \rightarrow D\pi^\pm$ and $B^\pm \rightarrow DK^\pm$ distributions on log scales, respectively. The total PDF (blue) is the sum of a Gaussian component (green) and Crystal Ball PDF (red).

background is only present for LL decays, where the K_S^0 can be reconstructed as short-lived, so that the tracks identified as K_S^0 pion daughters and D pion daughters could, in reality, be tracks coming from the same four-body D decay vertex.

For both $B^\pm \rightarrow D\pi^\pm$ and $B^\pm \rightarrow DK^\pm$, the contributions from background Categories 1 and 3 – 5 were evaluated using a large, approximately 100M (50M magnet up, 50M magnet down) event “cocktail” sample of MC10 $b \rightarrow DX$ decays, where b encompasses B^\pm , B_d^0 , B_s^0 and Λ_b and D represents D^0 , D^\pm , D_s and Λ_c mesons and their excited states. $B^\pm \rightarrow D(K_S^0\pi^+\pi^-)\pi^\pm$ and $B^\pm \rightarrow D(K_S^0\pi^+\pi^-)K^\pm$ LL candidates were reconstructed and selected as detailed in Section 4.2, using the full selection including trigger and stripping. It was found that very few (between 0 and 5 over the whole B mass range) Category 1 (phase-space combinatoric) candidates and no Category 3 (Dh -random) candidates passed the $B^\pm \rightarrow D\pi^\pm$ and $B^\pm \rightarrow DK^\pm$ selections. Categories 4 and 5 also had low numbers of candidates and so were combined to give a “low-mass background” category. The B^\pm mass distributions of the $B^\pm \rightarrow D(K_S^0\pi^+\pi^-)\pi^\pm$ and $B^\pm \rightarrow D(K_S^0\pi^+\pi^-)K^\pm$ candidates in the low-mass background category can be seen in Figure 4.4. In the $B^\pm \rightarrow D\pi^\pm$ case, the distribution was best fitted with a total RooFit PDF consisting of the sum of an exponential and two narrow Gaussian peaks. In the $B^\pm \rightarrow DK^\pm$ case, the available statistics were still very low and so the distribution was fitted with a total PDF consisting of the sum of an exponential and one broad Gaussian.

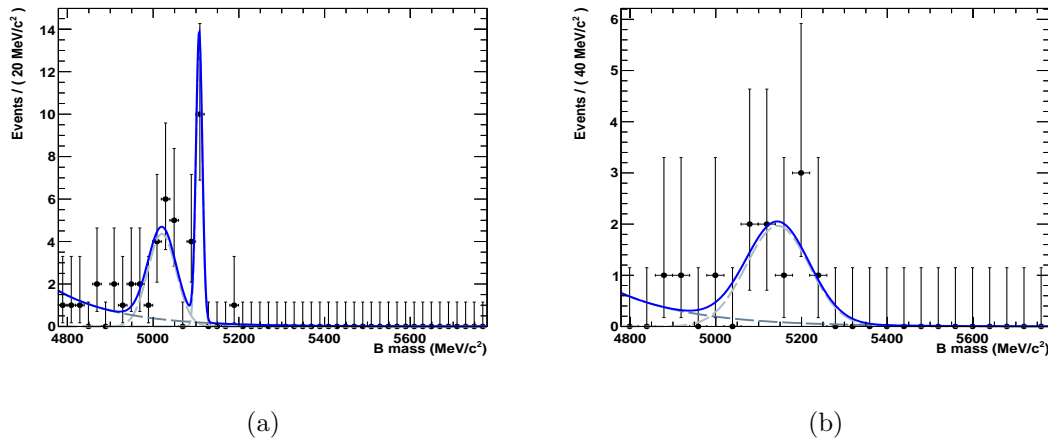


Figure 4.4: The background Category 4 and 5 (low-mass) $B^\pm \rightarrow D(K_S^0\pi^+\pi^-)h$ candidate mass distributions from MC. Figure 4.4(a) shows the $B^\pm \rightarrow D\pi^\pm$ distribution and Figure 4.4(b) shows the $B^\pm \rightarrow DK^\pm$ distribution.

The Category 2 (cross-feed) background contribution was found by selecting $B^\pm \rightarrow D(K_S^0\pi^+\pi^-)\pi^\pm$ LL candidates from $B^\pm \rightarrow D(K_S^0\pi^+\pi^-)K^\pm$ signal MC10 events, and vice versa, including the trigger and stripping. The B^\pm mass distributions of the $B^\pm \rightarrow D\pi^\pm$ and $B^\pm \rightarrow DK^\pm$ candidates in this category can be seen in Figure 4.5. The distributions were fitted with a double Crystal Ball PDF, DCB ,

$$DCB(M|\mu, \sigma, \alpha, n, \beta, l) = \begin{cases} \frac{\left(\frac{l}{|\beta|}\right)^l \cdot \exp\left(-\frac{1}{2}|\beta|^2\right)}{\left(l/|\beta| - |\beta| - \frac{M-\mu}{\sigma}\right)^l} & \frac{M-\mu}{\sigma} \leq -\beta \\ \exp\left(-\frac{1}{2}\left(\frac{M-\mu}{\sigma}\right)^2\right) & -\beta < \frac{M-\mu}{\sigma} < \alpha \\ \frac{\left(\frac{n}{|\alpha|}\right)^n \cdot \exp\left(-\frac{1}{2}|\alpha|^2\right)}{\left(n/|\alpha| - |\alpha| + \frac{M-\mu}{\sigma}\right)^n} & \frac{M-\mu}{\sigma} \geq \alpha \end{cases} \quad (4.8)$$

where M is the mass of the $B^\pm \rightarrow Dh$ candidates, μ is the Gaussian mean, σ is the Gaussian width, α and n are parameters describing the high-mass tail and β and l are parameters describing the low-mass tail.

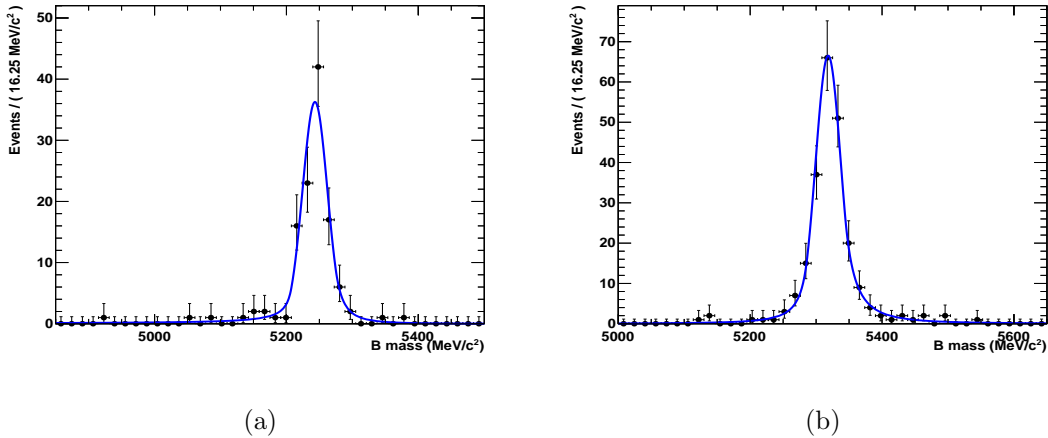


Figure 4.5: The background Category 2 (cross-feed) $B^\pm \rightarrow D(K_S^0\pi^+\pi^-)h$ candidate mass distributions from MC. Figure 4.5(a) shows the $B^\pm \rightarrow D\pi^\pm$ distribution and Figure 4.5(b) shows the $B^\pm \rightarrow DK^\pm$ distribution.

The Category 6 (non-resonant) background was estimated by selecting LL $B^\pm \rightarrow D(K_S^0\pi^+\pi^-)h$ candidates from $B^\pm \rightarrow D(\pi\pi\pi\pi)h$ MC10 samples (approximately 10M events in each case), including trigger and stripping selections. Fits to the candidate B^\pm mass distribution with a Gaussian plus a Crystal Ball PDF (Figure 4.6) resulted in fitted parameter values very similar to those from the fits to the signal shown in Figure 4.3. In both $B^\pm \rightarrow D\pi^\pm$ and $B^\pm \rightarrow DK^\pm$ cases, the Gaussian means were within 1σ and the Gaussian σ s were identical within 2σ ; there were some larger discrepancies in the

Crystal Ball PDF tail parameters, but these parts of the PDFs are susceptible to the effects of low statistics in the mass distribution tails. These results indicate that this background is indistinguishable from signal in the $B^\pm \rightarrow D\pi^\pm$ and $B^\pm \rightarrow DK^\pm$ data mass distributions. In the fit to the data described below, the evaluated yields $N_{B^\pm \rightarrow DK^\pm}^{sig,fit}$ and $N_{B^\pm \rightarrow D\pi^\pm}^{sig,fit}$ are therefore a sum of $B^\pm \rightarrow D(K_S^0\pi^+\pi^-)h$ and $B^\pm \rightarrow D(\pi\pi\pi\pi)h$ candidates, and the evaluated yields are not equal to the signal yields $N_{B^\pm \rightarrow Dh}^{signal}$ in Equation 4.2. It is possible, however, to correct for this background using the ratio of expected yields, where the yields are calculated as described in Equation 3.1 and the relevant efficiencies are found from MC. Certain terms in the yield ratio cancel, for example the $b\bar{b}$ cross-section. This leaves the fraction F_{Dh} , which is equal to the ratio of the total efficiencies $\epsilon_{B^\pm \rightarrow Dh}$ (acceptance, reconstruction, trigger, stripping and selection, as defined in Equations 4.3 and 4.4), evaluated with MC10, and the non-cancelling measured branching fractions from reference [18]. For example,

$$\begin{aligned} N_{B^\pm \rightarrow DK^\pm}^{sig,fit} &= N_{B^\pm \rightarrow D(K_S^0\pi^+\pi^-)K^\pm}^{sig,fit} + N_{B^\pm \rightarrow D(\pi\pi\pi\pi)K^\pm}^{sig,fit} \\ &= N_{B^\pm \rightarrow D(K_S^0\pi^+\pi^-)K^\pm}^{sig,fit} (1 + F_{DK}), \end{aligned} \quad (4.9)$$

where F_{DK} is

$$F_{DK} = \frac{\epsilon_{B^\pm \rightarrow D(\pi\pi\pi\pi)K^\pm} \cdot \text{Br}(D \rightarrow \pi\pi\pi\pi)}{\epsilon_{B^\pm \rightarrow D(K_S^0\pi^+\pi^-)K^\pm} \cdot \text{Br}(D \rightarrow K_S^0\pi^+\pi^-) \cdot \text{Br}(K_S^0 \rightarrow \pi^+\pi^-)}, \quad (4.10)$$

$\epsilon_{B^\pm \rightarrow D(K_S^0\pi^+\pi^-)K^\pm}$ is the total efficiency for $B^\pm \rightarrow D(K_S^0\pi^+\pi^-)K^\pm$ candidates from the $B^\pm \rightarrow D(K_S^0\pi^+\pi^-)K^\pm$ MC10 samples and $\epsilon_{B^\pm \rightarrow D(\pi\pi\pi\pi)K^\pm}$ is the total efficiency for $B^\pm \rightarrow D(K_S^0\pi^+\pi^-)K^\pm$ candidates from the $B^\pm \rightarrow D(\pi\pi\pi\pi)K^\pm$ MC10 samples.

It was found that $F_{DK} = 0.26 \pm 0.02$ and $F_{D\pi} = 0.25 \pm 0.02$, where the errors are evaluated using toy MC (see Section 4.6) and include errors on the global averages of branching fractions, statistical effects from limited MC sample sizes and uncertainties on the integrated luminosity measurements used to weight the efficiencies according to the proportions of data recorded in the magnet up and down detector configurations. In order to calculate the ratio of branching fractions in Equation 4.2, F_{DK} and $F_{D\pi}$ must be included so that

$$\frac{N_{B^\pm \rightarrow DK^\pm}^{signal}}{N_{B^\pm \rightarrow D\pi^\pm}^{signal}} = \frac{N_{B^\pm \rightarrow DK^\pm}^{sig,fit}}{N_{B^\pm \rightarrow D\pi^\pm}^{sig,fit}} \cdot \frac{(1 + F_{D\pi})}{(1 + F_{DK})}. \quad (4.11)$$

The full expression for the branching fraction ratio then becomes

$$\frac{\text{Br}(B^\pm \rightarrow DK^\pm)}{\text{Br}(B^\pm \rightarrow D\pi^\pm)} = \frac{N_{B^\pm \rightarrow DK^\pm}^{sig,fit}}{N_{B^\pm \rightarrow D\pi^\pm}^{sig,fit}} \cdot \frac{(1 + F_{D\pi})}{(1 + F_{DK})} \cdot \frac{\epsilon_{B^\pm \rightarrow D\pi^\pm}}{\epsilon_{B^\pm \rightarrow DK^\pm}}, \quad (4.12)$$

where

$$\epsilon_{B^\pm \rightarrow D\pi^\pm} = \epsilon_{B^\pm \rightarrow D\pi^\pm}^{acceptance} \cdot \epsilon_{B^\pm \rightarrow D\pi^\pm}^{reco} \cdot \epsilon_{B^\pm \rightarrow D\pi^\pm}^{trigger} \cdot \epsilon_{B^\pm \rightarrow D\pi^\pm}^{stripping} \cdot \epsilon_{B^\pm \rightarrow D\pi^\pm}^{sel,kin} \cdot \epsilon_{B^\pm \rightarrow D\pi^\pm}^{sel,PID} \quad (4.13)$$

and

$$\epsilon_{B^\pm \rightarrow DK^\pm} = \epsilon_{B^\pm \rightarrow DK^\pm}^{acceptance} \cdot \epsilon_{B^\pm \rightarrow DK^\pm}^{reco} \cdot \epsilon_{B^\pm \rightarrow DK^\pm}^{trigger} \cdot \epsilon_{B^\pm \rightarrow DK^\pm}^{stripping} \cdot \epsilon_{B^\pm \rightarrow DK^\pm}^{sel,kin} \cdot \epsilon_{B^\pm \rightarrow DK^\pm}^{sel,PID} \cdot \quad (4.14)$$

The contributions of cross-feed components from $B^\pm \rightarrow D(\pi\pi\pi\pi)h$ decays were also investigated. $B^\pm \rightarrow D(K_S^0\pi^+\pi^-)h$ LL candidates were fully reconstructed and selected from the $B^\pm \rightarrow D(\pi\pi\pi\pi)h$ MC10 samples and the resulting mass distributions fitted with a double Crystal Ball PDF (Figure 4.7). It was again found that the resulting fitted parameter values were almost identical within errors to those of the fits to cross-feed from $B^\pm \rightarrow D(K_S^0\pi^+\pi^-)h$ decays, shown in Figure 4.5, with the only differences greater than 1σ being in the fitted mean values; these were within 3σ in both $D\pi$ and DK cases. The $B^\pm \rightarrow D(\pi\pi\pi\pi)h$ cross-feed contribution is therefore indistinguishable from $B^\pm \rightarrow D(K_S^0\pi^+\pi^-)h$ cross-feed in the $B^\pm \rightarrow D\pi^\pm$ and $B^\pm \rightarrow DK^\pm$ data mass distributions.

4.3.2 Fit to 2010 data

In order to extract the ratio of numbers of candidates $N_{B^\pm \rightarrow DK^\pm}^{sig,fit} / N_{B^\pm \rightarrow D\pi^\pm}^{sig,fit}$ from the data, the mass distributions of the reconstructed $B^\pm \rightarrow DK^\pm$ and $B^\pm \rightarrow D\pi^\pm$ candidates, each including both magnet up and down candidates, were fitted simultaneously. The PDFs for the components of the fit were chosen according to the results of the MC signal and background fits described in the previous section.

For Category 1 background in both $B^\pm \rightarrow D\pi^\pm$ and $B^\pm \rightarrow DK^\pm$ cases, the number of selected candidates from the cocktail MC sample was too small to parameterise the PDF. It was therefore assumed that in both cases the Category 1 contribution could be included in the exponential PDF used to partially fit the low-mass background. As no candidates in Category 3 passed the selections on the MC cocktail sample, no specific PDF was

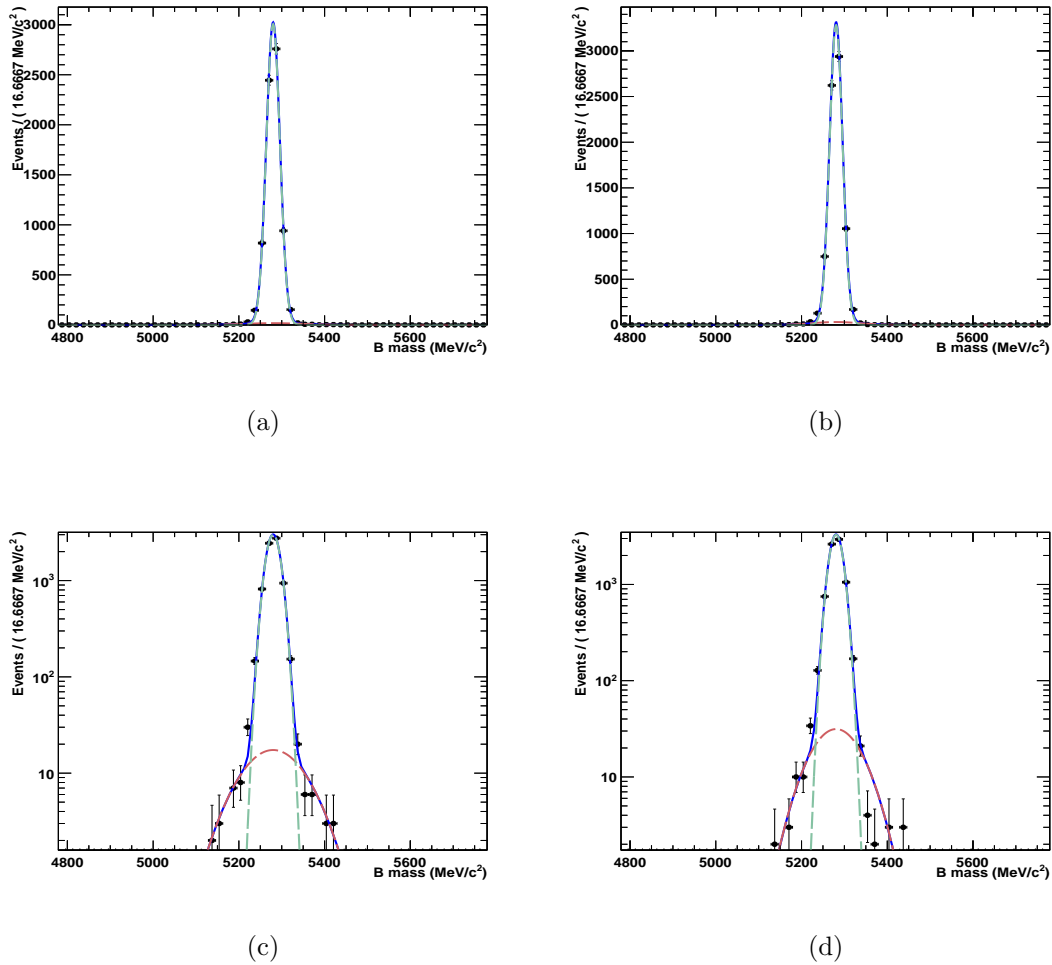


Figure 4.6: The Category 6 background B^\pm candidate mass distributions from MC. Figure 4.6(a) shows the $B^\pm \rightarrow D(K_S^0 \pi^+ \pi^-) \pi^\pm$ candidate distribution, selected from $B^\pm \rightarrow D(\pi\pi\pi\pi) \pi^\pm$ MC10, and Figure 4.6(b) shows the $B^\pm \rightarrow D(K_S^0 \pi^+ \pi^-) K^\pm$ distribution, selected from $B^\pm \rightarrow D(\pi\pi\pi\pi) K^\pm$ MC10. Figures 4.6(c) and 4.6(d) show the same $B^\pm \rightarrow D\pi^\pm$ and $B^\pm \rightarrow DK^\pm$ distributions on log scales, respectively. The total PDF (blue) is the sum of a Gaussian component (green) and Crystal Ball PDF (red).

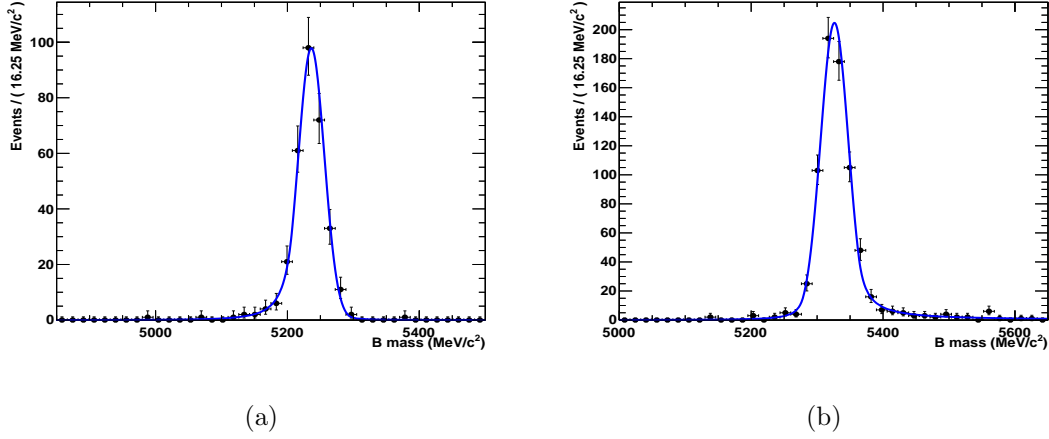


Figure 4.7: The Category 6 background cross-feed B^\pm candidate mass distributions from MC. Figure 4.7(a) shows the $B^\pm \rightarrow D(K_S^0 \pi^+ \pi^-) \pi^\pm$ candidate distribution, selected from $B^\pm \rightarrow D(\pi \pi \pi \pi) K^\pm$ MC10; Figure 4.7(b) shows the $B^\pm \rightarrow D(K_S^0 \pi^+ \pi^-) K^\pm$ candidate distribution, selected from $B^\pm \rightarrow D(\pi \pi \pi \pi) \pi^\pm$ MC10.

included for this category; it was assumed that any candidates could be included under the same exponential PDF, as previous studies showed this background to be flat in B^\pm mass [79]. The contribution from Category 6 was not included in the fit as the shape of the mass distribution is identical to the decays of interest.

The overall fit expression, \mathcal{F} , was therefore:

$$\begin{aligned}
 \mathcal{F} = & R \cdot N_{B^\pm \rightarrow D\pi^\pm}^{sig,fit} \cdot g_{DK^\pm}^{sig,fit} + N_{B^\pm \rightarrow DK^\pm}^{exp,comb and low-mass} \cdot g_{DK^\pm}^{exp,comb and low-mass} \\
 & + N_{B^\pm \rightarrow DK^\pm}^{low-mass} \cdot g_{DK^\pm}^{low-mass} + N_{B^\pm \rightarrow DK^\pm}^{cross-feed} \cdot g_{DK^\pm}^{cross-feed} \\
 & + N_{B^\pm \rightarrow D\pi^\pm}^{sig,fit} \cdot g_{D\pi^\pm}^{sig,fit} + N_{B^\pm \rightarrow D\pi^\pm}^{exp,comb and low-mass} \cdot g_{D\pi^\pm}^{exp,comb and low-mass} \\
 & + N_{B^\pm \rightarrow D\pi^\pm}^{low-mass a} \cdot g_{D\pi^\pm}^{low-mass a} + N_{B^\pm \rightarrow D\pi^\pm}^{low-mass b} \cdot g_{D\pi^\pm}^{low-mass b} \\
 & + N_{B^\pm \rightarrow D\pi^\pm}^{cross-feed} \cdot g_{D\pi^\pm}^{cross-feed}
 \end{aligned} \tag{4.15}$$

where $N_{B^\pm \rightarrow Dh}^{type}$ is the number of candidates of each *type* of background or signal, g_{Dh}^{type} is the PDF for each *type* and R is the ratio $N_{B^\pm \rightarrow DK^\pm}^{sig,fit} / N_{B^\pm \rightarrow D\pi^\pm}^{sig,fit}$. The sum over the number of candidates of each type is constrained to be equal to the total number of candidates in the data sample, $\sum_{type} N_{B^\pm \rightarrow Dh}^{type} = N_{B^\pm \rightarrow Dh}^{total}$.

The contributing $B^\pm \rightarrow DK^\pm$ PDF components for the signal and each type of background were:

- a Gaussian PDF, $g_{DK}^{sig,fit}$, for the signal and Category 6 background; due to low statistics, it was not necessary to include the Crystal Ball PDF component in order to fit the signal shape in the data;
- an exponential, $g_{DK}^{exp,comb \text{ and } low-mass}$, plus one Gaussian PDF $g_{DK}^{low-mass}$ for the combinatoric and low-mass backgrounds (background Categories 1, 3, 4 and 5); and
- a double Crystal Ball function, $g_{DK}^{cross-feed}$, for the cross-feed ($B^\pm \rightarrow D\pi^\pm$ misidentified as $B^\pm \rightarrow DK^\pm$, background Category 2).

The $B^\pm \rightarrow D\pi^\pm$ PDF components were:

- a Gaussian plus Crystal Ball PDF, $g_{D\pi}^{sig,fit}$, for the signal and Category 6 background, with the yield of candidates under the Crystal Ball PDF compared to the yield under the signal Gaussian fixed to be the same as the proportion from the MC signal fit;
- an exponential, $g_{D\pi}^{exp,comb \text{ and } low-mass}$, plus two Gaussian PDFs, $g_{D\pi}^{low-mass a}$ and $g_{D\pi}^{low-mass b}$, for the combinatoric and low-mass backgrounds (background Categories 1, 3, 4 and 5); and
- a double Crystal Ball function, $g_{D\pi}^{cross-feed}$, for the cross-feed ($B^\pm \rightarrow DK^\pm$ misidentified as $B^\pm \rightarrow D\pi^\pm$, background Category 2).

In total, 18 parameters were left free in the fit:

- the yields of candidates, $N_{B^\pm \rightarrow Dh}^{type}$, for signal $B^\pm \rightarrow D\pi^\pm$ and all backgrounds except for cross-feed (six yields in total);
- the ratio of yields R ;
- the mean and width of the Gaussian part of $g_{D\pi}^{sig,fit}$;
- the width and tail parameters of the Crystal Ball part of $g_{D\pi}^{sig,fit}$;
- the power of the combinatoric/low-mass exponential $g_{D\pi}^{exp,comb \text{ and } low-mass}$; and

- the parameters of the low-mass Gaussians, $g_{D\pi}^{low-mass a}$, $g_{D\pi}^{low-mass b}$ and $g_{DK}^{low-mass}$, except for the mean of $g_{D\pi}^{low-mass b}$.

The remaining parameters were constrained:

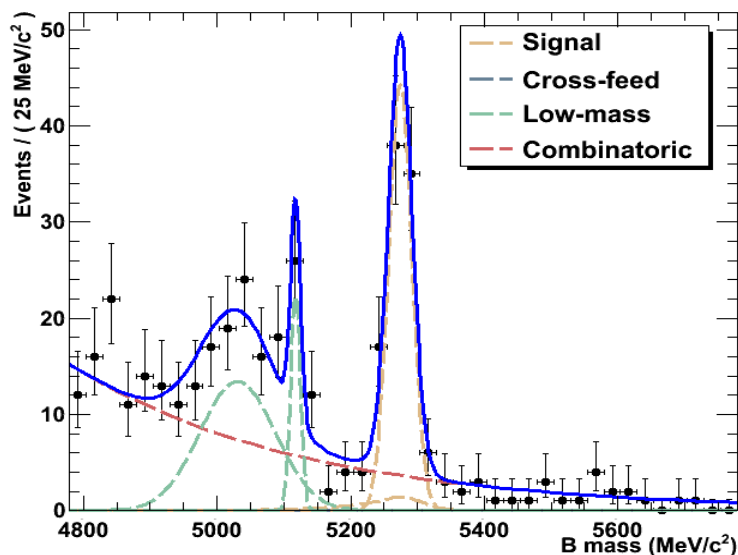
- the yields $N_{B^\pm \rightarrow DK^\pm}^{cross-feed}$ and $N_{B^\pm \rightarrow D\pi^\pm}^{cross-feed}$ were constrained to be greater than zero;
- the mean and width of the Gaussian $g_{DK}^{sig,fit}$ were constrained to be the same as for the $B^\pm \rightarrow D\pi^\pm$ case;
- the mean of the Crystal Ball part of $g_{D\pi}^{sig,fit}$ was constrained to be the same as the mean of the Gaussian part of $g_{D\pi}^{sig,fit}$;
- the power of the combinatoric/low-mass exponential $g_{DK}^{exp,comb and low-mass}$ was constrained to be the same as for the $B^\pm \rightarrow D\pi^\pm$ case;
- the difference in mean mass value of $g_{D\pi}^{low-mass b}$ and $g_{D\pi}^{low-mass a}$ was fixed to be the same as from the fit to the MC shown in Figure 4.4(a); and
- all parameters of the cross-feed double Crystal Ball functions $g_{Dh}^{cross-feed}$ were fixed; excluding the means, the parameters were fixed to values obtained from the fits to MC shown in Figure 4.5. In the data under consideration, a difference between reconstructed candidate masses and global average values from reference [18] was noted. This was due to a combination of detector mis-alignment, inaccuracies in the description of detector material (which affects energy loss) and mis-calibration of the magnetic field [173]. In order to estimate the shifted values of the double Crystal Ball means, an initial fit to the data was performed with the means fixed to the MC fit values. The mean of the signal $B^\pm \rightarrow D\pi^\pm$ Gaussian in data was found; the difference between this value and the global average B^\pm mass was $4.3 \text{ MeV}/c^2$. In the final fit, the double Crystal Ball function mean values were therefore fixed at $4.3 \text{ MeV}/c^2$ below the MC fitted values.

4.3.3 Fit results and ratio of yields

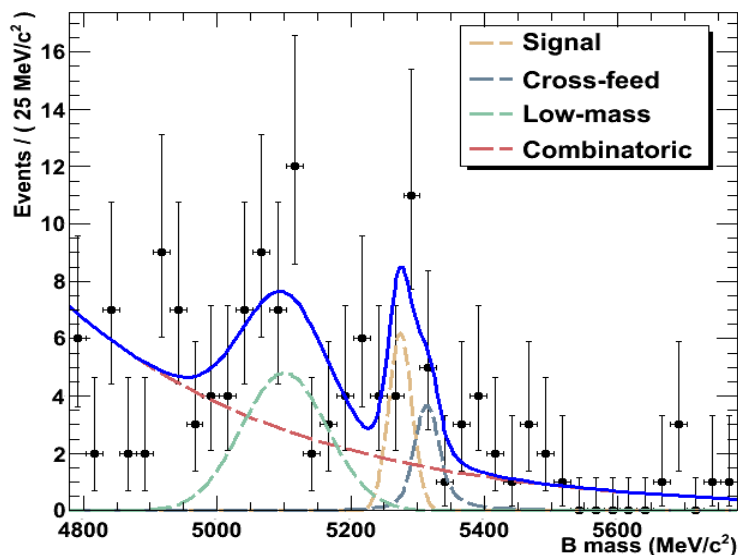
Table 4.2 shows the values of the fitted parameters and Figure 4.8 shows the resulting fits to the B^\pm mass distributions. The total $B^\pm \rightarrow D\pi^\pm$ yield observed in the data was 85_{-13}^{+11} candidates and the ratio of yields from the fit, R , was found to be

$$R = 0.13_{-0.05}^{+0.07}, \quad (4.16)$$

where the errors are statistical only.



(a)



(b)

Figure 4.8: The fitted $B^\pm \rightarrow D(K_S^0 \pi^+ \pi^-)h$ candidate mass distributions from 36.5 pb^{-1} of 2010 data. Figure 4.8(a) shows the fitted $B^\pm \rightarrow D\pi^\pm$ LL distribution and Figure 4.8(b) shows the fitted $B^\pm \rightarrow DK^\pm$ LL distribution. The total summed PDFs are blue.

Parameter	Fitted yield or value
R	$0.13^{+0.07}_{-0.05}$
$N_{B^\pm \rightarrow DK^\pm}^{exp,comb \text{ and low-mass}}$	93 ± 14
$N_{B^\pm \rightarrow DK^\pm}^{low-mass}$	31^{+12}_{-10}
$N_{B^\pm \rightarrow DK^\pm}^{cross-feed}$	8^{+6}_{-5}
$N_{B^\pm \rightarrow D\pi^\pm}^{sig,fit}$	85^{+11}_{-13}
$N_{B^\pm \rightarrow D\pi^\pm}^{exp,comb \text{ and low-mass}}$	200 ± 21
$N_{B^\pm \rightarrow D\pi^\pm}^{low-mass a}$	76^{+19}_{-18}
$N_{B^\pm \rightarrow D\pi^\pm}^{low-mass b}$	17^{+9}_{-6}
$N_{B^\pm \rightarrow D\pi^\pm}^{cross-feed}$	0.2 ± 6.7
$g_{D\pi}^{sig,fit} \text{ CB } \sigma$	$33 \pm 41 \text{ MeV}/c^2$
$g_{D\pi}^{sig,fit} \text{ CB } \alpha$	0.5 ± 0.1
$g_{D\pi}^{sig,fit} \text{ CB } n$	9.5 ± 4.6
$g_{D\pi}^{sig,fit}, g_{DK}^{sig,fit} \mu$	$5274^{+3}_{-2} \text{ MeV}/c^2$
$g_{D\pi}^{sig,fit}, g_{DK}^{sig,fit} \text{ Gaussian } \sigma$	$18 \pm 2 \text{ MeV}/c^2$
$g_{D\pi}^{exp,comb \text{ and low-mass}}, g_{DK}^{exp,comb \text{ and low-mass}} \text{ power}$	$(-2.9 \pm 0.3) \times 10^{-3}$
$g_{DK}^{low-mass} \mu$	$5101 \pm 22 \text{ MeV}/c^2$
$g_{DK}^{low-mass} \sigma$	$64 \pm 22 \text{ MeV}/c^2$
$g_{D\pi}^{low-mass a} \mu$	$5030^{+3}_{-4} \text{ MeV}/c^2$
$g_{D\pi}^{low-mass a} \sigma$	$56^{+15}_{-13} \text{ MeV}/c^2$
$g_{D\pi}^{low-mass b} \mu$	$5117^{+3}_{-4} \text{ MeV}/c^2$
$g_{D\pi}^{low-mass b} \sigma$	$7 \pm 3 \text{ MeV}/c^2$
$g_{DK}^{cross-feed} \alpha$	1.3
$g_{DK}^{cross-feed} \beta$	1.7
$g_{DK}^{cross-feed} \mu$	$5314 \text{ MeV}/c^2$
$g_{DK}^{cross-feed} \sigma$	$19.0 \text{ MeV}/c^2$
$g_{DK}^{cross-feed} l$	2.0
$g_{DK}^{cross-feed} n$	2.4
$g_{D\pi}^{cross-feed} \alpha$	16.7
$g_{D\pi}^{cross-feed} \beta$	19.3
$g_{D\pi}^{cross-feed} \mu$	$5239 \text{ MeV}/c^2$
$g_{D\pi}^{cross-feed} \sigma$	$18.8 \text{ MeV}/c^2$
$g_{D\pi}^{cross-feed} l$	1.1
$g_{D\pi}^{cross-feed} n$	2.8

Table 4.2: The fitted yields and parameter values.

4.4 Determination of efficiencies

In order to extract the ratio of branching fractions $\text{Br}(B^\pm \rightarrow DK^\pm) / \text{Br}(B^\pm \rightarrow D\pi^\pm)$ using Equation 4.12, the efficiencies appearing in Equations 4.13 and 4.14 were calculated, using data for the PID efficiencies and MC10 simulation for the remaining efficiencies.

The acceptance efficiencies, $\epsilon_{B^\pm \rightarrow Dh}^{\text{acceptance}}$, were given by the generator factors (described in Section 3.2) of the respective MC10 signal $B^\pm \rightarrow D(K_S^0 \pi^+ \pi^-)h$ samples. The generator factors shown in Table 4.3 were averaged according to the proportions of data recorded by the experiment in the magnet up and down states,

$$\langle \epsilon_{B^\pm \rightarrow Dh}^{\text{acceptance}} \rangle = \frac{18 \text{ pb}^{-1} \times \epsilon_{B^\pm \rightarrow Dh}^{\text{acceptance, magnet up}}}{36.5 \text{ pb}^{-1}} + \frac{18.5 \text{ pb}^{-1} \times \epsilon_{B^\pm \rightarrow Dh}^{\text{acceptance, magnet down}}}{36.5 \text{ pb}^{-1}}, \quad (4.17)$$

with resulting values

$$\langle \epsilon_{B^\pm \rightarrow DK^\pm}^{\text{acceptance}} \rangle = 0.1665 \pm 0.0001$$

and

$$\langle \epsilon_{B^\pm \rightarrow D\pi^\pm}^{\text{acceptance}} \rangle = 0.1629 \pm 0.0001.$$

The errors on the weighted averages include the statistical effects of the limited MC samples and the uncertainties on the integrated luminosity measurements. The average efficiencies were used in the calculation of the ratio of branching fractions because the low data statistics in the $B^\pm \rightarrow DK^\pm$ channel made it impractical to split the data set into magnet up and magnet down contributions in the mass fit.

MC sample	Generator factor, $\epsilon_{B^\pm \rightarrow Dh}^{\text{acceptance}}$
$B^\pm \rightarrow DK^\pm$ magnet up	0.1663 ± 0.0002
$B^\pm \rightarrow DK^\pm$ magnet down	0.1666 ± 0.0002
$B^\pm \rightarrow D\pi^\pm$ magnet up	0.1627 ± 0.0002
$B^\pm \rightarrow D\pi^\pm$ magnet down	0.1630 ± 0.0002

Table 4.3: The acceptance efficiencies (generator factors) for the signal MC samples.

The combined efficiencies $\epsilon_{B^\pm \rightarrow Dh}^{reco} \cdot \epsilon_{B^\pm \rightarrow Dh}^{trigger} \cdot \epsilon_{B^\pm \rightarrow Dh}^{stripping} \cdot \epsilon_{B^\pm \rightarrow Dh}^{sel,kin}$ in Equations 4.13 and 4.14 were also obtained from the MC10 $B^\pm \rightarrow D(K_S^0 \pi^+ \pi^-)h$ signal samples. $B^\pm \rightarrow D(K_S^0 \pi^+ \pi^-)h$ candidates with LL K_S^0 daughters were reconstructed with DaVinci and the full selection detailed in Section 4.2, including kinematic, stripping and trigger requirements, was applied. It was ensured that the candidates were true signal decays by matching with MC truth information and multiple candidates were removed in the same way as for data. One particular trigger setting was applied to the MC10 simulated events during sample production, with Moore being used to flag each event on the DST as having passed or failed each part of the trigger. The saved flagging information was extracted when the candidates were reconstructed with DaVinci and then used to apply the trigger criteria of Equation 4.6. The trigger setting, known as *0x002e002a*, was used towards the end of the 2010 data-taking period and approximately one fifth of the reconstructed and selected $B^\pm \rightarrow D\pi^\pm$ candidates were from data recorded with this setting in place.

The resulting combined efficiencies are shown in Table 4.4. Weighted average efficiencies, used in the ratio calculation, were calculated in a manner analagous to the acceptance efficiencies (Equation 4.17); values of

$$\langle \epsilon_{B^\pm \rightarrow DK^\pm}^{reco} \epsilon_{B^\pm \rightarrow DK^\pm}^{trigger} \epsilon_{B^\pm \rightarrow DK^\pm}^{stripping} \epsilon_{B^\pm \rightarrow DK^\pm}^{sel,kin} \rangle = (1.01 \pm 0.02) \times 10^{-3}$$

and

$$\langle \epsilon_{B^\pm \rightarrow D\pi^\pm}^{reco} \epsilon_{B^\pm \rightarrow D\pi^\pm}^{trigger} \epsilon_{B^\pm \rightarrow D\pi^\pm}^{stripping} \epsilon_{B^\pm \rightarrow D\pi^\pm}^{sel,kin} \rangle = (1.04 \pm 0.02) \times 10^{-3}$$

were found. Again, the errors on the weighted averages include those coming from the uncertainties on the integrated luminosity measurements as well as the statistical effects of limited MC samples.

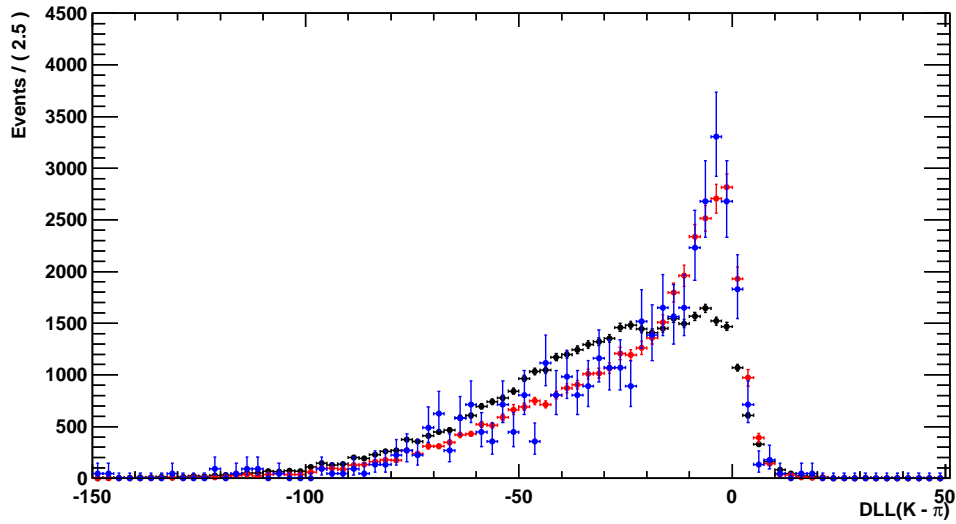
MC sample	$\epsilon_{B^\pm \rightarrow Dh}^{reco} \epsilon_{B^\pm \rightarrow Dh}^{trigger} \epsilon_{B^\pm \rightarrow Dh}^{stripping} \epsilon_{B^\pm \rightarrow Dh}^{sel,kin}$
$B^\pm \rightarrow DK^\pm$ magnet up	$(0.99 \pm 0.03) \times 10^{-3}$
$B^\pm \rightarrow DK^\pm$ magnet down	$(1.02 \pm 0.03) \times 10^{-3}$
$B^\pm \rightarrow D\pi^\pm$ magnet up	$(1.00 \pm 0.03) \times 10^{-3}$
$B^\pm \rightarrow D\pi^\pm$ magnet down	$(1.08 \pm 0.03) \times 10^{-3}$

Table 4.4: The combined reconstruction and selection efficiencies for the signal MC samples.

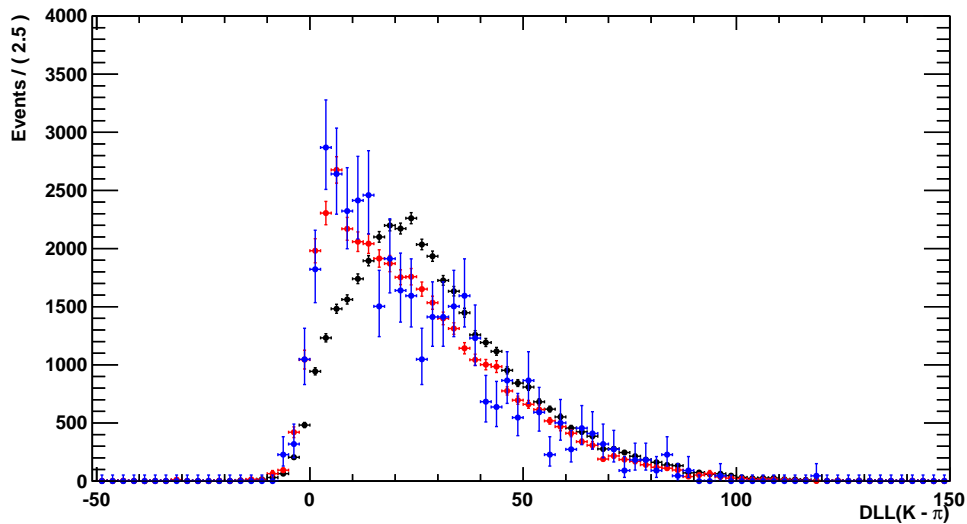
The PID performance was not well-described in the MC10 simulation and so a data-based calibration technique [121] was used to find the efficiencies of the PID selection requirements on the bachelor tracks. Large, high purity calibration samples of pions and kaons from prompt $D^*(2010)^\pm \rightarrow D(K\pi)\pi^\pm$ decays were available, reconstructed and selected from 2010 data without the use of PID information. The samples covered a wide range of track momentum, pseudo-rapidity and number of tracks per event; it is expected that the performance of the PID should principally depend on these variables. In order to emulate the PID performance for the signal decay bachelor tracks in data, the calibration samples were weighted according to the kinematic distributions of the bachelor tracks from selected $B^\pm \rightarrow D(K_S^0\pi^+\pi^-)h$ candidates in the signal MC, using a binning scheme of $18 \times 4 \times 4$ bins in momentum, pseudo-rapidity and number of tracks, respectively. MC was used to provide the kinematic distributions because there were too few $B^\pm \rightarrow Dh$ candidates from 2010 data to provide sufficient statistics in each bin of the weighting scheme.

If the kinematic variables used in the weighting perfectly describe the PID performance, the $\Delta LL(K - \pi)$ distributions of the weighted calibration sample should match that of the signal. The method was verified using calibration samples obtained from MC10 D^* decays, weighted in the same way as the 2010 data calibration samples. The unweighted and weighted MC calibration and signal distributions for positively charged pions and kaons are shown in Figure 4.9, with the signal samples taken from the bachelor tracks of selected $B^+ \rightarrow D(K_S^0\pi^+\pi^-)h^+$ candidates in magnet up signal MC. It can be seen that the agreement between the weighted (red) and signal (blue) distributions is good.

The efficiencies of the bachelor PID requirements found from the weighted data calibration sample are shown in Table 4.5, where the quoted errors are statistical. The kaon $\Delta LL(K - \pi) > 0.0$ criterion efficiency was found by applying this criterion to the calibration kaon sample after it had been weighted according to the kinematics of the MC signal $B^\pm \rightarrow DK^\pm$ bachelor. The pion $\Delta LL(K - \pi) < 0.0$ criterion efficiency was found by applying this criterion to the calibration pion sample after it had been weighted according to the kinematics of the MC signal $B^\pm \rightarrow D\pi^\pm$ bachelor. The available data calibration sample was a mixture of magnet up and down events containing both positively and negatively charged pion and kaon tracks. The weighting was performed with magnet up signal MC samples, as in MC the decay kinematics should be independent of the magnet polarity. It was found that the resulting PID efficiency values were consistent between the positively and negatively charged track cases. The efficiencies shown in the table



(a)



(b)

Figure 4.9: The verification of the PID weighting technique with MC. The unweighted calibration samples are shown in black, the weighted calibration samples in red and the signal samples in blue; Figure 4.9(a) shows the distributions for π^+ and Figure 4.9(b) shows the distributions for K^+ .

and used in further calculations are those for K^+/π^+ weighted by magnet up signal MC,

$$\epsilon_{B^\pm \rightarrow DK^\pm}^{sel,PID} = 0.9222 \pm 0.0008$$

and

$$\epsilon_{B^\pm \rightarrow D\pi^\pm}^{sel,PID} = 0.870 \pm 0.001.$$

MC weighting sample	$\epsilon_{B^\pm \rightarrow Dh}^{sel,PID}$
$B^\pm \rightarrow DK^\pm$ bachelor, magnet up, kaon $\Delta LL(K - \pi) > 0.0$	0.9222 ± 0.0008
$B^\pm \rightarrow D\pi^\pm$ bachelor, magnet up, pion $\Delta LL(K - \pi) < 0.0$	0.870 ± 0.001

Table 4.5: The PID requirement efficiencies for the weighted data calibration samples.

4.5 Evaluation of the ratio of branching fractions

The ratio of branching fractions was calculated, according to Equation 4.12. The yield ratio from the mass fit ($R = 0.13_{-0.05}^{+0.07}$), the correction factors for $B^\pm \rightarrow D(\pi\pi\pi\pi)h$ decays ($F_{DK} = 0.26$ and $F_{D\pi} = 0.25$) and the efficiencies from Section 4.4 were used to give the result

$$\begin{aligned} \frac{\text{Br}(B^\pm \rightarrow DK^\pm)}{\text{Br}(B^\pm \rightarrow D\pi^\pm)} &= R \cdot \frac{(1 + F_{D\pi})}{(1 + F_{DK})} \cdot \frac{\langle \epsilon_{B^\pm \rightarrow D\pi^\pm}^{acceptance} \rangle}{\langle \epsilon_{B^\pm \rightarrow DK^\pm}^{acceptance} \rangle} \\ &\quad \cdot \frac{\langle \epsilon_{B^\pm \rightarrow D\pi^\pm}^{reco} \epsilon_{B^\pm \rightarrow D\pi^\pm}^{trigger} \epsilon_{B^\pm \rightarrow D\pi^\pm}^{stripping} \epsilon_{B^\pm \rightarrow D\pi^\pm}^{sel,kin} \rangle}{\langle \epsilon_{B^\pm \rightarrow DK^\pm}^{reco} \epsilon_{B^\pm \rightarrow DK^\pm}^{trigger} \epsilon_{B^\pm \rightarrow DK^\pm}^{stripping} \epsilon_{B^\pm \rightarrow DK^\pm}^{sel,kin} \rangle} \cdot \frac{\epsilon_{B^\pm \rightarrow D\pi^\pm}^{sel,PID}}{\epsilon_{B^\pm \rightarrow DK^\pm}^{sel,PID}} \\ &= 0.12_{-0.05}^{+0.06} \end{aligned} \quad (4.18)$$

where the errors are statistical only, coming from the errors on R .

4.6 Systematic uncertainties

The measurement of the ratio of branching fractions for the two channels is advantageous as many systematic effects cancel due to their similar topologies. Certain systematic

errors on the ratio still need to be taken into account, however, including those related to:

1. the measurement of the accumulated integrated luminosity of data (10% uncertainty on the measurements);
2. the limited MC statistics for calculating the acceptance efficiencies (generator factor);
3. the limited MC statistics for calculating the reconstruction and selection efficiencies;
4. the limited data statistics for calculating the PID efficiencies;
5. the estimate of the relative levels of Category 6 $B^\pm \rightarrow D(\pi\pi\pi\pi)h$ background (limited MC statistics and global average branching fractions from reference [18]);
6. the use of a single trigger setting to estimate all trigger efficiencies;
7. the PID weighting technique; and
8. the PDF parameterisation used in the mass fit.

In order to evaluate the systematic errors 1 – 6 listed above, a toy MC study was performed. This was necessary as various luminosity-weighted average efficiencies were used to find the ratio $\frac{(1 + F_{D\pi})}{(1 + F_{DK})} \cdot \frac{\epsilon_{B^\pm \rightarrow D\pi^\pm}}{\epsilon_{B^\pm \rightarrow DK^\pm}}$ of Equation 4.12, leading to correlated errors between the different components. For each of the independently evaluated components under consideration, a Gaussian distribution with mean equal to the central value and σ equal to the error was randomly sampled. The ratio $\frac{(1 + F_{D\pi})}{(1 + F_{DK})} \cdot \frac{\epsilon_{B^\pm \rightarrow D\pi^\pm}}{\epsilon_{B^\pm \rightarrow DK^\pm}}$, expressed in terms of the independent components, was then calculated from the sampled values. This was repeated 1M times in order to create a distribution for the ratio; the distribution was fitted with a Gaussian PDF and the fitted value of the Gaussian σ was taken to be the error on the ratio.

Each of the systematic uncertainties will now be discussed in order.

4.6.1 Systematic error from integrated luminosity measurements and statistical errors

The error on the ratio $\frac{(1 + F_{D\pi})}{(1 + F_{DK})} \cdot \frac{\epsilon_{B^\pm \rightarrow D\pi^\pm}}{\epsilon_{B^\pm \rightarrow DK^\pm}}$ from Equation 4.12, due to the uncertainties on the integrated luminosity measurements and the statistical errors on acceptance, reconstruction, trigger, stripping, kinematic selection and PID efficiencies, was found. Gaussian distributions for each of these components were simultaneously randomly sampled with the global average branching fractions fixed. The resulting ratio distribution can be seen in Figure 4.10; the error is 0.02 and the fractional error on the ratio is 0.03.

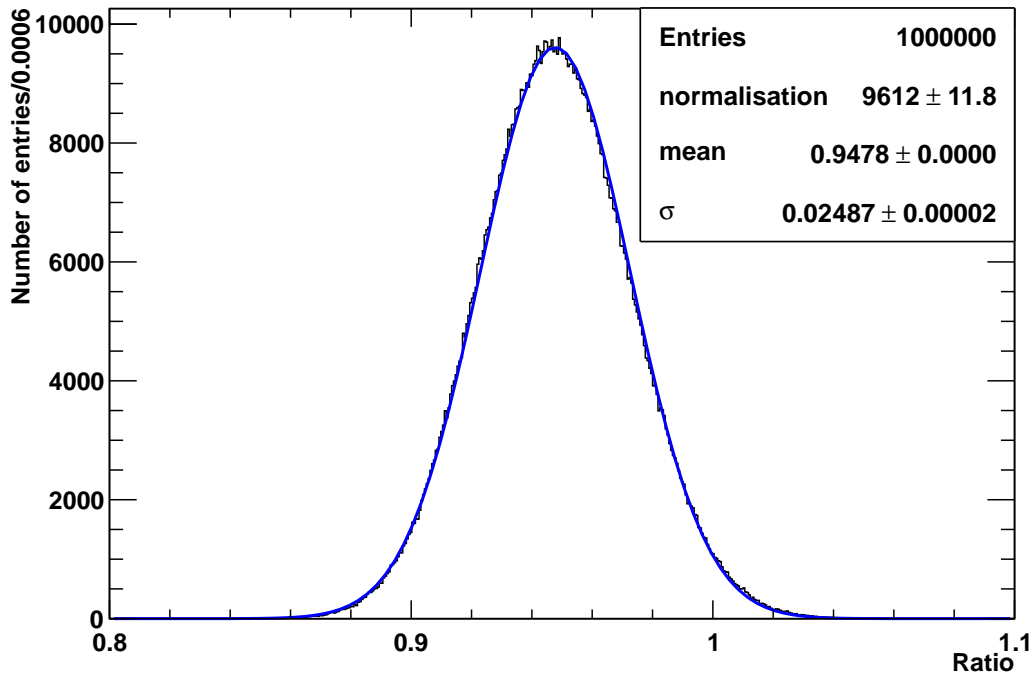


Figure 4.10: The toy MC distribution for the ratio $\frac{(1 + F_{D\pi})}{(1 + F_{DK})} \cdot \frac{\epsilon_{B^\pm \rightarrow D\pi^\pm}}{\epsilon_{B^\pm \rightarrow DK^\pm}}$, accounting for luminosity and statistical errors. The black histogram is the toy MC distribution and the blue Gaussian is fitted to this distribution.

4.6.2 Systematic error from global average branching fraction errors

The error on the ratio $\frac{(1 + F_{D\pi})}{(1 + F_{DK})} \cdot \frac{\epsilon_{B^\pm \rightarrow D\pi^\pm}}{\epsilon_{B^\pm \rightarrow DK^\pm}}$ from Equation 4.12, due to errors from the global average branching fractions, was found. Gaussian distributions for the branching fraction values were randomly sampled and the integrated luminosity measurements and the efficiencies were all fixed. The resulting ratio distribution can be seen in Figure 4.11; the error is 0.0004 and the fractional error on the ratio is also 0.0004.

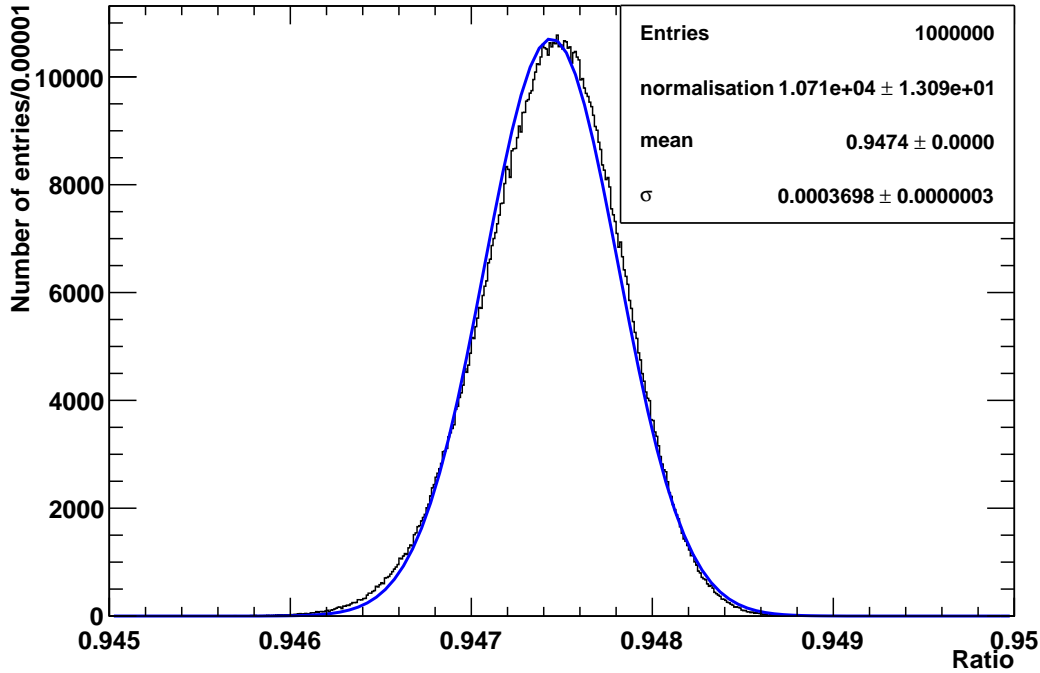


Figure 4.11: The toy MC distribution for the ratio $\frac{(1 + F_{D\pi})}{(1 + F_{DK})} \cdot \frac{\epsilon_{B^\pm \rightarrow D\pi^\pm}}{\epsilon_{B^\pm \rightarrow DK^\pm}}$, accounting for errors on the global average branching fractions. The black histogram is the toy MC distribution and the blue Gaussian is fitted to this distribution.

4.6.3 Systematic error from estimation of the trigger efficiency

As described in Section 4.4, one trigger setting (*0x002e002a*) was used to evaluate the overall efficiency of the trigger from MC. The data used in this analysis, however, were

taken with many different settings. By definition, events passing in the category TIS will have a ratio of efficiencies $\epsilon_{B^\pm \rightarrow D\pi^\pm}^{trigger} / \epsilon_{B^\pm \rightarrow DK^\pm}^{trigger}$ which will not be affected by the changes in trigger setting. TOS events are affected, however, with the potential source of differences in the ratio due to the various 2010 settings being dominated by differences in the L0 Hadron trigger transverse energy threshold. This is because the decays $B^\pm \rightarrow D\pi^\pm$ and $B^\pm \rightarrow DK^\pm$ should be kinematically and topologically very similar, but there are expected to be small differences in the momentum spectra of the bachelor hadrons in the two cases.

Table 4.6 shows the effect on the ratio $\frac{\epsilon_{B^\pm \rightarrow D\pi^\pm}^{reco} \epsilon_{B^\pm \rightarrow D\pi^\pm}^{trigger} \epsilon_{B^\pm \rightarrow D\pi^\pm}^{stripping} \epsilon_{B^\pm \rightarrow D\pi^\pm}^{sel,kin}}{\epsilon_{B^\pm \rightarrow DK^\pm}^{reco} \epsilon_{B^\pm \rightarrow DK^\pm}^{trigger} \epsilon_{B^\pm \rightarrow DK^\pm}^{stripping} \epsilon_{B^\pm \rightarrow DK^\pm}^{sel,kin}}$ of changing the p_T requirement, equivalent to the nominal level of the L0 Hadron threshold, for three of the 2010 trigger settings. Approximately 10% of the reconstructed and selected $B^\pm \rightarrow D\pi^\pm$ candidates were from data recorded with the setting *0x001e0030* and a similar proportion were from events with setting *0x0019001f*. The considered settings were chosen as they were indicative of the variations in L0 Hadron threshold affecting the majority of reconstructed and selected B^\pm candidates. Magnet up and down MC signal $B^\pm \rightarrow D(K_S^0 \pi^+ \pi^-)h$ candidates were studied in order to evaluate the combined efficiencies for each setting, with the requirement that the candidates had passed all of the selection steps. The trigger selection requirement of Equation 4.6 was, however, changed to

$$\begin{aligned} & ((\text{Track } p_T > \text{threshold value}) \text{ OR } (\text{L0 Global TIS})) \text{ AND} \\ & ((\text{HLT1 1Track TOS}) \text{ OR } (\text{HLT1 Global TIS})) \text{ AND} \\ & ((\text{HLT2 Topological 2-body TOS}) \text{ OR } (\text{HLT2 Topological 3-body TOS}) \text{ OR } (\text{HLT2 Global TIS})) \end{aligned} \quad (4.19)$$

so that the L0 Hadron TOS decision was replaced with a requirement that at least one of the pion or kaon final state tracks from the B^\pm candidate had p_T greater than a given threshold value. The ratio of integrated luminosity weighted average efficiencies was then found, as detailed in Section 4.4.

It has also been shown [174] that the L0 Hadron trigger was not well-calibrated in 2010; the transverse energy measured at L0 in the calorimeters was approximately 14% smaller than the energy measured in the tracking system. A nominal L0 Hadron threshold therefore corresponded to an actual higher threshold being applied to the tracks, for example a nominal $E_T > 3.6$ GeV threshold in the trigger (*0x002e002a*) meant a real E_T threshold of 4.2 GeV. Table 4.6 also shows the effect of these increases

in threshold. It can be seen that in all cases the change in the ratio from the value obtained using the trigger setting *0x002e002a* is $< 2\%$.

E_T threshold	$\frac{\epsilon_{B^\pm \rightarrow D\pi^\pm}^{reco} \cdot \epsilon_{B^\pm \rightarrow D\pi^\pm}^{trigger} \cdot \epsilon_{B^\pm \rightarrow D\pi^\pm}^{stripping} \cdot \epsilon_{B^\pm \rightarrow D\pi^\pm}^{sel,kin}}{\epsilon_{B^\pm \rightarrow DK^\pm}^{reco} \cdot \epsilon_{B^\pm \rightarrow DK^\pm}^{trigger} \cdot \epsilon_{B^\pm \rightarrow DK^\pm}^{stripping} \cdot \epsilon_{B^\pm \rightarrow DK^\pm}^{sel,kin}}$
$E_T > 3.6$ GeV (nominal, <i>0x002e002a</i>)	1.0223
$E_T > 4.2$ GeV (corrected, <i>0x002e002a</i>)	1.0184
$E_T > 2.6$ GeV (nominal, <i>0x001e0030</i>)	1.0339
$E_T > 3.06$ GeV (corrected, <i>0x001e0030</i>)	1.0336
$E_T > 2.26$ GeV (nominal, <i>0x0019001f</i>)	1.0372
$E_T > 2.65$ GeV (corrected, <i>0x0019001f</i>)	1.0336
Full trigger <i>0x002e002a</i> (for reference)	1.0350

Table 4.6: The effect of different L0 Hadron transverse energy thresholds on the combined reconstruction and selection efficiency ratio for the signal MC samples.

To estimate the uncertainty due to the use of a single trigger setting, the ratio $\frac{(1 + F_{D\pi})}{(1 + F_{DK})} \cdot \frac{\epsilon_{B^\pm \rightarrow D\pi^\pm}}{\epsilon_{B^\pm \rightarrow DK^\pm}}$ was expressed with the efficiency ratio $\frac{\epsilon_{B^\pm \rightarrow D\pi^\pm}^{reco} \cdot \epsilon_{B^\pm \rightarrow D\pi^\pm}^{trigger} \cdot \epsilon_{B^\pm \rightarrow D\pi^\pm}^{stripping} \cdot \epsilon_{B^\pm \rightarrow D\pi^\pm}^{sel,kin}}{\epsilon_{B^\pm \rightarrow DK^\pm}^{reco} \cdot \epsilon_{B^\pm \rightarrow DK^\pm}^{trigger} \cdot \epsilon_{B^\pm \rightarrow DK^\pm}^{stripping} \cdot \epsilon_{B^\pm \rightarrow DK^\pm}^{sel,kin}}$ represented as a single number rather than the combination of its component values. The toy MC method was then used, with a Gaussian distribution randomly sampled for the efficiency ratio only and all other measurements fixed. The Gaussian mean was set to be equal to the value obtained using trigger *0x002e002a* (last entry in Table 4.6) and the σ (0.017) to be the largest difference between the emulated values shown in Table 4.6 and the *0x002e002a* value. The resulting distribution for the ratio $\frac{(1 + F_{D\pi})}{(1 + F_{DK})} \cdot \frac{\epsilon_{B^\pm \rightarrow D\pi^\pm}}{\epsilon_{B^\pm \rightarrow DK^\pm}}$ from Equation 4.12 is shown in Figure 4.12; the error is 0.02 and the fractional error on the ratio is 0.02.

4.6.4 Systematic error from the determination of the PID efficiency

The statistical errors from the data samples used in the PID weighting technique were included in the toy MC error estimation described in Section 4.6.1. A further systematic uncertainty due to the PID weighting technique was estimated. A value for each of the

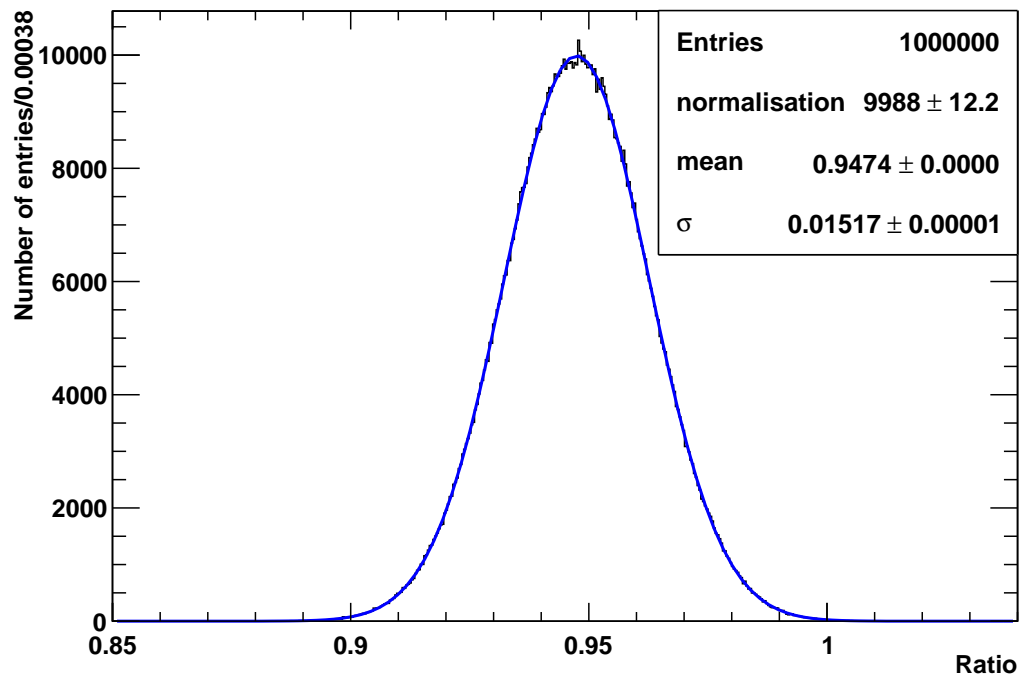


Figure 4.12: The toy MC distribution for the ratio $\frac{(1 + F_{D\pi})}{(1 + F_{DK})} \cdot \frac{\epsilon_{B^\pm \rightarrow D\pi^\pm}}{\epsilon_{B^\pm \rightarrow DK^\pm}}$, accounting for the error from estimation of the trigger efficiency.

PID requirement efficiencies was found from the unweighted data D^* decay calibration samples. The difference between the efficiency from the unweighted data and the efficiency from the weighted data was taken as a conservative estimate of the error on the efficiency from the weighted data. As the error was only estimated on one side of the weighted efficiency values, a half-normal distribution was assumed. The full error for each of the efficiencies was the σ of this distribution, equal to $\sqrt{(1 - \frac{2}{\pi})} \cdot \Delta\epsilon$, where $\Delta\epsilon$ is the difference between the weighted and unweighted efficiency values^a. Combining these full errors in quadrature gave a fractional error on the original efficiency ratio of

$$\frac{\sigma \left(\epsilon_{B^\pm \rightarrow D\pi^\pm}^{sel,PID} / \epsilon_{B^\pm \rightarrow DK^\pm}^{sel,PID} \right)}{\left(\epsilon_{B^\pm \rightarrow D\pi^\pm}^{sel,PID} / \epsilon_{B^\pm \rightarrow DK^\pm}^{sel,PID} \right)} = 0.03. \quad (4.20)$$

4.6.5 Systematic error from the mass fit PDF parameterisation

There were several possible sources of systematic error coming from the mass fit used to extract the yield ratio R , which is described in Section 4.3.

Signal Crystal Ball lineshape in $B^\pm \rightarrow D\pi^\pm$ fit

In the nominal fit, a Gaussian and a Crystal Ball PDF were used to describe the shape of the signal $B^\pm \rightarrow D\pi^\pm$ mass peak, with the yield of candidates in the Crystal Ball fixed to be a certain proportion of the yield of candidates in the Gaussian. In order to conservatively estimate a systematic error due to this, the Crystal Ball component was

^aIf x is a normally distributed variable with standard deviation σ , the half-normal distribution for $y = |x|$ is

$$P(y) = \frac{\sqrt{2}}{\sigma\sqrt{\pi}} \exp\left(-\frac{y^2}{2\sigma^2}\right)$$

so that

$$\begin{aligned} \text{Variance} &= \langle y^2 \rangle - \langle y \rangle^2 \\ &= \sigma^2 \left(1 - \frac{2}{\pi}\right). \end{aligned}$$

removed completely. This led to a fractional error on the original yield ratio of

$$\frac{\sigma(R)}{R} = 0.06. \quad (4.21)$$

Low-mass Gaussian description in $B^\pm \rightarrow D\pi^\pm$ fit

In the nominal fit, two Gaussian PDFs were used to describe the shape of the $B^\pm \rightarrow D\pi^\pm$ partially reconstructed background mass distribution in the region 5000 to 5150 MeV/ c^2 . If the two Gaussians were replaced with one, broader Gaussian, the yield ratio changed, giving a fractional error on the original yield ratio of

$$\frac{\sigma(R)}{R} = 0.009. \quad (4.22)$$

Exponential PDFs (combinatoric and low-mass backgrounds) in $B^\pm \rightarrow D\pi^\pm$ and $B^\pm \rightarrow DK^\pm$ fits

In both the $B^\pm \rightarrow D\pi^\pm$ and $B^\pm \rightarrow DK^\pm$ nominal fits, the combinatoric background and part of the low-mass background were described using exponential PDFs. Changing these to linear PDFs [175] in both cases, with the PDFs constrained to have the same gradient in both $B^\pm \rightarrow D\pi^\pm$ and $B^\pm \rightarrow DK^\pm$, gave a fractional error on the original yield ratio of

$$\frac{\sigma(R)}{R} = 0.02. \quad (4.23)$$

Cross-feed in $B^\pm \rightarrow D\pi^\pm$ and $B^\pm \rightarrow DK^\pm$ fits

Double Crystal Ball PDFs were used in both nominal fits to describe the cross-feed distributions; uncertainties from the cross-feed yields and the fixed cross-feed lineshapes were estimated.

In the $B^\pm \rightarrow D\pi^\pm$ case the fitted cross-feed yield was less than one candidate, but in the $B^\pm \rightarrow DK^\pm$ case the fitted yield was 8_{-5}^{+6} candidates. An estimate was made of the efficiency of selecting $B^\pm \rightarrow D(K_S^0\pi^+\pi^-)\pi^\pm$ as $B^\pm \rightarrow D(K_S^0\pi^+\pi^-)K^\pm$ and vice versa, using each selection (including PID criteria) to find candidates from the magnet up and down MC10 signal samples of the other decay; estimates were also made of the

signal efficiencies using the $B^\pm \rightarrow D(K_S^0\pi^+\pi^-)\pi^\pm$ and $B^\pm \rightarrow D(K_S^0\pi^+\pi^-)K^\pm$ selections (including PID criteria) on their respective MC samples. The efficiencies were then used to calculate expected yields in 36.5 pb^{-1} of data, using a $b\bar{b}$ cross-section of $284 \mu\text{b}$ [102]. The expected yields and the corresponding yields from the fit to 2010 data are shown in Table 4.7. It should be noted that the fitted yields contain contamination from $B^\pm \rightarrow D(\pi\pi\pi\pi)h$ decays at a level of approximately 20%. It can be seen that the fitted signal $B^\pm \rightarrow D(K_S^0\pi^+\pi^-)\pi^\pm$ yield was therefore approximately 55% of the expected yield; it was assumed that the $B^\pm \rightarrow D\pi^\pm$ yield was the best known of the four fitted yields. An attempt was made to quantify the cross-feed yield error by forcing a decrease and increase in the cross-feed yields. In the $B^\pm \rightarrow DK^\pm$ fit the cross-feed yield was changed by $\pm 90\%$ and rounding to the nearest integer; at the same time the cross-feed yield in the $B^\pm \rightarrow D\pi^\pm$ fit was changed by $\pm 90\%$ and rounded to one significant figure. The cross-feed yields were therefore initially forced to be 0.02 in the $B^\pm \rightarrow D\pi^\pm$ fit and 1 in the $B^\pm \rightarrow DK^\pm$ fit; the fit was then repeated with the cross-feed yields set as 0.4 and 15, respectively. The change in yield ratio from both fits gave the same fractional error on the yield ratio of

$$\frac{\sigma(R)}{R} = 0.2. \quad (4.24)$$

Category	Expected $B^\pm \rightarrow D(K_S^0\pi\pi)h$ yield	Fitted $B^\pm \rightarrow Dh$ yield	Approximate fitted $B^\pm \rightarrow D(K_S^0\pi\pi)h$ yield
$B^\pm \rightarrow DK^\pm$ signal	9.6 ± 0.4	11_{-5}^{+6}	9
$B^\pm \rightarrow DK^\pm$ cross-feed (really $D\pi^\pm$)	10 ± 1	8_{-5}^{+6}	6
$B^\pm \rightarrow D\pi^\pm$ signal	122 ± 5	85_{-13}^{+11}	68
$B^\pm \rightarrow D\pi^\pm$ cross-feed (really DK^\pm)	0.39 ± 0.07	0.2 ± 6.7	0.16

Table 4.7: The signal and cross-feed expected 36.5 pb^{-1} and fitted yields. Errors on the expected yields are statistical only.

In the fit, the cross-feed double Crystal Ball lineshape parameters were fixed, with all of the parameters except the means fixed to values obtained from fits to MC. The means were shifted with respect to the MC fitted values. In order to estimate a systematic

uncertainty due to this fixing, the σ s of both double Crystal Balls were increased. The Gaussian σ from the signal fit to $B^\pm \rightarrow D\pi^\pm$ MC is $(16.5 \pm 0.3) \text{ MeV}/c^2$; the value from the fit to data is $(18 \pm 2) \text{ MeV}/c^2$ (Table 4.2). The σ s of the cross-feed double Crystal Ball functions were therefore both increased by 9% to find the uncertainty due to the fixing of the cross-feed shape, giving a change in the fitted yield ratio and a fractional error on the original yield ratio of

$$\frac{\sigma(R)}{R} = 0.04. \quad (4.25)$$

4.6.6 Total systematic uncertainty

The contributing uncertainties, estimated as detailed above, are summarised in Table 4.8. Each of the quoted values in the table is a fractional error on the ratio of interest; for example the mass fit uncertainties are of the form $\frac{\sigma(R)}{R}$. The values were combined in quadrature to obtain the overall fractional error. The systematic uncertainty of ± 0.03 on the central value of the ratio of branching fractions was obtained by multiplying the central value by the overall fractional error.

Source of uncertainty	$\sigma(\text{ratio})/\text{ratio}$
Toy MC: integrated luminosity, efficiency statistical errors	0.03
Toy MC: global average branching fractions	0.0004
Use of single trigger setting	0.02
PID weighting, systematic	0.03
Mass fit signal Crystal Ball PDF ($B^\pm \rightarrow D\pi^\pm$)	0.06
Mass fit low-mass background Gaussian PDFs ($B^\pm \rightarrow D\pi^\pm$)	0.009
Mass fit exponential PDFs ($B^\pm \rightarrow D\pi^\pm$ and $B^\pm \rightarrow DK^\pm$)	0.02
Mass fit cross-feed yields ($B^\pm \rightarrow D\pi^\pm$ and $B^\pm \rightarrow DK^\pm$)	0.2
Mass fit cross-feed σ s ($B^\pm \rightarrow D\pi^\pm$ and $B^\pm \rightarrow DK^\pm$)	0.04
Total fractional error = $\sqrt{\sum (\sigma(\text{ratio})/\text{ratio})^2}$	0.2

Table 4.8: A summary of the systematic errors.

4.7 Summary

The ratio of branching fractions $\text{Br}(B^\pm \rightarrow DK^\pm) / \text{Br}(B^\pm \rightarrow D\pi^\pm)$ has been determined using $B^\pm \rightarrow D(K_S^0\pi^+\pi^-)K^\pm$ and $B^\pm \rightarrow D(K_S^0\pi^+\pi^-)\pi^\pm$ decays in approximately 36.5 pb^{-1} of $\sqrt{s} = 7 \text{ TeV}$ data collected in 2010 at LHCb. The resulting value,

$$\frac{\text{Br}(B^\pm \rightarrow DK^\pm)}{\text{Br}(B^\pm \rightarrow D\pi^\pm)} = 0.12_{-0.05}^{+0.06} \pm 0.03, \quad (4.26)$$

is consistent with previous measurements of the ratio using two and four-body charged track D decays and provides a useful cross-check of the first candidates reconstructed from data recorded by LHCb.

Chapter 5

A measurement of the ratio of branching fractions $\text{Br}(B^\pm \rightarrow DK^\pm) / \text{Br}(B^\pm \rightarrow D\pi^\pm)$ using 2011 data

This chapter describes a measurement of the ratio of branching fractions $\text{Br}(B^\pm \rightarrow DK^\pm) / \text{Br}(B^\pm \rightarrow D\pi^\pm)$ using $(342 \pm 9) \text{ pb}^{-1}$ of $\sqrt{s} = 7 \text{ TeV}$ data collected at LHCb in 2011 and the decays $B^\pm \rightarrow D(K_S^0 \pi^+ \pi^-) K^\pm$ and $B^\pm \rightarrow D(K_S^0 \pi^+ \pi^-) \pi^\pm$. The larger data set allows a more statistically accurate evaluation of the ratio than that described in Chapter 4. The expression used to find the ratio of branching fractions is identical to that given in Equation 4.2. Section 5.1 describes the candidate selection and Section 5.2 details the mass fit to data. This mass fit includes a more detailed description of the low-mass background contributions than the fit used in Chapter 4. Section 5.3 details the evaluation of the efficiencies needed to calculate the branching fraction ratio, with the efficiencies being found for three trigger settings which accounted for approximately 95% of the data events containing selected candidates. Section 5.4 contains the evaluation of the ratio of branching fractions, Section 5.5 summarises the systematic uncertainties on the ratio measurement and the final result is given in Section 5.6.

5.1 Decay selection criteria

In the first half of 2011, data corresponding to an integrated luminosity of $(143 \pm 5) \text{ pb}^{-1}$ were recorded in the dipole magnet up field configuration and $(199 \pm 7) \text{ pb}^{-1}$ were

recorded in the magnet down configuration at LHCb. The data were again processed as detailed in Chapter 2. The selection criteria shown in Table 5.1 were applied at the central stripping stage and the selected $B^\pm \rightarrow D(K_S^0\pi^+\pi^-)K^\pm$ and $B^\pm \rightarrow D(K_S^0\pi^+\pi^-)\pi^\pm$ LL and DD candidates were saved to the centrally stored DSTs. The stripping criteria were slightly different to those used in 2010 data-taking, with the majority of the criteria changed to be equal to those of the optimised selection detailed in Chapter 3. The mass windows remained larger than the optimised selection and additional requirements on track momentum and track fit quality (track $\chi^2/\text{d.o.f.}$) were applied in the same way as for the 2010 data set. The 2010 requirement of fewer than 240 reconstructed tracks per event was replaced by a requirement of fewer than 180 long type tracks per event. The stripping criteria were changed with respect to those described in Chapter 4 in order to meet LHCb-wide constraints on the number of fully reconstructed events in the stored data sets.

Particle	LL candidate criteria	DD candidate criteria
K_S^0 daughter π	- IP χ^2 (PV) > 9.0 $p > 2.0$ GeV/c $p < 100.0$ GeV/c track $\chi^2/\text{d.o.f.} < 5.0$	$\Delta LL(\pi - K) > 0.0$ IP χ^2 (PV) > 6.25 $p > 2.0$ GeV/c $p < 100.0$ GeV/c track $\chi^2/\text{d.o.f.} < 10.0$
K_S^0	$ \text{mass} - 497.61 < 30.0$ MeV/c ² vertex $\chi^2/\text{d.o.f.} < 16.0$ FD χ^2 (PV) > 4.0	$ \text{mass} - 497.61 < 42.0$ MeV/c ² vertex $\chi^2/\text{d.o.f.} < 16.0$ FD χ^2 (PV) > 4.0
D daughter π	IP χ^2 (PV) > 16.0 $p > 2.0$ GeV/c $p < 100.0$ GeV/c track $\chi^2/\text{d.o.f.} < 5.0$	IP χ^2 (PV) > 9.0 $p > 2.0$ GeV/c $p < 100.0$ GeV/c track $\chi^2/\text{d.o.f.} < 5.0$
D	$ \text{mass} - 1864.8 < 50.0$ MeV/c ² vertex $\chi^2/\text{d.o.f.} < 4.0$	$ \text{mass} - 1864.8 < 60.0$ MeV/c ² vertex $\chi^2/\text{d.o.f.} < 16.0$
Bachelor K^\pm or π^\pm	IP χ^2 (PV) > 16.0 $p > 2.0$ GeV/c $p < 100.0$ GeV/c $p_T > 1.0$ GeV/c track $\chi^2/\text{d.o.f.} < 5.0$	IP χ^2 (PV) > 6.25 $p > 2.0$ GeV/c $p < 100.0$ GeV/c $p_T > 500.0$ MeV/c track $\chi^2/\text{d.o.f.} < 5.0$
B^\pm	$ \text{mass} - 5279.2 < 500.0$ MeV/c ² FD χ^2 (PV) > 169.0 vertex $\chi^2/\text{d.o.f.} < 6.25$ IP χ^2 (PV) < 9.0 DIRA > 0.99999	$ \text{mass} - 5279.2 < 500.0$ MeV/c ² FD χ^2 (PV) > 100.0 vertex $\chi^2/\text{d.o.f.} < 9.0$ IP χ^2 (PV) < 16.0 DIRA > 0.9999
-	Number of long tracks in event < 180	Number of long tracks in event < 180

Table 5.1: The stripping selections for LL and DD B^\pm candidates in 2011 data.

Further selection criteria were applied to the candidates using DaVinci; the overall selection criteria were almost identical to the optimised selections shown in Tables 3.5 and 3.6. In summary, the differences to the optimised criteria were similar to those described in Section 4.2:

- an additional requirement of fewer than 180 long tracks per event;
- a momentum requirement of $p > 2.0 \text{ GeV}/c$ applied to all pions and kaons;
- requirements of track $\chi^2/\text{d.o.f.} < 5.0$ on long tracks and track $\chi^2/\text{d.o.f.} < 10.0$ on downstream tracks;
- the PID requirements on the bachelor pion and kaon were replaced with $\Delta LL(K - \pi) < 0.0$ and $\Delta LL(K - \pi) > 0.0$, respectively. No $\Delta LL(K - p)$ requirements were made; and
- B^\pm candidates were reconstructed in a mass window $\pm 500 \text{ MeV}/c^2$ around the global average value [18].

The detector description and conditions used to filter the B^\pm candidates were identical to those used to initially process the data.

Candidates were again required to pass the combined logical trigger decision criteria

$$\begin{aligned}
 & ((L0 \text{ Hadron TOS}) \text{ OR } (L0 \text{ Global TIS})) \text{ AND} \\
 & ((HLT1 \text{ 1Track TOS}) \text{ OR } (HLT1 \text{ Global TIS})) \text{ AND} \\
 & ((HLT2 \text{ Topological 2-body TOS}) \text{ OR } (HLT2 \text{ Topological 3-body TOS}) \text{ OR } (HLT2 \text{ Global TIS})).
 \end{aligned}
 \tag{5.1}$$

In an identical manner to the analysis described in Chapter 4, if multiple B^\pm candidates were reconstructed and selected in a single event, the candidate with the largest value of B^\pm flight distance χ^2 from the PV was retained and the other candidates discarded.

The resulting $B^\pm \rightarrow D(K_S^0 \pi^+ \pi^-)h$ candidate mass distributions, combining $\sim 143 \text{ pb}^{-1}$ magnet up and $\sim 199 \text{ pb}^{-1}$ magnet down data, are shown in Figure 5.1. All candidates in these distributions pass the full selection, including the combined trigger and stripping selections as detailed above. In all distributions, signal mass peaks can be seen around the global average B^\pm mass, meaning that it was possible to use both LL and DD candidates to find the ratio of branching fractions.

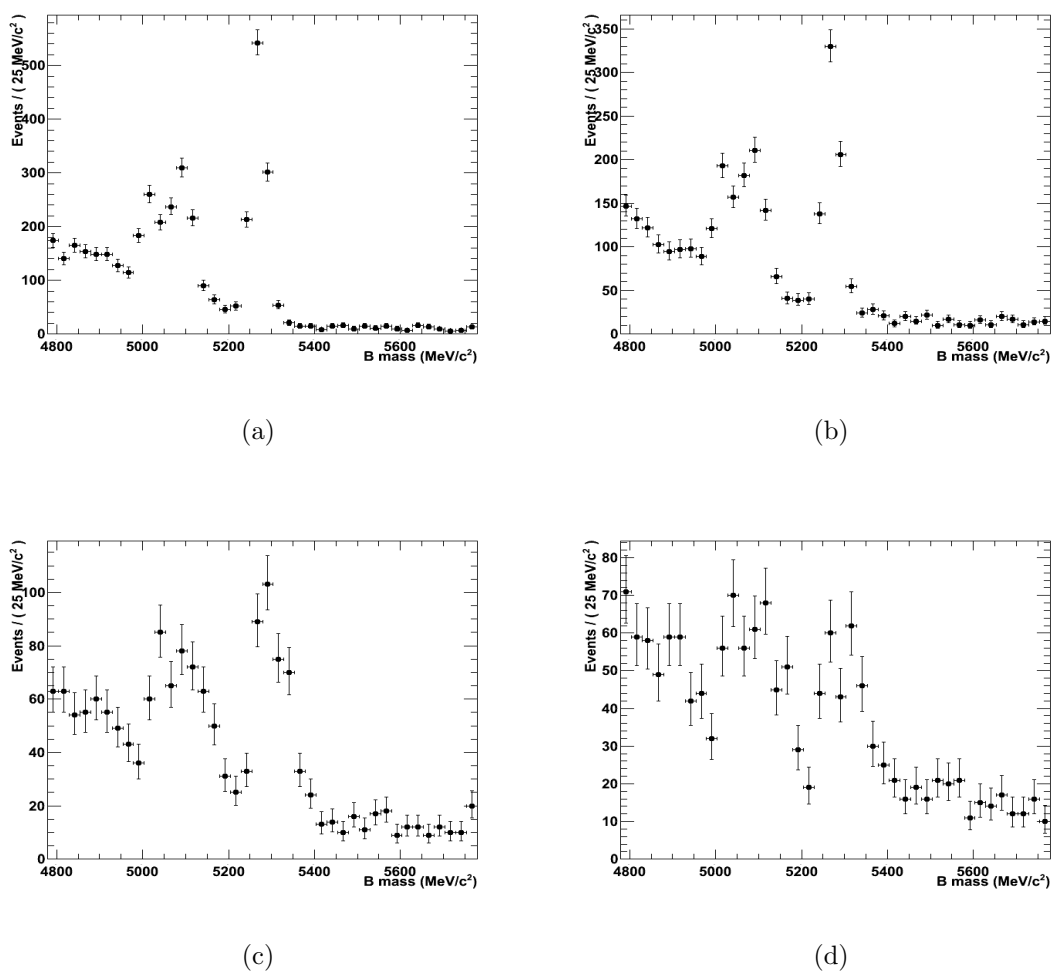


Figure 5.1: The $B^\pm \rightarrow D(K_S^0\pi^+\pi^-)h$ candidate mass distributions from 342 pb^{-1} of 2011 data. Figure 5.1(a) shows the $B^\pm \rightarrow D\pi^\pm$ LL distribution, Figure 5.1(b) the $B^\pm \rightarrow D\pi^\pm$ DD distribution, Figure 5.1(c) shows the $B^\pm \rightarrow DK^\pm$ LL distribution and Figure 5.1(d) the $B^\pm \rightarrow DK^\pm$ DD distribution.

5.2 Mass fit

The $B^\pm \rightarrow D\pi^\pm$ and $B^\pm \rightarrow DK^\pm$ mass distributions were fitted simultaneously with an extended unbinned likelihood fit, using RooFit, to evaluate the ratio of yields of Equation 4.2, $N_{B^\pm \rightarrow DK^\pm}^{signal} / N_{B^\pm \rightarrow D\pi^\pm}^{signal}$, and the yield of $B^\pm \rightarrow D\pi^\pm$ candidates. The pair of LL $B^\pm \rightarrow D\pi^\pm$ and $B^\pm \rightarrow DK^\pm$ mass distributions (Figures 5.1(a) and 5.1(c)) was fitted separately to the DD pair (Figures 5.1(b) and 5.1(d)), as different candidate selection criteria were used in the LL and DD cases. The data set was not separated into magnet up and down subsets.

5.2.1 Signal and background fits to Monte-Carlo

MC10 simulated event samples were again used to determine the individual RooFit PDFs to be used in the full data mass fits, with MC truth information used to separate candidates into the different possible background categories described in Section 4.3.1. It was possible to use the MC10 samples as the data-taking conditions and detector were similar at the end of 2010 and beginning of 2011. Candidates were selected in the same way as for data; the only exception was the application of trigger decisions, as the trigger setting used to flag the MC10 samples in production (*0x002e002a*) was taken from 2010. The data under consideration were recorded with several trigger settings in place, however three very similar settings (*0x005a0032*, *0x006d0032* and *0x00730035*) dominated, accounting for approximately 95% of the events containing selected candidates. The LHCb trigger software Moore was therefore run three times on reduced samples of $B^\pm \rightarrow D(K_S^0\pi^+\pi^-)\pi^\pm$ and $B^\pm \rightarrow D(K_S^0\pi^+\pi^-)K^\pm$ MC10 signal DSTs, consisting only of events containing selected signal candidates; the saved *0x002e002a* trigger information was replaced with the information from each of the three settings of 2011. The new saved flagging information was extracted when the candidates were reconstructed with DaVinci and was then used to apply the trigger criteria of Equation 5.1 in the signal and Category 3 cases. For the other background categories, the *0x002e002a* information was sufficient to extract the PDFs; this is discussed in detail below for the relevant categories.

The data were not split into magnet up and down contributions in the fit, therefore for signal and background studies the candidates from MC magnet up and down samples were summed to give the final distributions. In the sum, individual candidates were weighted according to the proportions of the total integrated luminosity recorded in the

magnet up and down configurations.

In order to find appropriate PDFs for the signal mass distributions, $B^\pm \rightarrow D(K_S^0\pi^+\pi^-)\pi^\pm$ and $B^\pm \rightarrow D(K_S^0\pi^+\pi^-)K^\pm$ candidates were reconstructed and selected, using the full selection including trigger and stripping, from the respective $B^\pm \rightarrow D(K_S^0\pi^+\pi^-)h$ MC10 signal samples with 2011 trigger information. The candidate mass distributions were each fitted with a sum of a Gaussian and a Crystal Ball PDF with a low-mass tail. The Crystal Ball and Gaussian were forced to have the same mean in the fits. The resulting distributions for trigger setting *0x00730035* are shown in Figures 5.2 and 5.3; the fits in all three trigger setting cases are identical within errors.

As for the 2010 data analysis, very few Category 1 (combinatoric) and no Category 3 (*Dh*-random) $B^\pm \rightarrow D(K_S^0\pi^+\pi^-)h$ candidates were selected from the large $b \rightarrow DX$ “cocktail” MC10 sample. It was also attempted to estimate the level of Category 3 background using the signal $B^\pm \rightarrow D(K_S^0\pi^+\pi^-)K^\pm$ and $B^\pm \rightarrow D(K_S^0\pi^+\pi^-)\pi^\pm$ samples with 2011 trigger decisions; either one or no candidates were selected in total from these samples in each case. To calculate upper limits on the yields for an integrated luminosity of 342 pb^{-1} , a $b\bar{b}$ cross-section of $284 \text{ }\mu\text{b}$ [102] was used, and Poisson statistics were assumed. This corresponds to < 3.89 or < 2.30 candidates being selected from each sample respectively at 90% confidence level [18]. Then

$$\text{Yield} = 2 \times N_{b\bar{b}} \cdot f(b \rightarrow D) \cdot \text{Br}(D \rightarrow K_S^0\pi^+\pi^-) \cdot \text{Br}(K_S^0 \rightarrow \pi^+\pi^-) \cdot \epsilon_{sel} \quad (5.2)$$

where ϵ_{sel} is the efficiency of selecting a true $D \rightarrow K_S^0\pi^+\pi^-$ decay and combining it with a random track to give a candidate passing the full selection. This calculation gave total (magnet up plus magnet down) upper limits of < 560 , < 730 , < 720 and < 800 candidates in the $\pm 500 \text{ MeV}/c^2$ B^\pm mass window in the LL $B^\pm \rightarrow D\pi^\pm$, LL $B^\pm \rightarrow DK^\pm$, DD $B^\pm \rightarrow D\pi^\pm$ and DD $B^\pm \rightarrow DK^\pm$ cases respectively. These limits were constrained by the sizes of the MC samples.

The Category 2 (cross-feed) background PDFs were found by selecting $B^\pm \rightarrow D(K_S^0\pi^+\pi^-)\pi^\pm$ candidates from $B^\pm \rightarrow D(K_S^0\pi^+\pi^-)K^\pm$ signal MC10 events, and vice versa, with the kinematic, stripping and *0x002e002a* L0 and HLT1 trigger criteria applied. The HLT2 trigger criteria from *0x002e002a* were not imposed. The 2011 trigger settings used in data-taking had very similar L0 Hadron and HLT1 1Track trigger thresholds to the *0x002e002a* setting, so requiring the L0 and HLT1 criteria with this setting gave a good representation of the effect of the 2011 L0 and HLT1 trigger settings on the B^\pm candidate

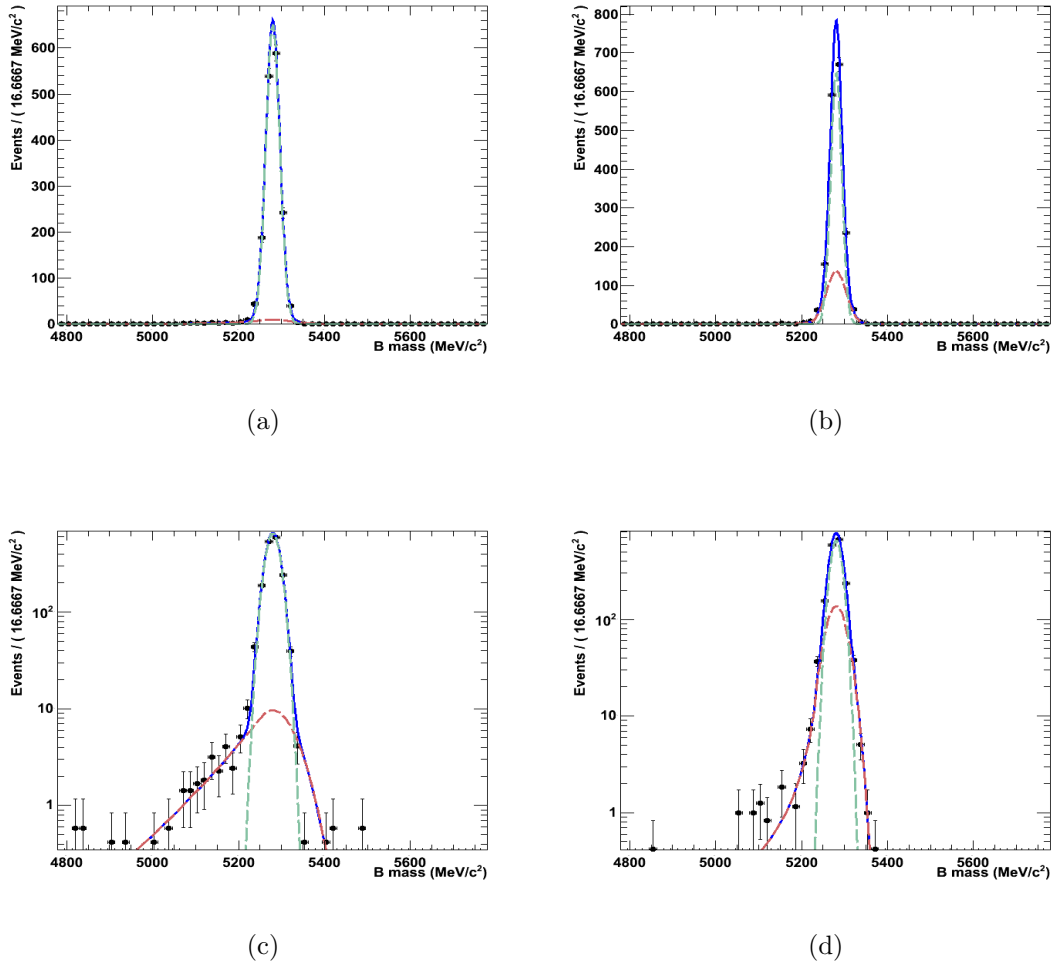


Figure 5.2: The signal LL $B^\pm \rightarrow D(K_S^0 \pi^+ \pi^-) h$ candidate mass distributions from MC, with trigger setting *0x00730035*. Figure 5.2(a) shows the LL $B^\pm \rightarrow D\pi^\pm$ signal distribution and Figure 5.2(b) shows the LL $B^\pm \rightarrow DK^\pm$ signal distribution. Figures 5.2(c) and 5.2(d) show the same $B^\pm \rightarrow D\pi^\pm$ and $B^\pm \rightarrow DK^\pm$ distributions on log scales, respectively. The total PDF (blue) is the sum of a Gaussian component (green) and Crystal Ball PDF (red).

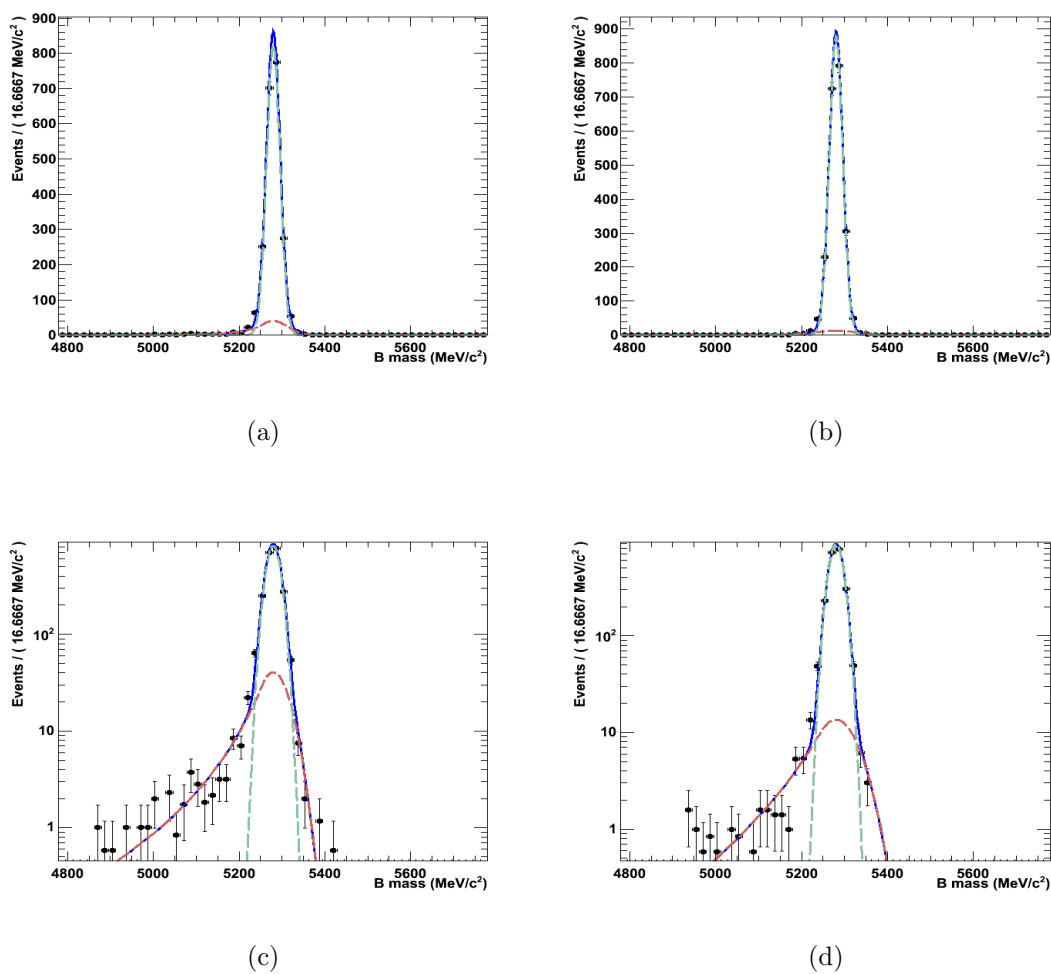


Figure 5.3: The signal DD $B^\pm \rightarrow D(K_S^0 \pi^+ \pi^-) h$ candidate mass distributions from MC, with trigger setting *0x00730035*. Figure 5.3(a) shows the DD $B^\pm \rightarrow D\pi^\pm$ signal distribution and Figure 5.3(b) shows the DD $B^\pm \rightarrow DK^\pm$ signal distribution. Figures 5.3(c) and 5.3(d) show the same $B^\pm \rightarrow D\pi^\pm$ and $B^\pm \rightarrow DK^\pm$ distributions on log scales, respectively. The total PDF (blue) is the sum of a Gaussian component (green) and Crystal Ball PDF (red).

mass distributions. The HLT2 Topological trigger was altered to use a Boosted Decision Tree (BDT) method in 2011, however, rather than the cut-based method of 2010; both versions of the Topological trigger were similar in exploiting the typical topology of B decays, but it was not possible to assume that applying the HLT2 selection criteria with the *0x002e002a* setting would give an accurate representation of the effects of the 2011 HLT2 trigger. The mass distributions of the $B^\pm \rightarrow D\pi^\pm$ and $B^\pm \rightarrow DK^\pm$ candidates in Category 2 can be seen in Figures 5.4 and 5.5, with either L0, HLT1 and HLT2 (cut-based) trigger criteria or only L0 and HLT1 criteria applied to the candidates; a double Crystal Ball PDF was used to fit these distributions. It was verified that the additional application of *0x002e002a* HLT2 criteria did not change the PDF fitted parameters within errors. As the selection ethos of the 2011 BDT Topological trigger was the same as that of the 2010 cut-based Topological trigger, it was assumed that the same would be true for the 2011 BDT Topological trigger, and so application of the *0x002e002a* L0 and HLT1 trigger criteria was sufficient to well-constrain the PDFs for the fits to the 2011 data mass distributions.

In order to better determine the low-mass background contributions (Categories 4 and 5), the reconstructed $B^\pm \rightarrow D(K_S^0\pi^+\pi^-)h$ candidates passing the full selection from the $b \rightarrow DX$ “cocktail” MC sample were studied in further detail to ascertain the exact nature of the decays involved. Large MC10 samples of the predominant background decays were produced and are detailed in Table 5.2; the charge conjugate decays of those given in the first column are included in each of the samples. All of the identified backgrounds contain a $D \rightarrow K_S^0\pi^+\pi^-$ decay, which was generated in MC according to phase space, without a decay amplitude model applied. The samples were all flagged in production with trigger setting *0x002e002a* information.

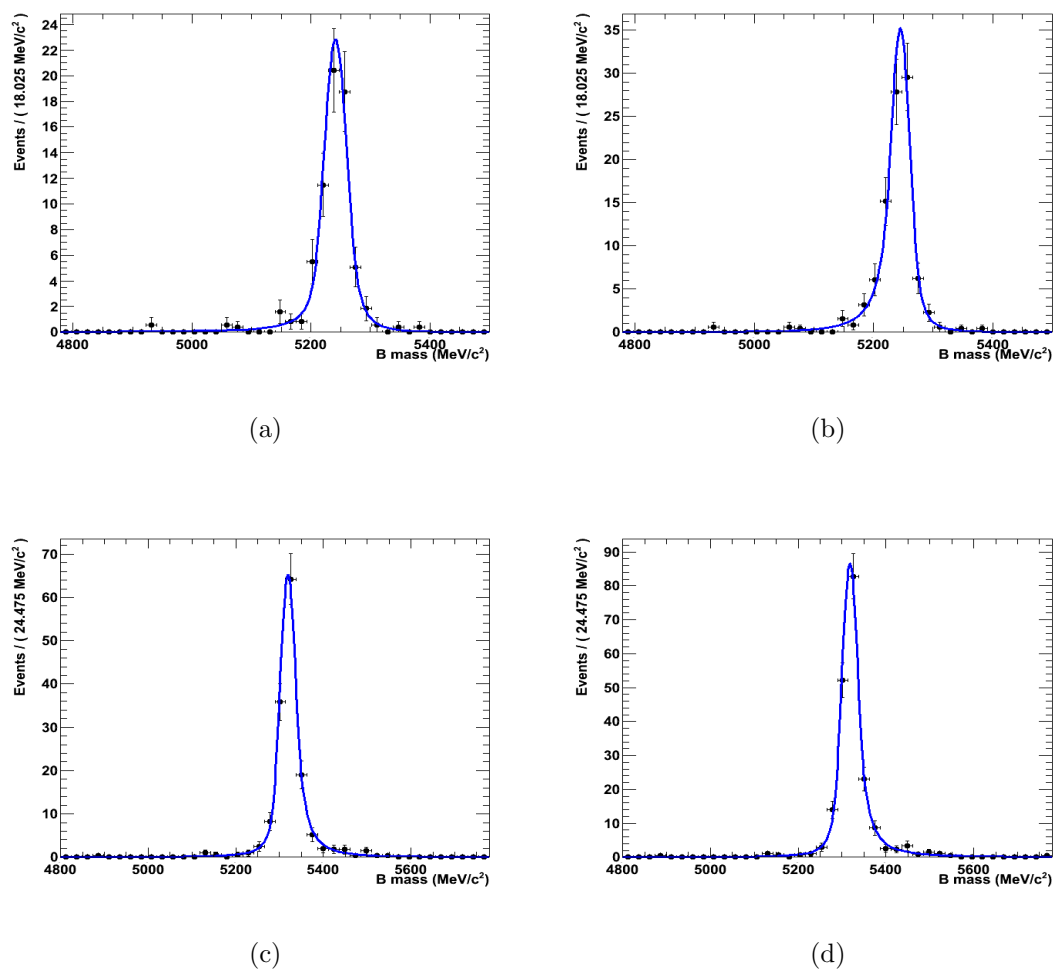


Figure 5.4: The background Category 2 (cross-feed) $B^\pm \rightarrow D(K_S^0\pi^+\pi^-)h$ LL candidate mass distributions from MC, with and without application of HLT2 cut-based criteria. Figure 5.4(a) shows the LL $B^\pm \rightarrow D\pi^\pm$ distribution with HLT2 criteria applied, Figure 5.4(b) shows the LL $B^\pm \rightarrow D\pi^\pm$ distribution without HLT2 criteria applied; Figure 5.4(c) shows the LL $B^\pm \rightarrow DK^\pm$ distribution with HLT2 criteria applied and Figure 5.4(d) shows the LL $B^\pm \rightarrow DK^\pm$ distribution without HLT2 criteria applied.

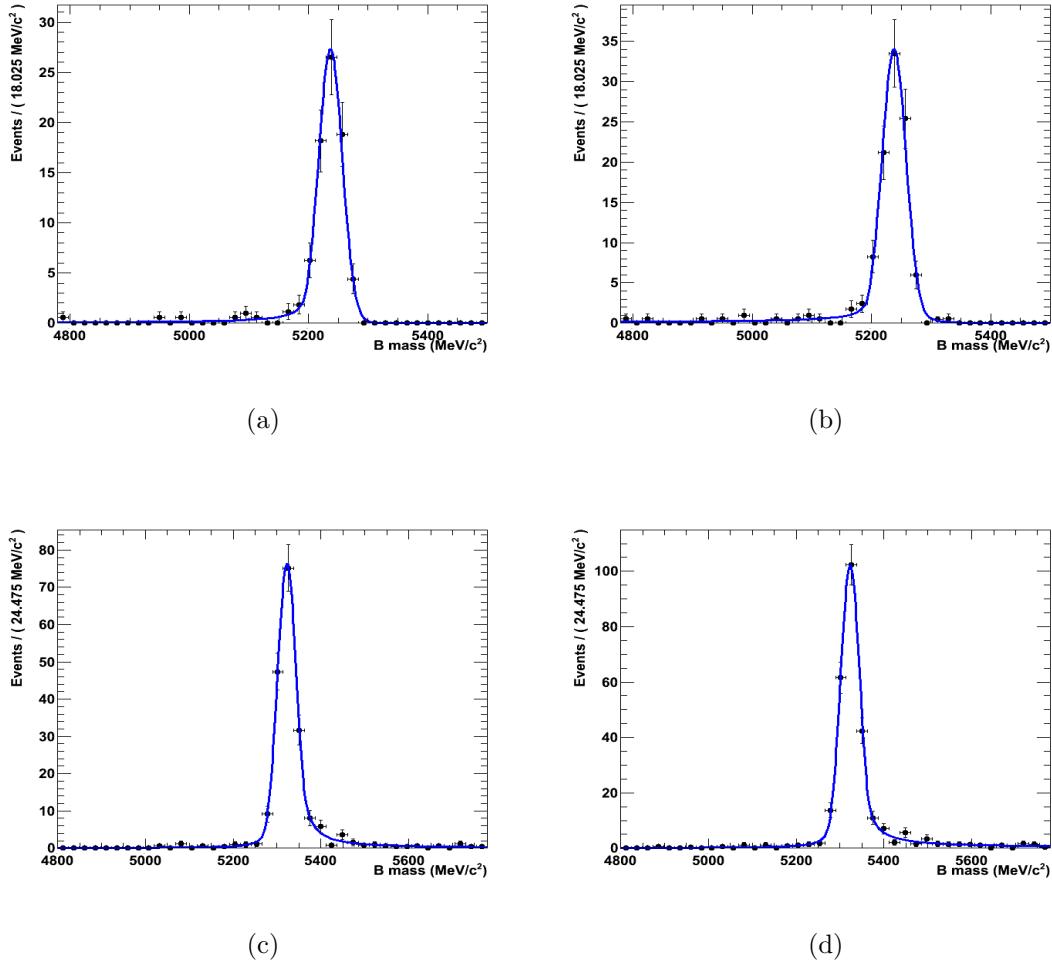


Figure 5.5: The background Category 2 (cross-feed) $B^\pm \rightarrow D(K_S^0\pi^+\pi^-)h$ DD candidate mass distributions from MC, with and without application of HLT2 cut-based criteria. Figure 5.5(a) shows the DD $B^\pm \rightarrow D\pi^\pm$ distribution with HLT2 criteria applied, Figure 5.5(b) shows the DD $B^\pm \rightarrow D\pi^\pm$ distribution without HLT2 criteria applied; Figure 5.5(c) shows the DD $B^\pm \rightarrow DK^\pm$ distribution with HLT2 criteria applied and Figure 5.5(d) shows the DD $B^\pm \rightarrow DK^\pm$ distribution without HLT2 criteria applied.

MC sample	Generated magnet up sample size	Generated magnet down sample size
$B_d^0 \rightarrow \bar{D}^0(K_S^0\pi^+\pi^-)\rho^0$	383597	383895
$B_d^0 \rightarrow D^*(2010)^-(\bar{D}^0(K_S^0\pi^+\pi^-)\pi^-)K^+$	259997	259998
$B_d^0 \rightarrow D^*(2010)^-(\bar{D}^0(K_S^0\pi^+\pi^-)\pi^-)\pi^+$	509990	509998
$B_d^0 \rightarrow D^*(2010)^-(\bar{D}^0(K_S^0\pi^+\pi^-)\pi^-)\rho^+$	1170685	1169285
$B^+ \rightarrow \bar{D}^0(K_S^0\pi^+\pi^-)\rho^+$	766096	760095
$B^+ \rightarrow \bar{D}^*(2007)^0(\bar{D}^0(K_S^0\pi^+\pi^-)\gamma, \pi^0)K^+$	259997	259998
$B^+ \rightarrow \bar{D}^*(2007)^0(\bar{D}^0(K_S^0\pi^+\pi^-)\gamma, \pi^0)\pi^+$	509994	549991
$B^+ \rightarrow \bar{D}^*(2007)^0(\bar{D}^0(K_S^0\pi^+\pi^-)\gamma, \pi^0)\rho^+$	911293	912889

Table 5.2: The MC10 samples used to evaluate the low-mass background PDFs.

$B^\pm \rightarrow D(K_S^0\pi^+\pi^-)\pi^\pm$ and $B^\pm \rightarrow D(K_S^0\pi^+\pi^-)K^\pm$ candidates were reconstructed and selected from these samples, using the kinematic and stripping selections plus the *0x002e002a* L0 and HLT1 trigger criteria. The HLT2 trigger criteria from *0x002e002a* were not imposed. In a similar manner to the Category 2 background case, it was verified that the additional application of *0x002e002a* HLT2 criteria to the selected candidates did not change the parameters of the PDFs fitted to their mass distributions, within errors. To perform the check, ARGUS [176]^a and Gaussian PDFs were fitted to the B^\pm candidate mass distributions from the $B_d^0 \rightarrow \bar{D}^0\rho^0$, $B^+ \rightarrow \bar{D}^*(2007)^0(\bar{D}^0\gamma, \pi^0)\pi^+$ and $B_d^0 \rightarrow D^*(2010)^-(D^0\pi^-)K^+$ MC samples, with either *0x002e002a* L0, HLT1 and HLT2 (cut-based) trigger criteria or only L0 and HLT1 criteria applied to the B^\pm candidates selected with the kinematic and stripping selections. Figures 5.6, 5.7, 5.8 and 5.9 show the mass distributions and fits concerned. It was verified that the fits were unchanged within errors for the two cases; for the D^* samples, the fitted PDF parameters of the distributions with and without HLT2 were all within one error in all cases. For the $B_d^0 \rightarrow \bar{D}^0\rho^0$ sample, the PDFs were less well-defined because of low statistics, with the ARGUS PDF high-mass cut-off m_0 being particularly affected; all of the parameters except the upper mass cut-off in the DD case were within twice the errors. The DD cut-off was within three times the errors. Therefore, application of the HLT2 cut-based Topological trigger criteria did not change the mass distributions significantly. It was assumed that the same would be true for the 2011 BDT Topological trigger, and so application of the *0x002e002a* L0 and HLT1 trigger criteria was sufficient to well-constrain the PDFs fitted to the mass distributions. Using the *0x002e002a* setting information meant that it was not possible to estimate the full 2011 selection efficiencies for these samples to high accuracy. It was found that the *0x002e002a* cut-based Topological trigger had similar efficiencies ($\sim 65 - 70\%$) on L0 \times HLT1 selected candidates from all of these decay modes, and in the full data fit (Section 5.2.2) the relative yields of the different components were not fixed.

^aThe ARGUS PDF is

$$\text{ARGUS}(M; m_0, c, p) = M \left(1 - (M/m_0)^2\right)^p \exp(c(1 - (M/m_0)^2)) , \quad (5.3)$$

where M is the mass, m_0 is the high-mass cut-off and c and p are slope parameters.

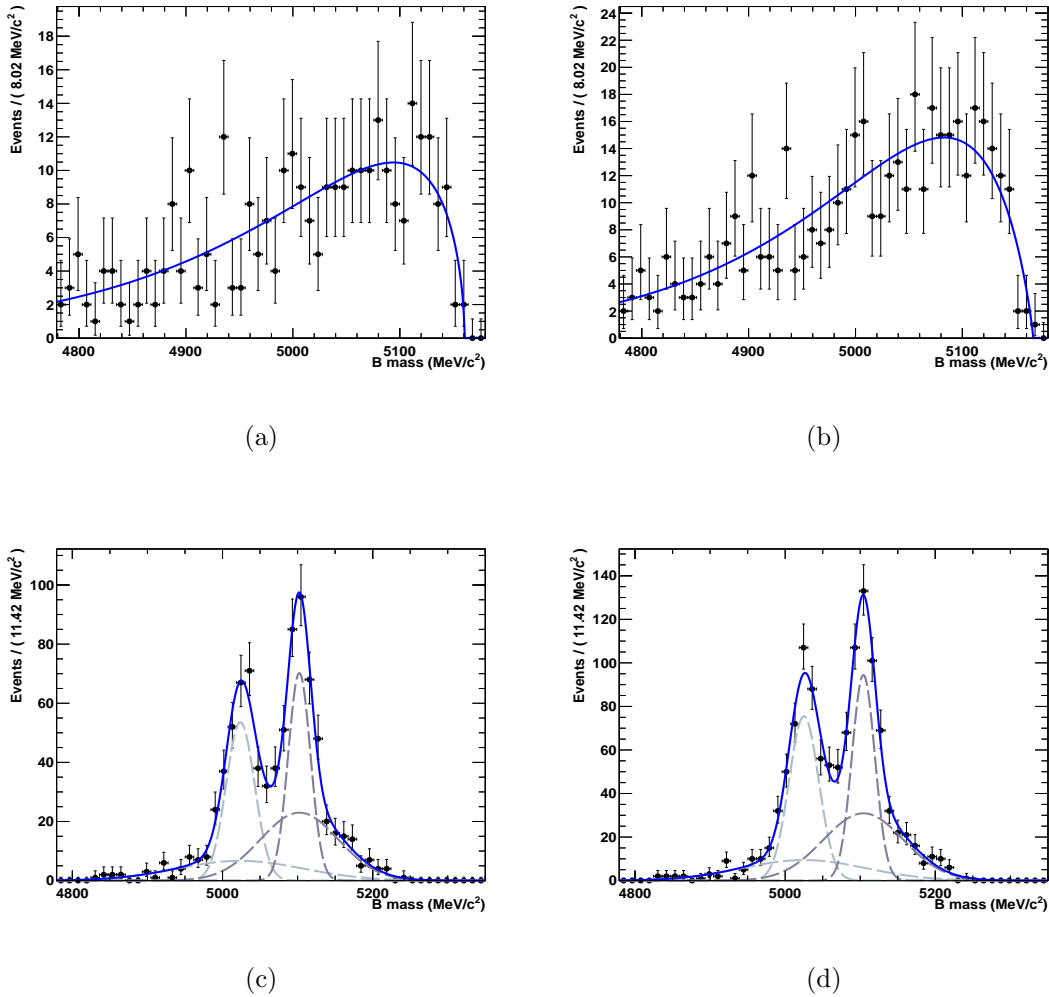


Figure 5.6: The $B^\pm \rightarrow D(K_S^0 \pi^+ \pi^-) \pi^\pm$ LL candidates from $B_d^0 \rightarrow \bar{D}^0 \rho^0$ and $B^+ \rightarrow \bar{D}^*(2007)^0 (\bar{D}^0 \gamma, \pi^0) \pi^+$ MC samples, with and without application of HLT2 cut-based criteria. Figure 5.6(a) shows candidates from $B_d^0 \rightarrow \bar{D}^0 \rho^0$ with HLT2 criteria, Figure 5.6(b) shows candidates from $B_d^0 \rightarrow \bar{D}^0 \rho^0$ without HLT2; both distributions are fitted with an ARGUS PDF. Figure 5.6(c) shows candidates from $B^+ \rightarrow \bar{D}^*(2007)^0 (\bar{D}^0 \gamma, \pi^0) \pi^+$ with HLT2 criteria and Figure 5.6(d) shows candidates from $B^+ \rightarrow \bar{D}^*(2007)^0 (\bar{D}^0 \gamma, \pi^0) \pi^+$ without HLT2; both distributions are fitted with a sum of four Gaussian PDFs in two pairs.

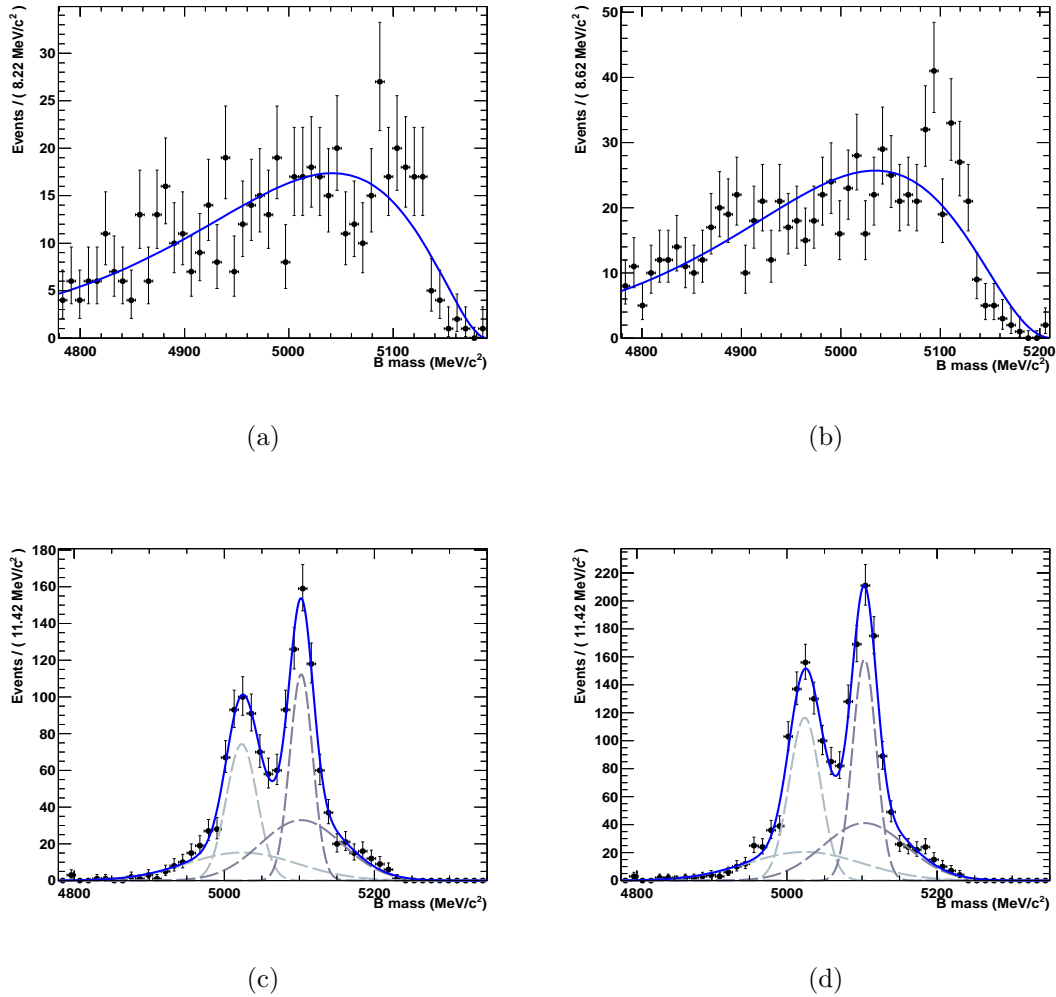


Figure 5.7: The $B^\pm \rightarrow D(K_S^0 \pi^+ \pi^-) \pi^\pm$ DD candidates from $B_d^0 \rightarrow \bar{D}^0 \rho^0$ and $B^+ \rightarrow \bar{D}^*(2007)^0 (\bar{D}^0 \gamma, \pi^0) \pi^+$ MC samples, with and without application of HLT2 cut-based criteria. Figure 5.7(a) shows candidates from $B_d^0 \rightarrow \bar{D}^0 \rho^0$ with HLT2 criteria, Figure 5.7(b) shows candidates from $B_d^0 \rightarrow \bar{D}^0 \rho^0$ without HLT2; both distributions are fitted with an ARGUS PDF. Figure 5.7(c) shows candidates from $B^+ \rightarrow \bar{D}^*(2007)^0 (\bar{D}^0 \gamma, \pi^0) \pi^+$ with HLT2 criteria and Figure 5.7(d) shows candidates from $B^+ \rightarrow \bar{D}^*(2007)^0 (\bar{D}^0 \gamma, \pi^0) \pi^+$ without HLT2; both distributions are fitted with a sum of four Gaussian PDFs in two pairs.

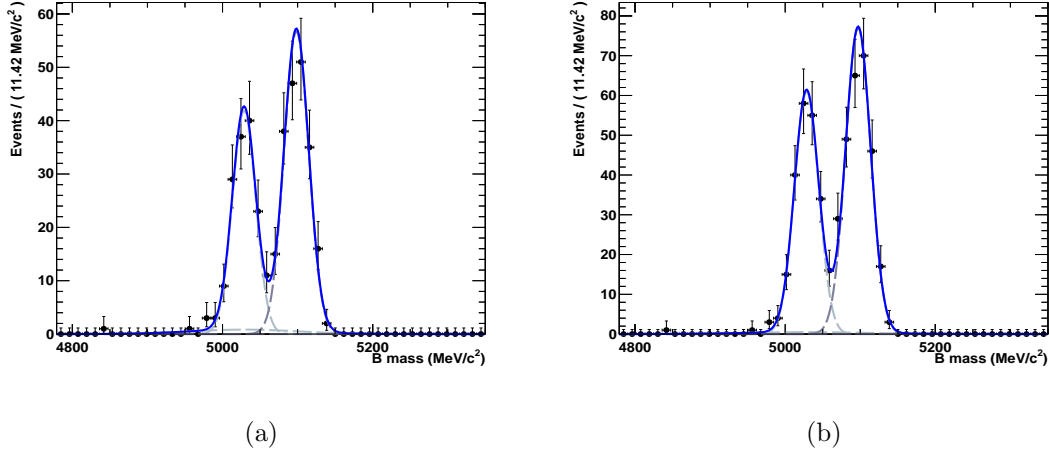


Figure 5.8: The $B^\pm \rightarrow D(K_S^0\pi^+\pi^-)K^\pm$ LL candidates from a $B_d^0 \rightarrow D^*(2010)^-(\bar{D}^0\pi^-)K^+$ MC sample, with and without application of HLT2 cut-based criteria. Figure 5.8(a) shows candidates with HLT2 criteria applied, Figure 5.8(b) shows candidates without HLT2; both distributions are fitted with a sum of four Gaussian PDFs in two pairs.

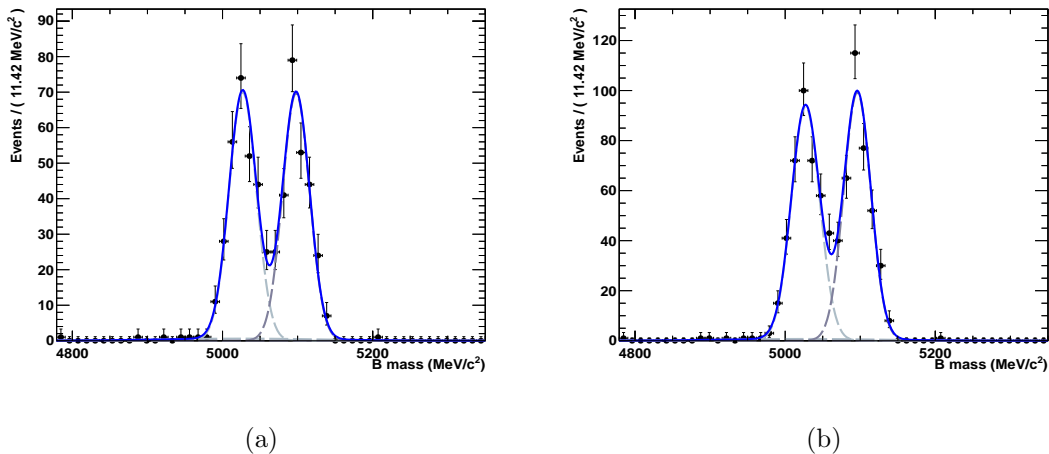


Figure 5.9: The $B^\pm \rightarrow D(K_S^0\pi^+\pi^-)K^\pm$ DD candidates from a $B_d^0 \rightarrow D^*(2010)^-(\bar{D}^0\pi^-)K^+$ MC sample, with and without application of HLT2 cut-based criteria. Figure 5.9(a) shows candidates with HLT2 criteria applied, Figure 5.9(b) shows candidates without HLT2; both distributions are fitted with a sum of four Gaussian PDFs in two pairs.

The $B^\pm \rightarrow D(K_S^0\pi^+\pi^-)h$ candidates passing the selections without HLT2 criteria from all of the samples were weighted according to their expected yields in 143 pb^{-1} of magnet up data and 199 pb^{-1} of magnet down data. Candidates from certain combinations of samples with similar mass distributions were combined and fitted to well-constrain the PDFs contributing to the overall low-mass distribution. For $B^\pm \rightarrow D\pi^\pm$ LL and DD cases, the combinations considered were:

- D^*h : candidates from $B_d^0 \rightarrow D^*(2010)^-(\bar{D}^0_{(K_S^0\pi^+\pi^-)}\pi^-)K^+$, $B_d^0 \rightarrow D^*(2010)^-(\bar{D}^0_{(K_S^0\pi^+\pi^-)}\pi^-)\pi^+$, $B^+ \rightarrow \bar{D}^*(2007)^0(\bar{D}^0_{(K_S^0\pi^+\pi^-)}\gamma, \pi^0)K^+$ and $B^+ \rightarrow \bar{D}^*(2007)^0(\bar{D}^0_{(K_S^0\pi^+\pi^-)}\gamma, \pi^0)\pi^+$ samples; in this case, the $D^*\pi$ contributions are dominant with very little contribution from D^*K . The PDFs used to fit the mass distributions were sums of four Gaussian PDFs in two pairs; in each pair, the means of the two Gaussian were fixed to be the same. The resulting fits can be seen in Figures 5.10(a) and 5.11(a);
- $D^*\rho$: candidates from $B_d^0 \rightarrow D^*(2010)^-(\bar{D}^0_{(K_S^0\pi^+\pi^-)}\pi^-)\rho^+$ and $B^+ \rightarrow \bar{D}^*(2007)^0(\bar{D}^0_{(K_S^0\pi^+\pi^-)}\gamma, \pi^0)\rho^+$ samples; here Gaussian PDFs with large σ values were used to fit the mass distributions, as shown in Figures 5.10(b) and 5.11(b); and
- $D\rho$: candidates from $B_d^0 \rightarrow \bar{D}^0(K_S^0\pi^+\pi^-)\rho^0$ and $B^+ \rightarrow \bar{D}^0(K_S^0\pi^+\pi^-)\rho^+$ samples; here ARGUS PDFs were used to fit the mass distributions, as shown in Figures 5.10(c) and 5.11(c).

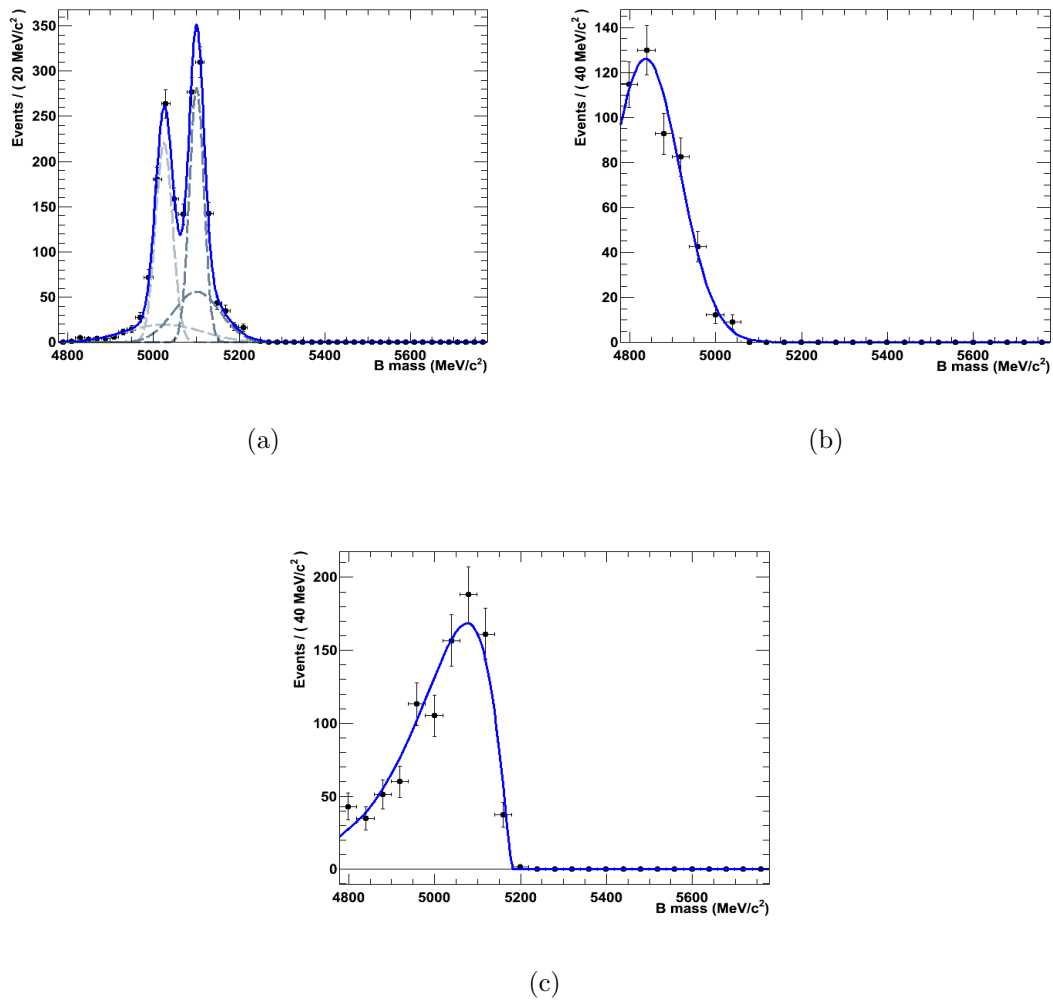


Figure 5.10: The components of the low-mass background $B^\pm \rightarrow D(K_S^0 \pi^+ \pi^-) \pi^\pm$ LL candidate mass distributions from MC. Figure 5.10(a) shows the distribution from D^*h , Figure 5.10(b) shows the distribution from $D^*\rho$ and Figure 5.10(c) shows the distribution from $D\rho$. In the D^*h case, the solid blue line is the total summed PDF.

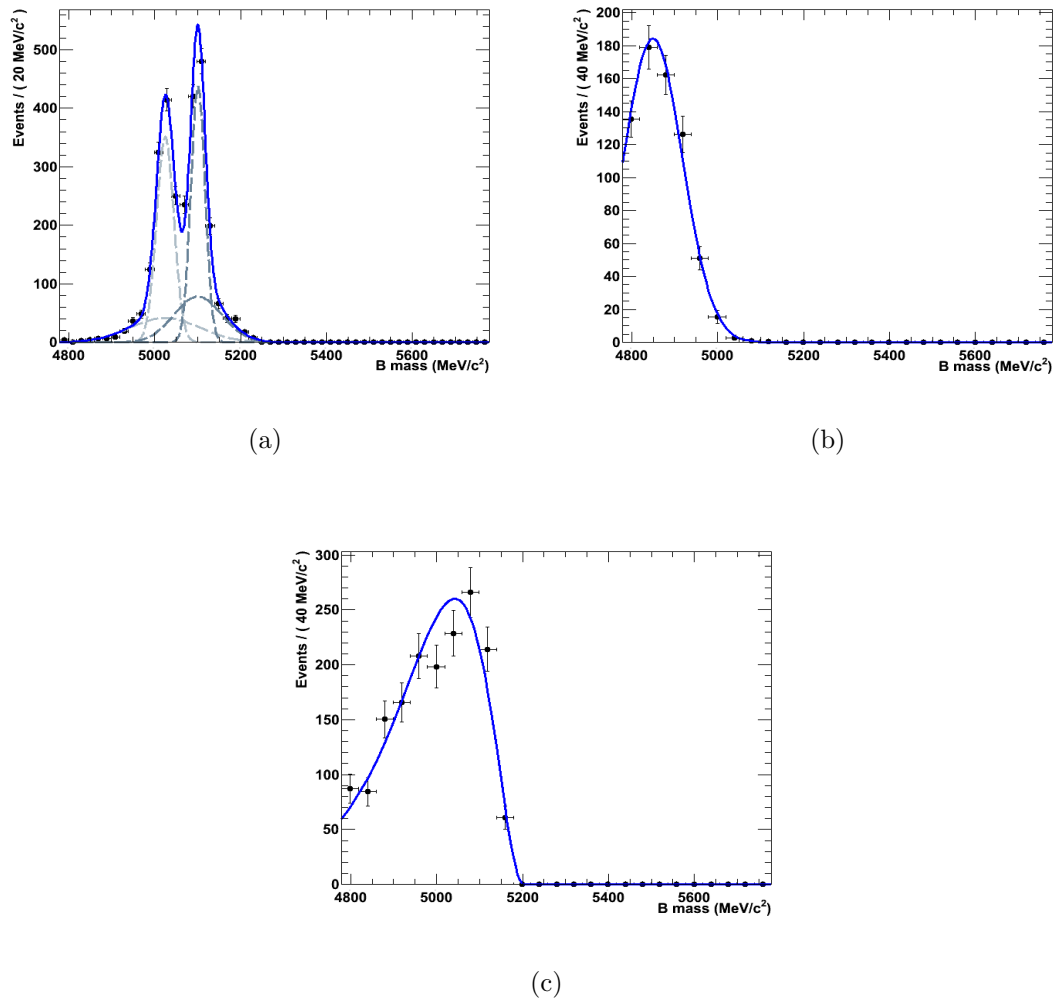


Figure 5.11: The components of the low-mass background $B^\pm \rightarrow D(K_S^0\pi^+\pi^-)\pi^\pm$ DD candidate mass distributions from MC. Figure 5.11(a) shows the distribution from D^*h , Figure 5.11(b) shows the distribution from $D^*\rho$ and Figure 5.11(c) shows the distribution from $D\rho$. In the D^*h case, the solid blue line is the total summed PDF.

For $B^\pm \rightarrow DK^\pm$ LL and DD cases, the combinations considered were:

- D^*K : candidates from $B_d^0 \rightarrow D^*(2010)^-(\bar{D}_{(K_S^0\pi^+\pi^-)}^0\pi^-)K^+$ and $B^+ \rightarrow \bar{D}^*(2007)^0(\bar{D}_{(K_S^0\pi^+\pi^-)}^0\gamma, \pi^0)K^+$ samples; in this case, the PDFs used to fit the mass distributions were sums of four Gaussian PDFs in two pairs; in each pair, the means of the two Gaussian were fixed to be the same. The resulting fits can be seen in Figures 5.12(a) and 5.13(a);
- $D^*\pi$: candidates from $B_d^0 \rightarrow D^*(2010)^-(\bar{D}_{(K_S^0\pi^+\pi^-)}^0\pi^-)\pi^+$ and $B^+ \rightarrow \bar{D}^*(2007)^0(\bar{D}_{(K_S^0\pi^+\pi^-)}^0\gamma, \pi^0)\pi^+$ samples; in this case, the $D^*\pi$ contributions have distorted mass distributions due to the mis-identification of π as K . The PDFs used to fit the mass distributions were sums of two double Crystal Ball PDFs and the resulting fits can be seen in Figures 5.12(b) and 5.13(b);
- $D^*\rho$: candidates from $B_d^0 \rightarrow D^*(2010)^-(\bar{D}_{(K_S^0\pi^+\pi^-)}^0\pi^-)\rho^+$ and $B^+ \rightarrow \bar{D}^*(2007)^0(\bar{D}_{(K_S^0\pi^+\pi^-)}^0\gamma, \pi^0)\rho^+$ samples; here Gaussian PDFs with large σ values were used to fit the mass distributions, as shown in Figures 5.12(c) and 5.13(c); and
- $D\rho$: candidates from $B_d^0 \rightarrow \bar{D}^0(K_S^0\pi^+\pi^-)\rho^0$ and $B^+ \rightarrow \bar{D}^0(K_S^0\pi^+\pi^-)\rho^+$ samples; here the sum of a Gaussian PDF and an exponential PDF were used to fit the mass distributions, as shown in Figures 5.12(d) and 5.13(d).

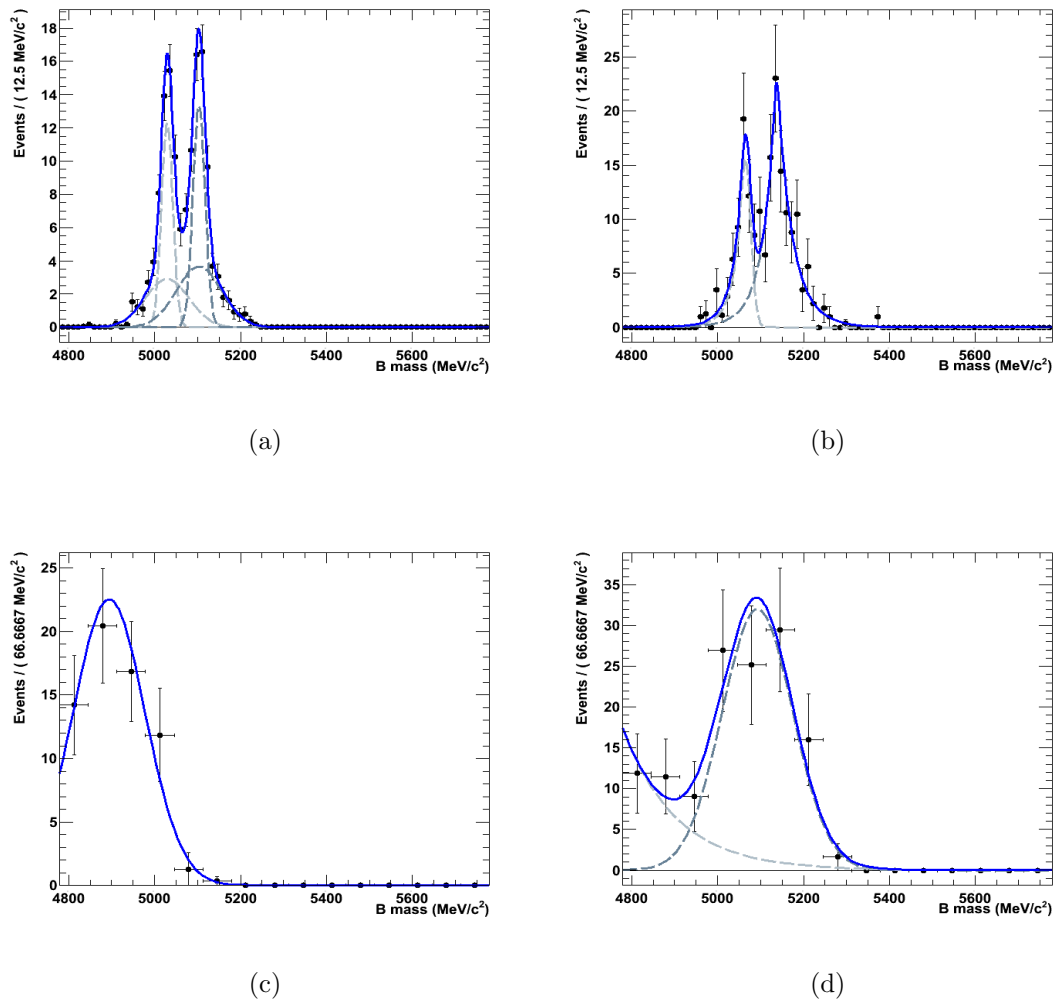


Figure 5.12: The components of the low-mass background $B^\pm \rightarrow D(K_S^0 \pi^+ \pi^-)K^\pm$ LL candidate mass distributions from MC. Figure 5.12(a) shows the distribution from D^*K , Figure 5.12(b) shows the distribution from $D\pi$, Figure 5.12(c) shows the distribution from $D^*\rho$ and Figure 5.12(d) shows the distribution from $D\rho$. In the D^*h and $D\rho$ cases, the solid blue lines are the total summed PDFs.

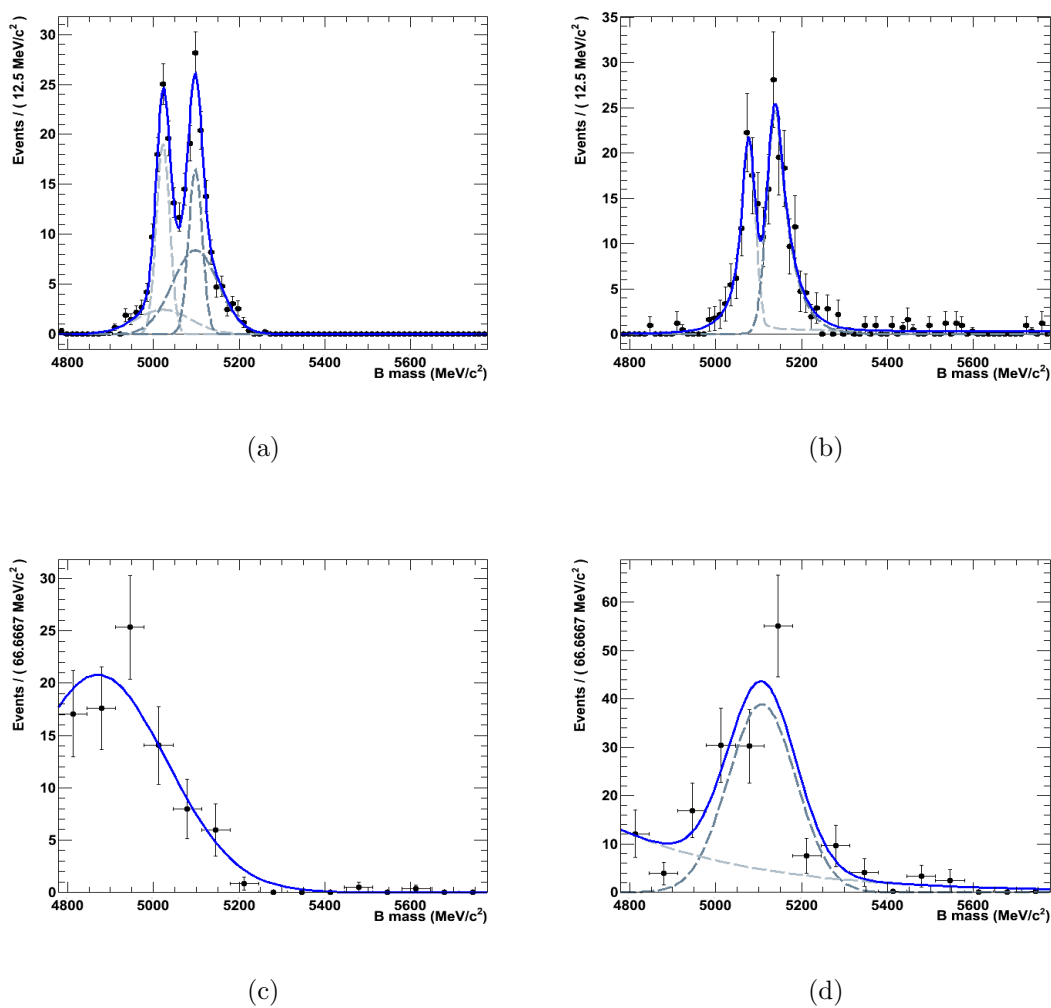


Figure 5.13: The components of the low-mass background $B^\pm \rightarrow D(K_S^0 \pi^+ \pi^-)K^\pm$ DD candidate mass distributions from MC. Figure 5.13(a) shows the distribution from D^*K , Figure 5.13(b) shows the distribution from $D^*\pi$, Figure 5.13(c) shows the distribution from $D^*\rho$ and Figure 5.13(d) shows the distribution from $D\rho$. In the D^*h and $D\rho$ cases, the solid blue lines are the total summed PDFs.

Fits to the sum of all the candidates were then performed as a cross-check, with the total PDFs a sum of the individual components listed above; the shapes and yields of the individual components were fixed. These fits are shown in Figure 5.14.

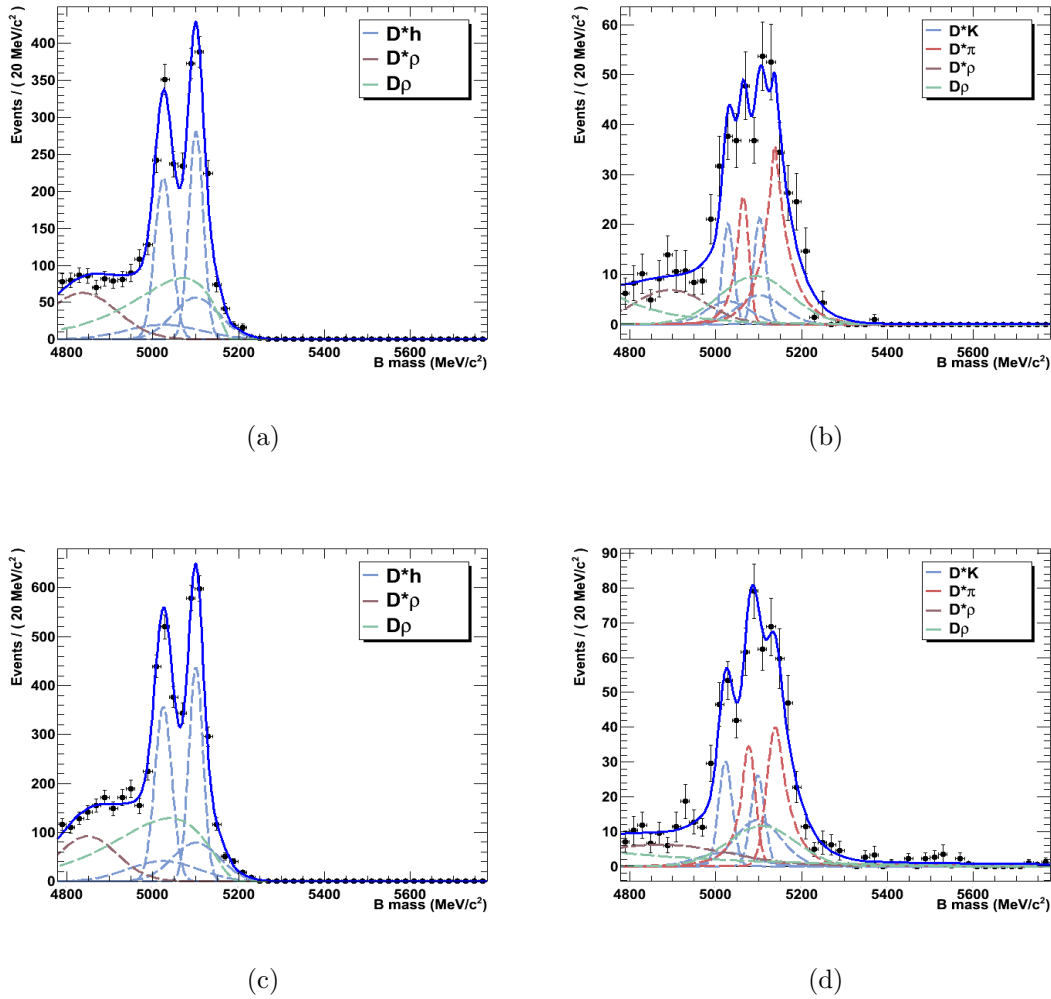


Figure 5.14: The total low-mass background $B^\pm \rightarrow D(K_S^0 \pi^+ \pi^-)h$ candidate mass distributions from MC. Figure 5.14(a) shows the LL $B^\pm \rightarrow D\pi^\pm$ distribution, Figure 5.14(b) shows the LL $B^\pm \rightarrow DK^\pm$ distribution; Figure 5.14(c) shows the DD $B^\pm \rightarrow D\pi^\pm$ distribution and Figure 5.14(d) shows the DD $B^\pm \rightarrow DK^\pm$ distribution. In all cases, the solid blue lines are the total summed PDFs.

The Category 6 (non-resonant) background was assumed to be indistinguishable from the signal or cross-feed contributions in the data mass fits of LL B^\pm candidates, as found in the studies of Chapter 4. Therefore, the ratio of yields extracted from the fit must be corrected for the background contribution in the LL case, so that

$$\frac{\text{Br}(B^\pm \rightarrow DK^\pm)}{\text{Br}(B^\pm \rightarrow D\pi^\pm)} = \frac{N_{B^\pm \rightarrow DK^\pm}^{sig,fit}}{N_{B^\pm \rightarrow D\pi^\pm}^{sig,fit}} \cdot \frac{(1 + F_{D\pi})}{(1 + F_{DK})} \cdot \frac{\epsilon_{B^\pm \rightarrow D\pi^\pm}}{\epsilon_{B^\pm \rightarrow DK^\pm}}. \quad (5.4)$$

To estimate F_{DK} and $F_{D\pi}$, the $B^\pm \rightarrow D(\pi\pi\pi\pi)h$ and $B^\pm \rightarrow D(K_S^0\pi^+\pi^-)h$ selection efficiency values obtained from MC10 in Chapter 4 were used, but the luminosity weighting was changed; the resulting values of F_{DK} and $F_{D\pi}$ were found to be $F_{DK} = 0.26 \pm 0.02$ and $F_{D\pi} = 0.25 \pm 0.02$, where the errors were estimated using toy MC (see Section 5.5).

It was confirmed using MC10 $B^\pm \rightarrow D(\pi\pi\pi\pi)h$ samples that the Category 6 background was negligible for the DD case, as expected. The expression for the ratio of branching fractions for DD candidates is therefore

$$\frac{\text{Br}(B^\pm \rightarrow DK^\pm)}{\text{Br}(B^\pm \rightarrow D\pi^\pm)} = \frac{N_{B^\pm \rightarrow DK^\pm}^{sig,fit}}{N_{B^\pm \rightarrow D\pi^\pm}^{sig,fit}} \cdot \frac{\epsilon_{B^\pm \rightarrow D\pi^\pm}}{\epsilon_{B^\pm \rightarrow DK^\pm}}. \quad (5.5)$$

In both LL and DD cases, the efficiencies appearing in the branching fraction ratio are the products

$$\epsilon_{B^\pm \rightarrow D\pi^\pm} = \epsilon_{B^\pm \rightarrow D\pi^\pm}^{acceptance} \cdot \epsilon_{B^\pm \rightarrow D\pi^\pm}^{reco} \cdot \epsilon_{B^\pm \rightarrow D\pi^\pm}^{trigger} \cdot \epsilon_{B^\pm \rightarrow D\pi^\pm}^{stripping} \cdot \epsilon_{B^\pm \rightarrow D\pi^\pm}^{sel,kin} \cdot \epsilon_{B^\pm \rightarrow D\pi^\pm}^{sel,PID} \quad (5.6)$$

and

$$\epsilon_{B^\pm \rightarrow DK^\pm} = \epsilon_{B^\pm \rightarrow DK^\pm}^{acceptance} \cdot \epsilon_{B^\pm \rightarrow DK^\pm}^{reco} \cdot \epsilon_{B^\pm \rightarrow DK^\pm}^{trigger} \cdot \epsilon_{B^\pm \rightarrow DK^\pm}^{stripping} \cdot \epsilon_{B^\pm \rightarrow DK^\pm}^{sel,kin} \cdot \epsilon_{B^\pm \rightarrow DK^\pm}^{sel,PID}. \quad (5.7)$$

5.2.2 Fit to 2011 data

In order to extract the ratio of numbers of signal candidates $N_{B^\pm \rightarrow DK^\pm}^{sig,fit} / N_{B^\pm \rightarrow D\pi^\pm}^{sig,fit}$ from the data, the mass distributions of the reconstructed $B^\pm \rightarrow DK^\pm$ and $B^\pm \rightarrow D\pi^\pm$ candidates, each including both magnet up and down candidates, were fitted simultaneously. The PDFs for the LL and DD candidate fits were chosen according to the results of the MC signal and background fits described in the previous section. It was assumed that an exponential PDF could be used for the combinatoric type Category 1 and 3

backgrounds.

The same contributing components were used in both the LL and DD fits. The overall fit expression, \mathcal{F} , was therefore:

$$\begin{aligned}
\mathcal{F} = & R \cdot N_{B^\pm \rightarrow D\pi^\pm}^{sig,fit} \cdot g_{DK}^{sig,fit} + N_{B^\pm \rightarrow DK^\pm}^{exp,comb} \cdot g_{DK}^{exp,comb} + N_{B^\pm \rightarrow DK^\pm}^{D^*K^a} \cdot g_{DK}^{D^*K^a} \\
& + N_{B^\pm \rightarrow DK^\pm}^{D^*K^b} \cdot g_{DK}^{D^*K^b} + N_{B^\pm \rightarrow DK^\pm}^{D^*\pi^a} \cdot g_{DK}^{D^*\pi^a} + N_{B^\pm \rightarrow DK^\pm}^{D^*\pi^b} \cdot g_{DK}^{D^*\pi^b} \\
& + N_{B^\pm \rightarrow DK^\pm}^{D^*\rho} \cdot g_{DK}^{D^*\rho} + N_{B^\pm \rightarrow DK^\pm}^{D\rho} \cdot g_{DK}^{D\rho} + N_{B^\pm \rightarrow DK^\pm}^{cross-feed} \cdot g_{DK}^{cross-feed} \\
& + N_{B^\pm \rightarrow D\pi^\pm}^{sig,fit} \cdot g_{D\pi}^{sig,fit} + N_{B^\pm \rightarrow D\pi^\pm}^{exp,comb} \cdot g_{D\pi}^{exp,comb} + N_{B^\pm \rightarrow D\pi^\pm}^{D^*h^a} \cdot g_{D\pi}^{D^*h^a} \\
& + N_{B^\pm \rightarrow D\pi^\pm}^{D^*h^b} \cdot g_{D\pi}^{D^*h^b} + N_{B^\pm \rightarrow D\pi^\pm}^{D^*\rho} \cdot g_{D\pi}^{D^*\rho} + N_{B^\pm \rightarrow D\pi^\pm}^{D\rho} \cdot g_{D\pi}^{D\rho} \\
& + N_{B^\pm \rightarrow D\pi^\pm}^{cross-feed} \cdot g_{D\pi}^{cross-feed}
\end{aligned} \tag{5.8}$$

where $N_{B^\pm \rightarrow Dh}^{type}$ is the number of candidates of each *type* of background or signal, g_{Dh}^{type} is the PDF for each *type* and R is the ratio $N_{B^\pm \rightarrow DK^\pm}^{sig,fit} / N_{B^\pm \rightarrow D\pi^\pm}^{sig,fit}$. In each of the LL and DD fits, the sum over the number of candidates of each type is constrained to be equal to the total number of LL or DD candidates in the data sample, $\sum_{type} N_{B^\pm \rightarrow Dh}^{type} = N_{B^\pm \rightarrow Dh}^{total}$.

The $B^\pm \rightarrow DK^\pm$ PDF components for the signal and each type of background were:

- a Gaussian plus Crystal Ball PDF, $g_{DK}^{sig,fit}$, for the signal (and Category 6 background in the LL case), with the same mean. The yield of candidates under the Crystal Ball PDF compared to the yield under the signal Gaussian was fixed to be the same as the proportion from the MC signal fit;
- an exponential PDF, $g_{DK}^{exp,comb}$, for the combinatoric type backgrounds (Categories 1 and 3);
- for the D^*K low-mass background (Category 4), sums of four Gaussian PDFs in two pairs, $g_{DK}^{D^*K^a}$ and $g_{DK}^{D^*K^b}$; in each pair, the yield of candidates under the broader Gaussian PDF compared to the yield under the narrower Gaussian PDF was fixed to be the same as the proportion from the MC signal fit;
- for the $D^*\pi$ low-mass background (Category 4), sums of two double Crystal Ball PDFs, $g_{DK}^{D^*\pi^a}$ and $g_{DK}^{D^*\pi^b}$;
- a Gaussian PDF, $g_{DK}^{D^*\rho}$, for the $D^*\rho$ low-mass background (Category 4);

- a Gaussian plus exponential PDF, $g_{DK}^{D\rho}$, for the $D\rho$ low-mass background (Category 5), with the yield of candidates under the exponential PDF compared to the yield under the Gaussian fixed to be the same as the proportion from the MC signal fit; and
- a double Crystal Ball function, $g_{DK}^{\text{cross-feed}}$, for the cross-feed ($B^\pm \rightarrow D\pi^\pm$ misidentified as $B^\pm \rightarrow DK^\pm$, Category 2).

The contributing $B^\pm \rightarrow D\pi^\pm$ PDF components were:

- a Gaussian plus Crystal Ball PDF, $g_{D\pi}^{\text{sig,fit}}$, for the signal (and Category 6 background in the LL case), with the same mean. The yield of candidates under the Crystal Ball PDF compared to the yield under the signal Gaussian was fixed to be the same as the proportion from the MC signal fit;
- an exponential PDF, $g_{D\pi}^{\text{exp,comb}}$, for the combinatoric type backgrounds (Categories 1 and 3);
- for the D^*h low-mass background (Category 4), sums of four Gaussian PDFs in two pairs, $g_{D\pi}^{D^*h a}$ and $g_{D\pi}^{D^*h b}$; in each pair, the yield of candidates under the broader Gaussian PDF compared to the yield under the narrower Gaussian PDF was fixed to be the same as the proportion from the MC signal fit;
- a Gaussian PDF, $g_{D\pi}^{D^*\rho}$, for the $D^*\rho$ low-mass background (Category 4);
- an ARGUS PDF, $g_{D\pi}^{D\rho}$, for the $D\rho$ low-mass background (Category 5); and
- a double Crystal Ball function, $g_{D\pi}^{\text{cross-feed}}$, for the cross-feed ($B^\pm \rightarrow DK^\pm$ misidentified as $B^\pm \rightarrow D\pi^\pm$, Category 2).

It was assumed that the various Category 4 and 5 background PDFs used were adequate in describing the low-mass regions of the distributions as each represents a different number and type of particle missed in candidate reconstruction. A specific PDF for background candidates from semi-leptonic decays, $B \rightarrow Dl\nu$, was not included in the fit. In the muonic case, this background has been found elsewhere [66] for $B^\pm \rightarrow D(hh)h$ decays to be non-peaking in the mass range considered in this analysis and well-fitted with a Gaussian PDF tail in the low-mass region. The most significant contribution from this background is far from the signal mass peak, however the upper extent of the tail infringes slightly on the signal mass peak region, particularly in the $B^\pm \rightarrow D\pi^\pm$ case.

In the case where l is an electron, the contribution should not extend under the signal mass peaks as the mass of an electron is much smaller than that of a kaon or pion. In either case, it was assumed that the candidates would be accounted for either by the combinatoric exponential PDF or one of the other low-mass background PDFs.

In total, eight parameters were left free in each fit:

- the yield of $B^\pm \rightarrow D\pi^\pm$ signal candidates $N_{B^\pm \rightarrow D\pi^\pm}^{sig,fit}$;
- the ratio of yields R ;
- the mean and width of the Gaussian part of $g_{D\pi}^{sig,fit}$;
- the powers of the combinatoric exponentials $g_{DK}^{exp,comb}$ and $g_{D\pi}^{exp,comb}$; and
- the widths of the cross-feed double Crystal Ball functions $g_{Dh}^{cross-feed}$.

The remaining parameters were constrained:

- the yields of candidates in each Category of background ($N_{B^\pm \rightarrow Dh}^{type}$) were constrained to be greater than or equal to zero;
- the cross-feed yields ($N_{B^\pm \rightarrow Dh}^{cross-feed}$) in each distribution were fixed using the signal yields from the other distribution and the efficiencies of the bachelor PID requirements; for example, in the $B^\pm \rightarrow DK^\pm$ distribution, the yield of $B^\pm \rightarrow D\pi^\pm$ mis-reconstructed as $B^\pm \rightarrow DK^\pm$ was fixed as

$$N_{B^\pm \rightarrow DK^\pm}^{cross-feed} = N_{B^\pm \rightarrow D\pi^\pm}^{sig,fit} \cdot \frac{\langle \epsilon_{\Delta LL(K-\pi)} > 0.0 \rangle}{\langle \epsilon_{\Delta LL(K-\pi)} < 0.0 \rangle}. \quad (5.9)$$

Individual magnet up and down PID requirement efficiencies were found using the data-based calibration technique described in detail in Section 4.4 and below in Section 5.3, and then luminosity-weighted averages of the efficiencies were used to evaluate the ratio appearing in Equation 5.9. For the example of Equation 5.9, the efficiencies were calculated from pion calibration samples, weighted with the kinematics of bachelor pion tracks from $B^\pm \rightarrow D\pi^\pm$ signal MC10 candidates;

- the mean and width of the Gaussian part of $g_{DK}^{sig,fit}$ was constrained to be the same as for the $B^\pm \rightarrow D\pi^\pm$ case;

- the parameters of the Crystal Ball parts of $g_{Dh}^{sig,fit}$, except the means, were fixed to the values obtained from the fits to MC; the means were constrained to be the same as the mean of the Gaussian parts of $g_{Dh}^{sig,fit}$;
- the parameters of the low-mass background PDFs were all fixed; excluding the mass-related parameters such as means and the ARGUS high mass cut-off, the parameters were fixed to values obtained from the fits to MC shown in Section 5.2.1; and
- the cross-feed double Crystal Ball function tail parameters were fixed to values obtained from the fits to MC shown in Section 5.2.1; the means were fixed but not to the values from the MC fits.

In the data set under consideration, there was a difference between the reconstructed candidate masses and the global average values from reference [18]. This was largely due to a mis-alignment of the detector [177]. In order to estimate the shifts of the double Crystal Ball means and the low-mass PDF means and ARGUS high mass cut-off from the MC fit values, an initial fit to the data was performed with the means fixed to the MC fit values. The mean of the signal $B^\pm \rightarrow D\pi^\pm$ Gaussian in data was found; the difference between this value and the global average B^\pm mass was $8.8 \text{ MeV}/c^2$ in the LL case and $8.2 \text{ MeV}/c^2$ in the DD case. In the final fits, the double Crystal Ball and low-mass PDF mean values and the ARGUS high mass cut-off value were therefore fixed at $8.8 \text{ MeV}/c^2$ below the MC fitted values in the LL case and $8.2 \text{ MeV}/c^2$ below the MC fitted values in the DD case.

5.2.3 Fit results and ratio of yields

Tables 5.3 and 5.4 show the fitted yields and parameter values and Figures 5.15 and 5.16 show the resulting fitted B^\pm mass distributions. The total $B^\pm \rightarrow D\pi^\pm$ yield observed in the data was 1100_{-36}^{+37} LL candidates and 669 ± 31 DD candidates. The ratio of yields from the fit, R , was found to be

$$R = 0.10 \pm 0.02 \tag{5.10}$$

in the LL case and

$$R = 0.07 \pm 0.02 \tag{5.11}$$

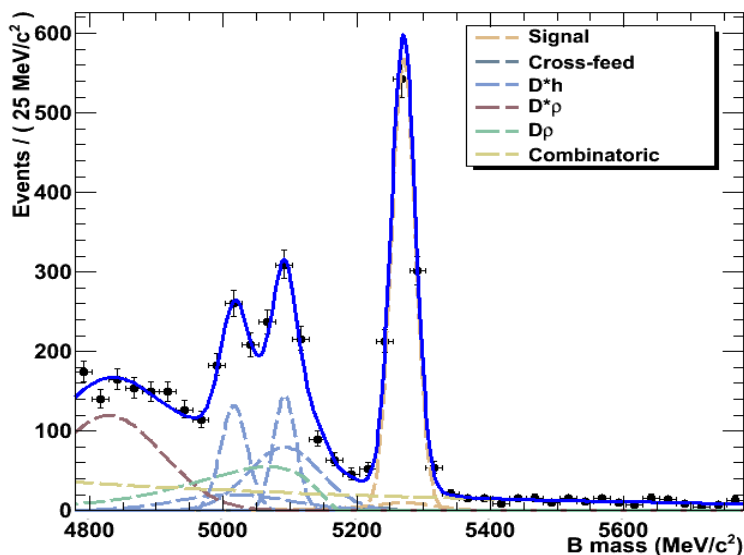
in the DD case, where the errors are statistical only.

Parameter	Fitted yield/value	Parameter	Fitted value
R	0.10 ± 0.02	$g_{DK}^{D^*K^a} \mu$	$5020 \text{ MeV}/c^2$
$N_{B^\pm \rightarrow DK^\pm}^{exp,comb}$	969_{-199}^{+159}	$g_{DK}^{D^*K^a} \sigma$	$13 \text{ MeV}/c^2$
$N_{B^\pm \rightarrow DK^\pm}^{D^*K^a}$	15 ± 16	$g_{DK}^{D^*K^a} \text{ resolution } \sigma$	$51 \text{ MeV}/c^2$
$N_{B^\pm \rightarrow DK^\pm}^{D^*K^b}$	44_{-19}^{+18}	$g_{DK}^{D^*K^b} \mu$	$5095 \text{ MeV}/c^2$
$N_{B^\pm \rightarrow DK^\pm}^{D^*\pi^a}$	63_{-26}^{+25}	$g_{DK}^{D^*K^b} \sigma$	$14 \text{ MeV}/c^2$
$N_{B^\pm \rightarrow DK^\pm}^{D^*\pi^b}$	101_{-48}^{+39}	$g_{DK}^{D^*K^b} \text{ resolution } \sigma$	$52 \text{ MeV}/c^2$
$N_{B^\pm \rightarrow DK^\pm}^{D^*\rho}$	82_{-78}^{+73}	$g_{DK}^{D^*\pi^a} \alpha$	5
$N_{B^\pm \rightarrow DK^\pm}^{D\rho}$	80 ± 258	$g_{DK}^{D^*\pi^a} \beta$	0.7
$N_{B^\pm \rightarrow D\pi^\pm}^{sig,fit}$	1100_{-36}^{+37}	$g_{DK}^{D^*\pi^a} \mu$	$5056 \text{ MeV}/c^2$
$N_{B^\pm \rightarrow D\pi^\pm}^{exp,comb}$	763_{-115}^{+136}	$g_{DK}^{D^*\pi^a} \sigma$	$13 \text{ MeV}/c^2$
$N_{B^\pm \rightarrow D\pi^\pm}^{D^*h^a}$	438_{-58}^{+59}	$g_{DK}^{D^*\pi^a} l$	9.5
$N_{B^\pm \rightarrow D\pi^\pm}^{D^*h^b}$	680 ± 62	$g_{DK}^{D^*\pi^a} n$	10
$N_{B^\pm \rightarrow D\pi^\pm}^{D^*\rho}$	703_{-81}^{+72}	$g_{DK}^{D^*\pi^b} \alpha$	0.35
$N_{B^\pm \rightarrow D\pi^\pm}^{D\rho}$	499 ± 130	$g_{DK}^{D^*\pi^b} \beta$	0.4
$g_{DK}^{sig,fit} \text{ CB } \sigma$	$23.0 \text{ MeV}/c^2$	$g_{DK}^{D^*\pi^b} \mu$	$5129 \text{ MeV}/c^2$
$g_{DK}^{sig,fit} \text{ CB } \alpha$	2.1	$g_{DK}^{D^*\pi^b} \sigma$	$12 \text{ MeV}/c^2$
$g_{DK}^{sig,fit} \text{ CB } n$	1.8	$g_{DK}^{D^*\pi^b} l$	15
$g_{D\pi}^{sig,fit} \text{ CB } \sigma$	$48.0 \text{ MeV}/c^2$	$g_{DK}^{D^*\pi^b} n$	20
$g_{D\pi}^{sig,fit} \text{ CB } \alpha$	0.62	$g_{DK}^{D^*\rho} \mu$	$4885 \text{ MeV}/c^2$
$g_{D\pi}^{sig,fit} \text{ CB } n$	10.0	$g_{DK}^{D^*\rho} \sigma$	$84 \text{ MeV}/c^2$
$g_{DK}^{sig,fit}, g_{D\pi}^{sig,fit} \mu$	$5270.1 \pm 0.6 \text{ MeV}/c^2$	$g_{DK}^{D\rho} \mu$	$5084 \text{ MeV}/c^2$
$g_{DK}^{sig,fit}, g_{D\pi}^{sig,fit} \text{ Gaus } \sigma$	$18.1_{-0.5}^{+0.6} \text{ MeV}/c^2$	$g_{DK}^{D\rho} \sigma$	$82 \text{ MeV}/c^2$
$g_{DK}^{exp,comb} \text{ power}$	$(-1.6_{-0.4}^{+0.6}) \times 10^{-3}$	$g_{DK}^{D\rho} \text{ exp power}$	-8×10^{-3}
$g_{D\pi}^{exp,comb} \text{ power}$	$(-1.4 \pm 0.4) \times 10^{-3}$	$g_{D\pi}^{D^*h^a} \mu$	$5016 \text{ MeV}/c^2$
$g_{DK}^{cross-feed} \alpha$	1.2	$g_{D\pi}^{D^*h^a} \sigma$	$20 \text{ MeV}/c^2$
$g_{DK}^{cross-feed} \beta$	1.6	$g_{D\pi}^{D^*h^a} \text{ resolution } \sigma$	$88 \text{ MeV}/c^2$
$g_{DK}^{cross-feed} \mu$	$5309 \text{ MeV}/c^2$	$g_{D\pi}^{D^*h^b} \mu$	$5092.2 \text{ MeV}/c^2$
$g_{DK}^{cross-feed} \sigma$	$24 \pm 3 \text{ MeV}/c^2$	$g_{D\pi}^{D^*h^b} \sigma$	$17 \text{ MeV}/c^2$
$g_{DK}^{cross-feed} l$	2.5	$g_{D\pi}^{D^*h^b} \text{ resolution } \sigma$	$54 \text{ MeV}/c^2$
$g_{DK}^{cross-feed} n$	2.4	$g_{D\pi}^{D^*\rho} \mu$	$4828 \text{ MeV}/c^2$
$g_{D\pi}^{cross-feed} \alpha$	1.7	$g_{D\pi}^{D^*\rho} \sigma$	$80 \text{ MeV}/c^2$
$g_{D\pi}^{cross-feed} \beta$	1.1	$g_{D\pi}^{D\rho} m_0$	$5174 \text{ MeV}/c^2$
$g_{D\pi}^{cross-feed} \mu$	$5236 \text{ MeV}/c^2$	$g_{D\pi}^{D\rho} c$	-35
$g_{D\pi}^{cross-feed} \sigma$	$16 \pm 5 \text{ MeV}/c^2$	$g_{D\pi}^{D\rho} p$	1.5
$g_{D\pi}^{cross-feed} l$	3		
$g_{D\pi}^{cross-feed} n$	3		

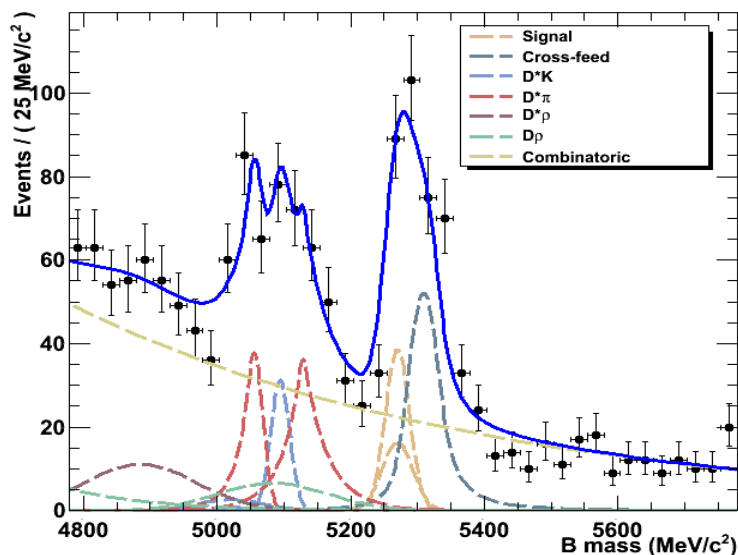
Table 5.3: The fitted yield and parameter values in the LL case.

Parameter	Fitted yield/value	Parameter	Fitted value
R	0.07 ± 0.02	$g_{DK}^{D^*K^a} \mu$	$5015 \text{ MeV}/c^2$
$N_{B^\pm \rightarrow DK^\pm}^{exp,comb}$	1191_{-195}^{+58}	$g_{DK}^{D^*K^a} \sigma$	$16 \text{ MeV}/c^2$
$N_{B^\pm \rightarrow DK^\pm}^{D^*K^a}$	11 ± 7	$g_{DK}^{D^*K^a} \text{ resolution } \sigma$	$64 \text{ MeV}/c^2$
$N_{B^\pm \rightarrow DK^\pm}^{D^*K^b}$	41_{-27}^{+25}	$g_{DK}^{D^*K^b} \mu$	$5090 \text{ MeV}/c^2$
$N_{B^\pm \rightarrow DK^\pm}^{D^*\pi^a}$	44_{-38}^{+30}	$g_{DK}^{D^*K^b} \sigma$	$16 \text{ MeV}/c^2$
$N_{B^\pm \rightarrow DK^\pm}^{D^*\pi^b}$	42_{-39}^{+21}	$g_{DK}^{D^*K^b} \text{ resolution } \sigma$	$54 \text{ MeV}/c^2$
$N_{B^\pm \rightarrow DK^\pm}^{D^*\rho}$	$5 \times 10^{-5} \pm 191$	$g_{DK}^{D^*\pi^a} \alpha$	2.3
$N_{B^\pm \rightarrow DK^\pm}^{D\rho}$	21 ± 369	$g_{DK}^{D^*\pi^a} \beta$	0.8
$N_{B^\pm \rightarrow D\pi^\pm}^{sig,fit}$	669 ± 31	$g_{DK}^{D^*\pi^a} \mu$	$5068 \text{ MeV}/c^2$
$N_{B^\pm \rightarrow D\pi^\pm}^{exp,comb}$	932_{-123}^{+142}	$g_{DK}^{D^*\pi^a} \sigma$	$16 \text{ MeV}/c^2$
$N_{B^\pm \rightarrow D\pi^\pm}^{D^*h^a}$	402 ± 57	$g_{DK}^{D^*\pi^a} l$	3.4
$N_{B^\pm \rightarrow D\pi^\pm}^{D^*h^b}$	487 ± 43	$g_{DK}^{D^*\pi^a} n$	0.3
$N_{B^\pm \rightarrow D\pi^\pm}^{D^*\rho}$	478_{-75}^{+67}	$g_{DK}^{D^*\pi^b} \alpha$	0.6
$N_{B^\pm \rightarrow D\pi^\pm}^{D\rho}$	130_{-120}^{+121}	$g_{DK}^{D^*\pi^b} \beta$	2.7
$g_{DK}^{sig,fit} \text{ CB } \sigma$	$46.0 \text{ MeV}/c^2$	$g_{DK}^{D^*\pi^b} \mu$	$5131 \text{ MeV}/c^2$
$g_{DK}^{sig,fit} \text{ CB } \alpha$	0.8	$g_{DK}^{D^*\pi^b} \sigma$	$20 \text{ MeV}/c^2$
$g_{DK}^{sig,fit} \text{ CB } n$	5.0	$g_{DK}^{D^*\pi^b} l$	9
$g_{D\pi}^{sig,fit} \text{ CB } \sigma$	$33.0 \text{ MeV}/c^2$	$g_{DK}^{D^*\pi^b} n$	125
$g_{D\pi}^{sig,fit} \text{ CB } \alpha$	0.8	$g_{DK}^{D^*\rho} \mu$	$4862 \text{ MeV}/c^2$
$g_{D\pi}^{sig,fit} \text{ CB } n$	3.0	$g_{DK}^{D^*\rho} \sigma$	$160 \text{ MeV}/c^2$
$g_{DK}^{sig,fit}, g_{D\pi}^{sig,fit} \mu$	$5271.1 \pm 0.9 \text{ MeV}/c^2$	$g_{DK}^{D\rho} \mu$	$5100 \text{ MeV}/c^2$
$g_{DK}^{sig,fit}, g_{D\pi}^{sig,fit} \text{ Gaus } \sigma$	$18.4 \pm 0.9 \text{ MeV}/c^2$	$g_{DK}^{D\rho} \sigma$	$79 \text{ MeV}/c^2$
$g_{DK}^{exp,comb} \text{ power}$	$(-1.8_{-0.1}^{+0.4}) \times 10^{-3}$	$g_{DK}^{D\rho} \text{ exp power}$	-3.1×10^{-3}
$g_{D\pi}^{exp,comb} \text{ power}$	$(-1.2 \pm 0.4) \times 10^{-3}$	$g_{D\pi}^{D^*h^a} \mu$	$5017 \text{ MeV}/c^2$
$g_{DK}^{cross-feed} \alpha$	1.7	$g_{D\pi}^{D^*h^a} \sigma$	$20 \text{ MeV}/c^2$
$g_{DK}^{cross-feed} \beta$	2.2	$g_{D\pi}^{D^*h^a} \text{ resolution } \sigma$	$81 \text{ MeV}/c^2$
$g_{DK}^{cross-feed} \mu$	$5315 \text{ MeV}/c^2$	$g_{D\pi}^{D^*h^b} \mu$	$5092.7 \text{ MeV}/c^2$
$g_{DK}^{cross-feed} \sigma$	$22_{-6}^{+8} \text{ MeV}/c^2$	$g_{D\pi}^{D^*h^b} \sigma$	$16.5 \text{ MeV}/c^2$
$g_{DK}^{cross-feed} l$	1.2	$g_{D\pi}^{D^*h^b} \text{ resolution } \sigma$	$55 \text{ MeV}/c^2$
$g_{DK}^{cross-feed} n$	1.0	$g_{D\pi}^{D^*\rho} \mu$	$4841 \text{ MeV}/c^2$
$g_{D\pi}^{cross-feed} \alpha$	2.3	$g_{D\pi}^{D^*\rho} \sigma$	$69 \text{ MeV}/c^2$
$g_{D\pi}^{cross-feed} \beta$	2.1	$g_{D\pi}^{D\rho} m_0$	$5196.7 \text{ MeV}/c^2$
$g_{D\pi}^{cross-feed} \mu$	$5230 \text{ MeV}/c^2$	$g_{D\pi}^{D\rho} c$	-38
$g_{D\pi}^{cross-feed} \sigma$	$16 \pm 14 \text{ MeV}/c^2$	$g_{D\pi}^{D\rho} p$	2.4
$g_{D\pi}^{cross-feed} l$	0.7		
$g_{D\pi}^{cross-feed} n$	3		

Table 5.4: The fitted yield and parameter values in the DD case.

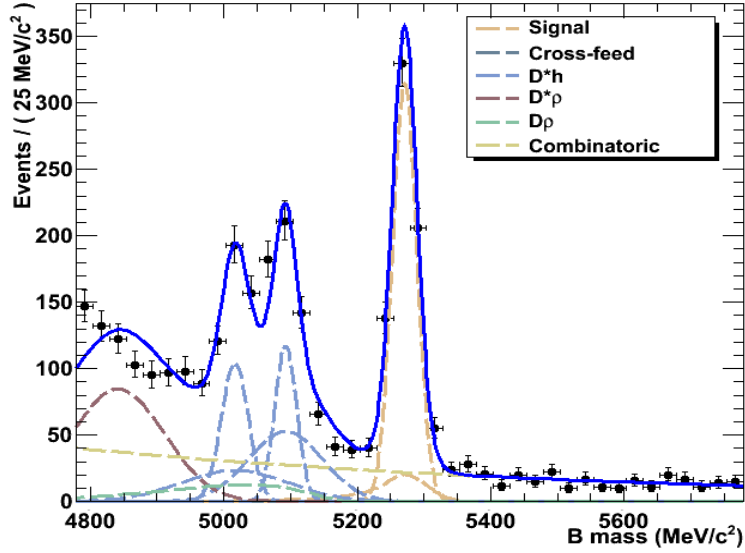


(a)

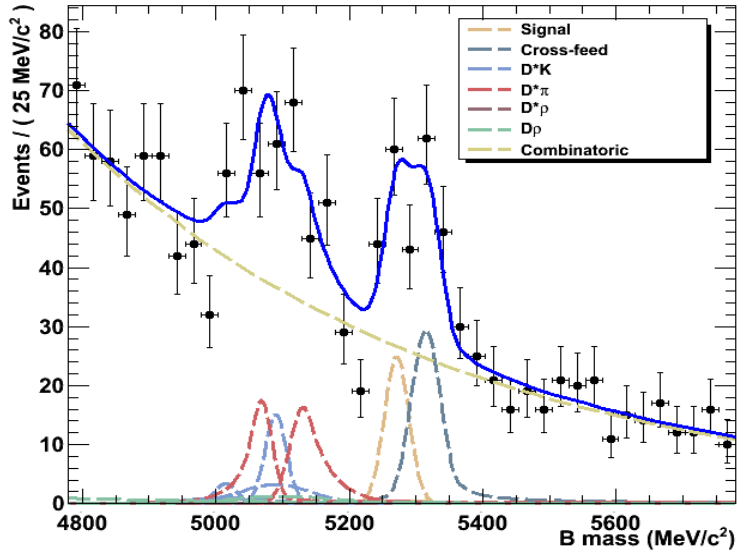


(b)

Figure 5.15: The fitted $B^\pm \rightarrow D(K_S^0 \pi^+ \pi^-) h$ LL candidate mass distributions from 342 pb^{-1} of 2011 data. Figure 5.15(a) shows the fitted $B^\pm \rightarrow D\pi^\pm$ LL distribution and Figure 5.15(b) shows the fitted $B^\pm \rightarrow DK^\pm$ LL distribution. The solid blue lines are the total PDFs.



(a)



(b)

Figure 5.16: The fitted $B^\pm \rightarrow D(K_S^0\pi^+\pi^-)h$ DD candidate mass distributions from 342 pb^{-1} of 2011 data. Figure 5.16(a) shows the fitted $B^\pm \rightarrow D\pi^\pm$ DD distribution and Figure 5.16(b) shows the fitted $B^\pm \rightarrow DK^\pm$ DD distribution. The solid blue lines are the total PDFs.

5.3 Determination of efficiencies

The efficiencies appearing in Equations 5.6 and 5.7 were calculated to allow the extraction of the ratio of branching fractions using Equations 5.4 and 5.5. It was again possible to use the MC10 simulation to find several of the relevant efficiencies, but not the PID efficiencies.

The acceptance efficiencies, $\epsilon_{B^\pm \rightarrow Dh}^{\text{acceptance}}$, were given by the generator factors of the respective MC10 signal $B^\pm \rightarrow D(K_S^0 \pi^+ \pi^-)h$ samples, as described in Chapter 4. Table 5.5 shows the generator factors found in the magnet up and magnet down cases. As the data set was not split into magnet up and magnet down contributions in the mass fit, average efficiencies, weighted according to the proportions of 2011 data recorded in the magnet up and down states, were used in the calculation of the ratio of branching fractions:

$$\langle \epsilon_{B^\pm \rightarrow Dh}^{\text{acceptance}} \rangle = \frac{143 \text{ pb}^{-1} \times \epsilon_{B^\pm \rightarrow Dh}^{\text{acceptance, magnet up}}}{342 \text{ pb}^{-1}} + \frac{199 \text{ pb}^{-1} \times \epsilon_{B^\pm \rightarrow Dh}^{\text{acceptance, magnet down}}}{342 \text{ pb}^{-1}}. \quad (5.12)$$

The resulting averages

$$\langle \epsilon_{B^\pm \rightarrow DK^\pm}^{\text{acceptance}} \rangle = 0.1665 \pm 0.0001$$

and

$$\langle \epsilon_{B^\pm \rightarrow D\pi^\pm}^{\text{acceptance}} \rangle = 0.1629 \pm 0.0001$$

are the same in the LL and DD cases. The statistical effects of the limited MC samples and the uncertainties on the integrated luminosity measurements both contribute to the errors on the weighted averages.

MC sample	Generator factor, $\epsilon_{B^\pm \rightarrow Dh}^{\text{acceptance}}$
$B^\pm \rightarrow DK^\pm$ magnet up	0.1663 ± 0.0002
$B^\pm \rightarrow DK^\pm$ magnet down	0.1666 ± 0.0002
$B^\pm \rightarrow D\pi^\pm$ magnet up	0.1627 ± 0.0002
$B^\pm \rightarrow D\pi^\pm$ magnet down	0.1630 ± 0.0002

Table 5.5: The acceptance efficiencies (generator factors) for the signal MC samples.

To obtain the combined efficiencies $\epsilon_{B^\pm \rightarrow Dh}^{reco} \cdot \epsilon_{B^\pm \rightarrow Dh}^{trigger} \cdot \epsilon_{B^\pm \rightarrow Dh}^{stripping} \cdot \epsilon_{B^\pm \rightarrow Dh}^{sel,kin}$ appearing in Equations 5.6 and 5.7, $B^\pm \rightarrow D(K_S^0 \pi^+ \pi^-)h$ candidates with LL and DD K_S^0 daughters were reconstructed from signal MC10 $B^\pm \rightarrow D(K_S^0 \pi^+ \pi^-)h$ samples with DaVinci and the full selection detailed in Section 5.1, including kinematic, stripping and trigger requirements, was applied. As for data, if multiple candidates were reconstructed and selected in a single event, the candidate with the largest value of B^\pm flight distance χ^2 from the PV was retained and the other candidates discarded. MC truth information was used to ensure the selected candidates were true signal decays. The flagged trigger information originally saved on the MC10 DSTs was not suitable for evaluating $\epsilon_{B^\pm \rightarrow Dh}^{trigger}$, because the trigger setting used in the MC10 production flagging step (*0x002e002a*) was not used in 2011 data-taking. Instead, the MC10 samples described in Section 5.2, where the trigger information had been replaced with the information from 2011 settings, were used to evaluate the efficiencies.

The resulting combined efficiencies are shown in Tables 5.6 and 5.7, with values quoted for each of the three 2011 trigger settings *0x005a0032*, *0x006d0032* and *0x00730035*. It can be seen that the combined efficiencies are identical for all three trigger settings. Weighted average efficiencies, calculated in a manner analagous to the acceptance efficiencies (Equation 5.12), are used in the branching fraction ratio calculation. Values of

$$\langle \epsilon_{B^\pm \rightarrow DK^\pm}^{reco} \epsilon_{B^\pm \rightarrow DK^\pm}^{trigger} \epsilon_{B^\pm \rightarrow DK^\pm}^{stripping} \epsilon_{B^\pm \rightarrow DK^\pm}^{sel,kin} \rangle = (1.20 \pm 0.02) \times 10^{-3}$$

and

$$\langle \epsilon_{B^\pm \rightarrow D\pi^\pm}^{reco} \epsilon_{B^\pm \rightarrow D\pi^\pm}^{trigger} \epsilon_{B^\pm \rightarrow D\pi^\pm}^{stripping} \epsilon_{B^\pm \rightarrow D\pi^\pm}^{sel,kin} \rangle = (1.21 \pm 0.02) \times 10^{-3}$$

were found in the LL case, and

$$\langle \epsilon_{B^\pm \rightarrow DK^\pm}^{reco} \epsilon_{B^\pm \rightarrow DK^\pm}^{trigger} \epsilon_{B^\pm \rightarrow DK^\pm}^{stripping} \epsilon_{B^\pm \rightarrow DK^\pm}^{sel,kin} \rangle = (1.50 \pm 0.02) \times 10^{-3}$$

and

$$\langle \epsilon_{B^\pm \rightarrow D\pi^\pm}^{reco} \epsilon_{B^\pm \rightarrow D\pi^\pm}^{trigger} \epsilon_{B^\pm \rightarrow D\pi^\pm}^{stripping} \epsilon_{B^\pm \rightarrow D\pi^\pm}^{sel,kin} \rangle = (1.58 \pm 0.02) \times 10^{-3}$$

were found in the DD case. The errors on the weighted averages include the uncertainties on the integrated luminosity measurements and the statistical effects of limited MC samples.

MC sample	Trigger setting	$\epsilon_{B^\pm \rightarrow Dh}^{reco} \epsilon_{B^\pm \rightarrow Dh}^{trigger} \epsilon_{B^\pm \rightarrow Dh}^{stripping} \epsilon_{B^\pm \rightarrow Dh}^{sel,kin}$
$B^\pm \rightarrow DK^\pm$ magnet up	<i>0x005a0032</i>	$(1.21 \pm 0.03) \times 10^{-3}$
$B^\pm \rightarrow DK^\pm$ magnet up	<i>0x006d0032</i>	$(1.21 \pm 0.03) \times 10^{-3}$
$B^\pm \rightarrow DK^\pm$ magnet up	<i>0x00730035</i>	$(1.21 \pm 0.03) \times 10^{-3}$
$B^\pm \rightarrow DK^\pm$ magnet down	<i>0x005a0032</i>	$(1.19 \pm 0.03) \times 10^{-3}$
$B^\pm \rightarrow DK^\pm$ magnet down	<i>0x006d0032</i>	$(1.19 \pm 0.03) \times 10^{-3}$
$B^\pm \rightarrow DK^\pm$ magnet down	<i>0x00730035</i>	$(1.19 \pm 0.03) \times 10^{-3}$
$B^\pm \rightarrow D\pi^\pm$ magnet up	<i>0x005a0032</i>	$(1.17 \pm 0.03) \times 10^{-3}$
$B^\pm \rightarrow D\pi^\pm$ magnet up	<i>0x006d0032</i>	$(1.17 \pm 0.03) \times 10^{-3}$
$B^\pm \rightarrow D\pi^\pm$ magnet up	<i>0x00730035</i>	$(1.17 \pm 0.03) \times 10^{-3}$
$B^\pm \rightarrow D\pi^\pm$ magnet down	<i>0x005a0032</i>	$(1.24 \pm 0.03) \times 10^{-3}$
$B^\pm \rightarrow D\pi^\pm$ magnet down	<i>0x006d0032</i>	$(1.24 \pm 0.03) \times 10^{-3}$
$B^\pm \rightarrow D\pi^\pm$ magnet down	<i>0x00730035</i>	$(1.24 \pm 0.03) \times 10^{-3}$

Table 5.6: The combined reconstruction and selection efficiencies for the signal MC samples, LL candidates.

MC sample	Trigger setting	$\epsilon_{B^\pm \rightarrow Dh}^{reco} \epsilon_{B^\pm \rightarrow Dh}^{trigger} \epsilon_{B^\pm \rightarrow Dh}^{stripping} \epsilon_{B^\pm \rightarrow Dh}^{sel,kin}$
$B^\pm \rightarrow DK^\pm$ magnet up	<i>0x005a0032</i>	$(1.48 \pm 0.03) \times 10^{-3}$
$B^\pm \rightarrow DK^\pm$ magnet up	<i>0x006d0032</i>	$(1.48 \pm 0.03) \times 10^{-3}$
$B^\pm \rightarrow DK^\pm$ magnet up	<i>0x00730035</i>	$(1.48 \pm 0.03) \times 10^{-3}$
$B^\pm \rightarrow DK^\pm$ magnet down	<i>0x005a0032</i>	$(1.51 \pm 0.03) \times 10^{-3}$
$B^\pm \rightarrow DK^\pm$ magnet down	<i>0x006d0032</i>	$(1.51 \pm 0.03) \times 10^{-3}$
$B^\pm \rightarrow DK^\pm$ magnet down	<i>0x00730035</i>	$(1.51 \pm 0.03) \times 10^{-3}$
$B^\pm \rightarrow D\pi^\pm$ magnet up	<i>0x005a0032</i>	$(1.57 \pm 0.03) \times 10^{-3}$
$B^\pm \rightarrow D\pi^\pm$ magnet up	<i>0x006d0032</i>	$(1.57 \pm 0.03) \times 10^{-3}$
$B^\pm \rightarrow D\pi^\pm$ magnet up	<i>0x00730035</i>	$(1.57 \pm 0.03) \times 10^{-3}$
$B^\pm \rightarrow D\pi^\pm$ magnet down	<i>0x005a0032</i>	$(1.59 \pm 0.03) \times 10^{-3}$
$B^\pm \rightarrow D\pi^\pm$ magnet down	<i>0x006d0032</i>	$(1.59 \pm 0.03) \times 10^{-3}$
$B^\pm \rightarrow D\pi^\pm$ magnet down	<i>0x00730035</i>	$(1.59 \pm 0.03) \times 10^{-3}$

Table 5.7: The combined reconstruction and selection efficiencies for the signal MC samples, DD candidates.

The efficiencies of the bachelor PID requirements were found using the data-based calibration technique described in detail in Section 4.4. Separate magnet up and mag-

net down calibration samples of pions and kaons from prompt $D^*(2010)^\pm \rightarrow D(K\pi)\pi^\pm$ decays in the 2011 data set were available. The calibration samples were weighted with the kinematic distributions of the bachelor tracks from selected $B^\pm \rightarrow D(K_S^0\pi^+\pi^-)h$ candidates in signal MC10, using a binning scheme of $18 \times 4 \times 4$ bins in momentum, pseudo-rapidity and number of tracks, respectively. Magnet up calibration tracks were weighted with magnet up MC tracks and magnet down calibration tracks with magnet down MC tracks; the weighting was performed three times in each case in order to find the efficiencies for the three trigger settings *0x005a0032*, *0x006d0032* and *0x00730035*. The resulting efficiencies are shown in Tables 5.8 and 5.9, where the quoted errors are statistical. Except for the DD $B^\pm \rightarrow D\pi^\pm$ magnet up case, the PID requirement efficiencies were the same for all three trigger settings.

The luminosity weighted average efficiencies were calculated to be

$$\langle \epsilon_{B^\pm \rightarrow DK^\pm}^{sel,PID} \rangle = 0.9458 \pm 0.0004$$

and

$$\langle \epsilon_{B^\pm \rightarrow D\pi^\pm}^{sel,PID} \rangle = 0.883 \pm 0.002$$

in the LL case and

$$\langle \epsilon_{B^\pm \rightarrow DK^\pm}^{sel,PID} \rangle = 0.9483 \pm 0.0004$$

and

$$\langle \epsilon_{B^\pm \rightarrow D\pi^\pm}^{sel,PID} \rangle = 0.8959 \pm 0.0007 \text{ (trigger settings } \textit{0x005a0032}, \textit{0x00730035})$$

or

$$\langle \epsilon_{B^\pm \rightarrow D\pi^\pm}^{sel,PID} \rangle = 0.8960 \pm 0.0007 \text{ (trigger setting } \textit{0x006d0032})$$

in the DD case. The errors on the luminosity weighted averages again include contributions from the uncertainties on the integrated luminosity measurements and the statistical errors from the limited sizes of the calibration samples used in the PID weighting technique. The averaged efficiencies were used for the calculation of the ratio of branching fractions; in the DD $B^\pm \rightarrow D\pi^\pm$ case, the value $\langle \epsilon_{B^\pm \rightarrow D\pi^\pm}^{sel,PID} \rangle = 0.8959 \pm 0.0007$ was used.

MC weighting sample	Trigger setting	$\epsilon_{B^\pm \rightarrow Dh}^{\text{sel},PID}$
$B^\pm \rightarrow DK^\pm$ bachelor, magnet up, kaon $\Delta LL(K - \pi) > 0.0$	<i>0x005a0032</i>	0.9495 ± 0.0005
$B^\pm \rightarrow DK^\pm$ bachelor, magnet up, kaon $\Delta LL(K - \pi) > 0.0$	<i>0x006d0032</i>	0.9495 ± 0.0005
$B^\pm \rightarrow DK^\pm$ bachelor, magnet up, kaon $\Delta LL(K - \pi) > 0.0$	<i>0x00730035</i>	0.9495 ± 0.0005
$B^\pm \rightarrow DK^\pm$ bachelor, magnet down, kaon $\Delta LL(K - \pi) > 0.0$	<i>0x005a0032</i>	0.9431 ± 0.0005
$B^\pm \rightarrow DK^\pm$ bachelor, magnet down, kaon $\Delta LL(K - \pi) > 0.0$	<i>0x006d0032</i>	0.9431 ± 0.0005
$B^\pm \rightarrow DK^\pm$ bachelor, magnet down, kaon $\Delta LL(K - \pi) > 0.0$	<i>0x00730035</i>	0.9431 ± 0.0005
$B^\pm \rightarrow D\pi^\pm$ bachelor, magnet up, pion $\Delta LL(K - \pi) < 0.0$	<i>0x005a0032</i>	0.9015 ± 0.0007
$B^\pm \rightarrow D\pi^\pm$ bachelor, magnet up, pion $\Delta LL(K - \pi) < 0.0$	<i>0x006d0032</i>	0.9015 ± 0.0007
$B^\pm \rightarrow D\pi^\pm$ bachelor, magnet up, pion $\Delta LL(K - \pi) < 0.0$	<i>0x00730035</i>	0.9015 ± 0.0007
$B^\pm \rightarrow D\pi^\pm$ bachelor, magnet down, pion $\Delta LL(K - \pi) < 0.0$	<i>0x005a0032</i>	0.870 ± 0.003
$B^\pm \rightarrow D\pi^\pm$ bachelor, magnet down, pion $\Delta LL(K - \pi) < 0.0$	<i>0x006d0032</i>	0.870 ± 0.003
$B^\pm \rightarrow D\pi^\pm$ bachelor, magnet down, pion $\Delta LL(K - \pi) < 0.0$	<i>0x00730035</i>	0.870 ± 0.003

Table 5.8: The PID requirement efficiencies for the weighted data calibration samples, LL candidates.

MC weighting sample	Trigger setting	$\epsilon_{B^\pm \rightarrow Dh}^{\text{sel},PID}$
$B^\pm \rightarrow DK^\pm$ bachelor, magnet up, kaon $\Delta LL(K - \pi) > 0.0$	<i>0x005a0032</i>	0.9499 ± 0.0006
$B^\pm \rightarrow DK^\pm$ bachelor, magnet up, kaon $\Delta LL(K - \pi) > 0.0$	<i>0x006d0032</i>	0.9499 ± 0.0006
$B^\pm \rightarrow DK^\pm$ bachelor, magnet up, kaon $\Delta LL(K - \pi) > 0.0$	<i>0x00730035</i>	0.9499 ± 0.0006
$B^\pm \rightarrow DK^\pm$ bachelor, magnet down, kaon $\Delta LL(K - \pi) > 0.0$	<i>0x005a0032</i>	0.9471 ± 0.0005
$B^\pm \rightarrow DK^\pm$ bachelor, magnet down, kaon $\Delta LL(K - \pi) > 0.0$	<i>0x006d0032</i>	0.9471 ± 0.0005
$B^\pm \rightarrow DK^\pm$ bachelor, magnet down, kaon $\Delta LL(K - \pi) > 0.0$	<i>0x00730035</i>	0.9471 ± 0.0005
$B^\pm \rightarrow D\pi^\pm$ bachelor, magnet up, pion $\Delta LL(K - \pi) < 0.0$	<i>0x005a0032</i>	0.9184 ± 0.0007
$B^\pm \rightarrow D\pi^\pm$ bachelor, magnet up, pion $\Delta LL(K - \pi) < 0.0$	<i>0x006d0032</i>	0.9185 ± 0.0007
$B^\pm \rightarrow D\pi^\pm$ bachelor, magnet up, pion $\Delta LL(K - \pi) < 0.0$	<i>0x00730035</i>	0.9184 ± 0.0007
$B^\pm \rightarrow D\pi^\pm$ bachelor, magnet down, pion $\Delta LL(K - \pi) < 0.0$	<i>0x005a0032</i>	0.8798 ± 0.0007
$B^\pm \rightarrow D\pi^\pm$ bachelor, magnet down, pion $\Delta LL(K - \pi) < 0.0$	<i>0x006d0032</i>	0.8798 ± 0.0007
$B^\pm \rightarrow D\pi^\pm$ bachelor, magnet down, pion $\Delta LL(K - \pi) < 0.0$	<i>0x00730035</i>	0.8798 ± 0.0007

Table 5.9: The PID requirement efficiencies for the weighted data calibration samples, DD candidates.

5.4 Evaluation of the ratio of branching fractions

The ratio of branching fractions was calculated, according to Equations 5.4 and 5.5. For LL candidates, the yield ratio from the mass fit ($R = 0.10 \pm 0.02$), the correction factors for $B^\pm \rightarrow D(\pi\pi\pi\pi)h$ decays ($F_{DK} = 0.26$ and $F_{D\pi} = 0.25$) and the efficiencies from Section 5.3 were used to give the result

$$\begin{aligned} \frac{\text{Br}(B^\pm \rightarrow DK^\pm)}{\text{Br}(B^\pm \rightarrow D\pi^\pm)} &= R \cdot \frac{(1 + F_{D\pi})}{(1 + F_{DK})} \cdot \frac{\langle \epsilon_{B^\pm \rightarrow D\pi^\pm}^{\text{acceptance}} \rangle}{\langle \epsilon_{B^\pm \rightarrow DK^\pm}^{\text{acceptance}} \rangle} \\ &\quad \cdot \frac{\langle \epsilon_{B^\pm \rightarrow D\pi^\pm}^{\text{reco}} \epsilon_{B^\pm \rightarrow D\pi^\pm}^{\text{trigger}} \epsilon_{B^\pm \rightarrow D\pi^\pm}^{\text{stripping}} \epsilon_{B^\pm \rightarrow D\pi^\pm}^{\text{sel,kin}} \rangle}{\langle \epsilon_{B^\pm \rightarrow DK^\pm}^{\text{reco}} \epsilon_{B^\pm \rightarrow DK^\pm}^{\text{trigger}} \epsilon_{B^\pm \rightarrow DK^\pm}^{\text{stripping}} \epsilon_{B^\pm \rightarrow DK^\pm}^{\text{sel,kin}} \rangle} \cdot \frac{\langle \epsilon_{B^\pm \rightarrow D\pi^\pm}^{\text{sel,PID}} \rangle}{\langle \epsilon_{B^\pm \rightarrow DK^\pm}^{\text{sel,PID}} \rangle} \\ &= 0.09 \pm 0.01 \end{aligned} \quad (5.13)$$

where the error is statistical only, coming from the error on R .

For DD candidates, the yield ratio from the mass fit ($R = 0.07 \pm 0.02$) and the efficiencies from Section 5.3 were used to give the result

$$\begin{aligned} \frac{\text{Br}(B^\pm \rightarrow DK^\pm)}{\text{Br}(B^\pm \rightarrow D\pi^\pm)} &= R \cdot \frac{\langle \epsilon_{B^\pm \rightarrow D\pi^\pm}^{\text{acceptance}} \rangle}{\langle \epsilon_{B^\pm \rightarrow DK^\pm}^{\text{acceptance}} \rangle} \cdot \frac{\langle \epsilon_{B^\pm \rightarrow D\pi^\pm}^{\text{reco}} \epsilon_{B^\pm \rightarrow D\pi^\pm}^{\text{trigger}} \epsilon_{B^\pm \rightarrow D\pi^\pm}^{\text{stripping}} \epsilon_{B^\pm \rightarrow D\pi^\pm}^{\text{sel,kin}} \rangle}{\langle \epsilon_{B^\pm \rightarrow DK^\pm}^{\text{reco}} \epsilon_{B^\pm \rightarrow DK^\pm}^{\text{trigger}} \epsilon_{B^\pm \rightarrow DK^\pm}^{\text{stripping}} \epsilon_{B^\pm \rightarrow DK^\pm}^{\text{sel,kin}} \rangle} \cdot \frac{\langle \epsilon_{B^\pm \rightarrow D\pi^\pm}^{\text{sel,PID}} \rangle}{\langle \epsilon_{B^\pm \rightarrow DK^\pm}^{\text{sel,PID}} \rangle} \\ &= 0.07 \pm 0.02 \end{aligned} \quad (5.14)$$

where the error is again statistical only, coming from the error on R . In this case the value of the combined ratio of efficiencies is such that the central value of the ratio of branching fractions is equal to the value of R at the level of precision of the measurement.

5.5 Systematic uncertainties

The systematic errors on the branching fraction ratios need to be taken into account, following the same procedures as detailed in Chapter 4. Errors related to:

1. the measurement of the accumulated integrated luminosity of data ($\sim 3.5\%$ uncertainty on the measurements);
2. the limited MC statistics for calculating the acceptance efficiencies (generator factor);

3. the limited MC statistics for calculating the reconstruction and selection efficiencies;
4. the limited data statistics for calculating the PID efficiencies;
5. the PID weighting technique; and
6. the PDF parameterisation used in the mass fit

need to be considered. In the LL case, the uncertainty from the evaluation of the level of Category 6 background was also included (limited MC statistics and global average branching fractions).

Errors 1 – 4 and the error related to Category 6 background in the LL case only were found using toy MC. The procedure was identical to that described in Section 4.6; in the LL case, errors on the ratio $\frac{(1 + F_{D\pi})}{(1 + F_{DK})} \cdot \frac{\epsilon_{B^\pm \rightarrow D\pi^\pm}}{\epsilon_{B^\pm \rightarrow DK^\pm}}$ from Equation 5.4 were evaluated, and in the DD case errors on the ratio $\frac{\epsilon_{B^\pm \rightarrow D\pi^\pm}}{\epsilon_{B^\pm \rightarrow DK^\pm}}$ from Equation 5.5 were estimated.

5.5.1 Systematic error from integrated luminosity measurements and statistical errors

The error on the ratio $\frac{(1 + F_{D\pi})}{(1 + F_{DK})} \cdot \frac{\epsilon_{B^\pm \rightarrow D\pi^\pm}}{\epsilon_{B^\pm \rightarrow DK^\pm}}$ from Equation 5.4, due to the uncertainties on the integrated luminosity measurements and the statistical errors on acceptance, reconstruction, trigger, stripping, kinematic selection and PID efficiencies, was found for the LL case. Gaussian distributions for each of these components were simultaneously randomly sampled with the global average branching fractions fixed. The resulting ratio distribution can be seen in Figure 5.17; the error is 0.02 and the fractional error on the ratio is also 0.02.

In the DD case, the error on the ratio $\frac{\epsilon_{B^\pm \rightarrow D\pi^\pm}}{\epsilon_{B^\pm \rightarrow DK^\pm}}$ from Equation 5.5 due to the uncertainties on the integrated luminosity measurements and the statistical errors on acceptance, selection and PID efficiencies was found. Gaussian distributions were simultaneously randomly sampled for all of the components. The resulting ratio distribution can be seen in Figure 5.18; the error is 0.02 and the fractional error on the ratio is also 0.02.

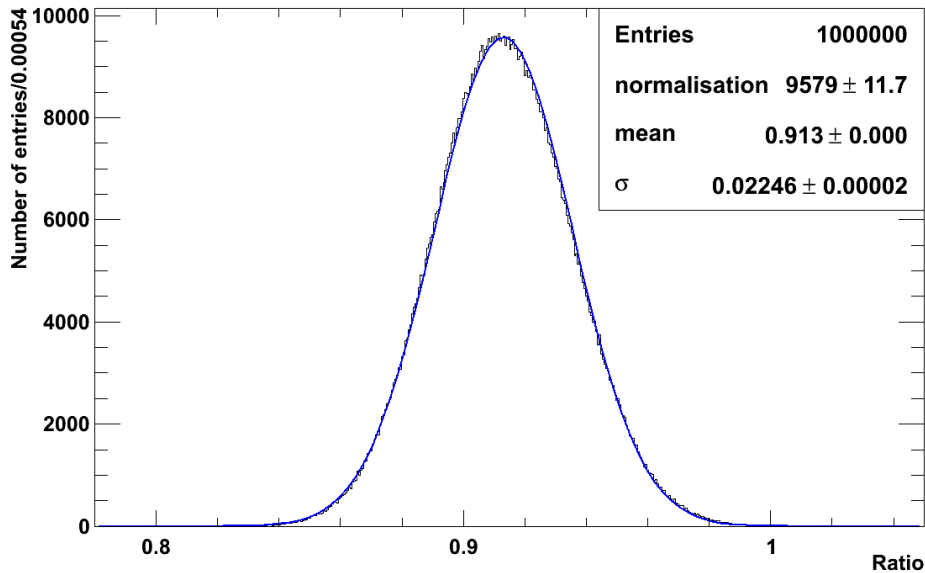


Figure 5.17: The toy MC distribution for the ratio $\frac{(1 + F_{D\pi})}{(1 + F_{DK})} \cdot \frac{\epsilon_{B^\pm \rightarrow D\pi^\pm}}{\epsilon_{B^\pm \rightarrow DK^\pm}}$, accounting for luminosity and statistical errors, LL case. The black histogram is the toy MC distribution and the blue Gaussian is fitted to this distribution.

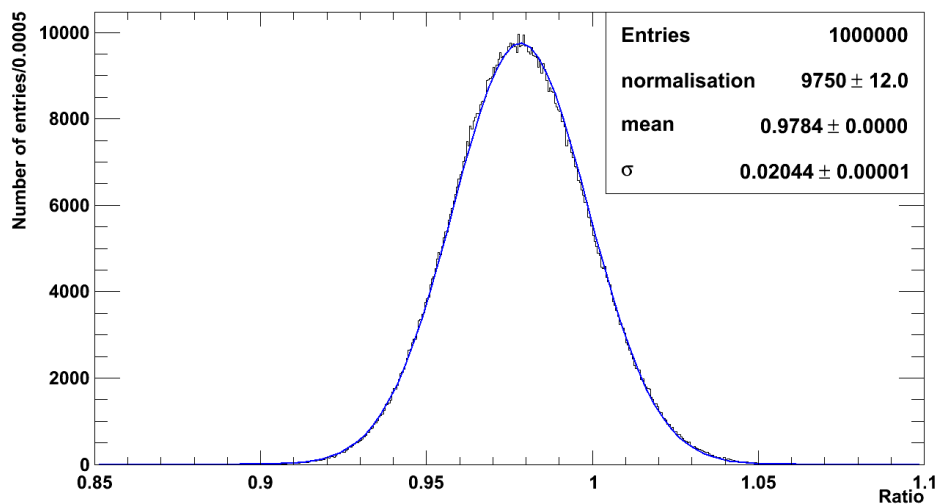


Figure 5.18: The toy MC distribution for the ratio $\frac{\epsilon_{B^\pm \rightarrow D\pi^\pm}}{\epsilon_{B^\pm \rightarrow DK^\pm}}$, accounting for luminosity and statistical errors, DD case. The black histogram is the toy MC distribution and the blue Gaussian is fitted to this distribution.

5.5.2 Systematic error from global average branching fraction errors

For LL candidates, the error on the ratio $\frac{(1 + F_{D\pi})}{(1 + F_{DK})} \cdot \frac{\epsilon_{B^\pm \rightarrow D\pi^\pm}}{\epsilon_{B^\pm \rightarrow DK^\pm}}$ from Equation 5.4 due to the inclusion of global average background fractions in $F_{D\pi}$ and F_{DK} was also found. Gaussian distributions for the branching fraction values were randomly sampled and the integrated luminosity measurements and the efficiencies were fixed. The resulting ratio distribution can be seen in Figure 5.19; the error is 0.0004 and the fractional error on the ratio is also 0.0004.

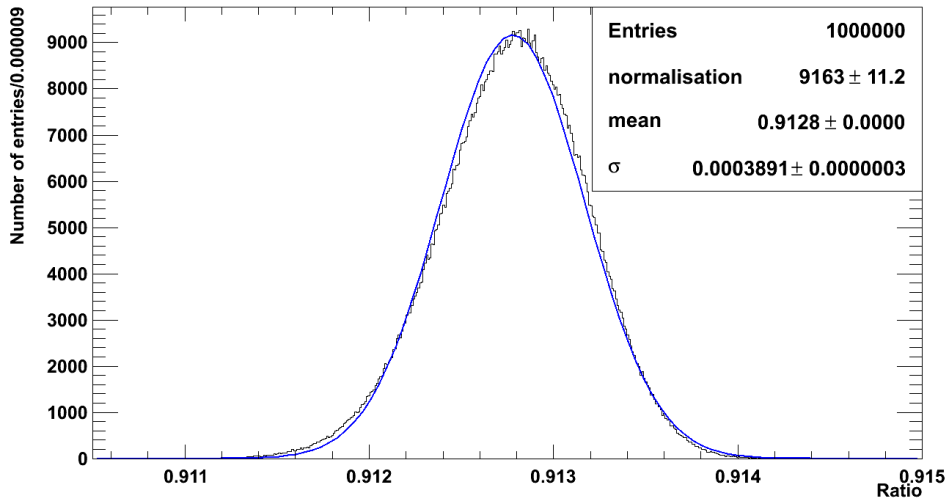


Figure 5.19: The toy MC distribution for the ratio $\frac{(1 + F_{D\pi})}{(1 + F_{DK})} \cdot \frac{\epsilon_{B^\pm \rightarrow D\pi^\pm}}{\epsilon_{B^\pm \rightarrow DK^\pm}}$, accounting for errors on the global average branching fractions, LL case. The black histogram is the toy MC distribution and the blue Gaussian is fitted to this distribution.

5.5.3 Systematic error from the determination of the PID efficiency

In order to estimate the non-statistical systematic uncertainty from the PID weighting technique, the values of magnet up and down PID requirement efficiencies were found from the unweighted data D^* decay calibration samples. As described in Section 4.6.4, the difference between the efficiency from the unweighted calibration data and the effi-

ciency from the weighted data was taken as a conservative estimate of the error on each efficiency from the weighted data. As the error was only estimated on one side of the weighted efficiency values, a half-normal distribution was assumed, and the full error was equal to the σ of this distribution, $\sqrt{\left(1 - \frac{2}{\pi}\right) \cdot |\epsilon_{weighted} - \epsilon_{unweighted}|}$. The full error on each of the efficiencies was propagated through the luminosity-weighted average efficiencies to give the overall error on the ratio of PID criterion efficiencies; uncertainties in the measurement of integrated luminosity and statistical errors from the PID weighting technique were not included in the propagation. This led to a fractional error on the efficiency ratio of

$$\frac{\sigma \left(\frac{\epsilon_{B^\pm \rightarrow D\pi^\pm}^{sel,PID}}{\epsilon_{B^\pm \rightarrow DK^\pm}^{sel,PID}} \right)}{\left(\frac{\epsilon_{B^\pm \rightarrow D\pi^\pm}^{sel,PID}}{\epsilon_{B^\pm \rightarrow DK^\pm}^{sel,PID}} \right)} = 0.01 \quad (5.15)$$

in the LL case and

$$\frac{\sigma \left(\frac{\epsilon_{B^\pm \rightarrow D\pi^\pm}^{sel,PID}}{\epsilon_{B^\pm \rightarrow DK^\pm}^{sel,PID}} \right)}{\left(\frac{\epsilon_{B^\pm \rightarrow D\pi^\pm}^{sel,PID}}{\epsilon_{B^\pm \rightarrow DK^\pm}^{sel,PID}} \right)} = 0.008 \quad (5.16)$$

in the DD case.

5.5.4 Systematic error from the mass fit PDF parameterisation

There were several possible sources of systematic error coming from the mass fits used to extract the yield ratio R , which is described in Section 5.2.

Signal Crystal Ball lineshape in $B^\pm \rightarrow D\pi^\pm$ and $B^\pm \rightarrow DK^\pm$ fits

In the nominal fits, a Gaussian and a Crystal Ball PDF were used to describe the shape of the signal $B^\pm \rightarrow D\pi^\pm$ and $B^\pm \rightarrow DK^\pm$ mass peaks, with the yield of candidates in the Crystal Balls fixed to be a certain proportion of the yield of candidates in the Gaussians. In order to conservatively estimate a systematic error due to this, the Crystal Ball components were removed completely from both fits. This led to a fractional error on the original yield ratio of

$$\frac{\sigma(R)}{R} = 0.006 \quad (5.17)$$

in the LL case and

$$\frac{\sigma(R)}{R} = 0.07 \quad (5.18)$$

in the DD case.

Low-mass PDFs in $B^\pm \rightarrow D\pi^\pm$ and $B^\pm \rightarrow DK^\pm$ fits

In the nominal fits, the low-mass background PDFs were constrained from various MC samples. These PDFs were replaced with two Gaussian PDFs in the $B^\pm \rightarrow D\pi^\pm$ case and one Gaussian PDF in the $B^\pm \rightarrow DK^\pm$ case, giving a fractional error on the original yield ratio of

$$\frac{\sigma(R)}{R} = 0.05 \quad (5.19)$$

in the LL case and

$$\frac{\sigma(R)}{R} = 0.1 \quad (5.20)$$

in the DD case.

Exponential PDFs in $B^\pm \rightarrow D\pi^\pm$ and $B^\pm \rightarrow DK^\pm$ fits

In both the $B^\pm \rightarrow D\pi^\pm$ and $B^\pm \rightarrow DK^\pm$ nominal fits, the combinatoric backgrounds were described using exponential PDFs. Changing these to second order polynomial PDFs in both cases gave a fractional error on the original yield ratio of

$$\frac{\sigma(R)}{R} = 0.04 \quad (5.21)$$

in the LL case and

$$\frac{\sigma(R)}{R} = 0.1 \quad (5.22)$$

in the DD case.

Cross-feed in $B^\pm \rightarrow D\pi^\pm$ and $B^\pm \rightarrow DK^\pm$ fits

In both LL and DD fits, the yield of cross-feed in each mass distribution was fixed using the signal yield from the other distribution and luminosity-averaged efficiencies from the PID weighting technique; see Equation 5.9. In order to estimate the systematic error due to fixing the ratio of PID efficiencies, $\langle \epsilon_{\Delta LL(K-\pi)>0.0} \rangle$ and $\langle \epsilon_{\Delta LL(K-\pi)<0.0} \rangle$ were increased and decreased by their errors (combined PID statistical and luminosity measurement) and the efficiency ratio was recalculated. The fit was then repeated with the changed efficiency ratio values in place. The maximum changes in the fitted yield ratio gave fractional errors on the original yield ratio of

$$\frac{\sigma(R)}{R} = 0.003 \quad (5.23)$$

in the LL case and

$$\frac{\sigma(R)}{R} = 0.005 \quad (5.24)$$

in the DD case.

5.5.5 Total systematic uncertainties

Tables 5.10 and 5.11 summarise the contributing systematic uncertainties, estimated as detailed above. The quoted errors are fractional errors on the ratio of interest, for example the mass fit uncertainties are of the form $\frac{\sigma(R)}{R}$. The errors were combined in quadrature to obtain the overall fractional error. The systematic uncertainties on the central branching fraction ratio values were found to be 0.006 for LL candidates and 0.01 for DD candidates.

Source of uncertainty	$\sigma(\text{ratio})/\text{ratio}$
Toy MC: global average branching fractions	0.0004
Toy MC: integrated luminosity, efficiency statistical errors	0.02
PID weighting, systematic	0.01
Mass fit signal Crystal Ball PDFs ($B^\pm \rightarrow D\pi^\pm$ and $B^\pm \rightarrow DK^\pm$)	0.006
Mass fit low-mass background PDFs ($B^\pm \rightarrow D\pi^\pm$ and $B^\pm \rightarrow DK^\pm$)	0.05
Mass fit exponential PDFs ($B^\pm \rightarrow D\pi^\pm$ and $B^\pm \rightarrow DK^\pm$)	0.04
Mass fit cross-feed ($B^\pm \rightarrow D\pi^\pm$ and $B^\pm \rightarrow DK^\pm$)	0.003
Total fractional error = $\sqrt{\Sigma (\sigma(\text{ratio})/\text{ratio})^2}$	0.07

Table 5.10: A summary of the systematic errors in the LL case.

Source of uncertainty	$\sigma(\text{ratio})/\text{ratio}$
Toy MC: integrated luminosity, efficiency statistical errors	0.02
PID weighting, systematic	0.008
Mass fit signal Crystal Ball PDFs ($B^\pm \rightarrow D\pi^\pm$ and $B^\pm \rightarrow DK^\pm$)	0.07
Mass fit low-mass background PDFs ($B^\pm \rightarrow D\pi^\pm$ and $B^\pm \rightarrow DK^\pm$)	0.1
Mass fit exponential PDFs ($B^\pm \rightarrow D\pi^\pm$ and $B^\pm \rightarrow DK^\pm$)	0.1
Mass fit cross-feed ($B^\pm \rightarrow D\pi^\pm$ and $B^\pm \rightarrow DK^\pm$)	0.005
Total fractional error = $\sqrt{\Sigma (\sigma(\text{ratio})/\text{ratio})^2}$	0.2

Table 5.11: A summary of the systematic errors in the DD case.

5.6 Summary

The ratio of branching fractions $\text{Br}(B^\pm \rightarrow DK^\pm) / \text{Br}(B^\pm \rightarrow D\pi^\pm)$ has been determined using $B^\pm \rightarrow D(K_S^0\pi^+\pi^-)K^\pm$ and $B^\pm \rightarrow D(K_S^0\pi^+\pi^-)\pi^\pm$ decays in approximately 342 pb^{-1} of $\sqrt{s} = 7 \text{ TeV}$ data collected in 2011 at LHCb. The resulting values from LL and DD decays are

$$\frac{\text{Br}(B^\pm \rightarrow DK^\pm)}{\text{Br}(B^\pm \rightarrow D\pi^\pm)} = 0.089_{-0.014}^{+0.015} \pm 0.006 \quad (5.25)$$

and

$$\frac{\text{Br}(B^\pm \rightarrow DK^\pm)}{\text{Br}(B^\pm \rightarrow D\pi^\pm)} = 0.07 \pm 0.02 \pm 0.01, \quad (5.26)$$

where the first errors are statistical and the second errors are systematic. These values are consistent with each other, with previous measurements and with the measurement described in Chapter 4 of this thesis. Combining the LL and DD decay results under the assumption of independent statistical errors and 100% correlated systematic errors gives a weighted average value for the ratio of branching fractions,

$$\frac{\text{Br}(B^\pm \rightarrow DK^\pm)}{\text{Br}(B^\pm \rightarrow D\pi^\pm)} = 0.08 \pm 0.01, \quad (5.27)$$

where the larger of the asymmetric statistical errors in each case has been used.

Chapter 6

Summary and outlook

6.1 Summary

This thesis describes studies performed at the LHCb experiment, primarily detailing the first analysis of $B^\pm \rightarrow \bar{D}^0/D^0(K_S^0\pi^+\pi^-)K^\pm$ and $B^\pm \rightarrow \bar{D}^0/D^0(K_S^0\pi^+\pi^-)\pi^\pm$ decays with LHCb data. The data used were recorded in proton-proton collisions at $\sqrt{s} = 7$ TeV in 2010 and early 2011.

Good performance of the LHCb RICH subdetectors is vital in separating decays such as $B^\pm \rightarrow \bar{D}^0/D^0(K_S^0\pi^+\pi^-)K^\pm$ and $B^\pm \rightarrow \bar{D}^0/D^0(K_S^0\pi^+\pi^-)\pi^\pm$. Selection criteria have been developed to select isolated Cherenkov light rings in the RICH subdetectors, both for rings with and without tracks associated to them. It has been shown that the isolated rings can be used for monitoring of the refractive indices of the RICH radiators with and without information from the tracking subdetectors. Since the start of proton-proton collisions in 2010, the isolated rings with tracks and isolated trackless rings have been used in offline and online RICH monitoring, to ensure that the information provided by the RICH system is of the highest quality.

The decay $B^\pm \rightarrow \bar{D}^0/D^0(K_S^0\pi^+\pi^-)K^\pm$ allows a Standard Model benchmark measurement of the CKM angle γ to be made using the GGSZ (Dalitz) method. Selection criteria for these decays have been optimised using Monte-Carlo simulated events. The optimised criteria were used to select $B^\pm \rightarrow \bar{D}^0/D^0(K_S^0\pi^+\pi^-)K^\pm$ and $B^\pm \rightarrow \bar{D}^0/D^0(K_S^0\pi^+\pi^-)\pi^\pm$ candidates from the first ~ 36.5 pb $^{-1}$ of proton-proton collision data at $\sqrt{s} = 7$ TeV recorded in 2010. Candidates with a K_S^0 decay near to the proton-proton interaction point

were used to evaluate the ratio of branching fractions $\frac{\text{Br}(B^\pm \rightarrow \bar{D}^0/D^0(K_S^0\pi^+\pi^-)K^\pm)}{\text{Br}(B^\pm \rightarrow \bar{D}^0/D^0(K_S^0\pi^+\pi^-)\pi^\pm)}$, giving the result

$$\frac{\text{Br}(B^\pm \rightarrow \bar{D}^0/D^0(K_S^0\pi^+\pi^-)K^\pm)}{\text{Br}(B^\pm \rightarrow \bar{D}^0/D^0(K_S^0\pi^+\pi^-)\pi^\pm)} = 0.12_{-0.05}^{+0.06} \pm 0.03, \quad (6.1)$$

where the first error is statistical and the second systematic. Preliminary measurements have also performed at LHCb using two- and four-body D decays and the same 2010 data set [66]. Using $B^\pm \rightarrow \bar{D}^0/D^0(K^\pm\pi^\mp\pi^\pm\pi^\mp)h$ and $B^\pm \rightarrow \bar{D}^0/D^0(K^\pm\pi^\mp)h$ decays, a value for the ratio of $0.0630 \pm 0.0038 \pm 0.0040$ was found. For $B^\pm \rightarrow \bar{D}^0/D^0(K^\pm K^\mp)h$ decays, a value of $0.0931 \pm 0.0189 \pm 0.0053$ was found; both results are consistent with the result of this thesis.

Further and more precise measurements of the ratio of branching fractions have been made using proton-proton collision data recorded in 2011 and corresponding to an integrated luminosity of $\sim 342 \text{ pb}^{-1}$ at $\sqrt{s} = 7 \text{ TeV}$. Values were found from two independent samples of $B^\pm \rightarrow \bar{D}^0/D^0(K_S^0\pi^+\pi^-)K^\pm$ and $B^\pm \rightarrow \bar{D}^0/D^0(K_S^0\pi^+\pi^-)\pi^\pm$ decays where the K_S^0 decay occurs either near to the proton-proton interaction point (LL) or further into the LHCb detector (DD). The resulting values are

$$\frac{\text{Br}(B^\pm \rightarrow \bar{D}^0/D^0(K_S^0\pi^+\pi^-)K^\pm)}{\text{Br}(B^\pm \rightarrow \bar{D}^0/D^0(K_S^0\pi^+\pi^-)\pi^\pm)} = 0.089_{-0.014}^{+0.015} \pm 0.006 \quad (6.2)$$

and

$$\frac{\text{Br}(B^\pm \rightarrow \bar{D}^0/D^0(K_S^0\pi^+\pi^-)K^\pm)}{\text{Br}(B^\pm \rightarrow \bar{D}^0/D^0(K_S^0\pi^+\pi^-)\pi^\pm)} = 0.07 \pm 0.02 \pm 0.01, \quad (6.3)$$

where the first errors are statistical and the second systematic. Figure 6.1 shows the likelihood curve for the published results of this measurement [18]; the average value is $(7.6 \pm 0.6)\%$. Superimposed on the curve are the two results presented in this thesis from the analysis of the early 2011 data. The indicated errors are the quadratic sum of the statistical and systematic uncertainties on the presented measurements. It can be seen that the results from this thesis are consistent with the previous measurements. It should be noted that, due to the different reconstructed D decay modes, the global average input measurements and the other LHCb results contain different contributions to the measured branching fraction ratio from the suppressed $B^+ \rightarrow D^0 h$ and $B^- \rightarrow \bar{D}^0 h$ decays than the contributions in the $B^\pm \rightarrow D(K_S^0\pi^+\pi^-)h$ decay case considered in this

thesis. A combination of the two results from the 342 pb^{-1} data set gives a weighted average value for the ratio of branching fractions,

$$\frac{\text{Br}(B^\pm \rightarrow \bar{D}^0/D^0(K_S^0\pi^+\pi^-)K^\pm)}{\text{Br}(B^\pm \rightarrow \bar{D}^0/D^0(K_S^0\pi^+\pi^-)\pi^\pm)} = 0.08 \pm 0.01. \quad (6.4)$$

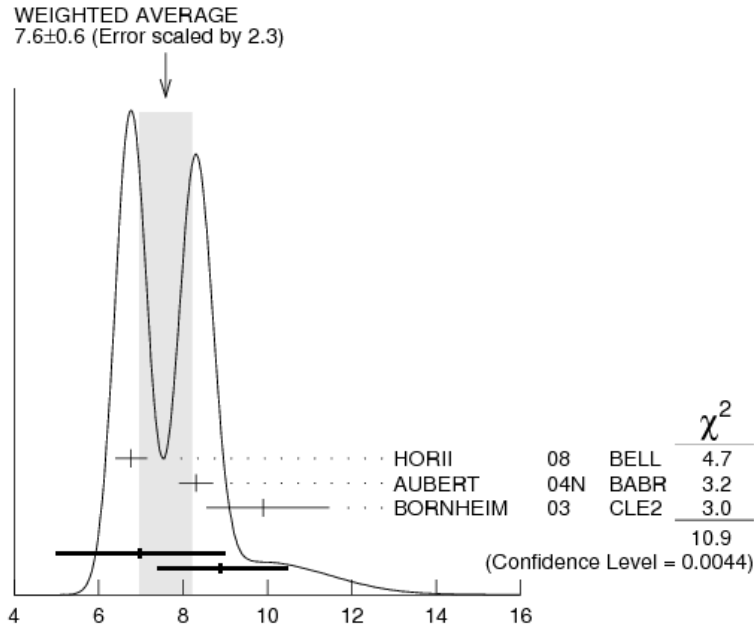


Figure 6.1: The likelihood curve for the ratio of branching fractions, $\text{Br}(B^\pm \rightarrow \bar{D}^0/D^0 K^\pm) / \text{Br}(B^\pm \rightarrow \bar{D}^0/D^0 \pi^\pm)$ [18], with results from this thesis superimposed. The values of the ratio are equal to the values indicated on the horizontal axis multiplied by 10^{-2} .

6.2 Outlook

The measurement of the ratio of branching fractions $\frac{\text{Br}(B^\pm \rightarrow \bar{D}^0/D^0 K^\pm)}{\text{Br}(B^\pm \rightarrow \bar{D}^0/D^0 \pi^\pm)}$ with the decays $B^\pm \rightarrow \bar{D}^0/D^0(K_S^0\pi^+\pi^-)K^\pm$ and $B^\pm \rightarrow \bar{D}^0/D^0(K_S^0\pi^+\pi^-)\pi^\pm$ establishes many of the necessary analysis components, for example detailed background studies, for the measurement of γ at LHCb using these decays. For the γ analysis, the background composition must be well-understood because the various backgrounds are distributed differently across the Dalitz plane. The B^\pm candidate mass distributions for $B^\pm \rightarrow \bar{D}^0/D^0(K_S^0\pi^+\pi^-)K^\pm$ and $B^\pm \rightarrow \bar{D}^0/D^0(K_S^0\pi^+\pi^-)\pi^\pm$ decays from the full 2011 data set of

$\sim 1 \text{ fb}^{-1}$ are shown in Figure 6.2. The candidates were selected using the same criteria as described in Chapter 5 [150]. The selection criteria will be reoptimised on data when sufficient statistics have been obtained.

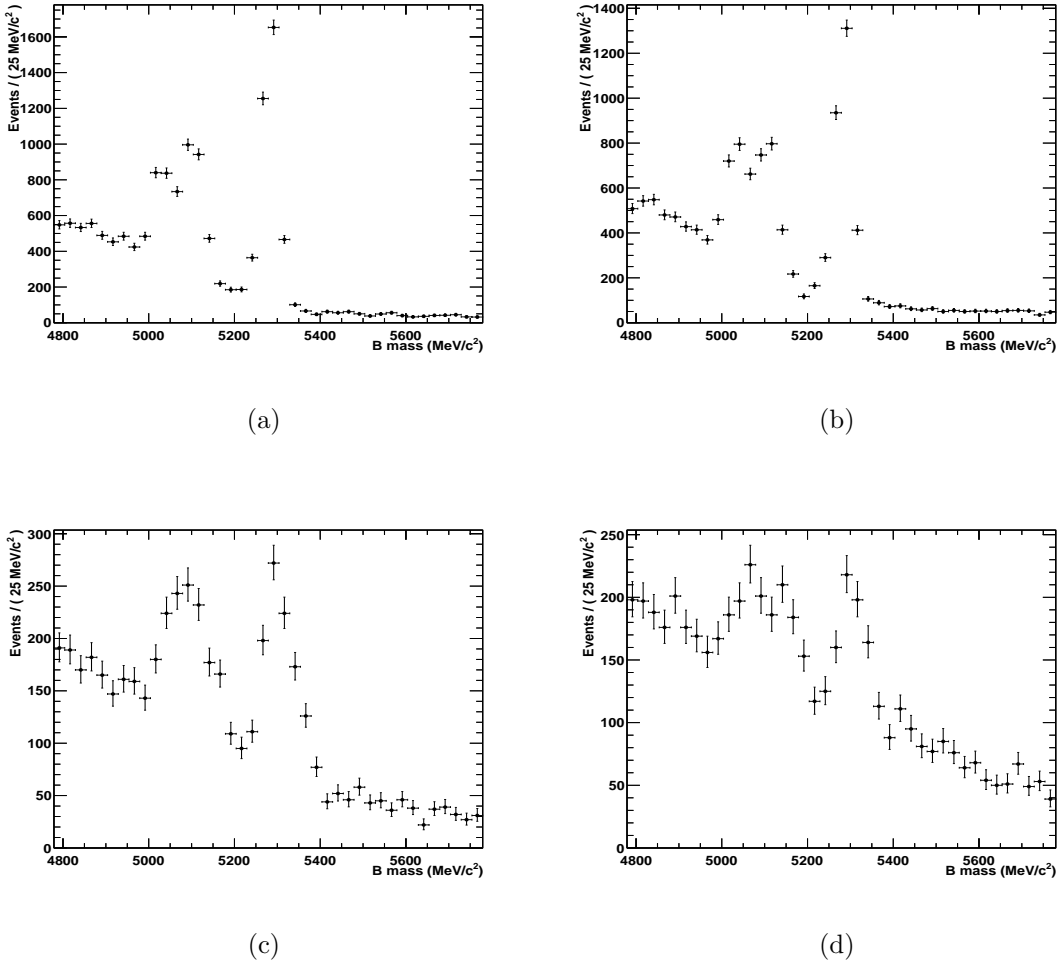
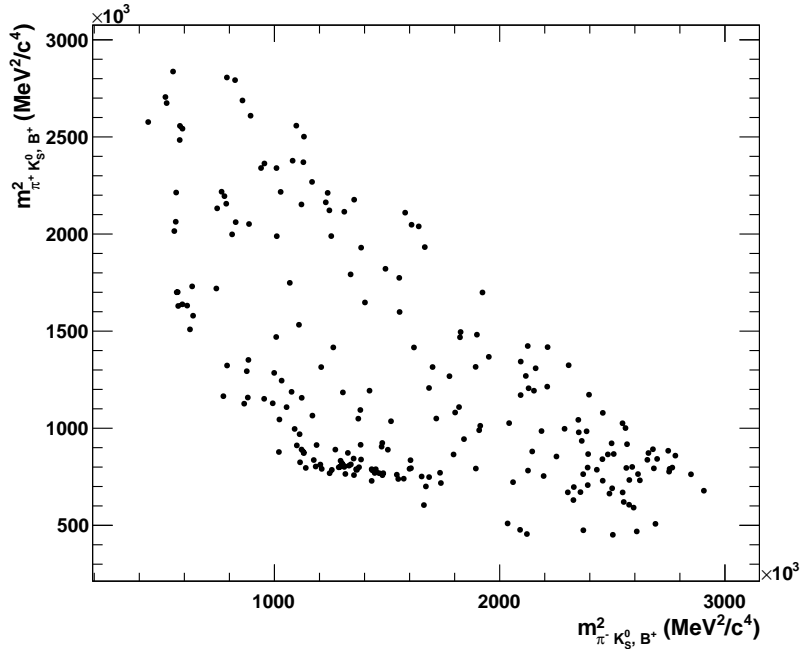


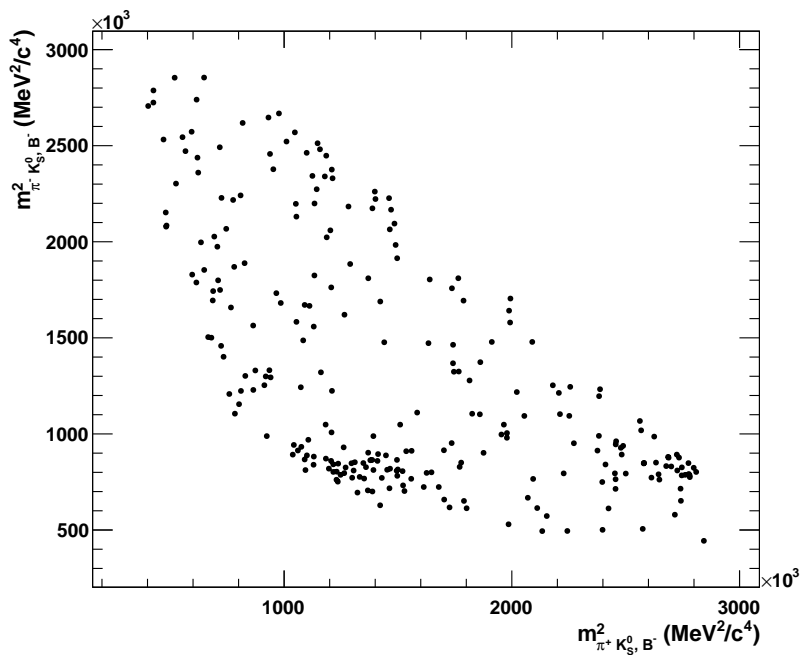
Figure 6.2: The B^\pm candidate mass distributions from $\sim 1 \text{ fb}^{-1}$ of 2011 data. Figure 6.2(a) shows the $B^\pm \rightarrow \bar{D}^0/D^0\pi^\pm$ LL distribution, Figure 6.2(b) the $B^\pm \rightarrow \bar{D}^0/D^0\pi^\pm$ DD distribution, Figure 6.2(c) shows the $B^\pm \rightarrow \bar{D}^0/D^0K^\pm$ LL distribution and Figure 6.2(d) the $B^\pm \rightarrow \bar{D}^0/D^0K^\pm$ DD distribution.

Figures 6.3 and 6.4 show the B^+ and B^- Dalitz plots from $B^\pm \rightarrow \bar{D}^0/D^0(K_S^0\pi^+\pi^-)K^\pm$ candidate decays, using the full 2011 data set. The candidates included in the Dalitz plots have been selected using the same criteria as described in Chapter 5, except for further requirements on B^\pm candidate mass and bachelor kaon particle identification [150]. The B^\pm candidates were also re-fitted with the D candidate mass constrained to the global average value from reference [18]. Scaling a sensitivity estimate from previous

studies in reference [79] according to candidate yields, a conservative estimate of the expected statistical sensitivity to γ from these candidates (~ 800 candidates in total) is approximately 25° with $\sim 1 \text{ fb}^{-1}$ of LHCb data. Global studies from LHCb, combining the potential sensitivity to γ from all $B \rightarrow DK^{(*)}$ decay modes under study and independent from the studies of this thesis, estimate that a precision of approximately 7° on γ can be achieved with the full 2011 data set [55, 85].

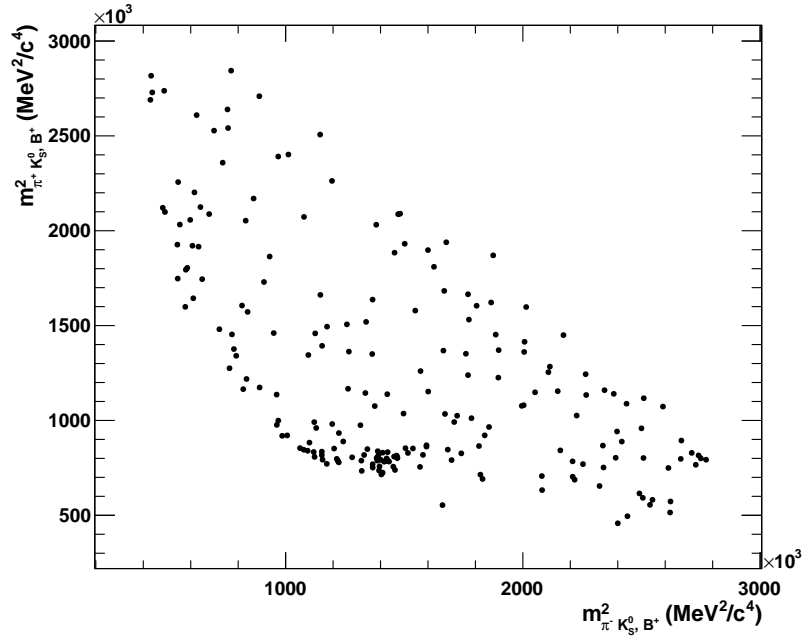


(a)

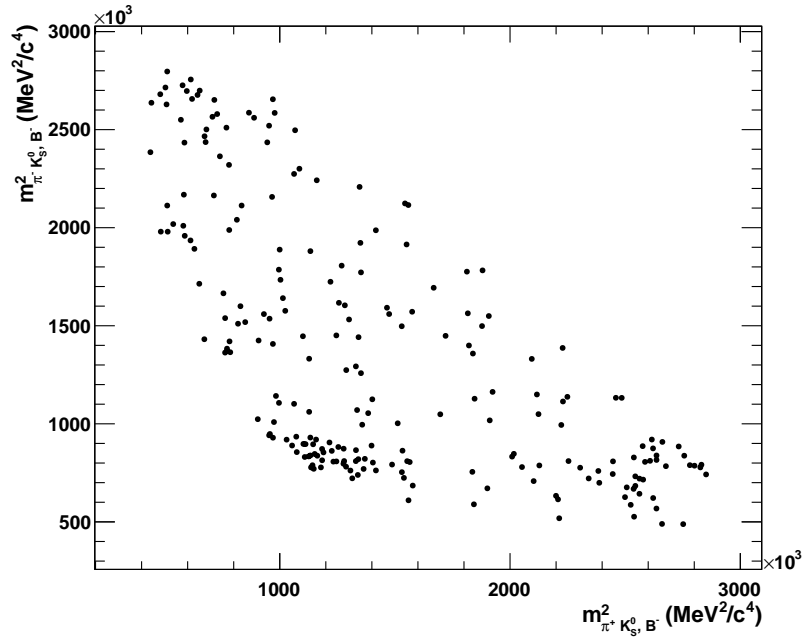


(b)

Figure 6.3: Dalitz plots for $B^\pm \rightarrow \bar{D}^0/D^0(K_S^0\pi^+\pi^-)K^\pm$ LL candidate decays from the full 2011 LHCb data set ($\sim 1 \text{ fb}^{-1}$). Figure 6.3(a) shows the Dalitz plot for B^+ candidates and Figure 6.3(b) shows the Dalitz plot for B^- candidates.



(a)



(b)

Figure 6.4: Dalitz plots for $B^\pm \rightarrow \bar{D}^0/D^0(K_S^0\pi^+\pi^-)K^\pm$ DD candidate decays from the full 2011 LHCb data set ($\sim 1 \text{ fb}^{-1}$). Figure 6.4(a) shows the Dalitz plot for B^+ candidates and Figure 6.4(b) shows the Dalitz plot for B^- candidates.

Appendix A

Cherenkov radiation

As a charged particle moves at a speed v through a dielectric medium with refractive index n , it polarises the material around it so that the surrounding atoms gain induced dipoles. If the particle speed is less than the local speed of light in the medium (c/n) these dipoles are causally connected and form a symmetric arrangement about the particle track, with no net dipole and hence no resulting emission of radiation. If the particle speed is greater than (c/n), however, the particle is travelling faster than information about it can propagate through the medium, so the dipoles are not causally connected and form an asymmetric distribution around the track. The net dipole leads to spontaneous emission of photons, known as Cherenkov radiation. The Cherenkov effect was first discovered in 1934 by P. A. Cherenkov and explained by I. M. Frank and I. E. Tamm [178, 179].

The characteristic angle of photon emission depends, in all practical cases, only on the speed of the particle and the refractive index of the dielectric medium. The principle of particle identification by RICH detectors depends entirely on this characteristic angle; a speed measurement, derived from the Cherenkov angle, combined with a momentum measurement from the tracking detectors, allows the particle to be identified.

Classically, the direction of radiation emission can be derived using a Huygens construction of interfering spherical wavefronts, as illustrated in Figure A.1. Consideration of secondary wavefronts emitted at $t = -T$ and $t = 0$ leads to constructive interference along a line at angle $\cos \theta = (cT/n)/vT = 1/\beta n$ to the particle trajectory [180] where $\beta = v/c$. A direct consequence of Cherenkov emission only occurring when the speed of the charged particle is greater than the local speed of light ($\beta > 1/n$) is that the re-

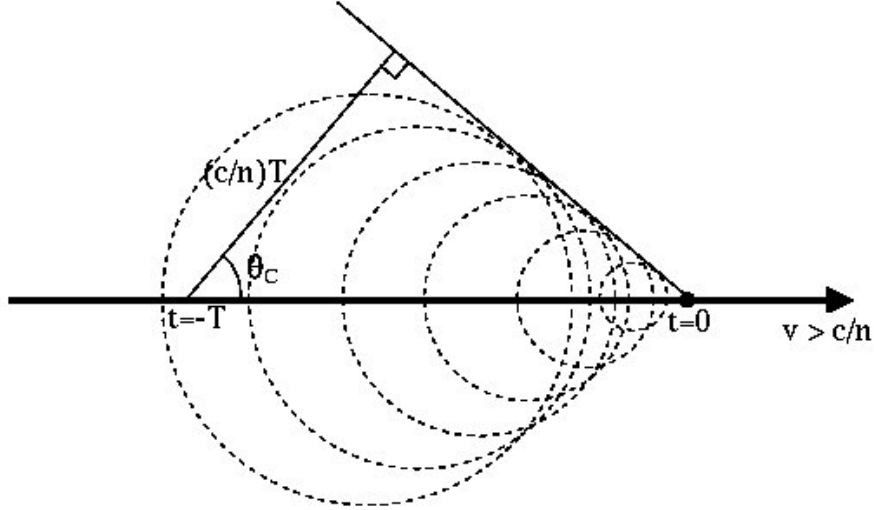


Figure A.1: A Huygens construction for Cherenkov radiation.

refractive index of the medium must be greater than one. At the threshold for Cherenkov emission ($v = c/n$), the radiation is emitted in the forward cone i.e. $\theta = 0$. At the other extreme ($\beta = 1$), the Cherenkov angle saturates so that $\theta = \arccos(1/n)$.

The energy loss per unit length by a charged particle travelling through a dielectric medium is given by the Frank-Tamm relation [181]

$$\left(\frac{dE}{dx}\right)_{rad} = \frac{Z^2 e^2}{4\pi\epsilon_0 c^2} \int_{\epsilon(\omega)\beta^2 > 1} \omega \left(1 - \frac{1}{\beta^2 n^2}\right) d\omega, \quad (\text{A.1})$$

where Ze is the charge of the radiating particle and $\sqrt{\epsilon(\omega)}$ is the refractive index of the medium. Assuming that the refractive index (n) is independent of photon frequency, this can be re-arranged to give the expected number of photons in an interval dE around energy E emitted from a particle traversing a radiator of length L

$$\frac{dN}{dE} = LZ^2 \left(\frac{\alpha}{c\hbar}\right) \sin^2 \theta \quad (\text{A.2})$$

where α is the electromagnetic fine structure constant.

This relation is independent of E and so the spectrum of Cherenkov radiation is flat in energy. A high frequency cut-off, when the refractive index of the medium falls below unity, prevents the divergence of the total energy emitted [179]. In the LHCb RICH detectors, photons are detected over the approximate wavelength range 200 – 600 nm [96].

Appendix B

Isolated Cherenkov rings in the LHCb RICH subdetectors

The LHCb experiment includes two RICH subdetectors, described in Section 2.2.8, which are crucial for charged particle identification. The RICH system performance for distinguishing different types of particle is highly dependent on accurate knowledge of the refractive indices of the RICH radiators, and good performance of kaon and pion particle identification is vital in separating decays such as $B^\pm \rightarrow \bar{D}^0/D^0(K_S^0\pi^+\pi^-)K^\pm$ and $B^\pm \rightarrow \bar{D}^0/D^0(K_S^0\pi^+\pi^-)\pi^\pm$. It is therefore important that the subdetector conditions affecting the refractive indices, such as pressure, temperature and gas purity [182], are closely monitored. To provide hardware monitoring, various sensors are included in the experimental apparatus. As described in this appendix, it is also possible to monitor for changes in refractive index using isolated Cherenkov light rings from the data.

In Section B.1, the development of selection criteria for the identification of isolated rings with associated tracks is described. The adaptation of the criteria to identify isolated rings without associated tracks is then discussed in Section B.2, with a Markov chain ring fitter [183, 184] being used to identify rings in the RICH subdetectors which do not have an associated track. Isolated rings selected with these approaches have been used within RICH monitoring since the start of proton-proton collision data-taking at LHCb, both online (for real-time monitoring of detector conditions) and offline (after full data reconstruction, for data quality purposes).

B.1 Isolated RICH rings with tracks

A typical low-occupancy event from proton-proton collision data, showing the RICH2 HPD planes as seen in Panoramix, the LHCb event display software, is shown in Figure B.1. The figure illustrates various objects related to the reconstructed tracks and detected Cherenkov photons which are used in the selection criteria described in this appendix. For example, HPD pixels which have detected photon “hits” are represented by small orange filled circles. The small triangles are the reconstructed track hit positions, corresponding to the extrapolated position on the HPD plane, in local coordinates, where the track particle would have been detected if it was a photon. The larger open circles passing through the pixel hits are the reconstructed Cherenkov ring fits for different track particle type hypotheses. The red line indicates the boundary between the two HPD planes.

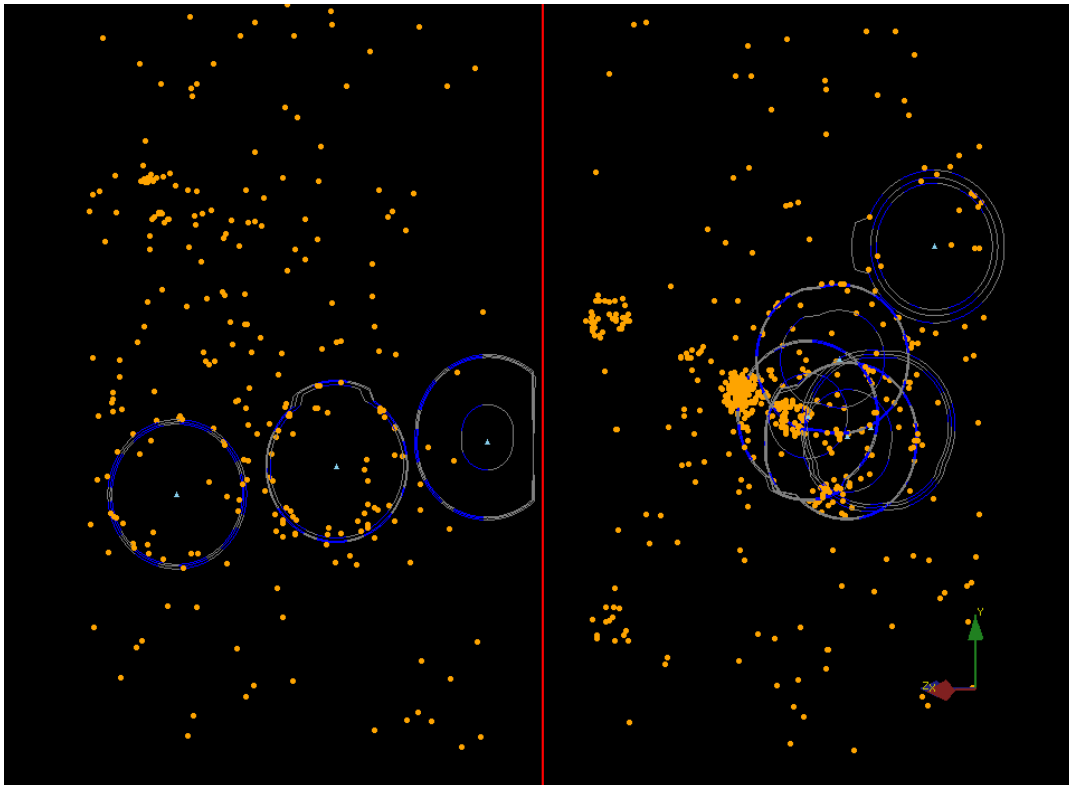


Figure B.1: A typical low-occupancy event from proton-proton collision data, showing the RICH2 HPD planes as seen in Panoramix, the LHCb event display software [150].

B.1.1 Cherenkov angles θ and ϕ

Two angles are necessary to describe the distribution of photons around a detected Cherenkov light ring in the RICH subdetectors. The azimuthal angle, Cherenkov ϕ , describes the position of an emitted photon around the circumference of the detected ring. The distribution of photons should show no variation with ϕ as there is no azimuthal angular preference for direction of photon emission from the track. The angle θ is the constant angle of emission between the track and each emitted photon and is referred to as the Cherenkov angle (see Appendix A). A typical distribution of reconstructed Cherenkov θ for MC events, including all photons, is shown in Figure B.2; a high level of background can be seen beneath the peak.

The resolution of θ , $\Delta\theta$, is defined as

$$\Delta\theta = \theta_{rec} - \theta_{exp}, \quad (\text{B.1})$$

where θ_{rec} is the reconstructed angle for a given track-photon pair and θ_{exp} is the expected angle for a track, given its measured momentum, knowledge of the radiator and a particular particle type hypothesis. Figure B.3 shows a Cherenkov θ resolution distribution for MC true photons only, with a fitted σ of 0.64 mrad.

The resolution distribution, $\Delta\theta$, is predicted to alter with unexpected variations of refractive index, because θ_{rec} will change but θ_{exp} will not. Changes in the resolution distribution can therefore be used to monitor fluctuations in the refractive index. For the most effective monitoring, a resolution distribution with as little background contribution as possible is required, and this can be obtained using a sample of clean, isolated Cherenkov rings.

B.1.2 Selection criteria

As described in the previous section, a clean sample of Cherenkov rings is required for the most effective refractive index monitoring; to provide this sample, isolation selection criteria are therefore applied to track segments and their associated HPD hit pixels and reconstructed photons, to determine whether or not each segment produced an isolated Cherenkov ring. A track segment is a software object, corresponding to the section of a reconstructed track lying within the RICH subdetectors, and has associated with it all of the RICH PID and Cherenkov emission information for the track. The isolation

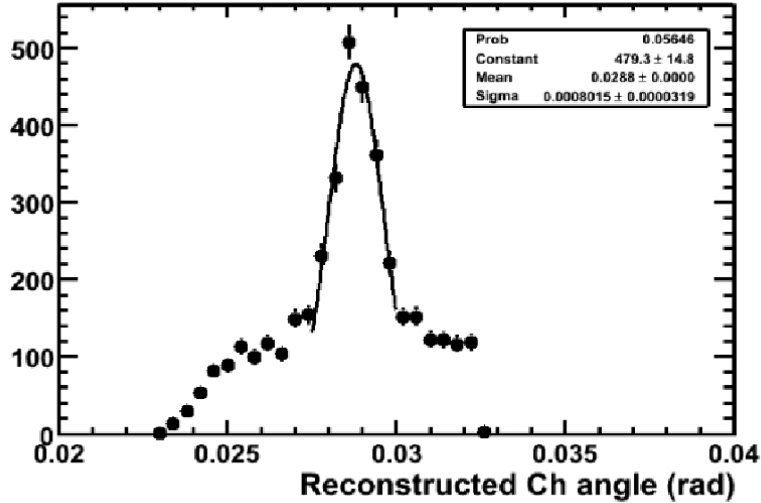


Figure B.2: The reconstructed Cherenkov θ distribution for all photons [185] (from MC).

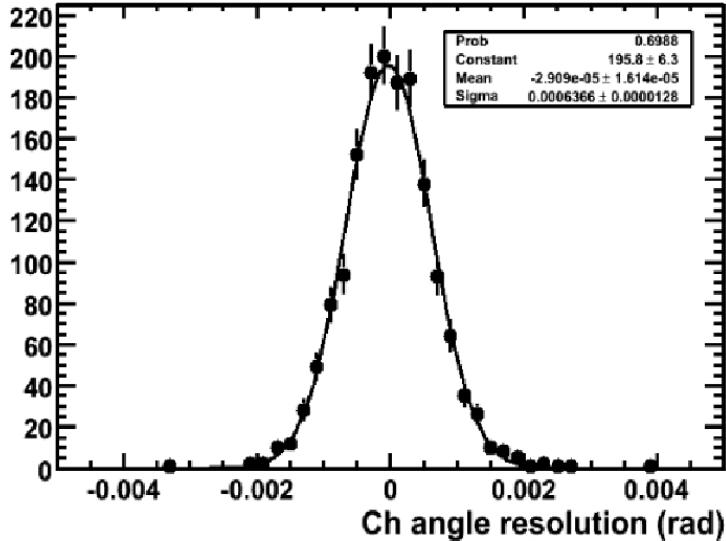


Figure B.3: The Cherenkov θ resolution distribution for MC true photons only [185].

selection criteria were initially developed for RICH2 rings and can be used for RICH1 gas radiator rings, as indicated below, by changing some of the requirements.

The isolation criteria were tested using approximately 100,000 MC simulated events, where each event contained at least one b-hadron decaying within the LHCb acceptance. They were simulated as described in Section 2.4.1 at centre-of-mass energy $\sqrt{s} = 14$ TeV

and with settings corresponding to DC06, the MC simulation performed with a 2006 detector description in GEANT4. This description included a RICH2 nominal subdetector pressure of 970 mbar.

MC truth information was used to flag all photons as “true” or “background” with respect to a given track segment. For each tested set of selection criteria, the Cherenkov θ resolution distribution for all photons from isolated rings with tracks was compared to the distribution from MC true photons from the same tracks. For clean, well-isolated rings, the distributions should be identical, as a truly isolated ring contains only photons produced by the corresponding track. To allow comparison of the two distributions, Gaussian functions were fitted to the distributions and the Gaussian σ values found. The σ value from Figure B.3 was used to check for potential biasing of the isolated ring resolution distributions due to the applied criteria.

Selection criteria were applied to the MC event test sample in different combinations and several numerical values were considered for each of the criteria. It was found that highly selective selection criteria could improve the resolution distribution greatly, so that the σ values from Gaussian fits to the distributions from all isolated photons and from MC true photons were almost identical. They also caused the number of tracks passing the criteria to be low, however, which is not ideal for real-time detector monitoring purposes. The following criteria, also summarised in Table B.1, were found to produce the best combination of clean rings with a suitable number of rings with tracks passing the criteria for RICH2:

- if the track segment lies in RICH2, the track segment exit point (the position of the track as it leaves the radiator) is required to be > 100 mm from the RICH2 discontinuity at $x=0$; if it is closer than this, the Cherenkov ring produced by the track is split across the two HPD planes. Similarly, for tracks in RICH1, a requirement on the distance from the $y=0$ discontinuity is used;
- a requirement on track segment momentum of > 20 GeV/ c is made. Tracks fulfilling this requirement will not necessarily produce saturated Cherenkov rings (see Figures 2.27 and 2.28), so that rings for different particle hypotheses will not have the same radii. In this case PID information must be used for some of the other selection criteria. A higher momentum requirement (e.g. > 80 GeV/ c) would mean that the rings would be saturated and different particle types would give rings of the same radius. The pion particle type hypothesis could therefore be used for other selection criteria. However, only a small proportion of the tracks in an event

would have a momentum high enough to meet this requirement;

- the reconstructed track hit position of the chosen track is required to be separated by > 260 mm from the other track hit positions in the same event, thereby removing track segments with overlapping rings. A separation requirement of > 260 mm is made because the radius of a saturated ring is calculated to be approximately 130 mm in RICH2 and the reconstructed track hit position can be taken as the centre of the Cherenkov ring formed by the track. A similar requirement is made for RICH1;
- the geometric efficiency of the ring, which is the fraction of the ring's circumference lying within the acceptance area of the HPDs, is required to be $> 70\%$. To evaluate this requirement, a particle type hypothesis is required for the segment;
- a requirement on the distribution of hit pixels in terms of Cherenkov θ is made (see Figure B.4). The average θ value around the track hit position is found using the track's particle type hypothesis and a band is defined around this average value. The width of the band on either side of the average is nominally 5σ from a Gaussian fit to the reconstructed θ distribution with no isolation criteria applied. This width (9.44 mrad) was chosen because it gives an indication of the scale of Cherenkov θ angle but is not small enough to bias the θ resolution distribution for isolated rings. All hit pixels within a circular region of interest centred on the track hit position are considered; the fraction of these lying within the predefined θ band is calculated and a requirement of fraction $> 80\%$ is made. The width of the θ band and the required fraction of hits within the chosen band can be configured. The radius of the circular region of interest is fixed to be 1.5 times the saturated ring radius. This criterion removes rings which have background photons near to the centre of the Cherenkov ring but not lying on the ring itself;
- a requirement on the distribution of hit pixels in terms of Cherenkov ϕ is made. The $[0, 2\pi]$ range of angle ϕ is divided into eight equally sized angular regions (see Figure B.5). The fraction of the reconstructed photons associated with the track in each of these regions is found and a maximum requirement is made on this fraction. For photons evenly distributed in ϕ , as expected for true Cherenkov photons, there should be on average 12.5% of the total number in each of the eight regions. Background photons are not expected to be evenly distributed in ϕ and small clusters of them are often observed. This criterion removes rings with clusters of background photon hits near to the true Cherenkov photon ring. The

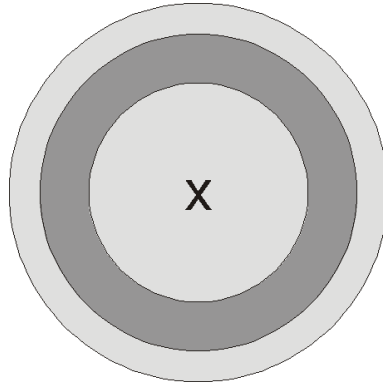


Figure B.4: A schematic illustrating the θ requirement (not to scale). Hit pixels within the larger circular area around the track hit position (central cross) are considered. The fraction of these within the darker θ band is calculated.

default requirement is that no more than 21.25% of the hits lie in any one of the eight regions. Both the number of angular regions and the allowed fraction in each can be configured; and

- it is ensured that $< 20\%$ of photons associated with the chosen track are also associated with other tracks. This requirement removes track segments with background photon contributions which are in fact signal from another track segment.

If a RICH ring and corresponding track segment pass all of these criteria, they are identified as isolated. Some examples of MC RICH2 rings, which were identified as isolated using the criteria of Table B.1, are shown in Figure B.6.

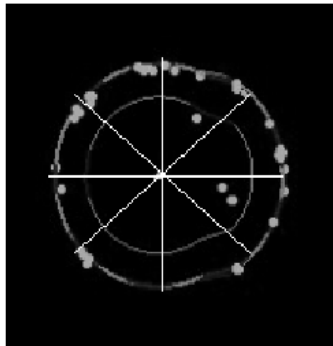


Figure B.5: A schematic illustrating the ϕ requirement. Lines showing the angular division are superimposed onto an isolated RICH2 ring from MC, viewed with Panoramix.

Criterion applied to track segment	Criterion value
Exit distance from RICH 2 discontinuity	> 100 mm
Momentum	> 20 GeV/ c
Separation of track hit positions	> 260 mm
Geometric efficiency	> 70%
Cherenkov θ ring width	9.44 mrad
Cherenkov θ requirement	> 80% within the defined ring
Cherenkov ϕ requirement	< 21.25% in each of eight ϕ regions
Photon association	> 80% not associated with another track

Table B.1: The nominal isolation selection criteria for rings with associated tracks.

B.1.3 Cherenkov angle resolution distributions from isolated rings with tracks

The Cherenkov angle resolution distribution for the criteria of Table B.1 is shown in Figure B.7 for all photons from selected isolated rings with tracks; Figure B.8 shows the distribution for MC true photons from the same tracks. It can be seen that the distributions are very similar, with fitted Gaussian σ values of 0.694 mrad and 0.685 mrad respectively. The fit is slightly sensitive to the fit range, due to non-Gaussian tails. For the isolated ring photon distribution, varying the fit range gave a possible range of σ values 0.689–0.700 mrad; for the MC true photons the range was 0.674–0.682 mrad. Hence, the errors due to choosing a particular Gaussian fit range are similar in size to the difference between the isolated and MC true σ values (0.009 mrad). Figure B.9 shows the same distribution as Figure B.7, with the remaining background photon contribution to this distribution superimposed. The low level of background in this distribution and the similar fitted Gaussian σ values for the distributions of Figures B.7 and B.8 indicate that the nominal selection criteria are effective in producing a clean set of Cherenkov rings.

The application of a momentum requirement of > 80 GeV/ c , selecting from the same MC events with all other criteria taking the values shown in Table B.1, led to only four track segments being identified as having isolated rings. This is due to the shape of the momentum distribution of tracks, as shown in Figure B.10; there are far fewer tracks with high momenta than with low momenta.

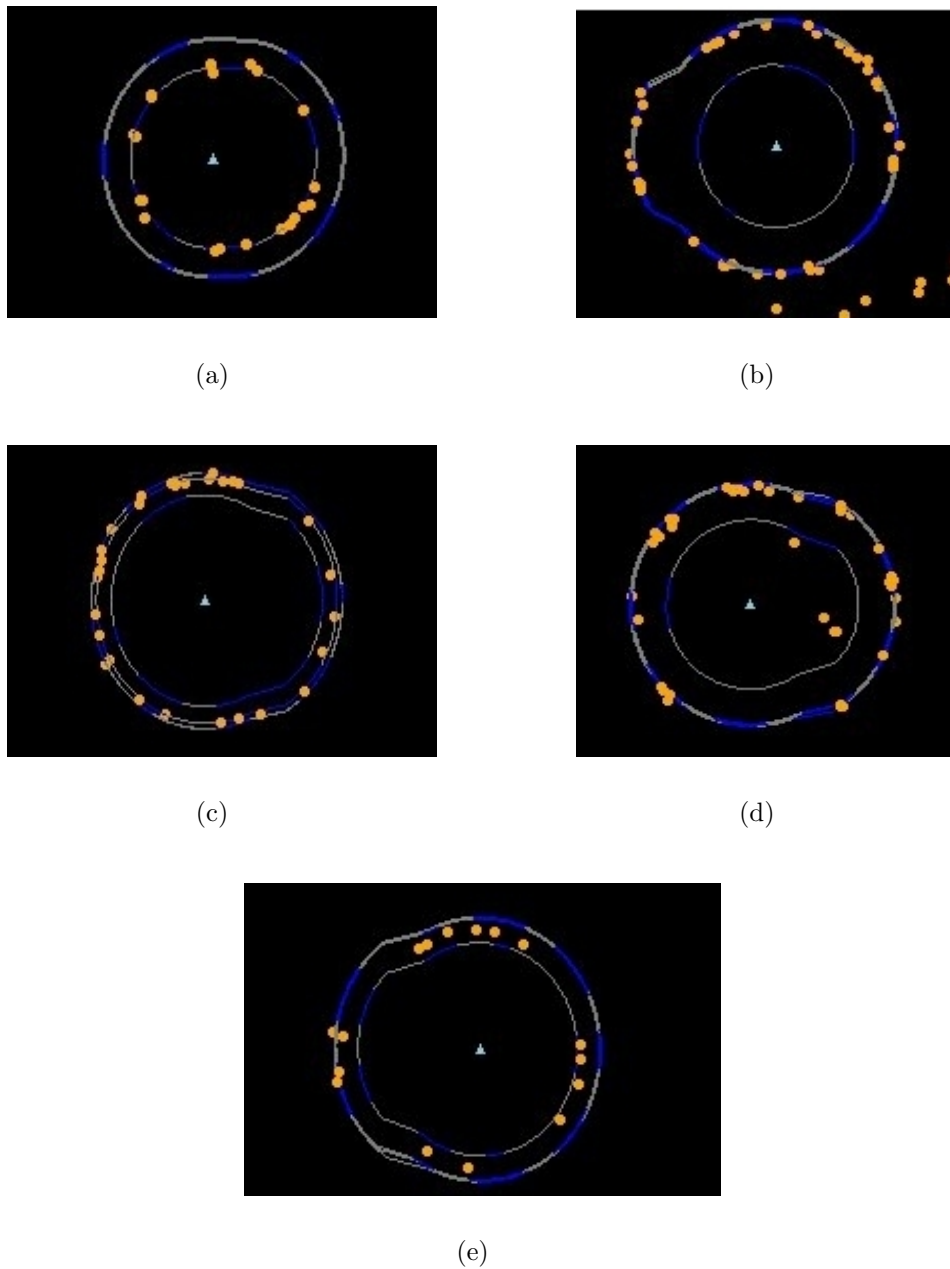


Figure B.6: RICH2 isolated rings with tracks, taken from different MC events, as seen in the Panoramix view of HPD planes.

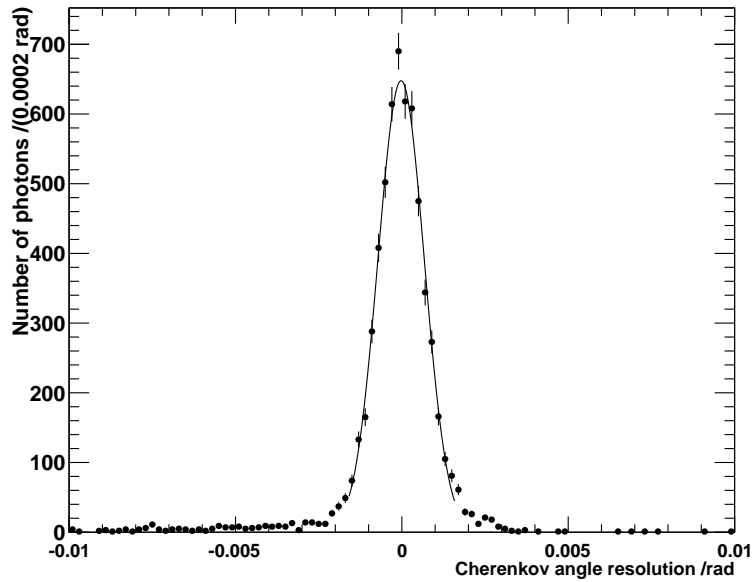


Figure B.7: The Cherenkov θ resolution distribution for all photons from isolated rings, with fitted Gaussian $\sigma = 0.694$ mrad (from MC).

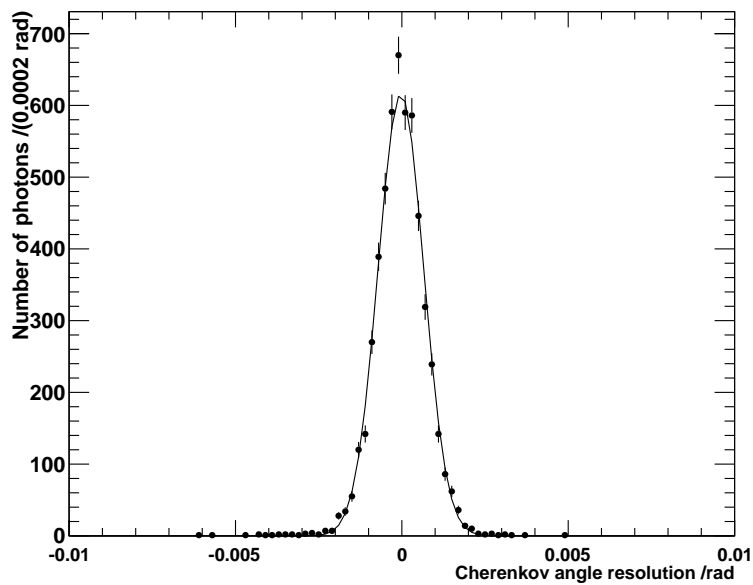


Figure B.8: The Cherenkov θ resolution distribution for MC true photons from isolated rings, with fitted Gaussian $\sigma = 0.685$ mrad.

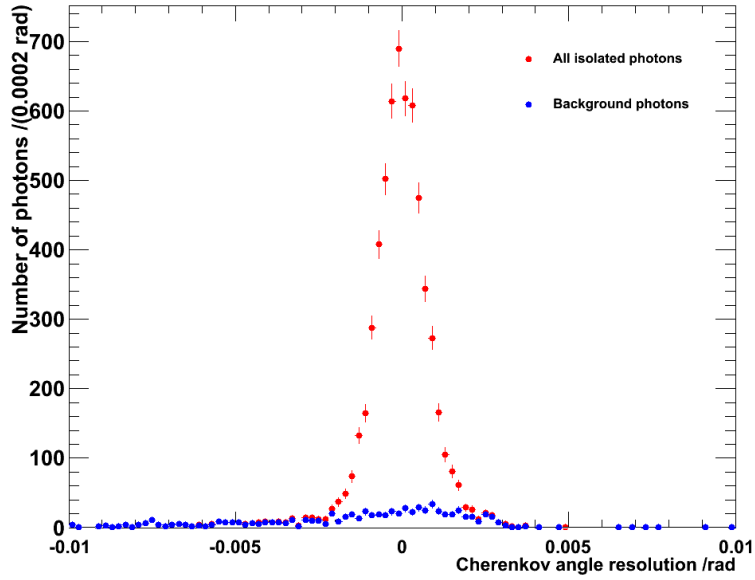


Figure B.9: The Cherenkov θ resolution distribution for all isolated ring photons (red); the remaining background photons contributing to the isolated rings are shown in blue (from MC).

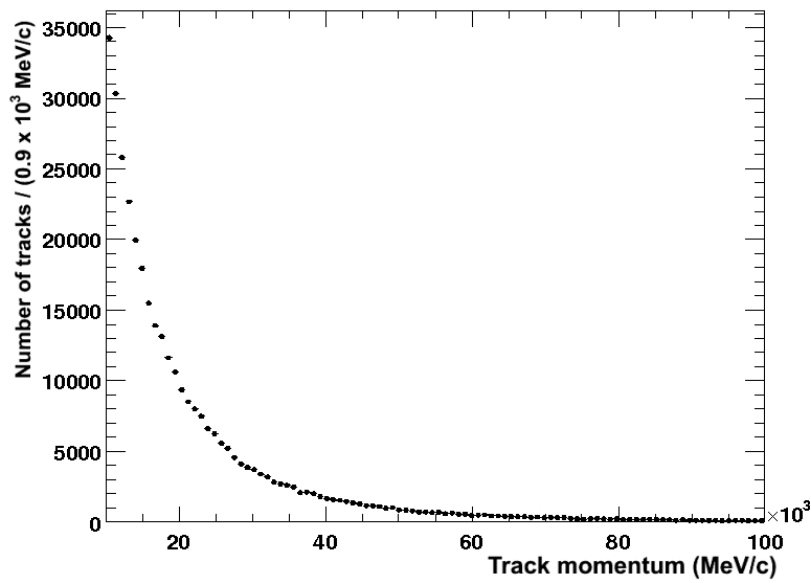


Figure B.10: The momentum distribution for tracks in MC events.

B.1.4 Background contributions

The types of background photon contributing to isolated rings selected with the criteria of Table B.1 were examined using MC history information for the hit pixels, to see if any further reduction in background could be achieved. The term “background” encompasses any photons which are not MC true for the track and so it includes both signal photons from another track segment and photons due to subdetector background. In RICH2 the subdetector background includes HPD charge share hits, in which the photon produces several hits across neighbouring HPD silicon pixels, dark hits and gas quartz window Cherenkov photons from a particle passing through the quartz window in the box separating the HPDs from the radiator gas. Also contributing to the subdetector background are Cherenkov photons from a particle traversing an HPD quartz front window and Cherenkov photons from a particle crossing nitrogen gas. It was found that the largest contribution to the total background was from signal photons from other tracks (see Figure B.11). The level of this background could not be reduced without making the selection criteria more discriminating and in turn reducing the number of rings with tracks identified as isolated.

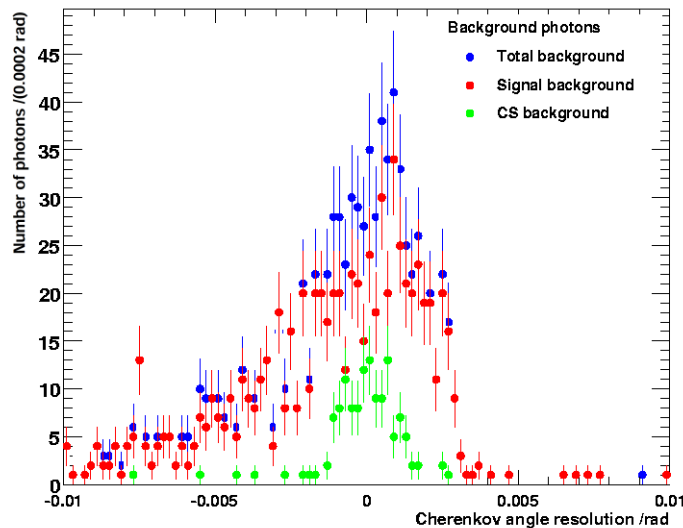


Figure B.11: The Cherenkov θ resolution distribution for background photons from isolated rings with tracks, showing the contributions from different background photon types in MC. “Total background” denotes all photons which are not MC true for a given track; “Signal background” denotes the subset of “Total background” photons which are signal for another track but background for the selected one and “CS background” the subset which are charge share photons.

The largest subdetector background contribution was due to HPD charge share hits, so an attempt was made to reduce this background by applying a clustering algorithm to the HPD pixel hits. Given a minimum and a maximum cluster size, the algorithm searched for hits in neighbouring pixels and then grouped them together to be treated as a single pixel hit. A typical background photon resolution distribution with clusters of size 1–4 pixels allowed is shown in Figure B.12. A slight reduction in background was found, but the number of tracks identified as isolated from a given set of events was also reduced. This, and the fact that the charge share contribution without clustering was still significantly smaller than background from other track signal photons, led to the decision not to pursue the application of the clustering algorithm further; no changes were made to the nominal isolation criteria described in Section B.1.2.

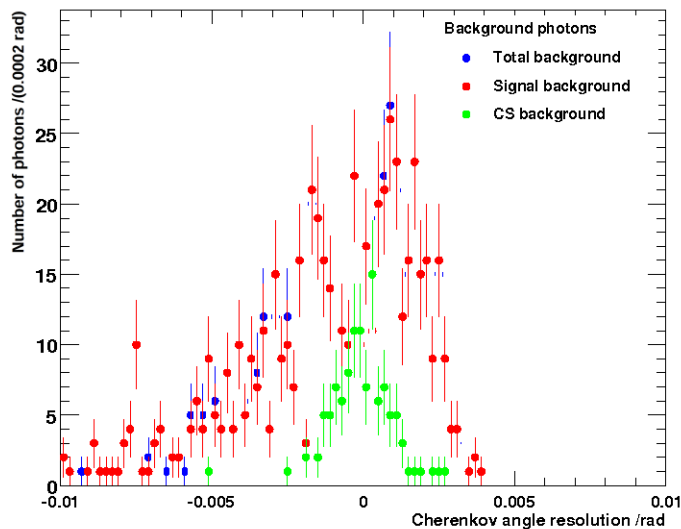


Figure B.12: The Cherenkov θ resolution distribution for background photons from isolated rings with tracks, with clustering applied (from MC).

B.1.5 Changes in resolution with variation of radiator pressure

It is expected that a change in radiator gas pressure will alter the refractive index of the gas [182] and in turn the Cherenkov θ resolution distribution. In order to check that the Cherenkov θ resolution distribution does indeed alter under a pressure variation, a further sample of MC events was simulated with a RICH2 pressure of 965 mbar. This pressure was chosen because the nominal running pressure for RICH2 is 970 mbar and a typical pressure fluctuation in the subdetector is of the order 5–10 mbar. The Cherenkov

resolution distribution for all MC true photons in the 965 mbar simulation (Figure B.13) shows the expected shift and is not well fitted by a Gaussian. As shown in Section B.1.3, with enough statistics the Cherenkov θ resolution distribution from isolated rings should resemble the MC true resolution distribution. It is therefore possible to use the resolution distribution from isolated rings to observe fluctuations in resolution due to changes in the subdetector conditions.

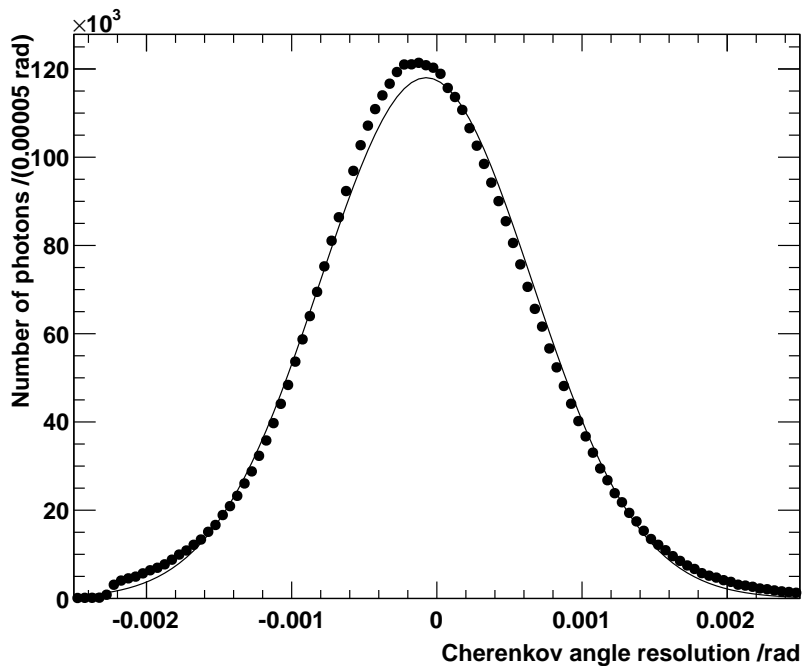


Figure B.13: The Cherenkov θ resolution distribution for MC true photons with a RICH2 pressure of 965 mbar. The points are the distribution and the line is a Gaussian function fitted to the distribution.

B.2 Isolated trackless rings

It is also valuable to be able to monitor the RICH radiator refractive indices without the input of information from the tracking subdetectors. “Trackless” rings, to be used for this monitoring, were identified in RICH2 using an algorithm [183, 184] which fits Cherenkov light rings. The algorithm uses a Markov chain sampler and only RICH pixel hit information and knowledge of the RICH subdetector to locate rings. It does not need any track seeding or information from the rest of the LHCb detector, so the fitted rings are ideal for use in tracking-independent monitoring of the RICH system. The fitter

produces perfectly circular rings, however, and cannot take into account the “keyhole” shape obtained when a ring is split across two sections of mirror in RICH2. In this case, an arc of the ring appears displaced from the rest of the ring on the HPD plane; some examples of these non-circular rings can be seen in Figure B.6. Visualisation of events in Panoramix showed that the inability to fit these shapes properly leads to mis-fitting of trackless rings in regions of high ring density and background. It was concluded that isolation criteria should be applied to the trackless rings to provide a clean sample for use in tracking-independent RICH monitoring.

B.2.1 Selection criteria

The selection criteria used to provide a sample of isolated Markov rings are similar to those applied to rings with tracks. As the information available for the Markov rings is limited, however, there are only three requirements. The Markov fitted rings have a centre, radius, RICH radiator type and a list of associated pixel hits. The selection criteria, which were again developed for RICH2 and can be suitably altered for usage in RICH1, were tested on the MC events described in Section B.1.2. The criteria are:

- a requirement on the separation of a Markov ring centre from others around it, in order to prevent overlapping rings from being selected as isolated. This is nominally set to > 260 mm between ring centres, as for the isolated rings with tracks, due to the RICH2 saturated ring radius;
- a requirement on the distribution of hit pixels in terms of Cherenkov θ is made. A band of θ is defined around the Markov ring radius, with a nominal width of 9.44 mrad again chosen. θ is calculated for each associated pixel hit and the fraction of the hits lying within the predefined θ band is found. Only pixel hits within a circular region of interest around the Markov ring centre are considered for association with the ring when it is fitted and all of these are then used within the fraction calculation. It is required that $> 40\%$ of the hits lie within the band around the average θ ; both the ring width and the demand for 40% within the chosen θ band can be altered; and
- a requirement on the distribution of hit pixels in terms of Cherenkov ϕ is made. The $[0, 2\pi]$ range of angle ϕ in which a pixel hit can lie on the ring is divided up into eight angular regions, then the angle ϕ for each associated pixel hit is calculated and the fraction of these lying in each region is found. It is required

that no region has more than 30% of the ring's associated pixel hits in it. As for the isolated rings with tracks, the number of ϕ regions and the maximum fraction in each region can be configured.

The final two criteria are, by default, less stringent than those for the rings with tracks; this is because further use of the Markov rings (see Section B.2.2) requires only that they are adequately well-fitted to the hits.

B.2.2 Ring radius distribution and changes with varying radiator pressure

If the Markov rings are well-fitted, the ring radius should be proportional to Cherenkov θ for the track which produced the photon ring. This means that the distribution of ring radii should change if the Cherenkov θ distribution changes. The ring radii can therefore be used to search for changes in the radiator refractive index.

The distributions of ring radii for isolated Markov rings found in MC events at RICH2 pressures of 970 mbar and 965 mbar were fitted using a polynomial \times Gaussian function and the ring radius corresponding to the maximum of this function was found. The ring radius distribution for 970 mbar, normal RICH2 running pressure, can be seen in Figure B.14. As previously stated, a typical pressure fluctuation in RICH2 is predicted to be of the order 5–10 mbar. Further MC events were produced at different RICH2 radiator pressures (930 mbar, 975 mbar, 985 mbar) and the ring radius distributions for the isolated Markov rings found in these data sets were also fitted. Figure B.15 shows the fitted distribution for 930 mbar data, which would be a large pressure change for normal data-taking conditions.

Figure B.16 shows the variation of the ring radius at distribution maximum with changing RICH2 pressure for isolated Markov rings. It can be seen that the expected variation in ring radius is present, although it is very small. It is therefore possible to use the distribution of ring radii to monitor fluctuations in the subdetector conditions.

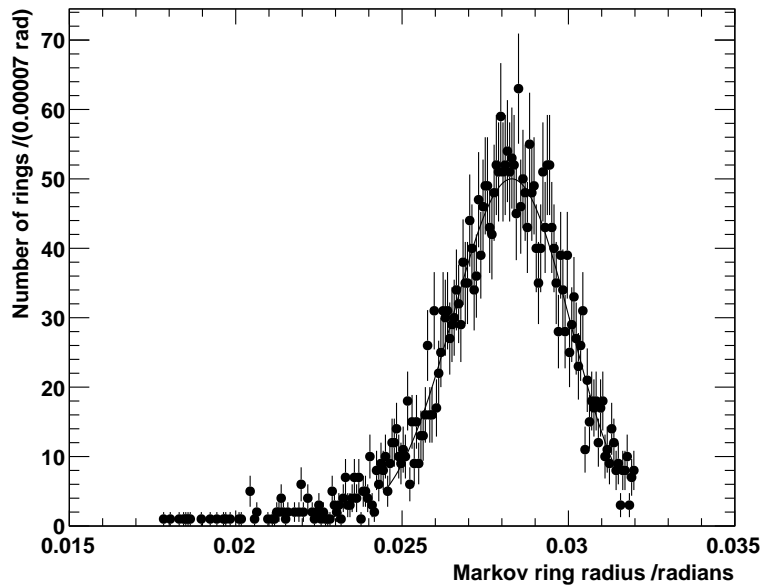


Figure B.14: The ring radius distribution of isolated Markov rings, at a RICH2 pressure of 970 mbar (from MC). The fitted radius at maximum is 0.0283 rad.

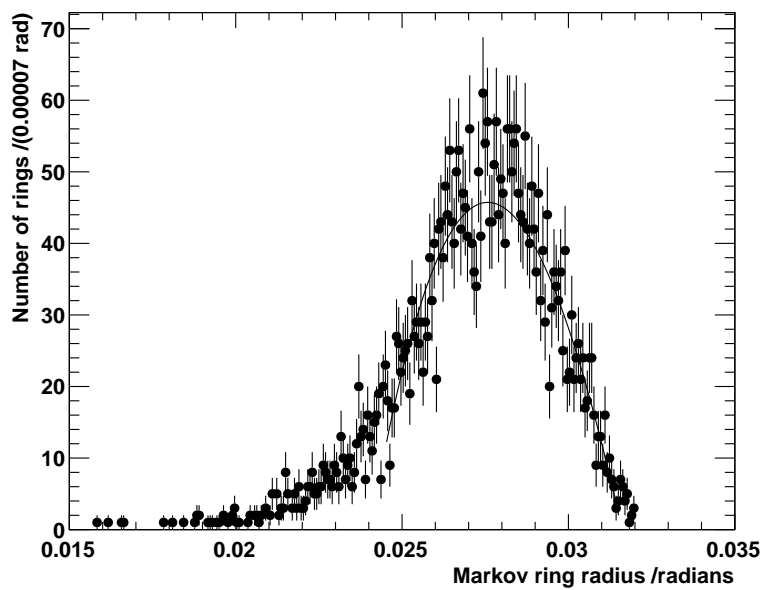


Figure B.15: The ring radius distribution of isolated Markov rings, at a RICH2 pressure of 930 mbar (from MC). The fitted radius at maximum is 0.0276 rad.

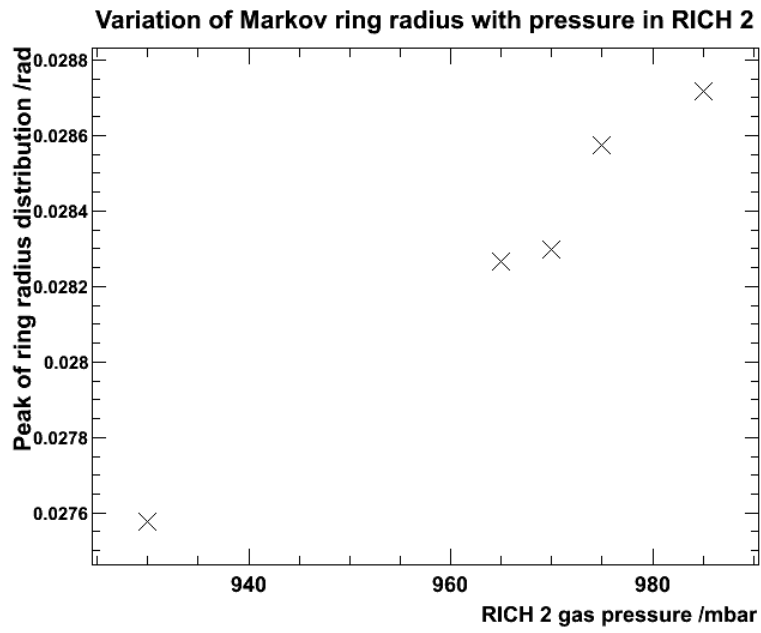


Figure B.16: The ring radius at distribution maximum versus RICH2 pressure, for isolated Markov rings (from MC).

B.3 Usage in proton-proton collision data-taking

Since the start of proton-proton collisions in 2010, the isolated rings with tracks (Section B.1) and isolated trackless rings (Section B.2) have been used in offline and online RICH monitoring. Although the selection criteria were initially developed and tested for RICH2 only, they have been extended to be applicable for RICH1 gas radiator rings [150].

B.3.1 Monitoring with isolated rings with tracks

Isolated rings with tracks are used for offline RICH monitoring purposes, with the ring selection criteria described in Section B.1.2 unchanged. An example of an isolated ring in RICH2 proton-proton collision data is shown in Figure B.17(a). A histogram of Cherenkov resolution for isolated rings is included in the offline data quality histogram presenter, along with a reference histogram, to allow fluctuations in radiator refractive index to be observed and reported. It is currently not possible to use these rings online as the full reconstruction software does not run in the online environment and the necessary information is therefore not available. A version of the reconstruction software for the online environment is under development for use in 2012 and should allow usage of the isolated rings with tracks online [150].

B.3.2 Monitoring with isolated trackless rings

Isolated trackless rings are used in the online RICH monitoring. As described in Section B.2 above, a Markov chain sampler ring finding algorithm was originally used to identify trackless rings, however it was found to use too much CPU time when run in the high detector occupancy environment experienced during proton-proton collisions. A faster trackless ring finding method was developed to replace it, using an elastic neural network approach [186–188]. The isolation criteria described in Section B.2.1 are still employed to provide a clean sample of these rings, however the requirements have been altered slightly to compensate for the different environment experienced in proton-proton collision data-taking compared to MC simulation and to fulfil the requirement of having an adequate number of rings identified in a given time period [150]. An example of an isolated trackless ring in RICH2 proton-proton collision data is shown in Figure B.17(b).

As track information is not available in online monitoring, isolated trackless rings are used by default to provide histograms. In particular, a histogram of ring radius is produced, along with a reference, for observing changes in the shape of the distribution or a shift in peak position which would indicate a fluctuation in refractive index. Figure B.18 shows a snapshot of the online presenter with histograms related to the isolated trackless rings.

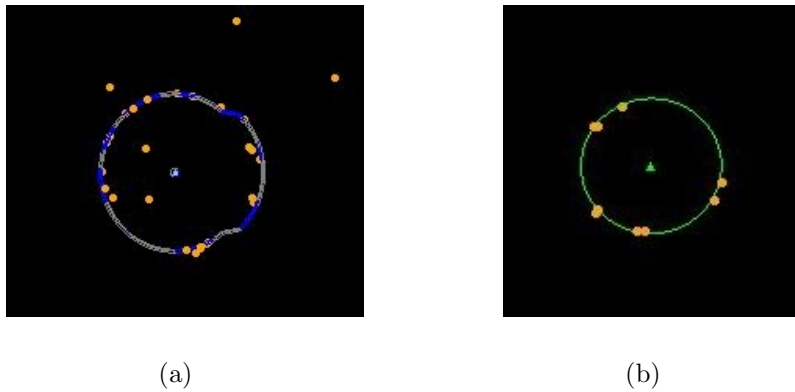


Figure B.17: RICH2 isolated rings taken from different proton-proton collision events. Ring (a) is a ring identified as an isolated ring with track. Ring (b) is an isolated trackless ring.

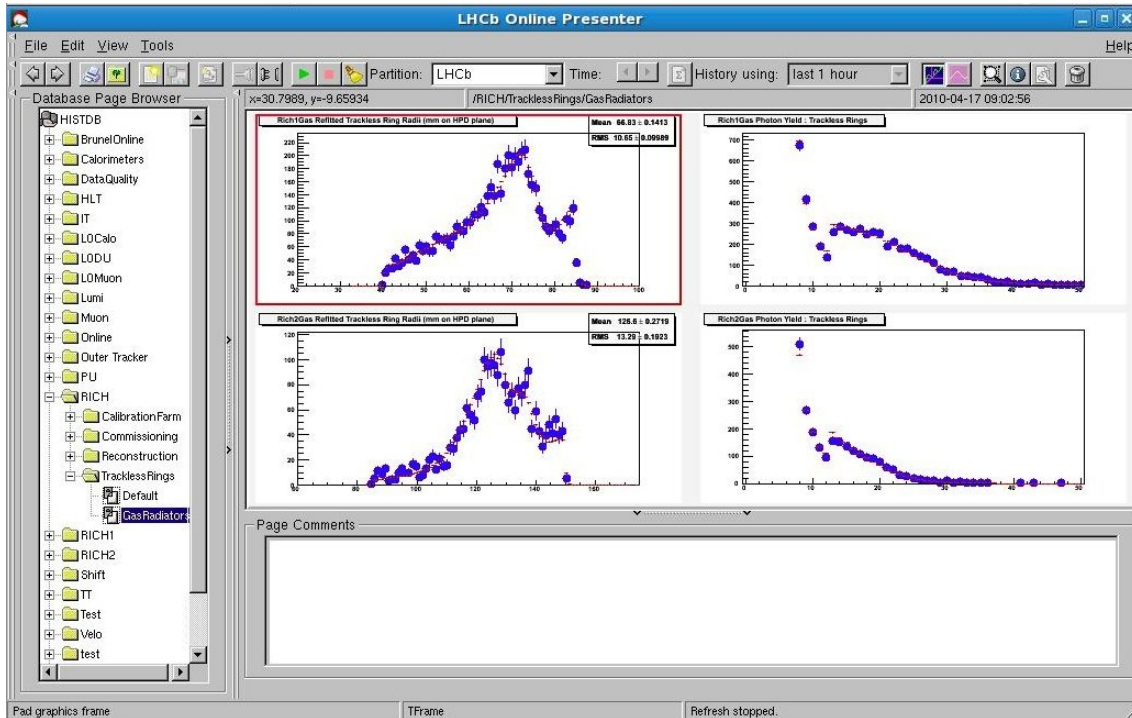


Figure B.18: A snapshot of the RICH online monitoring histogram presenter, showing histograms related to isolated trackless rings. The top left distribution is of ring radii from trackless gas radiator rings in RICH1 and the top right distribution is the photon yield from the same rings. Similar distributions for RICH2 are shown in the bottom two histograms.

B.4 Summary

Selection criteria have been developed to identify isolated Cherenkov rings, both with and without associated tracks, in the RICH subdetectors of LHCb. These rings provide clean samples which can be used to monitor the refractive indices of the RICH system radiators.

Isolation selection requirements on rings with tracks have been shown in MC simulated events to allow the reliable reproduction of Cherenkov θ resolution distributions similar to those found using MC truth. It has also been shown that the resolution distribution alters when detector conditions change, and so the distribution can be used to monitor the conditions, as expected.

Criteria for selecting isolated Cherenkov rings in the RICH subdetectors with no track associated to them have also been developed. The trackless rings were taken from a Markov chain ring fitter acting on MC events; these were then subjected to selection

criteria similar to those of the ring with track case, before a distribution of Markov ring radius was made and fitted. These rings can provide a method for refractive index monitoring independent of tracking information, as the Markov ring radius distribution showed small shifts under radiator pressure changes.

During proton-proton collision data-taking, isolated rings with tracks and isolated trackless rings are used within offline and online RICH monitoring respectively, to allow data quality checks to be performed and for detector conditions to be monitored.

Appendix C

Comparison of MC10 and 2010 data

In order to validate the use of the MC10 samples in extracting lineshapes and efficiencies, it was necessary to perform a comparison of distributions of key variables from the MC and data. $B^\pm \rightarrow D(K_S^0\pi^+\pi^-)h$ LL candidates were selected from the 2010 data and signal $B^\pm \rightarrow D(K_S^0\pi^+\pi^-)h$ MC10 samples, using the full selection criteria described in Chapter 4 including PID requirement and trigger and stripping. B mass windows of ± 50 MeV/ c^2 around the global average value were applied. Magnet up and down samples were summed to give the total distributions; MC truth information was used to ensure that the candidates from MC10 were true signal decays. Figures C.1 to C.13 show various distributions from the resulting candidate samples, with selection criteria indicated with black arrows. It should be noted that there will be some contribution to the 2010 data distributions from $B^\pm \rightarrow D(\pi\pi\pi\pi)h$ decays and other backgrounds. Unfortunately, due to the low statistics in the data (in the DK case in particular) it is difficult to draw firm conclusions about the agreement between the MC and data distributions. It appears that there is good agreement in many cases, with some small disagreement in variables where a detector resolution is used, such as impact parameter χ^2 , vertex χ^2 and flight distance χ^2 . These differences are understood as being due to the slightly worse detector resolution in data than in MC. The detector occupancy, described in terms of total number of tracks or number of long tracks per event, is also not perfectly described. It is expected, however, that these differences will be very similar in the $B^\pm \rightarrow D\pi^\pm$ and $B^\pm \rightarrow DK^\pm$ cases, so that they will effectively cancel in the ratios of efficiencies and are not a cause for concern. The distributions of PID variables $\Delta LL(K - \pi)$ and $\Delta LL(K - p)$ were not compared, as it was already known that the PID performance was not well-described in the MC.

A MC10-2010 data comparison has been performed elsewhere for $B^\pm \rightarrow D(hh)h$ decays, where the number of candidates in the 2010 dataset was much larger [189]. It was found that for almost all variables considered, agreement between MC10 and data was good. The notable exceptions were the PID variables, where the distributions were not well-matched, as expected. Other distributions involving detector resolution also exhibited small variations between data and MC. This confirms the conclusions drawn from the figures below.

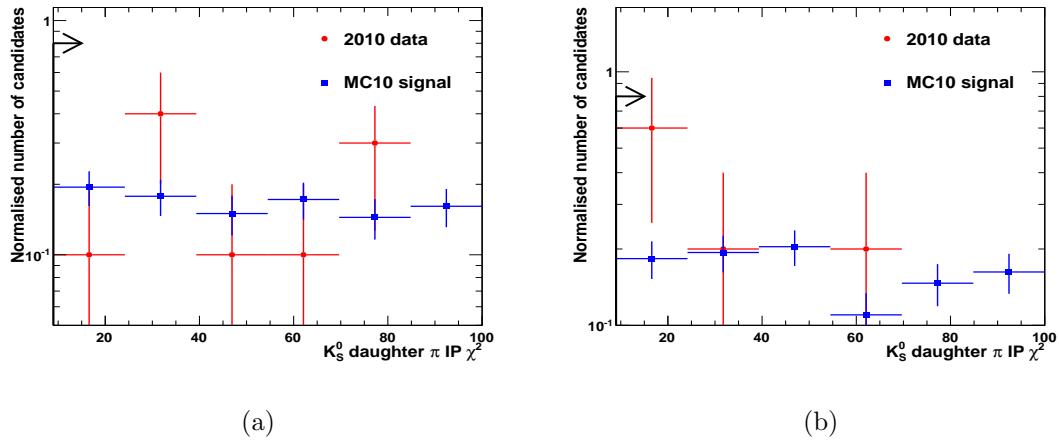


Figure C.1: A comparison of the IP χ^2 (PV) distributions for K_S^0 daughter π from MC10 and 2010 data. Figure C.1(a) shows the $B^\pm \rightarrow D\pi^\pm$ distributions and Figure C.1(b) shows the $B^\pm \rightarrow DK^\pm$ distributions.

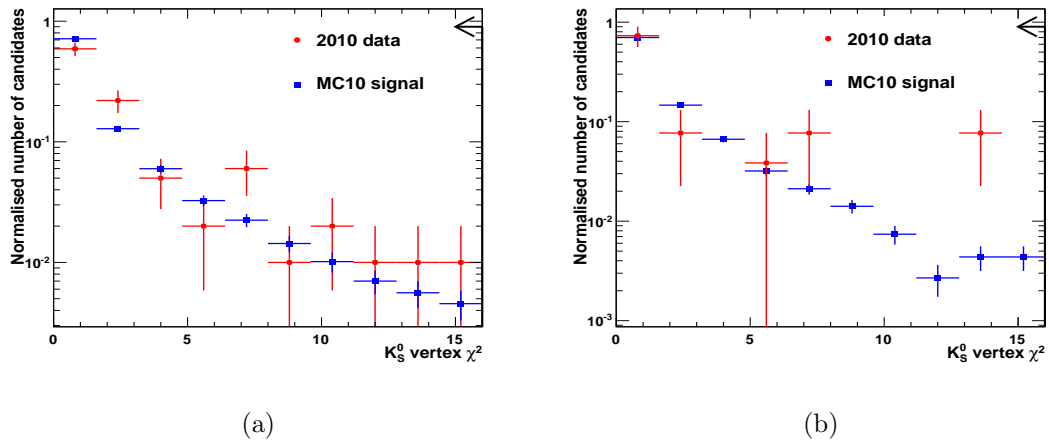


Figure C.2: A comparison of the vertex χ^2 distributions for K_S^0 candidates from MC10 and 2010 data. Figure C.2(a) shows the $B^\pm \rightarrow D\pi^\pm$ distributions and Figure C.2(b) shows the $B^\pm \rightarrow DK^\pm$ distributions.

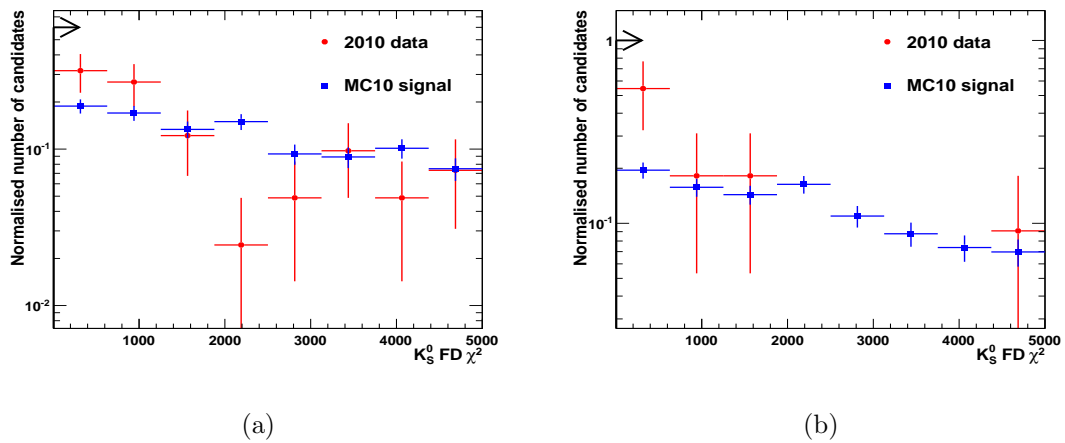


Figure C.3: A comparison of the FD χ^2 (PV) distributions for K_S^0 candidates from MC10 and 2010 data. Figure C.3(a) shows the $B^\pm \rightarrow D\pi^\pm$ distributions and Figure C.3(b) shows the $B^\pm \rightarrow DK^\pm$ distributions.

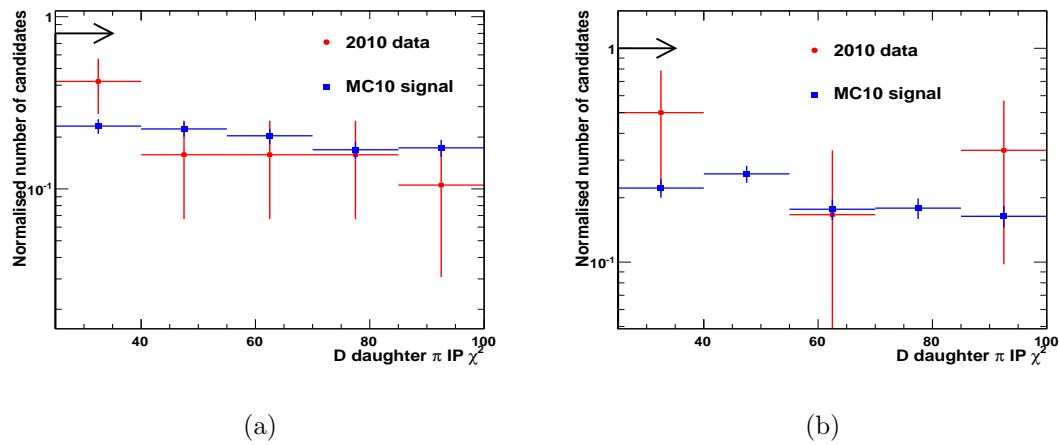


Figure C.4: A comparison of the IP χ^2 (PV) distributions for D daughter π from MC10 and 2010 data. Figure C.4(a) shows the $B^\pm \rightarrow D\pi^\pm$ distributions and Figure C.4(b) shows the $B^\pm \rightarrow DK^\pm$ distributions.

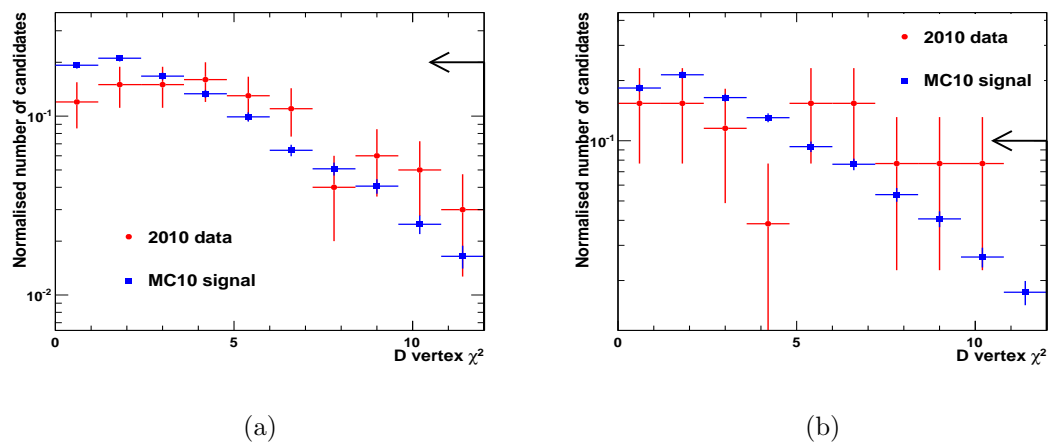


Figure C.5: A comparison of the vertex χ^2 distributions for D candidates from MC10 and 2010 data. Figure C.5(a) shows the $B^\pm \rightarrow D\pi^\pm$ distributions and Figure C.5(b) shows the $B^\pm \rightarrow DK^\pm$ distributions.

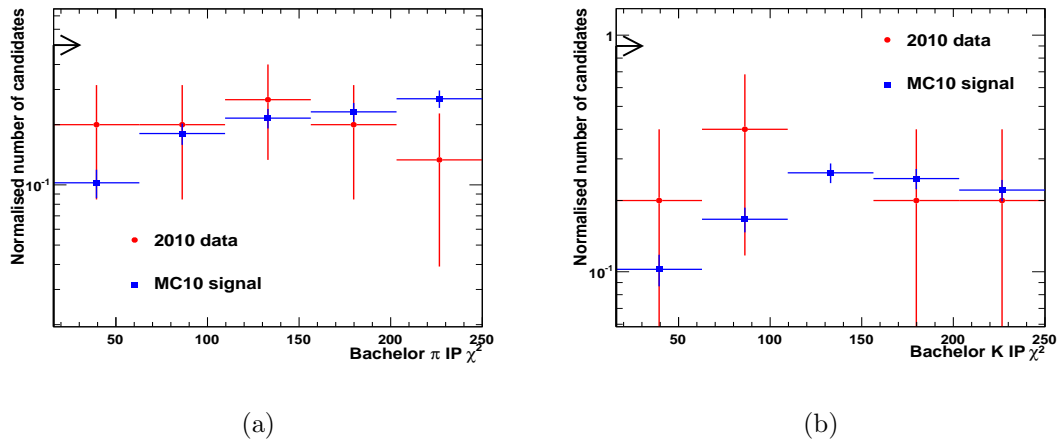


Figure C.6: A comparison of the IP χ^2 (PV) distributions for bachelor K/ π from MC10 and 2010 data. Figure C.6(a) shows the $B^\pm \rightarrow D\pi^\pm$ distributions and Figure C.6(b) shows the $B^\pm \rightarrow DK^\pm$ distributions.

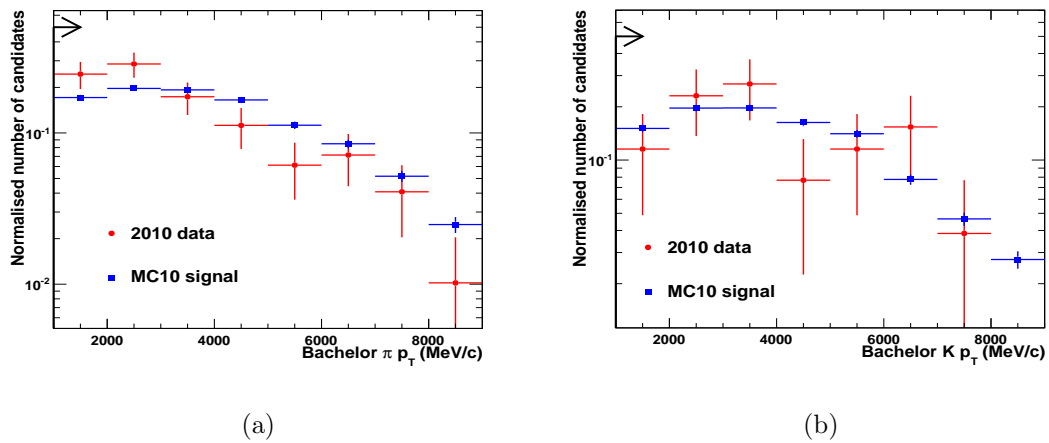


Figure C.7: A comparison of the p_T distributions for the bachelor K/ π from MC10 and 2010 data. Figure C.7(a) shows the $B^\pm \rightarrow D\pi^\pm$ distributions and Figure C.7(b) shows the $B^\pm \rightarrow DK^\pm$ distributions.

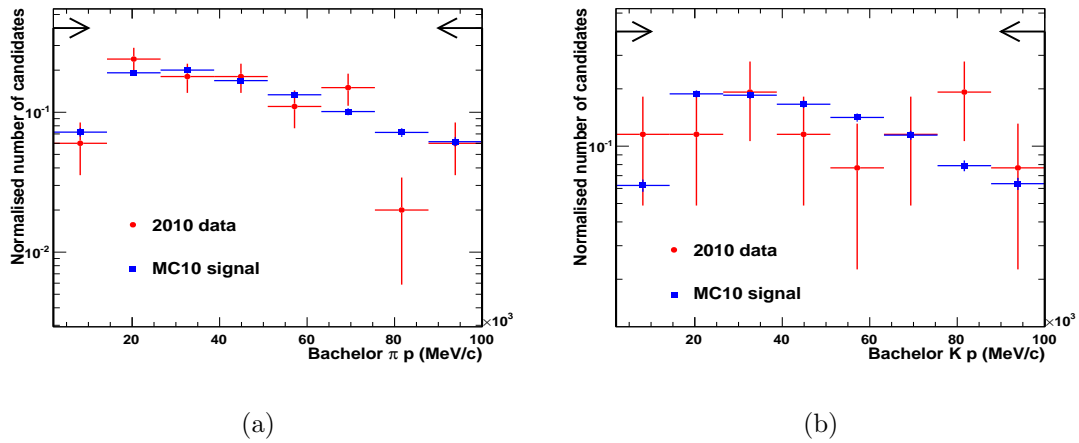


Figure C.8: A comparison of the p distributions for the bachelor K/π from MC10 and 2010 data. Figure C.8(a) shows the $B^\pm \rightarrow D\pi^\pm$ distributions and Figure C.8(b) shows the $B^\pm \rightarrow DK^\pm$ distributions.

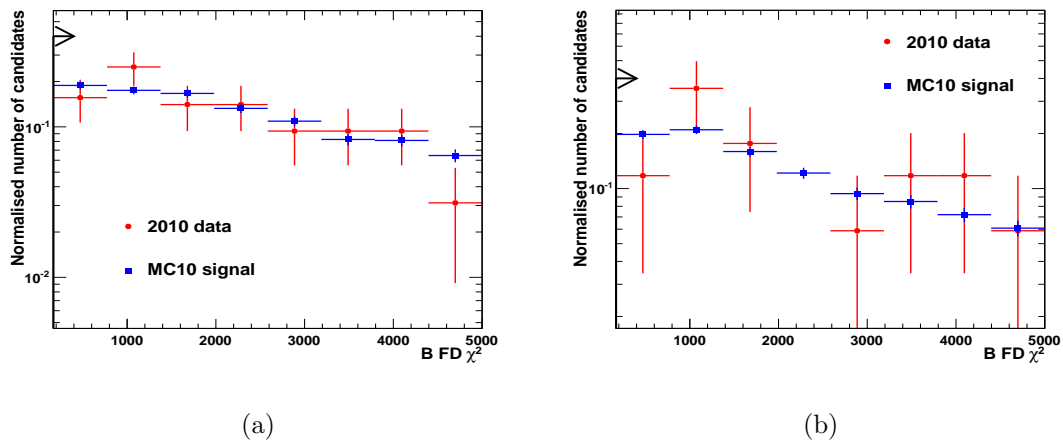


Figure C.9: A comparison of the FD χ^2 (PV) distributions for B candidates from MC10 and 2010 data. Figure C.9(a) shows the $B^\pm \rightarrow D\pi^\pm$ distributions and Figure C.9(b) shows the $B^\pm \rightarrow DK^\pm$ distributions.

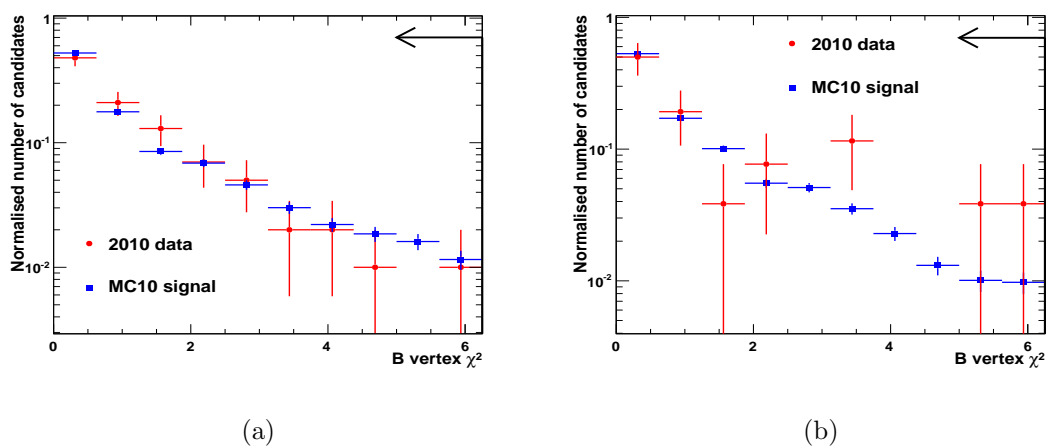


Figure C.10: A comparison of the vertex χ^2 distributions for B candidates from MC10 and 2010 data. Figure C.10(a) shows the $B^\pm \rightarrow D\pi^\pm$ distributions and Figure C.10(b) shows the $B^\pm \rightarrow DK^\pm$ distributions.

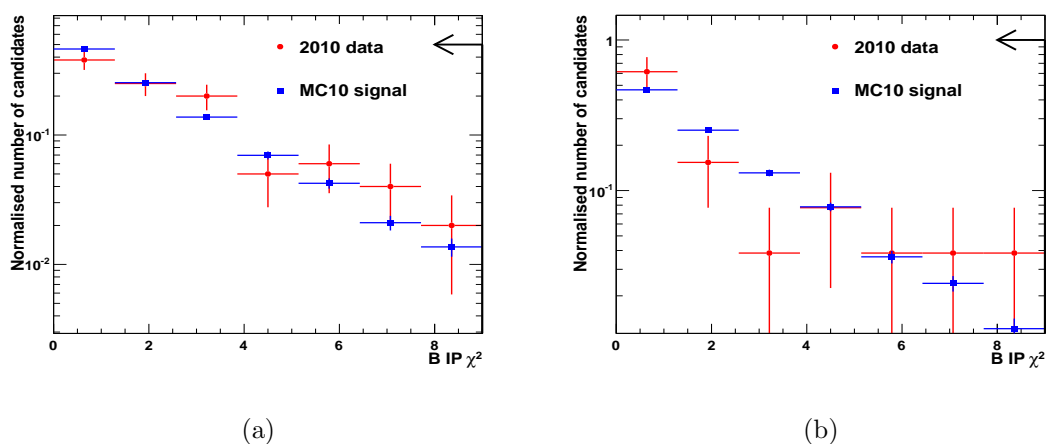


Figure C.11: A comparison of the IP χ^2 (PV) distributions for B candidates from MC10 and 2010 data. Figure C.11(a) shows the $B^\pm \rightarrow D\pi^\pm$ distributions and Figure C.11(b) shows the $B^\pm \rightarrow DK^\pm$ distributions.

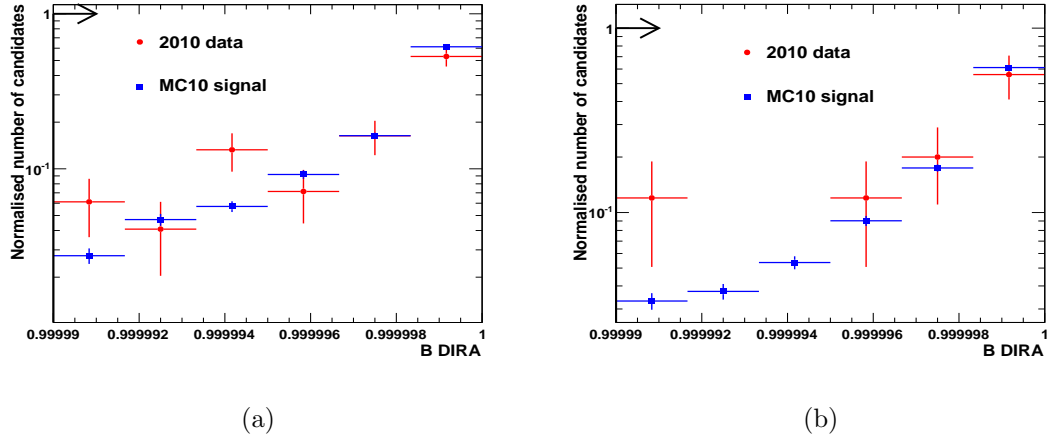


Figure C.12: A comparison of the DIRA distributions for B candidates from MC10 and 2010 data. Figure C.12(a) shows the $B^\pm \rightarrow D\pi^\pm$ distributions and Figure C.12(b) shows the $B^\pm \rightarrow DK^\pm$ distributions.

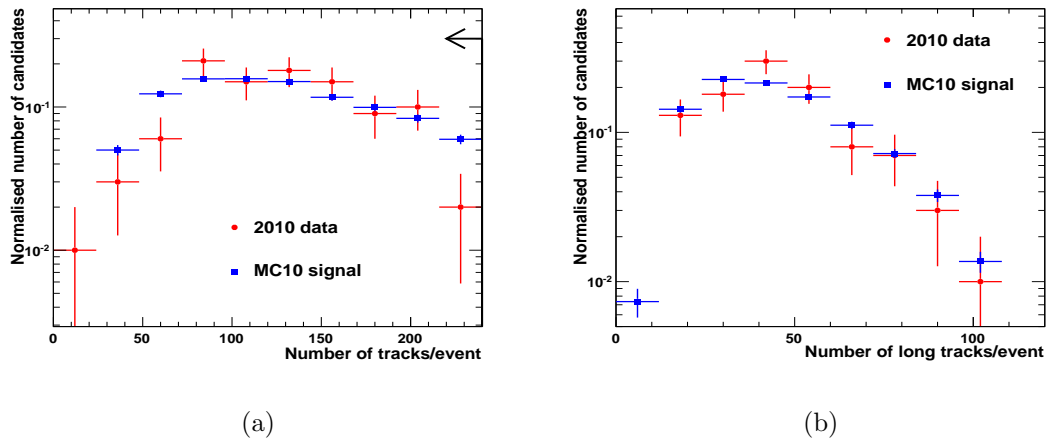


Figure C.13: A comparison of the number of tracks per event and number of long tracks per event from MC10 and 2010 data. Figure C.13(a) shows the number of tracks per event and Figure C.13(b) shows the number of long tracks per event; all entries are from events containing a reconstructed and selected $B^\pm \rightarrow D\pi^\pm$ candidate.

List of Figures

1.1	Feynman diagrams for neutral B-meson mixing.	3
1.2	The CKM unitarity triangles in the complex plane.	16
1.3	The constraints on the CKM unitarity triangle from indirect measurements.	19
1.4	The constraints on the CKM unitarity triangle from direct measurements.	22
1.5	The constraints on B_s^0 parameters $\phi_s^{J/\psi\phi}$ and $\Delta\Gamma_s$	23
1.6	The constraints on the CKM unitarity triangle, combining indirect and direct measurements.	24
1.7	Feynman diagrams for $B^- \rightarrow DK^-$	25
1.8	Feynman diagrams for $\bar{B}_d^0 \rightarrow D\bar{K}^{*0}$	26
1.9	The GLW amplitudes in the complex plane.	29
1.10	B^- decay modes used in the ADS method to maximise sensitivity to γ	30
1.11	Dalitz plots for $B^\pm \rightarrow D(K_S^0\pi^+\pi^-)K^\pm$	32
1.12	The global fit to direct measurements of the CKM angle γ	34
2.1	An LHC dipole magnet within the accelerator tunnel.	38
2.2	The LHC injector complex.	39
2.3	The LHC ring and the main experimental sites.	39
2.4	The proton-proton interaction probability, as function of LHC luminosity.	41
2.5	Examples of Feynman diagrams for dominant $b\bar{b}$ production processes.	42

2.6	The measured cross-section $\sigma(pp \rightarrow b\bar{b}X)$ as a function of pseudorapidity from LHCb data at $\sqrt{s} = 7$ TeV.	43
2.7	The polar production angle of b-hadrons at the LHC.	44
2.8	The LHCb detector.	45
2.9	The LHCb experimental cavern.	46
2.10	The LHCb VELO.	49
2.11	Three LHCb VELO modules.	50
2.12	VELO modules positioned along the RF foil.	51
2.13	VELO sensors.	52
2.14	VELO PV resolution in 2010 data.	52
2.15	VELO PV resolution in 2011 data and MC simulation.	53
2.16	VELO impact parameter resolution in 2010 data.	53
2.17	VELO impact parameter resolution in 2011 data.	54
2.18	An event from 2010 data, containing the first hadronic B decay candidate.	55
2.19	An illustration of track types in LHCb.	57
2.20	A comparison of the tracking efficiency from 2010 data and Monte-Carlo simulation.	57
2.21	A comparison of the tracking efficiency from 2011 data and Monte-Carlo simulation.	58
2.22	The LHCb dipole magnet, from downstream edge.	59
2.23	The measured on-axis field of the LHCb dipole magnet.	60
2.24	The polar angle and momentum coverage of the RICH detectors in MC simulated events.	60
2.25	A schematic of the RICH1 subdetector.	61
2.26	A photograph of the RICH2 subdetector under construction.	62
2.27	The Cherenkov angle as a function of particle momentum from simulation.	63

2.28	The Cherenkov angle in the RICH gas radiators as a function of particle momentum, 2010 data.	64
2.29	The Hybrid Photon Detector for the RICH subdetectors.	65
2.30	The arrangement of HPDs in the upper box of RICH1.	66
2.31	The RICH system performance in 2010 and early 2011 data.	67
2.32	An illustration of the LHCb calorimeter internal structure.	69
2.33	Invariant mass distributions from 2010 data using calorimeter information.	70
2.34	The LHCb muon system.	71
2.35	Sector division of muon stations M2 and M3.	72
2.36	The dimuon mass spectrum from 2010 data, showing Υ resonances.	73
2.37	The integrated luminosity delivered to and recorded by LHCb in 2010 proton-proton collisions.	81
2.38	The peak μ per LHC fill at LHCb in 2010.	81
2.39	The peak instantaneous luminosity per LHC fill at LHCb in 2010.	82
2.40	The integrated luminosity delivered to and recorded by LHCb in 2011 proton-proton collisions.	82
2.41	The peak μ per LHC fill at LHCb in 2011.	83
2.42	The peak instantaneous luminosity per LHC fill at LHCb in 2011.	83
3.1	The topology of the decay $B^\pm \rightarrow D(K_S^0 \pi^+ \pi^-) K^\pm$	86
3.2	The mass distributions for true B^\pm candidates from $B^\pm \rightarrow D(K_S^0 \pi^+ \pi^-) K^\pm$ MC.	95
3.3	The mass distributions for true D candidates from $B^\pm \rightarrow D(K_S^0 \pi^+ \pi^-) K^\pm$ MC.	96
3.4	The mass distributions for true K_S^0 candidates from $B^\pm \rightarrow D(K_S^0 \pi^+ \pi^-) K^\pm$ MC.	96
3.5	The IP χ^2 (PV) distributions for K_S^0 daughter π in preselected MC events.	101

3.6	The $\Delta LL(K - \pi)$ distributions for K_S^0 daughter π in preselected DD MC events.	102
3.7	The vertex χ^2 distributions for K_S^0 candidates in preselected MC events. .	102
3.8	The FD χ^2 (PV) distributions for K_S^0 candidates in preselected MC events.	103
3.9	The IP χ^2 (PV) distributions for D daughter π in preselected MC events.	103
3.10	The $\Delta LL(K - \pi)$ distributions for D daughter π in preselected MC events.	104
3.11	The vertex χ^2 distributions for D candidates in preselected MC events. .	104
3.12	The $\Delta LL(K - \pi)$ distributions for the bachelor K^\pm in preselected MC events.	105
3.13	The $\Delta LL(K - p)$ distributions for the bachelor K^\pm in preselected MC events.	105
3.14	The IP χ^2 (PV) distributions for the bachelor K^\pm in preselected MC events.	106
3.15	The p_T distributions for the bachelor K^\pm in preselected MC events. . . .	106
3.16	The FD χ^2 (PV) distributions for B^\pm candidates in preselected MC events.	107
3.17	The vertex χ^2 distributions for B^\pm candidates in preselected MC events. .	107
3.18	The IP χ^2 (PV) distributions for B^\pm candidates in preselected MC events.	108
3.19	The DIRA distributions for B^\pm candidates in preselected MC events. . .	108
4.1	The likelihood curve for the ratio of branching fractions, $\text{Br}(B^\pm \rightarrow DK^\pm) / \text{Br}(B^\pm \rightarrow D\pi^\pm)$	112
4.2	The $B^\pm \rightarrow D(K_S^0\pi^+\pi^-)h$ candidate mass distributions from 36.5 pb ⁻¹ of 2010 data.	118
4.3	The signal $B^\pm \rightarrow D(K_S^0\pi^+\pi^-)h$ candidate mass distributions from MC. .	121
4.4	The background Category 4 and 5 (low-mass) $B^\pm \rightarrow D(K_S^0\pi^+\pi^-)h$ candidate mass distributions from MC.	122
4.5	The background Category 2 (cross-feed) $B^\pm \rightarrow D(K_S^0\pi^+\pi^-)h$ candidate mass distributions from MC.	123

4.6	The Category 6 background B^\pm candidate mass distributions from MC.	126
4.7	The Category 6 background cross-feed B^\pm candidate mass distributions from MC.	127
4.8	The fitted $B^\pm \rightarrow D(K_S^0\pi^+\pi^-)h$ LL candidate mass distributions from 36.5 pb ⁻¹ of 2010 data.	131
4.9	The verification of the PID weighting technique with MC.	136
4.10	The toy MC distribution for estimation of the systematic error from luminosity and statistical errors.	139
4.11	The toy MC distribution for estimation of the systematic error from global average branching fractions.	140
4.12	The toy MC distribution for estimation of the systematic error from the trigger efficiency.	143
5.1	The $B^\pm \rightarrow D(K_S^0\pi^+\pi^-)h$ candidate mass distributions from 342 pb ⁻¹ of 2011 data.	153
5.2	The signal LL $B^\pm \rightarrow D(K_S^0\pi^+\pi^-)h$ candidate mass distributions from MC.	156
5.3	The signal DD $B^\pm \rightarrow D(K_S^0\pi^+\pi^-)h$ candidate mass distributions from MC.	157
5.4	The background Category 2 (cross-feed) $B^\pm \rightarrow D(K_S^0\pi^+\pi^-)h$ LL candidate mass distributions from MC, with and without application of HLT2 cut-based criteria.	159
5.5	The background Category 2 (cross-feed) $B^\pm \rightarrow D(K_S^0\pi^+\pi^-)h$ DD candidate mass distributions from MC, with and without application of HLT2 cut-based criteria.	160
5.6	The $B^\pm \rightarrow D(K_S^0\pi^+\pi^-)\pi^\pm$ LL candidates from $B_d^0 \rightarrow \bar{D}^0\rho^0$ and $B^+ \rightarrow \bar{D}^*(2007)^0(\bar{D}^0\gamma, \pi^0)\pi^+$ MC samples, with and without application of HLT2 cut-based criteria.	163
5.7	The $B^\pm \rightarrow D(K_S^0\pi^+\pi^-)\pi^\pm$ DD candidates from $B_d^0 \rightarrow \bar{D}^0\rho^0$ and $B^+ \rightarrow \bar{D}^*(2007)^0(\bar{D}^0\gamma, \pi^0)\pi^+$ MC samples, with and without application of HLT2 cut-based criteria.	164

5.8	The $B^\pm \rightarrow D(K_S^0 \pi^+ \pi^-) K^\pm$ LL candidates from a $B_d^0 \rightarrow D^*(2010)^-(\bar{D}^0 \pi^-) K^+$ MC sample, with and without application of HLT2 cut-based criteria.	165
5.9	The $B^\pm \rightarrow D(K_S^0 \pi^+ \pi^-) K^\pm$ DD candidates from a $B_d^0 \rightarrow D^*(2010)^-(\bar{D}^0 \pi^-) K^+$ MC sample, with and without application of HLT2 cut-based criteria.	165
5.10	The components of the low-mass background $B^\pm \rightarrow D(K_S^0 \pi^+ \pi^-) \pi^\pm$ LL candidate mass distributions from MC.	167
5.11	The components of the low-mass background $B^\pm \rightarrow D(K_S^0 \pi^+ \pi^-) \pi^\pm$ DD candidate mass distributions from MC.	168
5.12	The components of the low-mass background $B^\pm \rightarrow D(K_S^0 \pi^+ \pi^-) K^\pm$ LL candidate mass distributions from MC.	170
5.13	The components of the low-mass background $B^\pm \rightarrow D(K_S^0 \pi^+ \pi^-) K^\pm$ DD candidate mass distributions from MC.	171
5.14	The total low-mass background $B^\pm \rightarrow D(K_S^0 \pi^+ \pi^-) h$ candidate mass distributions from MC.	172
5.15	The fitted $B^\pm \rightarrow D(K_S^0 \pi^+ \pi^-) h$ LL candidate mass distributions from 342 pb ⁻¹ of 2011 data.	181
5.16	The fitted $B^\pm \rightarrow D(K_S^0 \pi^+ \pi^-) h$ DD candidate mass distributions from 342 pb ⁻¹ of 2011 data.	182
5.17	The toy MC distribution for estimation of the systematic error from luminosity and statistical errors, LL case.	191
5.18	The toy MC distribution for estimation of the systematic error from luminosity and statistical errors, DD case.	191
5.19	The toy MC distribution for estimation of the systematic error from global average branching fractions, LL case.	192
6.1	The likelihood curve for the ratio of branching fractions, $\text{Br}(B^\pm \rightarrow \bar{D}^0/D^0 K^\pm) / \text{Br}(B^\pm \rightarrow \bar{D}^0/D^0 \pi^\pm)$, with results from this thesis superimposed.	201
6.2	The B^\pm candidate mass distributions from $\sim 1 \text{ fb}^{-1}$ of 2011 data.	202
6.3	Dalitz plots for $B^\pm \rightarrow \bar{D}^0/D^0(K_S^0 \pi^+ \pi^-) K^\pm$ LL candidate decays from the full 2011 LHCb data set.	204

6.4	Dalitz plots for $B^\pm \rightarrow \bar{D}^0/D^0(K_S^0\pi^+\pi^-)K^\pm$ DD candidate decays from the full 2011 LHCb data set.	205
A.1	A Huygens construction for Cherenkov radiation.	208
B.1	A typical low-occupancy event from proton-proton collision data, showing the RICH2 HPD planes as seen in Panoramix.	210
B.2	The reconstructed Cherenkov θ distribution, all photons (from MC).	212
B.3	The Cherenkov θ resolution distribution, MC true photons.	212
B.4	A schematic illustrating the isolated ring θ requirement.	215
B.5	A schematic illustrating the isolated ring ϕ requirement.	215
B.6	RICH2 MC isolated rings with tracks, viewed in Panoramix.	217
B.7	The Cherenkov θ resolution distribution, all photons from isolated rings (from MC).	218
B.8	The Cherenkov θ resolution distribution, MC true photons from isolated rings (from MC).	218
B.9	The Cherenkov θ resolution distribution, all isolated ring and background only photons (from MC).	219
B.10	The momentum distribution for tracks in MC events.	219
B.11	The Cherenkov θ resolution distribution, background photon types from isolated rings with tracks (from MC).	220
B.12	The Cherenkov θ resolution distribution, background photon types from isolated rings with tracks, pixel clustering applied (from MC).	221
B.13	The Cherenkov θ resolution distribution, MC true photons; 965 mbar.	222
B.14	The ring radius distribution of isolated Markov rings, at a RICH2 pressure of 970 mbar (from MC).	225
B.15	The ring radius distribution of isolated Markov rings, at a RICH2 pressure of 930 mbar (from MC).	225

B.16	The ring radius at distribution maximum versus RICH2 pressure, for isolated Markov rings (from MC).	226
B.17	RICH2 data isolated rings, viewed in Panoramix.	228
B.18	A snapshot of the RICH online monitoring histogram presenter.	229
C.1	A comparison of the IP χ^2 (PV) distributions for K_S^0 daughter π from MC10 and 2010 data.	232
C.2	A comparison of the vertex χ^2 distributions for K_S^0 candidates from MC10 and 2010 data.	233
C.3	A comparison of the FD χ^2 (PV) distributions for K_S^0 candidates from MC10 and 2010 data.	233
C.4	A comparison of the IP χ^2 (PV) distributions for D daughter π from MC10 and 2010 data.	234
C.5	A comparison of the vertex χ^2 distributions for D candidates from MC10 and 2010 data.	234
C.6	A comparison of the IP χ^2 (PV) distributions for bachelor K/ π from MC10 and 2010 data.	235
C.7	A comparison of the p_T distributions for the bachelor K/ π from MC10 and 2010 data.	235
C.8	A comparison of the p distributions for the bachelor K/ π from MC10 and 2010 data.	236
C.9	A comparison of the FD χ^2 (PV) distributions for B candidates from MC10 and 2010 data.	236
C.10	A comparison of the vertex χ^2 distributions for B candidates from MC10 and 2010 data.	237
C.11	A comparison of the IP χ^2 (PV) distributions for B candidates from MC10 and 2010 data.	237
C.12	A comparison of the DIRA distributions for B candidates from MC10 and 2010 data.	238

C.13 A comparison of the number of tracks per event and number of long tracks
per event from MC10 and 2010 data. 238

List of Tables

3.1	The sizes of MC samples used in the optimisation of the signal event selection.	87
3.2	The preselection criteria applied to the signal and background MC B^\pm candidates.	90
3.3	The signal branching fractions and hadronisation fraction.	92
3.4	The variables considered by the optimisation algorithm.	94
3.5	The optimised selection criteria for LL candidates.	98
3.6	The optimised selection criteria for DD candidates.	100
4.1	The stripping selections for LL and DD B^\pm candidates in 2010 data.	115
4.2	The fitted yields and parameter values.	132
4.3	The acceptance efficiencies (generator factors) for the signal MC samples.	133
4.4	The combined reconstruction and selection efficiencies for the signal MC samples.	134
4.5	The PID requirement efficiencies for the weighted data calibration samples.	137
4.6	The effect of different L0 Hadron transverse energy thresholds on the combined reconstruction and selection efficiency ratio for the signal MC samples.	142
4.7	The signal and cross-feed expected 36.5 pb^{-1} and fitted yields.	146
4.8	A summary of the systematic errors.	147

5.1	The stripping selections for LL and DD B^\pm candidates in 2011 data.	151
5.2	The low-mass background MC10 samples.	161
5.3	The fitted yield and parameter values in the LL case.	179
5.4	The fitted yield and parameter values in the DD case.	180
5.5	The acceptance efficiencies (generator factors) for the signal MC samples.	183
5.6	The combined reconstruction and selection efficiencies for the signal MC samples, LL candidates.	185
5.7	The combined reconstruction and selection efficiencies for the signal MC samples, DD candidates.	185
5.8	The PID requirement efficiencies for the weighted data calibration samples, LL candidates.	187
5.9	The PID requirement efficiencies for the weighted data calibration samples, DD candidates.	188
5.10	A summary of the systematic errors in the LL case.	196
5.11	A summary of the systematic errors in the DD case.	196
B.1	The nominal isolation selection criteria for rings with associated tracks. .	216

Bibliography

- [1] A. D. Sakharov. Violation of CP Invariance, C Asymmetry, and Baryon Asymmetry of the Universe. *Pisma Zh. Eksp. Teor. Fiz.*, 5:32–35, 1967.
- [2] S. L. Glashow. Partial Symmetries of Weak Interactions. *Nucl. Phys.*, 22:579–588, 1961.
- [3] S. Weinberg. A Model of Leptons. *Phys. Rev. Lett.*, 19(21):1264–1266, 1967.
- [4] S. L. Glashow, J. Iliopoulos, and L. Maiani. Weak Interactions with Lepton-Hadron Symmetry. *Phys. Rev. D*, 2:1285–1292, 1970.
- [5] J. Schwinger. The Theory of Quantized Fields. II. *Phys. Rev.*, 91:713–728, 1953.
- [6] J. Schwinger. The Theory of Quantized Fields. VI. *Phys. Rev.*, 94:1362–1384, 1954.
- [7] G. Lüders. Proof of the TCP Theorem. *Annals Phys.*, 2:1–15, 1957.
- [8] R. L. Garwin et al. Observations of the Failure of Conservation of Parity and Charge Conjugation in Meson Decays: the Magnetic Moment of the Free Muon. *Phys. Rev.*, 105:1415–1417, 1957.
- [9] T. D. Lee and C.-N. Yang. Question of Parity Conservation in Weak Interactions. *Phys. Rev.*, 104:254–258, 1956.
- [10] C. S. Wu et al. Experimental Test of Parity in Beta Decay. *Phys. Rev.*, 105:1413–1414, 1957.

-
- [11] J. H. Christenson et al. Evidence for the 2π Decay of the K_2^0 Meson. *Phys. Rev. Lett.*, 13:138–140, 1964.
- [12] A. B. Carter and A. I. Sanda. CP Violation in B Meson Decays. *Phys. Rev. D*, 23:1567, 1981.
- [13] I. Dunietz and J. L. Rosner. Time-dependent CP-violation Effects in $B^0\text{-}\bar{B}^0$ Systems. *Phys. Rev. D*, 34(5):1404–1417, 1986.
- [14] A. Abashian et al. Measurement of the CP violation Parameter $\sin 2\phi_1$ in B_d^0 Meson Decays. *Phys. Rev. Lett.*, 86:2509–2514, 2001.
- [15] B. Aubert et al. Measurement of CP-Violating Asymmetries in B^0 Decays to CP Eigenstates. *Phys. Rev. Lett.*, 86:2515–2522, 2001.
- [16] B. Aubert et al. Observation of CP Violation in the B^0 Meson System. *Phys. Rev. Lett.*, 87:091801, 2001.
- [17] K. Abe et al. Observation of Large CP violation in the Neutral B Meson System. *Phys. Rev. Lett.*, 87:091802, 2001.
- [18] K. Nakamura et al. Review of particle physics. *J. Phys. G*, 37:075021, 2010. Plus 2011 partial update for the 2012 edition.
- [19] R. Aaij et al. Measurement of Δm_d in $B^0 \rightarrow D^-(K^+\pi^-\pi^-)\pi^+$. CERN-LHCb-CONF-2011-010.
- [20] R. Aaij et al. Measurement of Δm_s in the decay $B_s^0 \rightarrow D_s^-(K^+K^-\pi^-)\pi^+$ using opposite-side and same-side flavour tagging algorithms. CERN-LHCb-CONF-2011-050.
- [21] G. C. Branco, L. Lavoura, and J. P. Silva. CP violation. *Int. Ser. Monogr. Phys.*, 103:1–536, 1999.
- [22] R. Aaij et al. Measurement of direct CP violation in charmless charged two-body B decays at LHCb. CERN-LHCb-CONF-2011-011.

- [23] B. Aubert et al. Measurement of time-dependent CP asymmetry in $B^0 \rightarrow c\bar{c}K^{(*)0}$ decays. *Phys. Rev. D*, 79:072009, 2009.
- [24] H. Sahoo et al. Measurements of time-dependent CP violation in $B^0 \rightarrow \psi(2S)K_S^0$ decays. *Phys. Rev. D*, 77:091103, 2008.
- [25] R. Aaij et al. Search for CP violation in $B^0 \rightarrow J/\psi K_S^0$ decays with first LHCb data. CERN-LHCb-CONF-2011-004.
- [26] P. Ball. The theory of CP-violation: In as much of a nutshell as will fit on 8 pages. 2004. arXiv:hep-ph/0406326.
- [27] P. W. Higgs. Spontaneous Symmetry Breakdown without Massless Bosons. *Phys. Rev.*, 145:1156–1163, 1966.
- [28] F. Englert and R. Brout. Broken Symmetry and the Mass of Gauge Vector Mesons. *Phys. Rev. Lett.*, 13:321–322, 1964.
- [29] N. Cabibbo. Unitary Symmetry and Leptonic Decays. *Phys. Rev. Lett.*, 10(12):531–533, 1963.
- [30] M. Kobayashi and T. Maskawa. CP Violation in the Renormalizable Theory of Weak Interaction. *Prog. Theor. Phys.*, 49:652–657, 1973.
- [31] L-L. Chau and W-Y. Keung. Comments on the Parametrization of the Kobayashi-Maskawa Matrix. *Phys. Rev. Lett.*, 53(19):1802–1805, 1984.
- [32] L. Wolfenstein. Parametrization of the Kobayashi-Maskawa Matrix. *Phys. Rev. Lett.*, 51(21):1945–1947, 1983.
- [33] C. Jarlskog. Commutator of the Quark Mass Matrices in the Standard Electroweak Model and a Measure of Maximal CP Nonconservation. *Phys. Rev. Lett.*, 55(10):1039–1042, 1985.
- [34] CKMfitter Group (J. Charles et al.). *Eur. Phys. J. C*, 41:1–131, 2005. Updated results and plots available at: <http://ckmfitter.in2p3.fr>.

-
- [35] J. Zupan. Penguin Pollution Estimates relevant for α/ϕ_2 Extraction. *Nucl. Phys. B Proc. Suppl.*, 170:33–38, 2007.
- [36] M. Gronau and D. London. Isospin Analysis of CP Asymmetries in B Decays. *Phys. Rev. Lett.*, 65:3381–3384, 1990.
- [37] H. Ishino et al. Observation of direct CP Violation in $B^0 \rightarrow \pi^+\pi^-$ decays and model-independent constraints on the quark-mixing angle ϕ_2 . *Phys. Rev. Lett.*, 98:211801, 2007.
- [38] B. Aubert et al. Measurement of CP asymmetries and branching fractions in $B^0 \rightarrow \pi^+\pi^-$, $B^0 \rightarrow K^+\pi^-$, $B^0 \rightarrow \pi^0\pi^0$, $B^0 \rightarrow K^0\pi^0$ and isospin analysis of $B \rightarrow \pi\pi$ decays. arXiv:0807.4226v2.
- [39] C.-C. Chiang et al. Measurement of $B^0 \rightarrow \pi^+\pi^-\pi^+\pi^-$ decays and search for $B^0 \rightarrow \rho^0\rho^0$. *Phys. Rev. D*, 78:111102, 2008.
- [40] B. Aubert et al. Improved measurement of $B^+ \rightarrow \rho^+\rho^0$ and determination of the quark-mixing phase angle α . *Phys. Rev. Lett.*, 102:141802, 2009.
- [41] A. Kusaka et al. Measurement of CP asymmetries and branching fractions in a time-dependent Dalitz analysis of $B^0 \rightarrow (\rho\pi)^0$ and a constraint on the quark mixing angle ϕ_2 . *Phys. Rev. D*, 77:072001, 2008.
- [42] B. Aubert et al. Measurement of CP-violating asymmetries in $B^0 \rightarrow (\rho\pi)^0$ using a time-dependent Dalitz plot analysis. *Phys. Rev. D*, 76:012004, 2007.
- [43] R. Aaij et al. Measurements of the relative and absolute branching fractions of the decays $B_s \rightarrow D_s^\mp K^\pm$ and $B_s \rightarrow D_s^- \pi^+$. CERN-LHCb-CONF-2011-057.
- [44] T. Aaltonen et al. First Flavor-Tagged Determination of Bounds on Mixing-Induced CP Violation in $B_s^0 \rightarrow J/\psi\phi$ Decays. *Phys. Rev. Lett.*, 100:161802, 2008.
- [45] T. Aaltonen et al. An Updated Measurement of the CP Violating Phase $\beta_s^{J/\psi\phi}$ in $B_s \rightarrow J/\psi\phi$ Decays using 5.2 fb^{-1} of Integrated Luminosity. CDF/ANAL/BOTTOM/PUBLIC/10206.

- [46] V. M. Abazov et al. Measurement of B_s^0 mixing parameters from the flavor-tagged decay $B_s^0 \rightarrow J/\psi\phi$. *Phys. Rev. Lett.*, 101:241801, 2008.
- [47] V.M. Abazov et al. Measurement of CP violation in the B_s system at D0. Proceedings of Science (EPS-HEP), 2011.
- [48] R. Aaij et al. Tagged time-dependent angular analysis of $B_s \rightarrow J/\psi\phi$ decays with 337 pb^{-1} at LHCb. CERN-LHCb-CONF-2011-049.
- [49] A.S. Dighe, I. Dunietz, and R. Fleischer. Extracting CKM phases and B_s - \bar{B}_s mixing parameters from angular distributions of non-leptonic B decays. *Eur. Phys. J. C*, 6:647–662, 1999.
- [50] D. Asner et al. Averages of b-hadron, c-hadron and tau-lepton properties, 2011. Heavy Flavor Averaging Group (HFAG), <http://www.slac.stanford.edu/xorg/hfag>.
- [51] R. Aaij et al. Measurement of ϕ_s in $\bar{B}_s \rightarrow J/\psi f_0(980)$. CERN-LHCb-CONF-2011-051.
- [52] R. Aaij et al. Combination of ϕ_s measurements from $B_s \rightarrow J/\psi\phi$ and $\bar{B}_s \rightarrow J/\psi f_0(980)$. CERN-LHCb-CONF-2011-056.
- [53] J. Charles et al. Predictions of selected flavor observables within the standard model. *Phys. Rev. D*, 84:033005, 2011.
- [54] Y. Grossman, A. Soffer, and J. Zupan. The Effect of $D - \bar{D}$ Mixing on the Measurement of γ in $B \rightarrow DK$ decays. *Phys. Rev. D*, 72:031501, 2005.
- [55] B. Adeva et al. Roadmap for selected key measurements of LHCb. CERN-LHCb-PUB-2009-029.
- [56] B. Aubert et al. Constraints on the CKM angle γ in $B^0 \rightarrow \bar{D}^0 K^{*0}$ and $B^0 \rightarrow D^0 K^{*0}$ from a Dalitz analysis of D^0 and \bar{D}^0 decays to $K_S \pi^+ \pi^-$. *Phys. Rev. D*, 79:072003, 2009.

- [57] M. Gronau. Improving bounds on γ in $B^\pm \rightarrow DK^\pm$ and $B^{\pm,0} \rightarrow DX_s^{\pm,0}$. *Phys. Lett. B*, 557(3-4):198 – 206, 2003.
- [58] T. E. Browder, K. Honscheid, and D. Pedrini. Nonleptonic decays and lifetimes of charm and beauty particles. *Ann. Rev. Nucl. Part. Sci.*, 46:395 – 469, 1996.
- [59] M. Gronau and J. L. Rosner. Final state interaction effects on γ from $B \rightarrow DK$. *Phys. Lett. B*, 439(1-2):171 – 175, 1998.
- [60] B. Blok, M. Gronau, and J. L. Rosner. Annihilation, Rescattering, and CP Asymmetries in B Meson Decays. *Phys. Rev. Lett.*, 78:3999–4002, 1997.
- [61] M. Gronau and D. London. How to Determine All the Angles of the Unitarity Triangle from $B_d^0 \rightarrow DK_S$ and $B_s^0 \rightarrow D\phi$. *Phys. Lett. B*, 253:483–488, 1991.
- [62] M. Gronau and D. Wyler. On Determining a Weak Phase from Charged B Decay Asymmetries. *Phys. Lett. B*, 265:172–176, 1991.
- [63] P. del Amo Sanchez et al. Measurement of CP observables in $B^\pm \rightarrow D_{CP}K^\pm$ decays and constraints on the CKM angle γ . *Phys. Rev. D*, 82:072004, 2010.
- [64] T. Gershon on behalf of the Belle Collaboration. Preliminary result, presented at Lepton-Photon 2011. BELLE-CONF-1112.
- [65] T. Aaltonen et al. Measurements of branching fraction ratios and CP asymmetries in $B^\pm \rightarrow D_{CP}K^\pm$ decays in hadron collisions. *Phys. Rev. D*, 81:031105, 2010.
- [66] R. Aaij et al. A measurement of the ratio of branching fractions: $\frac{B(B^\pm \rightarrow DK^\pm)}{B(B^\pm \rightarrow D\pi^\pm)}$ for $D \rightarrow K\pi$, $D \rightarrow KK$, $D \rightarrow K\pi\pi\pi$ and $D \rightarrow K_s^0\pi\pi$. CERN-LHCb-CONF-2011-031.
- [67] A. Soffer. Discrete Ambiguities in the Measurement of the Weak Phase γ . *Phys. Rev. D*, 60:054032, 1999.
- [68] I. Dunietz. CP violation with self tagging B_d modes. *Phys. Lett. B*, 270:75–80, 1991.

- [69] I. Dunietz. $B_s - \bar{B}_s$ mixing, CP violation and Extraction of CKM Phases from Untagged B_s Data Samples. *Phys. Rev. D*, 52:3048–3064, 1995.
- [70] D. Atwood, I. Dunietz, and A. Soni. Enhanced CP violation with $B \rightarrow K D^0 (\bar{D}^0)$ Modes and Extraction of the CKM Angle γ . *Phys. Rev. Lett.*, 78:3257–3260, 1997.
- [71] Y. Horii et al. Evidence for the Suppressed Decay $B^- \rightarrow DK^-$, $D \rightarrow K^+\pi^-$. *Phys. Rev. Lett.*, 106:231803, 2011.
- [72] P. del Amo Sanchez et al. Search for $b \rightarrow u$ transitions in $B^- \rightarrow DK^-$ and $B^- \rightarrow D^{(*)}K^-$ Decays. *Phys. Rev. D*, 82:072006, 2010.
- [73] T. Aaltonen et al. Measurements of branching fraction ratios and CP-asymmetries in suppressed $B^- \rightarrow D(K^+\pi^-)K^-$ and $B^- \rightarrow D(K^+\pi^-)\pi^-$ decays. FERMILAB-PUB-11-404-E-PPD.
- [74] R. Aaij et al. Evidence for the suppressed decay $B^\pm \rightarrow (K^\mp\pi^\pm)_D K^\pm$. CERN-LHCb-CONF-2011-044.
- [75] A. Giri, Y. Grossman, A. Soffer, and J. Zupan. Determining γ using $B^\pm \rightarrow DK^\pm$ with Multibody D Decays. *Phys. Rev. D*, 68(5):054018, 2003.
- [76] V. Gibson, C. Lazzeroni, and J. Libby. Measuring γ at LHCb with $B^\pm \rightarrow \bar{D}^0/D^0(K_S\pi^+\pi^-)K^\pm$ Decays. CERN-LHCb-2007-048.
- [77] C. Zemach. Three-Pion Decays of Unstable Particles. *Phys. Rev.*, 133:B1201, 1964.
- [78] J. Libby. An Amplitude-model Independent Measurement of γ at LHCb with $B^\pm \rightarrow \bar{D}^0/D^0(K_S\pi^+\pi^-)K^\pm$ Decays. CERN-LHCb-2007-141.
- [79] Y. Y. Li. *A study of the CKM angle γ using the LHCb experiment and a distributed workload management system*. PhD thesis, University of Cambridge, 2009. CERN-THESIS-2009-140.
- [80] B. Aubert et al. Constraints on the CKM angle γ in $B^0 \rightarrow \bar{D}^0(D^0)K^{*0}$ from a Dalitz analysis of $D^0 \rightarrow K_S^0\pi^+\pi^-$. *Phys. Rev. D*, 79:072003, 2009.

- [81] A. Poluektov et al. Evidence for direct CP violation in the decay $B \rightarrow D^{(*)}K, D \rightarrow K_S^0\pi^+\pi^-$ and measurement of the CKM phase ϕ_3 . *Phys. Rev. D*, 81:112002, 2010.
- [82] P. del Amo Sanchez et al. Evidence for direct CP violation in the measurement of the Cabibbo-Kobayashi-Maskawa angle γ with $B^\mp \rightarrow D^{(*)}K^{(*)\mp}$ decays. *Phys. Rev. Lett.*, 105:121801, 2010.
- [83] I. Adachi et al. First measurement of ϕ_3 with a binned model-independent Dalitz plot analysis of $B^\pm \rightarrow DK^\pm, D \rightarrow K_S^0\pi^+\pi^-$ decay. BELLE-CONF-1103. arXiv:1106.4046v1.
- [84] J. Libby et al. Model-independent determination of the strong-phase difference between D^0 and $\bar{D}^0 \rightarrow K_{S,L}^0 h^+ h^-$ ($h = \pi, K$) and its impact on the measurement of the CKM angle γ/ϕ_3 . *Phys. Rev. D*, 82:112006, 2010.
- [85] K. Akiba et al. Determination of the CKM angle γ with tree-level processes at LHCb. CERN-LHCb-2008-031.
- [86] W. Bernreuther. CP-violation and Baryogenesis. 2002. arXiv:hep-ph/0205279.
- [87] S. Barr, G. Segrè, and H. A. Weldon. Magnitude of the cosmological baryon asymmetry. *Phys. Rev. D*, 20:2494–2498, 1979.
- [88] P. Lefevre, T. Petterson et al. The Large Hadron Collider: Conceptual design. CERN-AC-95-05-LHC.
- [89] O. Brüning, P. Collier, P. Lebrun, S. Myers, R. Ostojic, J. Poole, and P. Proudlock. LHC Design Report Vol. I: The LHC main ring. CERN-2004-003.
- [90] L. Evans (ed.) and P. Bryant (ed.). LHC Machine. *JINST*, 3:S08001, 2008.
- [91] M. Benedikt, P. Collier, V. Mertens, J. Poole, and K. Schindl. LHC Design Report Vol III. The LHC injector chain. CERN-2004-003.
- [92] *Tests of the CERN Proton Linac Performance for LHC-type Beams*, 2000. 20th International Linear Accelerator Conference, Monterey, CA, USA.

-
- [93] *Present Performance of the CERN Proton Linac*, 1998. 19th International Linear Accelerator Conference (Linac 98), Chicago, IL.
- [94] G. Aad et al. The ATLAS Experiment at the CERN Large Hadron Collider. *JINST*, 3:S08003, 2008.
- [95] S. Chatrchyan et al. The CMS experiment at the CERN LHC. *JINST*, 3:S08004, 2008.
- [96] A. A. Alves et al. The LHCb Detector at the LHC. *JINST*, 3:S08005, 2008.
- [97] S. Chatrchyan et al. The ALICE experiment at the CERN LHC. *JINST*, 3:S08002, 2008.
- [98] S. Amato et al. LHCb technical proposal. CERN-LHCC-98-04.
- [99] LHCb Collaboration. LHCb technical design report: Reoptimized detector design and performance. CERN-LHCC-2003-030.
- [100] V. P. Andreev. B production at the LHC / QCD aspects. 2007. arXiv:hep-ex/0706.1789.
- [101] R. K. Ellis, W. J. Stirling, and B. R. Webber. QCD and collider physics. *Camb. Monogr. Part. Phys. Nucl. Phys. Cosmol.*, 8:1–435, 1996.
- [102] R. Aaij et al. Measurement of $\sigma(pp \rightarrow b\bar{b}X)$ at $\sqrt{s} = 7$ TeV in the forward region. *Phys. Lett. B*, 694(3):209, 2010.
- [103] M. L. Mangano. Two lectures on heavy quark production in hadronic collisions. 1997. arXiv:hep-ph/9711337.
- [104] LHCb Collaboration. LHCb Velo Technical Design Report. CERN-LHCC-2001-011.
- [105] S. Redford on behalf of the LHCb Collaboration. LHCb VELO Closing Control, Beam Reconstruction, and Luminosity from Vertex Reconstruction. PoS(VERTEX 2010)018; CERN-LHCb-PROC-2010-043.

-
- [106] K. Rinnert on behalf of the LHCb Collaboration. First Results from the LHCb VELO. Presented at IEEE NSS, November 2010; CERN-LHCb-TALK-2010-180.
- [107] A. Leflat on behalf of the LHCb Collaboration. Performance of the LHCb Vertex Locator. Presented at ICATPP, October 2011; CERN-LHCb-TALK-2011-205.
- [108] M. Gersabeck on behalf of the LHCb Collaboration. LHCb Tracking, Alignment and Physics Performance. PoS(VERTEX 2010)014; CERN-LHCb-PROC-2010-065.
- [109] A. Jaeger on behalf of the LHCb Collaboration. Tracking performance of the LHCb spectrometer. Presented at ICATPP 2011; CERN-LHCb-PROC-2011-057.
- [110] LHCb Collaboration. LHCb Magnet Technical Design Report. CERN-LHCC-2000-007.
- [111] LHCb Collaboration. LHCb trigger system technical design report. CERN-LHCC-2003-031.
- [112] H. Dijkstra et al. The relevance of the magnetic field in the Level-1 trigger. CERN-LHCb-2003-110.
- [113] LHCb Collaboration. LHCb RICH Technical Design Report. CERN-LHCC-2000-037.
- [114] M. Coombes. Private communication.
- [115] LHCb Collaboration. Photon Detectors for the LHCb RICH: Addendum to the Technical Design Report. CERN-LHCC-2003-059.
- [116] M. Campbell et al. Performance of hybrid photon detector prototypes with encapsulated silicon pixel detector and readout for the RICH counters of LHCb. *Nucl. Instrum. Meth. A*, 504:286–289, 2003.
- [117] M. Moritz et al. Performance study of new pixel hybrid photon detector prototypes for the LHCb RICH counters. *IEEE Trans. Nucl. Sci.*, 51:1060–1066, 2004.

-
- [118] R. Cardinale et al. Analysis and correction of the magnetic field effects in the Hybrid Photo-Detectors of the RICH2 detector of LHCb. CERN-LHCb-PUB-2011-013.
- [119] R. Forty and O. Schneider. RICH Pattern Recognition. CERN-LHCb-98-040.
- [120] G. Wilkinson. In Search of the Rings: Approaches to Cherenkov Ring Finding and Reconstruction in High Energy Physics. *Nucl. Instrum. Meth. A*, 595:228–232, 2008.
- [121] A. Powell. Private communication.
- [122] A. Powell. Private communication.
- [123] LHCb Collaboration. LHCb Calorimeters Technical Design Report. CERN-LHCC-2000-036.
- [124] S. Filippov et al. Experimental Performance of SPD/PS Detector Prototypes. CERN-LHCb-2000-031.
- [125] J. Badier et al. Shashlik Calorimeter: Beam Test Results. *Nucl. Instrum. Meth. A*, 348:74–86, 1994.
- [126] C. Beigbeder-Beau et al. An Update of the 2x2 Implementation for the Level 0 Calorimeter Triggers. CERN-LHCb-99-007.
- [127] X. Vilasis-Cardona. Commissioning the LHCb calorimeters with cosmic rays. *Nucl. Inst. Methods Phys. Res. A*, 623(1):222 – 224, 2010. 1st International Conference on Technology and Instrumentation in Particle Physics.
- [128] F. Machefert on behalf of the LHCb Collaboration. First Year of Running of the LHCb Calorimeter System. Presented at TIPP, June 2011; CERN-LHCb-TALK-2011-106.
- [129] I. Machikhiliyan on behalf of the LHCb Collaboration. Current status and performance of the LHCb electromagnetic and hadron calorimeters. CERN-LHCb-PROC-2010-030.

-
- [130] G. Bencivenni et al. A triple-GEM detector with pad readout for high rate charged particle triggering. CERN-LHCb-MUON-2001-051.
- [131] B. Botchine et al. Wire Pad Chambers and Cathode Pad Chambers for the LHCb Muon System. CERN-LHCb-2000-114.
- [132] A. Kachtchouk et al. Design and Construction of the Wire Chambers for the LHCb Muon System. CERN-LHCb-2001-026.
- [133] M. Anelli et al. Performance of the LHCb muon system with cosmic rays. *JINST*, 5:10003, 2010.
- [134] A. Powell on behalf of the LHCb Collaboration. Particle Identification at LHCb. Presented at ICHEP 2010; CERN-LHCb-PROC-2011-008.
- [135] X. Cid Vidal on behalf of the LHCb Collaboration. Muon Identification in the LHCb experiment. CERN-LHCb-PROC-2010-013.
- [136] A. Sarti et al. Calibration Strategy and Efficiency Measurement of the Muon Identification Procedure at LHCb. CERN-LHCb-PUB-2010-002.
- [137] E. Rodrigues. The LHCb Trigger System. CERN-LHCb-2006-065.
- [138] A. Barczyk, G. Haefeli, R. Jacobsson, B. Jost, and N. Neufeld. 1 MHz Readout. CERN-LHCb-2005-062.
- [139] J. Christiansen. Requirements to the L0 Front-end Electronics. CERN-LHCb-2001-014.
- [140] E. Aslanides et al. A Realistic Algorithm for the L0 Muon Trigger. CERN-LHCb-2002-042.
- [141] E. Aslanides et al. A Synchronous Architecture for the L0 Muon Trigger. CERN-LHCb-2001-010.
- [142] Z. Ajaltouni et al. Status of the L0 Trigger Decision Unit Design. CERN-LHCb-1999-019.

-
- [143] A. Perez-Calero Yzquierdo on behalf of the LHCb Collaboration. LHCb trigger system design and commissioning with $\sqrt{s} = 7$ TeV proton-proton collisions at LHC. Presented at 12th Topical Seminar on Innovative Particle and Radiation Detectors, 2010; CERN-LHCb-PROC-2010-035.
- [144] R. Aaij and J. Albrecht. Muon triggers in the High Level Trigger of LHCb. CERN-LHCb-PUB-2011-017.
- [145] R. Aaij on behalf of the LHCb Collaboration. The LHCb Trigger: present and future. Presented at TIPP, June 2011; LHCb-TALK-2011-108.
- [146] V. Gligorov. A single track HLT1 trigger. LHCb-PUB-2011-003.
- [147] V. Gligorov, C. Thomas, and M. Williams. The HLT inclusive B triggers. LHCb-PUB-2011-016.
- [148] V. Gligorov et al. The HLT2 Topological Lines. LHCb-PUB-2011-002.
- [149] LHCb Collaboration. LHCb Online System Technical Design Report. CERN-LHCC-2001-040.
- [150] C. Jones. Private communication.
- [151] G. Corti. LHCb computing. *Nucl. Instrum. Meth. A*, 462:265–269, 2001.
- [152] G. Barrant et al. GAUDI - A software architecture and framework for building HEP data processing applications. *Comput. Phys. Commun.*, 140:45–55, 2001.
- [153] <http://lcg.web.cern.ch/lcg/>.
- [154] <http://ganga.web.cern.ch/ganga/>.
- [155] S. Paterson and A. Tsaregorodtsev. DIRAC Infrastructure for Distributed Analysis. CERN-LHCb-2006-015.
- [156] <http://diracgrid.org/>.
- [157] <http://lhcb-release-area.web.cern.ch/LHCb-release-area/DOC/gauss/>.

- [158] <http://lhcb-release-area.web.cern.ch/LHCb-release-area/DOC/boole/>.
- [159] <http://home.thep.lu.se/~torbjorn/Pythia.html>.
- [160] <http://lhcb-release-area.web.cern.ch/LHCb-release-area/DOC/gauss/generator/evtgen.php>.
- [161] S. Agostinelli et al. GEANT4: A simulation toolkit. *Nucl. Instrum. Meth. A*, 506:250–303, 2003.
- [162] <http://geant4.cern.ch/>.
- [163] <http://lhcb-release-area.web.cern.ch/LHCb-release-area/DOC/moore/>.
- [164] <http://lhcb-release-area.web.cern.ch/LHCb-release-area/DOC/brunel/>.
- [165] <http://lhcb-release-area.web.cern.ch/LHCb-release-area/DOC/davinci/>.
- [166] <http://lhcb-release-area.web.cern.ch/LHCb-release-area/DOC/panoramix/>.
- [167] M. Patel and H. Skottowe. A cut based selection for $B_d \rightarrow K^* \mu \mu$ at LHCb. CERN-LHCb-2009-008.
- [168] Y. Horii et al. Study of the suppressed B meson decay $B^- \rightarrow DK^-$, $D \rightarrow K^+ \pi^-$. *Phys. Rev. D*, 78(7):071901, 2008.
- [169] B. Aubert et al. Measurement of the Branching Fractions and CP Asymmetry of $B^- \rightarrow D(\text{CP})K^-$ Decays with the BABAR Detector. *Phys. Rev. Lett.*, 92(20):202002, 2004.
- [170] A. Bornheim et al. Measurements of charmless hadronic two-body B meson decays and the ratio $B(B \rightarrow DK)/B(B \rightarrow D\pi)$. *Phys. Rev. D*, 68(5):052002, 2003.
- [171] <http://roofit.sourceforge.net>.
- [172] M. Oreglia. *A study of the reactions $\psi' \rightarrow \gamma\gamma\psi$* . PhD thesis, SLAC, 1980.
- [173] M. Needham. Private communication.
- [174] A. Martin-Sanchez et al. Private communication.

- [175] P. L. Chebyshev. Théorie des mécanismes connus sous le nom de parallélogrammes. *Mémoires des Savants étrangers présentés à l'Académie de Saint-Pétersbourg*, 7:539–586, 1854.
- [176] H. Albrecht et al. Search for hadronic $b \rightarrow u$ decays. *Phys. Lett. B*, 241(2):278 – 282, 1990.
- [177] W. Hulsbergen. Private communication.
- [178] P. A. Cherenkov. Visible Radiation Produced by Electrons Moving in a Medium with Velocities Exceeding that of Light. *Phys. Rev.*, 52:378–379, 1937.
- [179] J. Jelley. Cherenkov Radiation and its Applications, July 1955.
- [180] D. Green. The Physics of Particle Detectors. *Camb. Monogr. Part. Phys. Nucl. Phys. Cosmol.*, 12:1–361, 2000.
- [181] J. Jackson. *Classical Electrodynamics*. John Wiley and Sons Inc., 1975.
- [182] A. Pickford. Measurement of RICH Gas Refractive Index from Data. CERN-LHCb-2002-070.
- [183] C. G. Lester. Ring Identification and Pattern Recognition in Ring Imaging Cherenkov (RICH) detectors. *Nucl. Instrum. Meth. A*, 560:621–632, 2006.
- [184] A. Buckley. *A study of $B \rightarrow K\pi$ decays with the LHCb experiment*. PhD thesis, University of Cambridge, 2005. CERN-THESIS-2005-058.
- [185] A. Papanestis. The Calibration and Alignment of the LHCb RICH System. *Nucl. Instrum. Meth. A*, 595:248–251, 2008.
- [186] U. Kerzel and M. van de Klundert. Private communication.
- [187] S. Gorbunov and I. Kisel. Elastic Net for Standalone RICH Ring Finding. *Nucl. Instrum. Meth. A*, 559:139–142, 2006.
- [188] I. Antoniou, S.V. Gorbunov, V. V. Ivanov, I.V. Kisel, and E.V. Konotopskaya. Elastic Neural Nets for the Traveling Salesman Problem. 2000.

- [189] C. Thomas and M. John. Private communication.